EPR AND FLUORESCENCE STUDIES ON ERYTHROCYTE MEMBRANE SKELETAL PROTEINS: CDB3 AND ANKYRIN

By

Zheng Zhou

Dissertation

Submitted to the Faculty of the

Graduate School of Vanderbilt University

in partial fulfillment of the requirements

for the degree of

DOCTOR OF PHILOSOPHY

in

Molecular Physiology and Biophysics

May, 2006

Nashville, Tennessee

Approved:

Hassane S. Mchaourab

P. Anthony Weil

Phoebe Stewart

Terry P. Lybrand

Charles R. Sanders II

To My Family,

Though An Ocean Apart,

My Mind Is With You Everyday.

ACKNOWLEDGEMENTS

I would like to express my sincere gratitude to all those individuals for giving me selfless help. Without their support, the completion of my dissertation could not have been possible.

Most of all, I must thank my advisor, Dr. Albert H. Beth, who always has trust in me especially when my career was down the drain, has given me this great opportunity to pursue my Ph. D., has supported me financially and scientifically ever since. His rigorous scholarship in scientific research, insightful perception of biomedical problems, and excellent leadership both in our group and in our department has always been impressing on me. His encouragements and heuristic approaches are inspiring me and are of great benefit to my whole life.

I would like to acknowledge the members of my dissertation committee. They are Dr. Hassane Mchaourab, Dr. Phoebe Stewart, Dr. Tony Weil, Dr. Chuck Sanders and Dr. Terry Lybrand. Their expertise and guidance has helped me to overcome the obstacles along my training path towards the doctor degree.

I really appreciate Dr. Jim Staros, who came all the way down to Vandy from SUNY, for brainstorm sessions every month. It is a great pleasure to work with everyone in Dr. Beth's laboratory. Without their help, I could not have finished my degree in three years' lab work. Dr. Eric Hustedt has helped me to set up all the EPR experiments including spectral simulations and answered my naive questions on quantum physics. Dr. Chuck Cobb performed the preliminary purification of cdb3 and intrinsic tryptophan fluorescence experiment and always gives me great suggestions on biochemical

techniques. Suzanne Brandon has provided me tremendous assistance in protein purification and has taught me lots of things about American culture. Dr. Rich Stein has always been there for discussing my research as well as helped me with EPR spectral analysis. Dr. Nina Dixit's experience on molecular biology and cdb3 purification is very valuable to my research. Dr. Kristin Whitson who graduated from Dr. Staros' lab before me is like my big sister, giving me thoughtful suggestion on both scientific research and career choices.

In addition to my coworkers in Dr. Beth's lab, our collaborators have given me invaluable support. Without the generous help of Drs. Peter Fajer and Likai Song (National High Magnetic Field Laboratory, Tallahassee, FL), I would still be waiting for the pulsed EPR machine from Bruker. The bump checking program written by Susan DeSensi has facilitated the analysis of DEER results on cdb3. She is also making great progress on molecular dynamics simulation of spin labels.

Finally, none of these could have happened without the love and encouragement of my family. They are the source of my health, perseverance, optimism and happiness. As a kid, I was awed by my parents' dedication to heal the wounded and rescue the dying. Being a scientific researcher, my frustration and hesitation is thawed by their endless love. Words could hardly express my feeling to their gifts. Maybe I could quote Bertrand Russell, 'Three passions, simple but overwhelmingly strong have governed my life---the longing for love, the search for knowledge and the unbearable pity for the suffering of mankind.'

TABLE OF CONTENTS

Page

LIST OF TABLES

LIST OF FIGURES

Figure Page

LIST OF ABBREVIATIONS

53BP2	p53 binding protein
AE1	anion exchanger 1, as termed band 3
Badan	6-bromoacetyl-2-(dimethylamino)naphthalene
CAM	cell adhesion molecule
CD	circular dichroism
CD47	cell determinant marker 47
cdb3	cytoplasmic domain of band 3
CRASH	a syndrome of corpus callosum agenesis, mental retardation, adducted thumbs, spastic paraplegia and hydrocephalus, caused by L1 CAM mutation on the X chromosome
Cryo-EM	cryo-electron microscopy
CW	continuous wave
DEER	double electron electron resonance
DQC	double quantum coherence
dRTA	distal renal tubular acidosis
DSC	differential scanning calorimetry
EPR	electron paramagnetic resonance
FID	free induction decay
FRET	fluorescence resonance energy transfer
GAPDH	glyceraldehyde-3-phosphate dehydrogenase, G3PD
H_2DIDS	4,4'-diisothiocyanodihydrostibene-2,2'-disulfonate
HS	hereditary spherocytosis

INK4	Cyclin-dependent kinase 4 inhibitor A, p16
LW	Landsteiner-Wiener blood group
MTSSL	1-oxyl-2,2,5,5-tetramethyl-Δ3-pyrroline-3methyl methanethio-sulfonate spin label
NBC	Na^+-bicarbonate cotransporter
NDCBE	Na^+-dependent Cl^-/HCO_3^- exchangers
NiEDDA	nickel(II) ethylenediaminediacetate
NRDB	the nonredundant protein database
PBS	phosphate buffered saline
Rb	retinoblastoma protein
RBC	red blood cell
Rh	Rhesus blood group
SAO	Southeast Asian ovalocytosis
SDSL	site directed spin labeling
SDS-PAGE	sodium dodecyl sulfate polyacrylamide gel electrophoresis
SMART	Simple Modular Architecture Research Tool database
tdb3	transmembrane domain of band 3
Tiam-1	T-lymphoma invasion and metastasis 1, a GDP/GTP exchange factor (GEFs) for Rho GTPases, expressed in breast tumor cells (e.g., SP-1)
TPX	trademark for polymethylpentene
TRP	transient receptor potential

CHAPTER I

INTRODUCTION

Rationale for the Dissertation Research

Anion exchanger 1 (AE1), also known as band 3, is the most abundant integral membrane protein in human erythrocytes (Fairbanks *et al.* 1971). AE1 consists of two structurally and functionally distinct domains (Steck *et al.* 1976; Tanner *et al.* 1988; Lux *et al.* 1989). The transmembrane domain of band 3 (tdb3) exchanges bicarbonate and chloride anions across the membrane (Lepke and Passow 1976; Grinstein *et al.* 1978; Tanner 1997), which facilitates CO_2 excretion (Wieth *et al.* 1982; Jennings 1989) and regulates acid-base balance (Sterling and Casey 2002). The cytoplasmic domain of band 3 (cdb3) functions as one of the major organizing centers for various proteins associated with the lipid bilayer (Low 1986). These protein-protein interactions stabilize the red blood cell membrane and control cell flexibility and deformability (Peters *et al.* 1996; Southgate *et al.* 1996). The proteins that interact with cdb3 include membrane skeleton components, glycolytic enzymes, hemoglobin and protein kinase (Low 1986; Zhang *et al.* 2000). AE1 mutations are associated with hereditary spherocytosis (HS) (Gallagher and Forget 1997), Southeast Asian ovalocytosis (SAO) and distal renal tubular acidosis (dRTA) (Wrong *et al.* 2002). Although there is no atomic resolution structure of tdb3 available (Lemieux *et al.* 2002), the crystal structure of cdb3 (55-356) has been determined at the nonphysiological pH of 4.8 (Zhang *et al.* 2000). However, the highly packed dimer structure of cdb3 observed in the crystal lattice challenges the classical

view of a rod like domain with an axial ratio of 10:1 (Colfen *et al.* 1996). Given that the previous fluorescence studies and analytical ultracentrifugation experiments have suggested that cdb3 undergoes a reversible pH dependent conformational change (Appell and Low 1981; Low *et al.* 1984; Low 1986; Thevenin *et al.* 1994; Salhany *et al.* 1998), an evaluation of the high resolution structure of cdb3 under physiological condition is critical for understanding the functions of normal cdb3 and pathological changes caused by abnormal cdb3s at the molecular level. Even though several recent fluorescence-based studies are aimed at reconciling the elongated structure (Zhou and Low 2001; Pal *et al.* 2005a), major changes in fluorescence intensity occur also in a nonphysiological pH range (pH 8 ~ 10) and distance constraints from fluorescence data are limited by the size, orientation and number of reporter groups. In addition, the acidic N terminus of cdb3 that is critical for cdb3-protein interactions and the flexible C terminus of cdb3 that connects the membrane skeleton and cdb3 to tdb3 in the membrane have not been resolved in the crystal structure reported by Zhang et al (Zhang *et al.* 2000).

Given these controversies and unresolved regions, the first step of this dissertation study is focused on investigating the structure of cdb3 in solution at physiological pH using powerful biophysical tools, mainly based on site-directed spin labeling (SDSL) coupled with conventional continuous-wave electron paramagnetic resonance (CW-EPR) and advanced pulsed-EPR. This thesis work has shown that the EPR approach can not only successfully complement other biophysical studies but also circumvent certain limitations of traditional spectroscopic studies. For example, there is no upper limit for protein size with SDSL, and EPR can provide information on secondary structure, as well as tertiary structure in terms of orientation and distance constraints.

Based on the solution structure of cdb3 at neutral pH, we took the initiative to address pathophysiologically important mutations from the angle of structure biology. Among various cdb3 mutations, band 3 Tuscaloosa (P327R) appeared to have normal band 3 content but decreased protein 4.2 in red blood cell ghost membrane preparations (Jarolim *et al.* 1992). The P327R mutation occurs in the turning loop region that connects a β-strand and an α-helix of the highly conserved dimerization arm (Zhang *et al.* 2000). Dr. Low's group, who solved the cdb3 crystal structure, hypothesized that the P327R mutation might allow the continuation of the helix, and dissociate the cdb3 dimer (Low *et al.* 2001). In the P327R mutant, if the loop region or part of the loop builds extra turns of α-helix, the α-helix downstream of R327 and/or upstream in the β-strand may have relative movements toward or away from their counterparts in the other monomer. A series of biochemical and biophysical experiments have been carried out to characterize the effects of the P327R mutation on stability and structure of the cdb3 dimer. Again, EPR techniques have proven to be very advantageous to obtain a large number of distance constraints from 8 Å up to 50 Å.

Another important question is how the cdb3 dimer interacts with other proteins, organizes the membrane skeleton complex of band 3-ankyrin-spectrin, and thereby stabilizes the erythrocyte membrane. Ankyrins are multifunctional adapters that connect diverse transmembrane proteins and the spectrin skeleton in most tissues. Canonical ankyrins are comprised of three conserved domains: the ANK repeat domain, the spectrin-binding domain, the death domain and the highly diversified regulatory domain. The ANK repeat domain contains 4 subdomains, each with 6 ANK repeats. The ANK repeat motif serves as the scaffold for protein recognition and it is widely distributed

among diverse proteins. An array of the ANK repeats stacking together may provide the interface for protein-protein interactions (Mosavi *et al.* 2004). In spite of the fact that the crystal structure of 12 ANK repeats (ANK_D34) from ankyrin 1 subdomain 3 and 4 has been solved (Michaely *et al.* 2002), very little information about the band 3-ankyrin complex is known. SDFL (site-directed fluorescence labeling) experiments have been employed to map the interface between cdb3 and ANK_D34. These data strengthen our understanding about the organization of membrane skeleton proteins and promote new approaches to construct protein complexes using high resolution structures of each individual component.

The design of this dissertation is a comprehensive study of significant biological structural problems. This work is facilitated by biophysical methods. The highlights of this thesis work lie in not only that '...the double electron electron resonance data is the best reported for a true biological sample to date...' (quote from one of the reviewers for our first paper), but also that it provides a promising structural approach to elucidate the dynamics and function of normal and defective protein structures under physiological conditions.

Accompanied by the completion of the Human Genomic Project in 2003 and the ongoing progress in genomic studies of model organisms and important microbial pathogens, structural biology is entering a new era. Structural genomics equipped with high throughput methodology and whole genome analysis will provide tens of thousands of experimental protein structures and many more calculated comparative protein structure models in the near future (Burley 2000). How to evaluate the large amount of structural information, how to relate the protein structure to its function and how to

construct biomolecular complexes based on available structures have become emergent and prominent questions. This dissertation work presents a new approach for combining biochemical and biophysical studies to address these intriguing issues. Results are also presented for one specific case related to human disease.

Membrane Skeleton

Evolution of membrane skeleton proteins

Cell membranes form the boundary or permeation barrier between the intracellular and extracellular spaces. The membrane skeleton lines the cytoplasmic surface of the lipid bilayer, maintaining structural support to the membrane and facilitating intercellular signaling. In the aspect of evolution, spectrin-ankyrin based skeletal proteins are likely to appear in the genesis of metazoans, following the divergence of plants and fungi. The physiological roles of spectrins, ankyrins, and their associated proteins include mechanical stabilization at the cell level and tissue level, targeting of ion channels and cell adhesion molecules to specialized compartments (not limited to the intracellular face of the cell membrane), morphogenesis of epithelial tissues and orientation of mitotic spindles in asymmetric cell divisions (Bennett and Baines 2001).

Among the diversified cell types, the erythrocyte membrane skeleton remains the best studied and is regarded as the model system for other membrane-associated cytoskeletons. Although the basic structural and functional principles established in erythrocytes are likely to apply in other tissues, the protein components, interactions,

functions and localizations of the spectrin-ankyrin based structures are more diverse in other cell types.

Organization of erythrocyte membrane skeleton

The membrane skeleton of red blood cells is organized as a polygonal mesh network formed by 5 to 7 extended spectrin tetramers linked to short F-actin filaments at each node (junction point) (Liu *et al.* 1987) (Figure 1A). α Spectrin and β spectrin both contain large numbers of triple helical repeats that are associated laterally to form antiparallel heterodimers. The C-terminus of the β subunit and the N-terminus of the α subunit from one heterodimer interact with the N-terminus of the α subunit and the C-terminus of the β subunit from another heterodimer respectively to form a non-covalent triple helix, thereby constructing the spectrin heterotetramer (Figure 1B) (Cherry *et al.* 1999). The tetramer is the basic functional unit of spectrin, though higher oligomers are possible.

Two major types of linkages exist between spectrin tetramers and the lipid bilayer (Figure 1B). First, in the middle of the spectrin tetramer is the ankyrin-binding site, assigned to the triple helical repeat number 15 of β spectrin (Kennedy *et al.* 1991). Each ankyrin is capable of recruiting two anion exchanger dimers (Figure 1B). The anion exchanger is the organizing center of the protein macrocomplex including a number of integral and peripheral membrane proteins. The anion exchanger and ankyrin will be described next in detail. Second, at two ends of the spectrin tetramer, the N termini of β spectrin each composed of two calponin homology domains (CH1 and CH2) and the first two triple helical repeats (Rpt1 and Rpt2) are responsible for actin binding (Li and

Bennett 1996; Carugo *et al.* 1997; Moores *et al.* 2000). At each node, the short F-actin filament, containing 14-16 monomers, interact with approximately six spectrin tetramers. The positive (+) end of the F-actin filament is capped by adducin (Gardner and Bennett 1987). The negative (-) end of the F-actin filament is blocked by tropomodulin (Weber *et al.* 1994). A nonmuscle isoform of tropomyosin with similar length of the F-actin filament is associated with tropomodulin and the sides of the F-actin filament (Fowler and Bennett 1984). Protein 4.1 stabilizes the spectrin-actin complex (Tyler *et al.* 1980) and forms a complex with the transmembrane protein glycophorin C and the membrane-associated guanylate kinase protein p55 (Marfatia *et al.* 1995; Chang and Low 2001) (Figure 1B and 1C). In addition, the N terminus and C terminus of β spectrin have been reported to associate with phospholipids of brain membranes depleted of peripheral proteins (Steiner and Bennett 1988; Davis and Bennett 1994b). The N terminal interaction is inhibited by Ca^{2+}/calmodulin (Steiner *et al.* 1989). The C terminal region contains a pleckstrin homology domain (PH), which presumably interacts with phosphatidylinositol (PI) lipids (Wang and Shaw 1995).

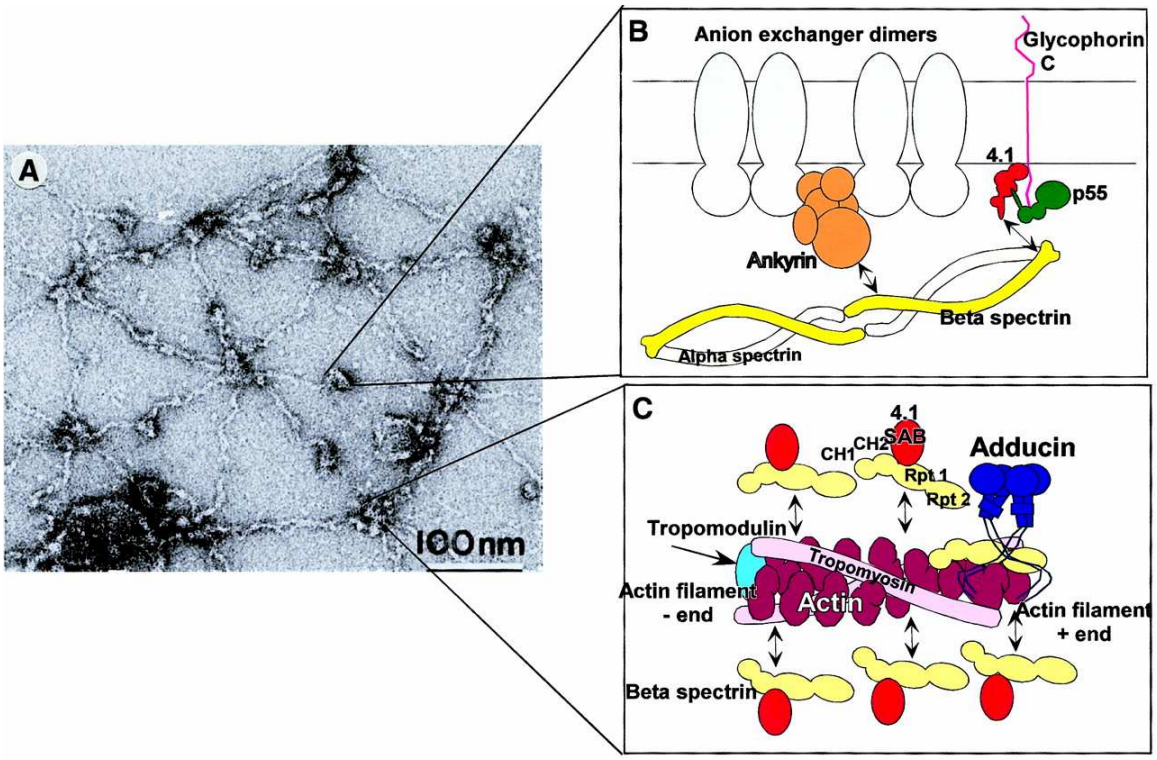

Figure 1. Organization of the erythrocyte membrane skeleton

A: Electron microscopy of the membrane skeleton. Spectrin tetramers are cross-linked at nodes (junction points) by short filaments of F-actin and 4.1/adducin. Approximately six spectrins interact with each node. Ankyrin/anion exchanger complexes are bound at the central region of the spectrin tetramers ankyrin/anion exchanger complexes. (Liu *et al.* 1987)

B: Membrane-cytoskeleton connections in erythrocytes. The 15th helical repeat of β-spectrin (yellow) interacts with ankyrin. Each ankyrin is capable of cross-linking two anion exchanger dimers (gray). At the NH_2-terminal region of β-spectrin is a binding site for protein 4.1 (red). Protein 4.1 forms a ternary complex with glycophorin C (pink) and guanylate kinase p55 (green).

C: The spectrin-actin junction. Short filaments of F-actin tether spectrin at the nodes shown in *A*. The negative (-) end of the filaments is blocked by tropomodulin, and nonmuscle tropomyosin lies along the filament. β spectrin binds actin via its NH_2-terminal CH domains (CH_1 and CH_2) and the first two triple helical repeats (Rpt 1 and Rpt 2). Approximately six spectrins would fit a short actin filament if the spectrins were arranged along the side of the filament. Spectrin-actin interaction is promoted by protein 4.1 and adducin. Adducin has a high affinity for the positive (+) end of the filaments. (Bennett and Baines 2001)

Mechanical properties of erythrocyte membrane skeleton

The primary role of the spectrin-ankyrin based membrane skeleton in erythrocytes is to provide mechanical support for the lipid bilayer and allow red blood cells to survive

in the circulation. Genetic mutations (see hereditary spherocytosis section) and targeted gene knockouts of components in the membrane skeleton have demonstrated their key structural role in animal models (Gilligan *et al.* 1999; Tse and Lux 1999). At the molecular level, the crystal structure of the α spectrin brain isoform in chicken has illustrated that the linker region connecting two triple helical repeats is a continuous α helix. Flexibility may be involved in a loop-to-helix transformation and/or bending of the linker region other than the disorder of the unstructured linker region (Grum *et al.* 1999). Atomic force microscopic studies of stretching a single spectrin tetramer chain showed that spectrin is a highly elastic biopolymer similar to a nonlinear spring: the extending force increases disproportionately with relative chain extension (Discher *et al.* 1998; Rief *et al.* 1999). Recently, similar studies on ankyrin repeats indicated ankyrin possesses spring properties too (Lee *et al.* 2006). Furthermore, micropipette aspiration of singe cells leads to deformation suggesting that the sustainable network extensions in dilation of a factor 2 (Discher *et al.* 1994). Together, the entire membrane skeleton underlying the lipid bilayer provides the red blood cell remarkable deformability and viscoelastic properties (Discher 2000). The function of the membrane skeleton related proteins involved in targeting membrane proteins will be discussed in the AE1 and ankyrin section in detail.

Disorders of spectrin-ankyrin based assembly

Physiological functions and clinical implications of spectin-ankyrin based structures are not limited to the erythrocyte model system. Gene knockouts of spectrins, ankyrins and their associated proteins of model organisms have indicated that these genes

are not essential at the level of fundamental cellular functions, but at the level of integration of cells into tissues. These genes are potential candidates in human disease because mutations in the encoded proteins may be compatible with survival but with impaired physiological functions. In addition to the direct implication of hereditary hemolytic anemia in erythroid tissues, known and potential disorders due to abnormal membrane skeleton may also occur in many non-erythroid tissues including brain, heart and skeletal muscle. The representative disorders are functional channelopathies due to defects in ankyrin-dependent targeting (see ankyrin section for detail), such as type 4 long QT cardiac arrhythmia (Schott *et al.* 1995; Mohler *et al.* 2003), use-dependent dystrophies of muscle and nerve due to defects in the spectrin-based transcellular mechanical coupling pathway, such as multiple sclerosis (Trapp *et al.* 1998), and abnormal nervous system development caused by defects of cell adhesion molecules (L1 CAM), such as CRASH syndrome (Fransen *et al.* 1995; Kenwrick *et al.* 2000; Bennett and Baines 2001).

Structure and Function of Anion Exchanger 1

AE1 in the bicarbonate transporter superfamily

Bicarbonate (HCO_3^-) is the primary pH buffer of the human body and the main waste product of cellular energy production. It also figures prominently in the processes used to secret acid. Therefore bicarbonate transporters, which catalyze the transmembrane movement of HCO_3^-, are key to cellular and whole-body pH regulation (Sterling and Casey 2002) and CO_2 delivery. They include proteins in the SLC4 (Solute

Carrier 4) human gene family and some members of the SLC26 gene family. The SLC4 gene family in mammals comprises Cl^-/HCO_3^- anion exchangers (AEs, e.g. AE1, AE2, AE3) and Na^+-dependent Cl^-/HCO_3^- exchangers (NDCBE) and Na^+-bicarbonate cotransporters (NBC) (Boron 2001; Alper *et al.* 2002; Sterling and Casey 2002). The SLC26 is a recently identified family whose gene products either have been shown to transport sulfate or have homology to sulfate transporters. Some of them function as bicarbonate/anion exchangers. Phylogenetic analysis shows that there is a distant evolutionary relationship between the SLC4 (AE/NBC) family of bicarbonate transporters and the SLC26 family though there is <20% amino acid identity between AE1 and any SLC26 family member (Markovich 2001; Sterling and Casey 2002).

The three AEs share 65% amino acid sequence identity in the transmembrane domain, varying in their N-terminal cytoplasmic domain. AE1 (band 3, SLC4A1) is the prototype member of the SLC4 gene family. It has been studied for decades and was first cloned in 1985 (Kopito and Lodish 1985). AE1 is largely expressed in the red blood cell membrane (eAE1 or band 3) and the basolateral membrane of the α–intercalated cell in distal and collecting renal tubules (kAE1) (Tanner 1997; Wrong *et al.* 2002). In contrast, AE2 is the most widely expressed AE isoform with highest expression in gastric parietal cells (Stuart-Tilley *et al.* 1994), choroids plexus epithelial cells (Alper *et al.* 1994), colonic surface enterocytes (Alper *et al.* 1999) and renal thick ascending limb cells (Martinez-Anso *et al.* 1994). AE3 is predominantly expressed in excitable tissues including brain (Kopito *et al.* 1989), heart (Linn *et al.* 1992) and retina (Kobayashi *et al.* 1994). The 10^6 copies of eAE1 per red blood cell constitute nearly 25% of the protein mass of red cell membranes (Fairbanks *et al.* 1971). kAE1 is a truncated isoform lacking

the N-terminal 65 residues (Kollert-Jons *et al.* 1993), which is transcribed under the internal promoter in intron 3 and translated from exon 5 (Sahr *et al.* 1994). In this thesis, eAE1 is the main focus. Band 3 can be cleaved into 2 independent structural and functional domains by mild proteolysis at Tyr359Lys360 (Lepke and Passow 1976; Grinstein *et al.* 1978). The N-terminal (1-360) 41 kDa cytoplasmic domain (cdb3) functions primarily as an anchoring site for other membrane-associated proteins. The C-terminal (361-911) 55 kDa transmembrane domain (tdb3) is thought to traverse the lipid bilayer 12-14 times and serves as an anion exchanger (Tanner 1997; Zhang *et al.* 2000).

Topology and function of AE1 transmembrane domain

The primary physiological role of AE1 in HCO_3^--Cl^- exchange has been well studied due to its abundance in erythrocytes. AE1 was first called band 3, which is the third major band identified in the gel electrophoresis pattern of SDS solubilized red cell membranes stained with Coomassie Blue (Fairbanks *et al.* 1971). It is involved in anion transport since anion transport inhibitors including the stilbenedisulfonates ($^3H_2$DIDS) predominantly bind to band 3 (Cabantchik and Rothstein 1972; Cabantchik and Rothstein 1974). A large body of evidence has indicated that the kinetics of obligatory one-for-one anion exchange (Hunter 1971; Knauf *et al.* 1977) exhibits a ping-pong mechanism, in which one anion moves in one direction, followed by another anion moving in the opposite direction (Gunn and Frohlich 1979; Furuya *et al.* 1984; Frohlich and Gunn 1986). One of the main features of the ping-pong model is the assumption that the protein can exist in two stable conformations: inward-facing and outward-facing, which is supported by steady state and pre-steady state transport measurements (Gunn and

Frohlich 1979; Jennings 1982) and the characteristics of various anion transport inhibitors, including stilbenedisulfonates (Furuya *et al.* 1984; Knauf *et al.* 1989). The turnover rate of Cl^- and HCO_3^- exchange is approximately 5×10^4 s^{-1} at 37ºC, one order of magnitude slower than a channel (Jennings 1989). More intriguing, both transmembrane anion (Cl^-) gradient (Jennings 1982; Furuya *et al.* 1984) and extracellular stilbenedisulfonates (Jennings *et al.* 1998; Tang and Casey 1999) can trap different conformations. This observation has contributed to studies of AE1 structure rearrangement during anion exchange.

Although the tdb3 has been relatively refractory to high level recombinant expression system in contrast to the cdb3, some structural information of band 3 is available for us to annotate its function due to its abundance in red blood cell membrane. A large body of evidence, including chemical cross-linking (Steck 1972; Staros and Kakkad 1983; Jennings and Nicknish 1985) and rotational diffusion (Nigg and Cherry 1979; Hustedt and Beth 1995), indicated dimeric association of band 3. Larger oligomers also exist under certain conditions, such as nonionic detergent $C_{12}E_8$ (Casey and Reithmeier 1991). Formation of tetramers has been implicated in binding to ankyrin (Thevenin and Low 1990; Michaely and Bennett 1995a). Fluorescence resonance energy homotransfer experiments demonstrated that the oligomeric states of band 3 in ghost membrane are substantially small oligomers such as dimers or tetramers (Blackman *et al.* 1998).

Hydropathy analysis combined with experimental evidence derived from covalent labeling studies with impermeable reagents, proteolysis and antibody epitope mapping has led to the model of 14 membrane spans (Tanner 1993; Tanner 1997). However, N-

glycosylation mutagenesis scanning (Asn-X-Ser/Thr) (Popov *et al.* 1997; Tanner 1997) and cysteine scanning (Zhu *et al.* 2003) suggested 12 transmembrane segments (Figure 2) and 13 transmembrane folding models, respectively. There is general agreement regarding the topology of most of the first eight transmembrane segments (residue~400-690) and intracellular loop 4 (IC loop 4, residue 690-700) (Kuma *et al.* 2002). Electron microscopy and three-dimensional image reconstruction of negatively stained two-dimensional crystals of dimeric tdb3 revealed a U-shaped structure (60×110×80 Å at 20 Å resolution) (Wang *et al.* 1993; Wang *et al.* 1994). The solution structures of the first and second transmembrane-spanning segments (405-424, 436-456) (Gargaro *et al.* 1994) and the sixth cytoplasmic surface loop (796-841) (Askin *et al.* 1998) in the 14-span model have been studied by solid-phase peptide synthesis and NMR spectroscopy. Three-dimensional crystals were obtained from trypsinized ghost membranes. Unfortunately, the high resolution crystal structure could not be resolved when diffraction was observed at 14 Å due to heterogeneity of native tdb3 (Lemieux *et al.* 2002).

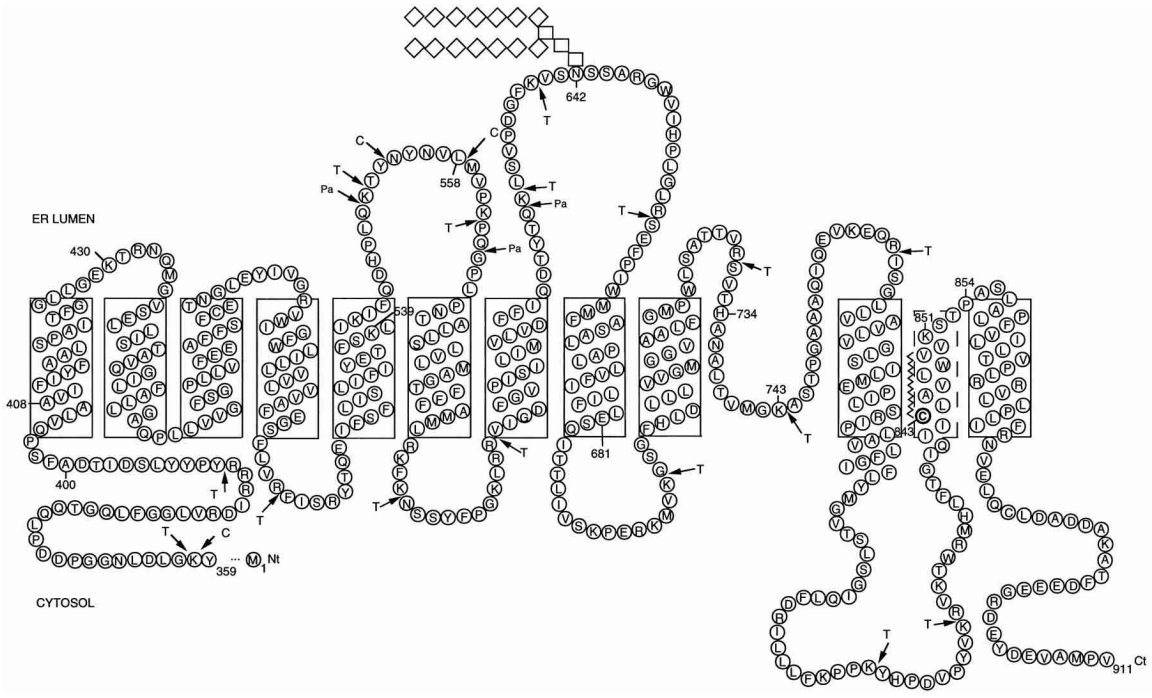

Figure 2. Hypothetical topology of AE1 transmembrane domain

Proposed topology of AE1 transmembrane domain containing 12 transmembrane segments determined from N-glycosylation scanning experiments. Proteolytic cleavage sites are indicated by T (trypsin cleavage site), C (chymotrypsin cleavage site) and Pa (papain cleavage site) The single endogenous N-glycosylation position is located at N642 in the extracellular loop 4. The palmitoylation site is also highlighted at residue C843 (Popov *et al.* 1997).

Structure and function of AE1 cytoplasmic domain

Band 3 forms the central element of a macrocomplex of integral and peripheral proteins in the red blood cell membrane (Figure 3) (Bruce *et al.* 2003). The primary function of cdb3 is to anchor the red blood cell membrane to the underlying membrane skeleton by binding ankyrin (Michaely and Bennett 1995a) and protein 4.2 (Rybicki *et al.* 1996). It is also shown that the acidic N terminus of cdb3 has interactions with protein 4.1 (Pasternack *et al.* 1985; An *et al.* 1996), glyceraldehyde-3-phosphatete dehydrogenase (GAPDH) (Rogalski *et al.* 1989), phosphofructokinase (Jenkins *et al.* 1984), aldolase (Murthy *et al.* 1981), hemoglobin (Walder *et al.* 1984; Salhany and

Cassoly 1989), hemichromes (Waugh and Low 1985) and the protein tyrosine kinase (p72syk) (Harrison *et al.* 1994). The C terminus of tdb3 binds carbonic anhydrase (CAII), forming a metabolon that transports HCO_3^- at the cytoplasmic face of band 3 (Sterling *et al.* 2001). It is suggested that the band 3 complex (band 3, GPA, protein 4.2, ankyrin, CAII, glycolytic enzymes, Hb, etc) and Rh protein complex (Rh-associated glycoprotein (RhAG), Rh polypeptides, GPB, CD47, LW) may form a macrocomplex in the RBC membrane and play a central role in red blood cell CO_2/O_2 exchange (Bruce *et al.* 2003). Cdb3 has recently been proposed to transfer nitric oxide groups from SNO-hemoglobin to the red blood cell membrane-cytosol interface (Pawloski *et al.* 2001; Pawloski and Stamler 2002). Through these interactions, AE1 plays important roles in maintaining red blood cell shape and mechanical stability (Low *et al.* 1991; Peters *et al.* 1996; Southgate *et al.* 1996), providing flexibility and viscoelasticity for erythrocytes (Moriyama *et al.* 1992; Schofield *et al.* 1992; Blackman *et al.* 2001), mediating anion transport (Malik *et al.* 1993), and modulating glucose metabolism (Low *et al.* 1993; Weber *et al.* 2004).

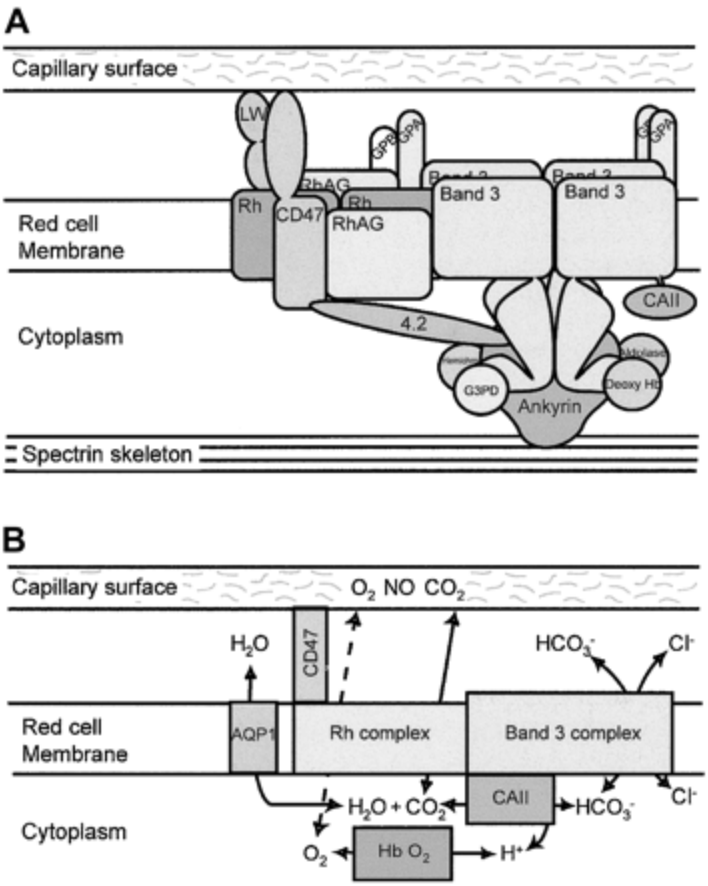

Figure 3. Band 3 macrocomplex and proposed gas exchange metabolon.

(A) Schematic diagram of the band 3 macrocomplex. Tetramers of band 3 are attached to the spectrin cytoskeleton through ankyrin. The acidic N-terminal region of cdb3 binds deoxy-hemoglobin, hemichromes, glyceraldehyde-3-phosphate dehydrogenase (G3PD), and aldolase. The short C-terminal cytoplasmic tail of band 3 binds CAII. The GPA dimer is close to the membrane domain of band 3. Protein 4.2 binds ankyrin, band 3, and CD47 (in human), providing one link between the Rh complex and the band 3 complex. CD47 and LW are closely associated with the Rh tetramers and may be involved in adhesive interactions with the capillary surface. The Rh tetramer associates directly with band 3. GPB associates with the Rh tetramers, and GPA and GPB may form heterotetramers, providing another link between the Rh complex and the band 3 complex.

(B) Proposed gas exchange metabolon in the RBC membrane. The model suggests that in systemic capillaries, CO_2 passes from the capillary endothelial cell to the RBC through the Rh proteins. CAII converts CO_2 and H_2O to HCO_3^- and a H^+, and HCO_3^- passes out of the RBC through band 3 in exchange for a Cl^-. The removal of HCO_3^- leaves a H^+ that promotes the local acidification in the vicinity of band 3 and the release of O_2 from oxy-hemoglobin by the Bohr effect. O_2 may then leave the RBC through the Rh gas channel and pass into the endothelial cells. The channeling of substrate through this metabolon reduces substrate loss by diffusion from the system. In the pulmonary capillaries, the system would be reversed. Water movements involved in the hydration/dehydration of CO_2 may be mediated by AQP1 (Bruce *et al.* 2003).

Several animal models of deficient AE1 have been described in the past few years. Hereditary total absence of AE1 in cattle due to a nonsense mutation (Arg646Stop) led to defective anion transport in red blood cells and marked spherocytosis with a distorted-disrupted membrane skeletal network and distinct invagination, vesiculation and extrusion of microvesicules (Inaba *et al.* 1996). However, mouse $AE1^{-/-}$, produced by targeted disruption of exon9-11, had normal or nearly normal membrane skeletal architecture. The phenotypes of severe spherocytosis and hemolysis result, in part, from spontaneously shedding membrane vesicles and tubules (Peters *et al.* 1996). Similarly, selectively inactivating mouse erythroid band 3 (eAE1) but not kidney AE1 (kAE1) by disrupting exon 3 confirmed the above observation of spherocytosis and hemolytic anemia despite a normal membrane skeleton. The erythroid band 3 null mice also showed retarded growth and died within two weeks after birth (Southgate *et al.* 1996). Those results suggested that AE1 does not regulate red blood cell membrane skeleton assembly in vivo but is essential for membrane stability through AE1-lipid interaction. Erythroid-specific mitotic defect and dyserythropoiesis associated with erythroid band 3 deficiency was reported in the study of a zebrafish mutant, retsina (ret), indicating that AE1 has a specific role in erythroid cytokinesis (Paw *et al.* 2003).

The crystal structure (2.6 Å) of cdb3 was reported at nonphysiological pH 4.8 (Figure 4 and Table 1). One unit cell contains four monomers. Each monomer belongs to the α+β fold class (10 α helices, 11 β strands and several loops), containing a large peripheral globular domain and a dimerization arm. The globular domain consists of a central β sheet surrounded by helices and loops, (Zhang *et al.* 2000). The compact quasi-symmetric dimer is stabilized by interlocking dimerization arms. The crystal structure

confirmed that cdb3 exists as a dimer over a wide range of protein concentration and solution conditions (Appell and Low 1981; Colfen *et al.* 1996). With the crystal structure of cdb3, it has become possible to locate important sites in cdb3 such as a β-hairpin loop as an ankyrin-binding motif (Chang and Low 2003) and the absent N-terminal residues 1-65 of kAE1, which results in deletion of a β-strand in the central β-sheet (Zhang *et al.* 2000). However, the reversible, pH-dependent conformational equilibrium was detected by intrinsic fluorescence, sedimentation analysis, differential scanning calorimetry, fluorescence resonance energy transfer, gel filtration chromatography, native gel electrophoresis, and a variety of functional assays (Appell and Low 1981; Low *et al.* 1984; Low 1986; Thevenin *et al.* 1994; Salhany *et al.* 1998). Furthermore, sedimentation measurements of cdb3 dimer at pH 8 predicted an axial ratio of 10:1 (Colfen *et al.* 1996), in contrast to 1.9:1 calculated from the atomic coordinates (Zhang *et al.* 2000). Thus, it is possible that the crystal structure of cdb3 determined at pH 4.8 does not accurately reflect the structure at physiological pH and, by extension, the structure of this domain in the intact erythrocyte (Zhou *et al.* 2005b).

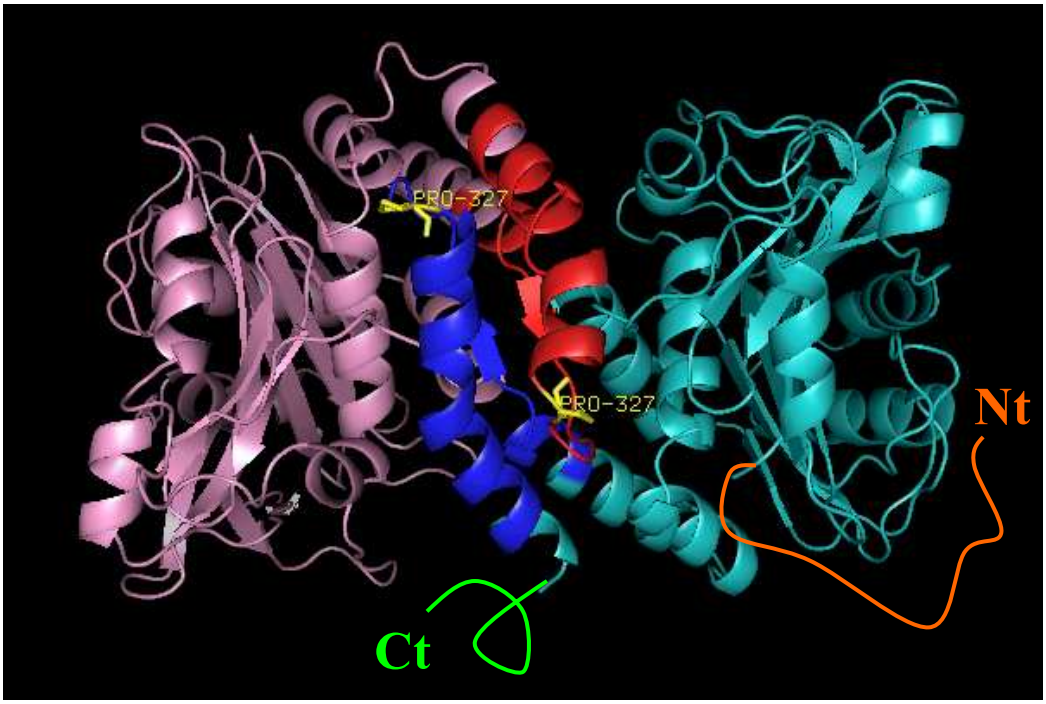

Figure 4. Crystal structure of recombinant cdb3 at pH 4.8

The cdb3 dimer is shown in ribbon diagram. Pink and cyan represent the globular domains of two monomers. Dimerization arms are in red and blue. The unresolved N terminus and C terminus of one monomer are labeled by Nt in orange and Ct in green, respectively. Proline 327 is drawn in yellow stick.

Table 1. Summary of cdb3 crystal structure

Residues	2° structure	3° structure or putative function
1-54		Poorly defined, 20 acidic residues, involved in most peripheral protein interaction (Low 1986)
202-211		Poorly defined by the electron density
357-379		Poorly defined by the electron density
55-290	Central β-sheet surrounded by α-helices and loops	Globular domain or peripheral protein binding domain
55-65	β-strand in central β-sheet	Missing in kAE1
176-185	β-hairpin loop	Ankyrin-binding, homologous to Na^+/K^+-ATPase (Chang and Low 2003)
291-303	α-helix and loop	Connector between dimerization arm and globular domain
304-357	α-helices, β-strand and loop	Dimerization arm, two arms from two monomers form the dimerization domain
291, 302	Loop	Putative hinges, depends on pH
105, 316	Trp-Asp H bond	Quench Trp fluorescence at low pH (Zhou and Low 2001)
201, 317	Cys-Cys disulfide bind	Treat with oxidizing agent and pH>7.5

Structure and Function of Ankyrins

Ankyrin family

The ankyrin family has a general role as an adapter between a variety of integral membrane proteins and the spectrin-actin network. Ankyrins are involved in targeting diverse proteins to specialized membrane domains in both the plasma membrane and the endoplasmic reticulum. In the mammalian genome, the ankyrin family includes ankyrinR (R for restricted; also called ankyrin 1), first characterized in erythrocytes (Lambert *et al.* 1990; Lux *et al.* 1990; Lambert and Bennett 1993); ankyrinB (B for broadly expressed, also called ankyrin 2), first studied in brain (Otto *et al.* 1991) and ankyrinG (G for general or giant, also called ankyrin3), independently discovered in nodes of Ranvier, axonal initial segments (Kordeli *et al.* 1995) and epithelial cells (Peters *et al.* 1995; Devarajan *et al.* 1996; Thevananther *et al.* 1998). In general, ankyrins are expressed in most tissues, and many cell types may have all three ankyrins (Bennett and Baines 2001).

Most ankyrin family members are modular proteins comprised of three highly conserved domains, which are the ANK repeat domain, the spectrin-binding domain and the death domain. There are also specialized domains that can result from alternative splicing. A large number of isoforms have different combinations of functional domains. These alternatively spliced variants can be categorized into three groups. Canonical ankyrins (190-220 kDa) have a N-terminal ANK repeat domain with 24 repeats, which can be further divided into 4 subdomains with 6 repeats each, a spectrin-binding domain, a death domain and a C-terminal regulatory domain (Figure 5, top panel). Giant ankyrins of 270-480 kDa have insertions of up to 2,400 amino acid residues, such as the tail

domain, between the spectrin-binding domain and the death domain. Small ankyrins of 26-120 kDa are missing various domains found in canonical ankyrins. The ANK repeat motif existing in hundreds of proteins is involved in intermolecular interactions with a diverse array of macromolecular targets as discussed in the following paragraphs (Bork 1993; Sedgwick and Smerdon 1999). The spectrin-binding domain of ankyrins is crucial for cellular localization at the cell membrane (Bennett and Stenbuck 1979a; Davis and Bennett 1984) and intracellular compartment (Mohler *et al.* 2004d) via mediating ankyrin-spectrin interactions. Death domains were first reported in Fas and the TNF receptor that participate in apoptosis pathways (Tschopp *et al.* 1999). The death domain of ankyrin may be involved in self-association and/or interactions with the death domain of other proteins, for example, the death domain association of ankyrinG and Fas promotes renal tubule cell death (Del Rio *et al.* 2004). The divergent regulatory domain may provide additional specificity for ankyrin function (Mohler *et al.* 2002). For instance, the regulatory domain of ankyrin-R modulates both binding of the anion exchanger and binding of spectrin (Hall and Bennett 1987; Davis *et al.* 1992). The possible functions of the tail domains are axonal targeting, separating the regulatory domain and the ANK repeat domain to deregulate protein interactions of the ANK repeats, and long-range connection between the death domain binding proteins and ANK repeat binding proteins (Bennett and Baines 2001).

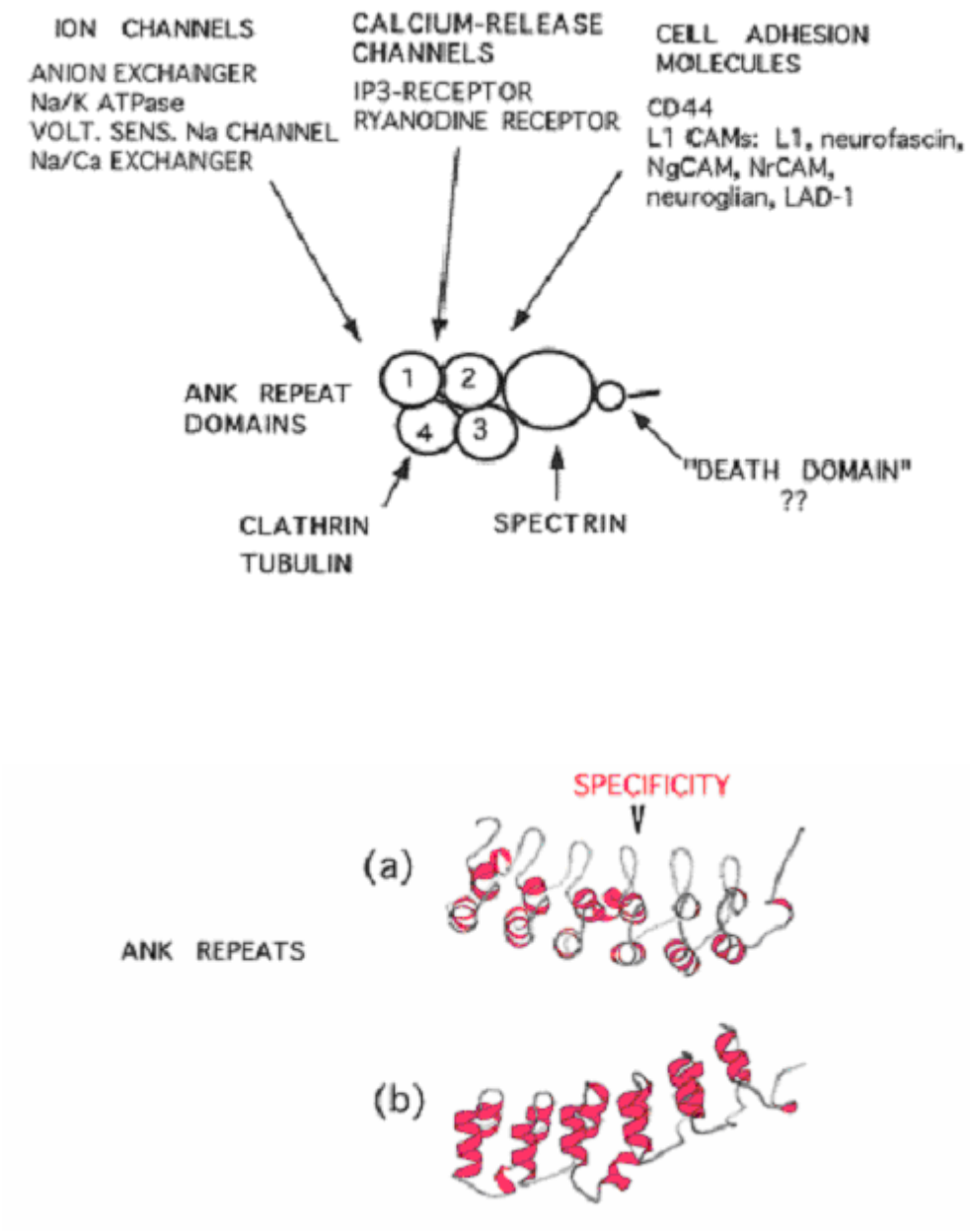

Figure 5. Schematic view of ankyrin-protein interactions

Top panel. Ankyrin domains and corresponding protein interactions. From left N terminus to right C terminus, ankyrin domains are ANK repeats, spectrin-binding domain, death domain and regulatory domain. The 24 ANK repeats form four subdomains, labeled by 1, 2, 3, 4. Each subdomain contains 6 ANK repeats (Bennett and Baines 2001).

Bottom panel. Ribbon structures of one subdomain of 6 ankyrin repeats in I-κB (Jacobs and Harrison 1998). The image (b) is from rotating image (a) by 90°.

Ankyrin-binding proteins

A prominent feature of the ankyrins is their ability to interact with structurally diverse, sequence unrelated proteins mainly through the ANK repeat domain. The spectrin-binding domain anchors the ankyrin and its binding partners onto the spectrin-based skeleton. The death domain may associate with death domains from ankyrins or other proteins involved in programmed cell death. The regulatory domain can also mediate ankyrin-protein interactions. Therefore, based solely on the wide spectrum of ankyrin-binding proteins, ankyrins have extensive potential to coordinate diversified cellular functions (Bennett and Baines 2001; Mohler and Bennett 2005a).

Biochemical and biophysical evidence, cellular colocalization and gene knockout studies have shown that ankyrin associates with a variety of proteins that can be categorized into four groups. First, ankyrin interacts with ion channels/transporters including anion exchangers AE1, AE2, AE3 (Bennett and Stenbuck 1979b; Bennett and Stenbuck 1979a; Morgans and Kopito 1993; Jons and Drenckhahn 1998), Na^+/Ca^{2+} exchanger (Li *et al.* 1993), voltage-dependent Na^+ channels (Srinivasan *et al.* 1988; Malhotra *et al.* 2000), Na^+/K^+ ATPase (Nelson and Veshnock 1987; Koob *et al.* 1988; Morrow *et al.* 1989), H^+/K^+ ATPase (Smith *et al.* 1993; Festy *et al.* 2001), and ammonia transporter RhBG (Lopez *et al.* 2005). Second, ankyrin associates with receptor mediated Ca^{2+} release channels such as the ryanodine receptor (Bourguignon *et al.* 1995; Tuvia *et al.* 1999), the IP_3 receptor (Bourguignon *et al.* 1993; Joseph and Samanta 1993; Tuvia *et al.* 1999), and the complex of IP_3 receptor 3 and sigma-1 receptor (Hayashi and Su 2001). Third, ankyrin also binds to cell adhesion molecules (CAM) that include CD44 (Kalomiris and Bourguignon 1988; Lokeshwar *et al.* 1994), and the L1 CAM family

(L1/neurofascin/NrCAM/CHL1/NgCAM) (Lundberg *et al.* 1992; Davis *et al.* 1993; Davis and Bennett 1994a; Dubreuil *et al.* 1996; Hortsch *et al.* 1998; Zhang *et al.* 1998a; Bouley *et al.* 2000). Finally, cytoplasmic proteins including tubulin (Bennett and Davis 1981; Davis and Bennett 1984; Davis *et al.* 1991), vesicle coating protein clathrin (Michaely *et al.* 1999), molecular co-chaperone Hdj1/Hsp40, Rho-GEF proteins obscurin (Bagnato *et al.* 2003; Kontrogianni-Konstantopoulos *et al.* 2003) and Tiam-1 (Bourguignon *et al.* 2000), β-spectrin (Bennett and Stenbuck 1979a) and death receptor Fas (Del Rio *et al.* 2004) also interact with ankyrin (Figure 5 top panel and summary in Table 2).

Ankyrin-based cellular pathways play critical roles in the development and maintenance of membrane domains in metazoan physiology (Mohler and Bennett 2005b). Dysfunction of the molecular adaptor ankyrins and their binding partners has significant effects on the integrity and stability of the spectrin lattice and the distribution of ankyrin-targeted proteins in many tissues, thus influencing the normal physiological function of erythrocyte, kidney, brain and heart.

AE1-ankyrinR-spectrin is one of the two major contacts between the membrane bilayer and the underlying membrane skeleton in erythrocytes. Defects and deficiencies of protein ankyrinR are one major cause of hereditary spheorcytosis (HS) in humans. Current estimates are that about 50% of HS cases among Caucasians are caused by ankyrinR mutations (Delaunay 2002) (More discussion in HS section).

Since ankyrins provide anchor sites for numerous ion transport proteins, it is predicted that defects in ankyrin-channel interactions may cause functional channelopathies equivalent in phenotype to mutations in the channels themselves that

cannot traffic to the correct cellular compartment. Indeed, ankyrinB loss-of-function mutations (E1425G in spectrin-binding domain (Schott *et al.* 1995; Mohler *et al.* 2003) and L1622I, T1626N, R1788W, E1813K in the regulatory domain (Mohler *et al.* 2004c)) cause cardiac arrhythmia due to loss of cellular targeting of Na^+/K^+ ATPase, Na^+/Ca^{2+} exchanger and IP_3 receptor to cardiomyocyte membrane domains. Although ankyrinB (-/-) mice exhibited severe disorders in nervous system development, myopathy, megacolon, atrophy of the thymus, and abnormal kidney development and did not survive the neonatal period (Scotland *et al.* 1998; Tuvia *et al.* 1999), ankyrinB (+/-) mice showed abnormalities in heart conduction, bradycardia and an increased Q-T interval provide models for autosomal dominant human channelopathies with loss-of-function mutations due to missorting rather than altering structures and biophysical properties of ion channels and transporters (Mohler *et al.* 2003; Mohler *et al.* 2004c). Furthermore, the severe disorders in the nervous system of ankyrinB(-/-) mice include hypoplasia of the corpus callosum and pyramidal tracts, dilated ventricules, all features of the CRASH syndrome (corpus callosum agenesis, mental retardation, adducted thumbs, spastic paraplegia and hydrocephalus) caused by L1 CAM mutations (Scotland *et al.* 1998). Hence, ankyrinB defect is a probable candidate for L1 CAM associated disorder in nervous system development.

AnkyrinG dependent targeting in neurons and cardiomyocytes is required for their normal function. The cerebellar-specific ankyrinG knockout mice display phenotypes of cerebellar dysfunction including decreased locomotion, abnormal gait and significant tremor (Zhou *et al.* 1998). AnkyrinG -/- causes Na_v channel isoforms and L1 CAMs improperly localized at critical membrane sites leading to abnormalities in cerebellar

Purkinje cell neuron action potentials (Zhou *et al.* 1998; Jenkins and Bennett 2001). Additionally, loss of ankyrinG-based localization of L1 CAMs destroys the gradient of 186 kDa neurofascin along the Purkinje axon initial segment-soma axis, resulting in abnormal directional basket axon growth and reduced GABAergic synapse formation, therefore abnormal development of interneuron circuit (Ango *et al.* 2004). The $Na_v1.5$ mutation E1053K in the ankyrin-binding motif is associated with Brugada Syndrome (a cardiac arrhythmia with $Na_v1.5$ loss-of-function and sudden cardiac death) due to loss of 190 kDa ankyrinG binding and failure of trafficking to the membrane surface of ventricular cardiomyocytes (Mohler *et al.* 2004b).

Table 2. Summary of ankyrin-associated proteins

Protein	Ankyrin	Ankyrin-domain	Primary Reference(s)
Anion Exchanger (AE1, AE2, AE3)	R	ANK	(Bennett and Stenbuck 1979b; Bennett and Stenbuck 1979a; Morgans and Kopito 1993; Jons and Drenckhahn 1998)
Na/K ATPase	B, G	ANK, SBD	(Nelson and Veshnock 1987; Koob *et al.* 1988; Morrow *et al.* 1989)
H/K ATPase	G	ANK, SBD	(Festy *et al.* 2001)
Na/Ca exchanger	R, B	ANK	(Li *et al.* 1993)
Na Channels	G	ANK, SBD	(Srinivasan *et al.* 1988; Malhotra *et al.* 2000)
RhBG, ammonium transporter	G	ANK	(Lopez *et al.* 2005)
RYR, Ryanodine receptor	B	ANK	(Bourguignon *et al.* 1995)
InsP3 receptor	B	ANK	(Bourguignon *et al.* 1993; Joseph and Samanta 1993)
Sig-1R, Sigma Receptors	B	?	(Hayashi and Su 2001)
CD44	R	ANK	(Kalomiris and Bourguignon 1988; Lokeshwar *et al.* 1994)
L1CAMs	R, B, G	ANK	(Davis *et al.* 1993; Davis and Bennett 1994a; Hortsch *et al.* 1998; Zhang *et al.* 1998a)
Beta-spectrin	R, B, G	SBD	(Bennett and Stenbuck 1979a)
Tubulin	R, B	ANK	(Bennett and Davis 1981; Davis and Bennett 1984; Davis *et al.* 1991)
Clathrin	R	ANK	(Michaely *et al.* 1999)
Tiam-1	R, G	ANK	(Bourguignon *et al.* 2000)
Hdj1/Hsp40	B	R-domain	(Mohler *et al.* 2004a)
Fas	G	D-domain	(Del Rio *et al.* 2004)
Obscurin	R	R-domain	(Bagnato *et al.* 2003; Kontrogianni-Konstantopoulos *et al.* 2003)

ANK: ankyrin repeat domain, SBD: spectrin-binding domain, D-domain: death domain, R-domain: regulatory domain (Mohler and Bennett 2005b).

The ANK repeat as the scaffold for protein recognition

Many proteins contain relatively short, tandem repeat motifs that act as building blocks that stack side by side, thereby constructing the underlying architecture of a modular, specific protein-binding interface. The most abundant repeat motifs are the

ankyrin repeat (ANK repeat), leucine rich repeat, armadillo repeat and tetratricopeptide repeat. Typically, these modular repeats do not recognize specific amino acid residue sequences but form an elongated surface. The variations in the adaptive surface residues determine the specificity for the repeat motif binding proteins.

The ANK repeat is a 33-residue motif that folds into two antiparallel α-helices followed by a β-hairpin or a long loop. Consecutive repeats, up to 34 of them, stack together to form a slightly curved shape. The β-hairpins or loops point toward the inner curve, roughly perpendicular to the helices (Mosavi *et al.* 2004). The protein-binding surface of most ANK repeats predominantly resides in the groove region. The ANK repeat has been found in a large variety of proteins spanning a wide range of functions. The SMART database contains 19,276 ANK repeat sequences in 3608 proteins identified from the nonredundant protein database (NRDB) (Schultz *et al.* 1998; Letunic *et al.* 2002). ANK repeats have been found in a myriad of proteins with functions that cover cytoskeleton integrity, cell cycle control, transcription, inflammatory response, development, cell-cell signaling, and transport activity. So far, no enzymatic function has been detected for any ANK repeats. A unifying trait of ANK repeats is to mediate specific protein-protein interactions. Besides ankyrins, the biologically significant proteins with ANK repeats include the INK4 tumor suppressor family (p15, p16, p18, p19), p53 binding protein (53BP2), I-κB which is an inhibitor of the transcription factor Nf-κB in inflammatory response, the signaling protein Notch that is involved in cell fate decisions during development, Gankyrin which is an oncoprotein and regulator of Rb, and TRP cation channel family in heat, cold, as well as mechanical sensing, etc. ANK repeat domains and other domains may often work together synergetically or

cooperatively, attributing at least partially to the functional diversity of ANK repeats (Mosavi *et al.* 2004).

Hereditary Spherocytosis

Physiology of the red blood cell

Commitment of pluripotent hematopoietic stem cells (HSC) to the erythroid lineage induces the production of red blood cells. This process is known as erythropoiesis (Perry and Soreq 2002). This process is mainly regulated by transcription starting from HSC, through BFU-E (burst-forming units-erythroid), CFU-E (colony-forming units-erythroid), Pro EB (proerythroblast), Baso EB (basophilic erythroblast), Poly EB (polychromatophilic erythroblast), Ortho EB (orthochromatic erythroblast), RET (reticulocyte), finally to RBC (red blood cell or erythrocyte). After the Poly EB stage, erythroid cells stop dividing and undergo highly specialized maturation. Mature erythrocytes have a lifetime of approximate 120 days in the peripheral circulation. The undivided cells exhibit a biconcave disk shape with an 8 μm diameter. It is very efficient at oxygen and nitric oxide delivery since it contains a large amount of hemoglobin and lacks internal organelles (Koury *et al.* 2002). At the molecular level, caspase-3 is involved in the enucleation process through a nonapoptotic pathway (Zermati *et al.* 2001; Carlile *et al.* 2004; Krauss *et al.* 2005). 15-lipoxygenase has been suggested to play a role in mediating the degradation of intracellular organelles in reticulocytes (Kuhn *et al.* 1990; van Leyen *et al.* 1998).

Proteins related to erythrocyte structure and function, including membrane proteins and membrane skeleton components, are translated and targeted to the correct location before red blood cell maturation. The membrane skeleton network (see membrane skeleton section for detailed description) endows the red blood cell with remarkable mechanical stability, deformability and elasticity. These properties are essential for the survival of erythrocytes in the circulation. During blood flow, the red blood cells experience a hydrodynamic pressure gradient. The pressure drops in the direction of the flow, while the higher pressure in the rear tends to compress the rear portion of the cell. As illustrated in Figure 6, in a 7 μm diameter capillary, red blood cells show a parachute shape along the blood flow axis and in a 4 μm diameter capillary, red blood cells are deformed to a torpedo shape (Skalak and Branemark 1969). Dysfunction in the membrane skeleton causes hereditary hemolytic anemia. Generally, defects in the 'horizontal' interactions, such as loss of spectrin heterodimer/heterotetramer associations (Tse *et al.* 1990) and deficiency of protein 4.1 (Feo *et al.* 1980; Tchernia *et al.* 1981; Conboy *et al.* 1986), are associated with hereditary elliptocytosis (HE) and hereditary pyropoikilocytosis (HPP). Defects in the 'vertical' interactions, such as an abnormal band3-ankyrin-spectrin junction, result in hereditary spherocytosis (HS) (Bennett and Baines 2001; Birkenmeier and Barker 2004).

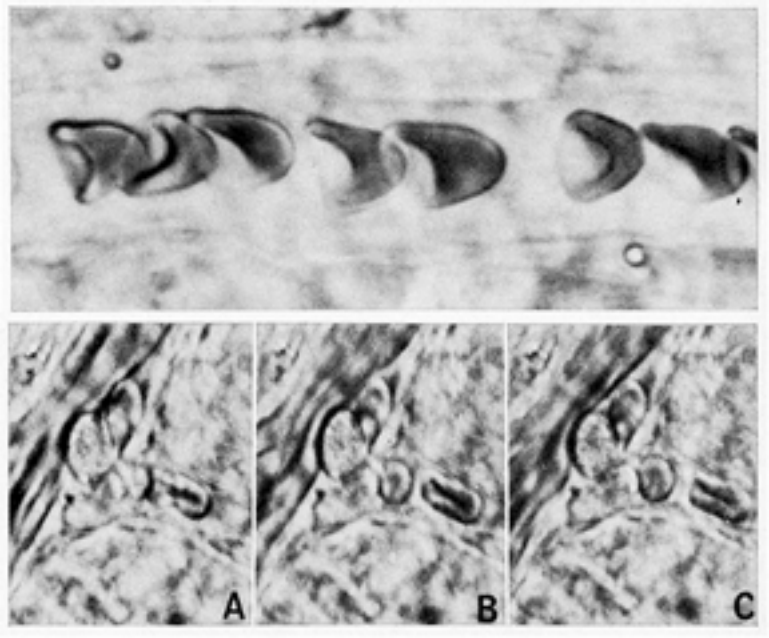

Figure 6. Deformation of red blood cells in capillaries

Top panel. The parachute shape of red blood cells in vivo in a 7 μm diameter capillary. The cell on the left showed in addition the tail-flap appearance.

Bottom panel. The U-shape or hollow torpedo shape of red blood cells in vivo in a capillary of about 4 μm diameter (Skalak and Branemark 1969).

Pathophysiology of HS

The incidence of HS is one family out 2,000-3,000. Among Caucasians, approximate 15-20% of HS cases result from band 3 defects and 50% of HS cases result from ankyrin defects (Delaunay 2002). In these HS patients, the erythrocytes appear as different degrees of spherical shape with decreased cell size instead of the normal size and biconcave-disk shape (Figure 7). These spherical red cells are more osmotically fragile and less deformable than normal red cells (Gallagher and Ferriera 1997; Tanner 1997). Mutations causing HS have been mapped to gene SPTA1, SPTB, ANK1, EPB42 and SLC4A1, which encode spectrin α-chain, spectrin β-chain, ankyrin, protein 4.2, and anion exchanger1 (AE1 or band 3), respectively (Delaunay 2002). These culprit genes are

critical for the ‘vertical’ interactions between the erythrocyte membrane skeleton and the lipid bilayer (Gallagher and Forget 1997).

The pathophysiology of HS has been viewed at the molecular, cellular and organic level. Defects of forementioned proteins weaken the support of membrane skeleton for the lipid bilayer. Disruption of the membrane skeleton and its attachment to the bilayer causes vesiculation of the unsupported surface components, leading to progressive reduction in membrane surface area and to the spherical cell shape (spherocyte). It can be mathematically proven that the sphere shape is the most economic way to contain identical volume with the least surface area. The rheologic consequence of continuingly decreased surface-to-volume ratio is destruction, or spherocytosis in the case of red blood cell. The spherocyte membrane is flexible but can only expand its surface area 2% to 3% before rupturing. As surface area is lost, the cell becomes increasingly less deformable. The HS red cells are further damaged (‘conditioned’) and ultimately removed in the spleen. The exact mechanism of splenic conditioning is not clear. Spherocytes are selectively sequestered at the cordal-sinus junction causing massively congested cords and relatively empty sinuses. Spherocytes are trapped in the metabolically inhospitable environment. High concentrations of acids and oxidants may exacerbate the loss of membrane, water and potassium. Membrane proteases probably activated by splenic retention may cause proteolysis to destabilize the membrane skeleton and accelerate the membrane loss. Macrophages also participate in ingesting trapped HS red cells (Eber and Lux 2004).

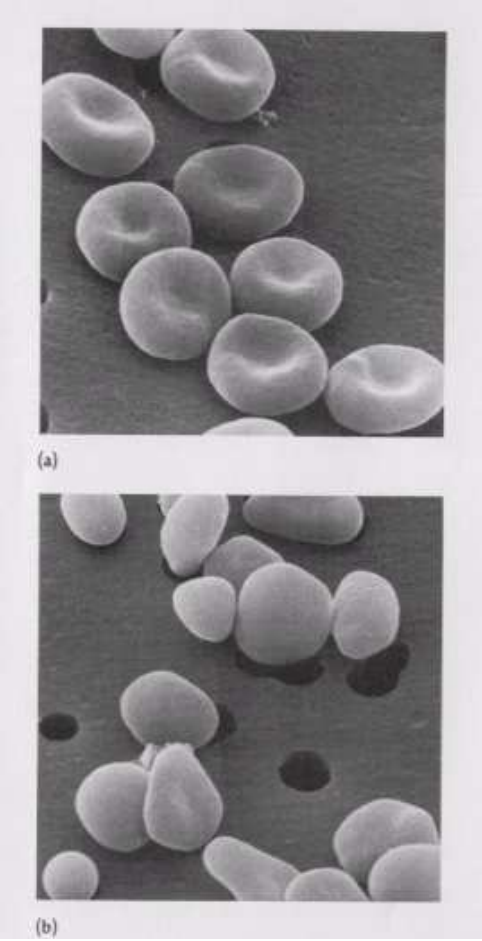

Figure 7. Scanning electron micrograph of red blood cells

(a): The normal biconcave disk appearance of erythrocytes at rest.
(b): Erythrocytes from a HS patient have spherical shape and smaller cell size (Agre *et al.* 1982).

Complications and therapies of HS

The complications of HS include anemic crises, splenomegaly, jaundice and cholelithiasis. Most patients with typical moderate HS suffer a few hemolytic crises, often triggered by viral infections. Splenomegaly occurs due to the destruction of rigid spherocytic red blood cells by the sieving function of the spleen. The increased bilirubin, the degradation product of released heme due to hemolysis, may produce jaundice and

gallstones ($\text{Heme} \xrightarrow{\text{heme oxygenase}} \text{Biliverdin} \xrightarrow{\text{biliverdin reductase}} \text{Bilirubin}$) (Bahar *et al.* 1999; Birkenmeier and Barker 2004).

Splenectomy is an effective therapy for HS patients in reducing hemolysis, increasing hemoglobin and prolonging the red cell lifespan, however, at the price of an increased risk of lethal sepsis and fulminant infection from parasites like babesia and malaria. Partial splenectomy sustains the phagocytic function of the splenic remnants and presumably decreases the risk of postsplenectomy sepsis, but maintaining function of the splenic remnants in humoral immunity is still unclear, thus immunizations and prophylaxis are still recommended to patients. It is possible that regrowth of the splenic remnants will eventually cause the recurrence of HS (Eber and Lux 2004; Lopez *et al.* 2005).

CHAPTER II

ELECTRON PARAMAGNETIC RESONANCE SPECTROSCOPY

Basic Principles of EPR

Zeeman effect and hyperfine interaction in EPR

In quantum mechanics, both angular momentum and energy are quantized. A rotating diatomic molecule possesses a set of stable rotational states. The total angular momentum L_{tot} has one of the values:

$$L_{tot} = [J(J+1)]^{1/2}\hbar,$$

where J is the primary angular momentum quantum number (J = 0, 1, 2, 3,…), $\hbar = h/(2\pi) \approx 1.054 \times 10^{-34}$ Js, (h is the Planck constant). For a rigid molecule, the energies of stable rotational states are:

$$E_J = BJ(J+1),$$

where B is the rotational constant for the molecule.

The information on the direction of rotation is given by the secondary (azimuthal) quantum number M_J (M_J = -J, -J+1, ...0, …, J-1, J). It contains 2J+1 possible components along an arbitrary direction. In the absence of an external field, each of the 2J+1 states with the same value of J, but different values of M_J, is degenerate, meaning that they have the same energy. In the presence of an external field, the degeneracy is lifted. Each of the 2J+1 sublevels has a slightly different energy, known as the Zeeman effect.

Each elementary particle possesses an intrinsic spin angular momentum. A single electron has a primary quantum number S (S = 1/2) and a secondary quantum number M_S (M_S = -1/2, 1/2). A nucleus ^{14}N has a primary quantum number I (I = 1) and a secondary quantum number M_I (M_I = -1, 0, +1).

In classical mechanics, an analog of an orbital magnetic dipole is a particle of mass *m* and charge *q*, rotating with velocity *v* in a circle of radius *r* in the *xy* plane. The magnetic moment along the direction *z* is

$$\mu_z = iA = \frac{q}{t}\pi r^2 = \frac{qv\pi r^2}{2\pi r} = \frac{q}{2m}mvr = \frac{q}{2m}l_z = \gamma l_z .$$

In quantum mechanics, the fundamental Wigner-Eckart theorem states that the magnetic moment and the spin angular momentum are proportional to each other (in units of ħ):

$$\hat{\boldsymbol{\mu}} = \gamma \hat{\boldsymbol{S}} = g\beta\hat{\boldsymbol{S}} ,$$

where the z component of the angular momentum operator $\hat{\boldsymbol{S}}$ obeys the eigenvalue equation

$$\hat{S}_z \underline{\phi_e} \quad M_S\phi_e \text{ (for electron-spin)}$$

$$\hat{S}_z\left|\phi_e\right\rangle = M_S\left|\phi_e\right\rangle \text{ or } \hat{S}_z\left|\alpha(e)\right\rangle = +\frac{1}{2}\left|\alpha(e)\right\rangle, \hat{S}_z\left|\beta(e)\right\rangle = -\frac{1}{2}\left|\beta(e)\right\rangle \text{ (Dirac notation)}$$

In case of a single unpaired electron, the component μ_z of the free electron spin magnetic moment along the direction of the magnetic field **H** applied along the direction *z* is given by

$$\mu_z = \frac{g_e e}{2m_e}M_S\hbar = \gamma_e\hbar M_S = -g_e\beta_e M_S ,$$

where g_e is the Zeeman (correction) factor for the free electron g_e = 2.00232, γ_e is the electron gyromagnetic ratio $\gamma_e = \frac{g_e e}{2m_e}$, the constant β_e is called electron Bohr magneton, which is the natural unit of electronic magnetic moment

$$\beta_e = \frac{|e|\hbar}{2m_e} = 9.2740154(31)\times 10^{-24}\,\mathrm{JT}^{-1}.$$

The interaction energy of the electron magnetic moment with a magnetic field B ($B = \mu_m H = \kappa_m \mu_0 H$, μ_m is the permeability, in vacuum $\kappa_m = 1$, $\mu_0 = 4\pi X10^{-7}$ $JC^{-2}s^2m^{-1}$ or $T^2J^{-1}m^3$) is calculated by the Hamiltonian (in units of ħ):

$$\hat{\mathcal{H}} = -\boldsymbol{B}^{\boldsymbol{T}} \cdot \hat{\boldsymbol{\mu}}$$

where the Hamiltonian operator $\hat{\mathcal{H}}$ obeys the time-independent Schrödinger equation:

$\hat{\mathcal{H}}\phi_k = E_k\phi_k$ (k : the labels of the eigenstates of the system, E : the total energy)

$$\phi_k^*\hat{\mathcal{H}}\phi_k = \phi_k^* E_k \phi_k = E_k \phi_k^*\phi_k \text{ or } \left\langle \phi_k \middle| \hat{\mathcal{H}} \middle| \phi_k \right\rangle = E_k \left\langle \phi_k \middle| \phi_k \right\rangle = E_k$$

ϕ_k^* is the complex conjugate of ϕ_k, for normalized functions $\left\langle \phi_k \middle| \phi_k \right\rangle = 1$

For a single unpaired electron, the possible values of M_S are +1/2 and -1/2, if the direction z is chosen to be along B, the two allowed energy states are:

$$E = -\mu_z B = g_e \beta_e M_S B = \pm\frac{1}{2} g_e \beta_e B$$

Transitions between the two electronic Zeeman levels can be induced by an electromagnetic field of the appropriate frequency v if the photon energy hv matches the energy-level separation ΔE, described by the resonance equation:

$$\Delta E = h\nu = g_e \beta_e B$$

The total magnetic field $\boldsymbol{B}_{effective}$ at each spin species is the vector addition of external field and local field:

$$\boldsymbol{B}_{effective} = \boldsymbol{B}_{external} + \boldsymbol{B}_{local}$$

The local fields can be categorized into two groups, 1) those that are induced by the external field and hence have a magnitude dependent on $\boldsymbol{B}_{external}$ and 2) those that are permanent and independent of $\boldsymbol{B}_{external}$ except in their orientations. When considering only the first type, such as one part of the electron spin-orbit coupling, an effective g factor can be introduced to replace g_e for the convenient practice of using the external magnetic field.

$$\boldsymbol{B}_{effective} = \boldsymbol{B}_{external} - \sigma \boldsymbol{B}_{external} = \frac{g}{g_e} \boldsymbol{B}_{external}$$

Thus, the corrected electron spin Hamiltonian becomes:

$$\hat{\mathcal{H}}_e = -\boldsymbol{B}^T \cdot \hat{\boldsymbol{\mu}} = -\boldsymbol{B}_{effective}^T \cdot \gamma_e \hat{\boldsymbol{S}} = \boldsymbol{B}_{effective}^T \cdot g_e \beta_e \hat{\boldsymbol{S}} = \boldsymbol{B}_{external}^T \cdot g \beta_e \hat{\boldsymbol{S}},$$

where the variable g takes account of field-induced local magnetic fields, for example, local fields originating from the orbital motion of the unpaired electron.

Nearby magnetic dipoles (electronic or nuclear) also contribute to the local field $\boldsymbol{B}_{local}$ that belongs to the second type. In EPR, the interaction between the unpaired electron and neighboring nuclear dipole moments is called nuclear hyperfine interaction. The spin Hamiltonian of isotropic hyperfine interaction (contact interaction) is given approximately by:

$$\hat{\mathcal{H}}_{iso} = -\frac{2\mu_0}{3} |\psi(0)|^2 \, \hat{\boldsymbol{\mu}}_{\boldsymbol{e}}^T \cdot \hat{\boldsymbol{\mu}}_{\boldsymbol{n}} = -\frac{2\mu_0}{3} g \beta_e g_n \beta_n |\psi(0)|^2 \, \hat{\boldsymbol{S}}^T \cdot \hat{\boldsymbol{I}} = A_0 \hat{\boldsymbol{S}}^T \cdot \hat{\boldsymbol{I}},$$

where $\psi(0)$ represents the electron wavefunction evaluated at the nucleus. A_0 is called the isotropic hyperfine coupling constant. For nitroxide spin labels, the unpaired electron

(S=1/2) interacts with the nitrogen nucleus ^{14}N (I=1). According to the selection rules $\Delta M_S = \pm 1$ and $\Delta M_I = 0$ for EPR absorption, there are three allowed transitions (Figure 8a). In the field-sweep experiment at constant frequency, resonance conditions satisfy the following equations (Figure 8b):

$$\Delta E = h\nu = U_{+\frac{1}{2},+1} - U_{-\frac{1}{2},+1} = g\beta_e B_k + A_0 = g\beta_e[B_k + (g_e/g)a_0]$$
$$\Delta E = h\nu = U_{+\frac{1}{2},0} - U_{-\frac{1}{2},0} = g\beta_e B_l$$
$$\Delta E = h\nu = U_{+\frac{1}{2},-1} - U_{-\frac{1}{2},-1} = g\beta_e B_m - A_0 = g\beta_e[B_k - (g_e/g)a_0]$$

Here $a_0 = A_0 / g_e\beta_e$ is the hyperfine splitting constant in magnetic-filed units. The first order energies of the six spin states (represented by $\left|M_S, M_I\right\rangle$) are:

$$U_{M_S,M_I} = g\beta_e B\hat{S}_z - g_n\beta_n\hat{I}_z + A_0\hat{I}_z\hat{S}_z$$

$$U_{+\frac{1}{2},+1} = \tfrac{1}{2}g\beta_e B - g_n\beta_n B + \tfrac{1}{2}A_0 \qquad U_{-\frac{1}{2},0} = -\tfrac{1}{2}g\beta_e B$$
$$U_{+\frac{1}{2},0} = \tfrac{1}{2}g\beta_e B \qquad U_{+\frac{1}{2},-1} = \tfrac{1}{2}g\beta_e B + g_n\beta_n B - \tfrac{1}{2}A_0$$
$$U_{-\frac{1}{2},-1} = -\tfrac{1}{2}g\beta_e B + g_n\beta_n B + \tfrac{1}{2}A_0 \qquad U_{-\frac{1}{2},+1} = -\tfrac{1}{2}g\beta_e B - g_n\beta_n B - \tfrac{1}{2}A_0$$

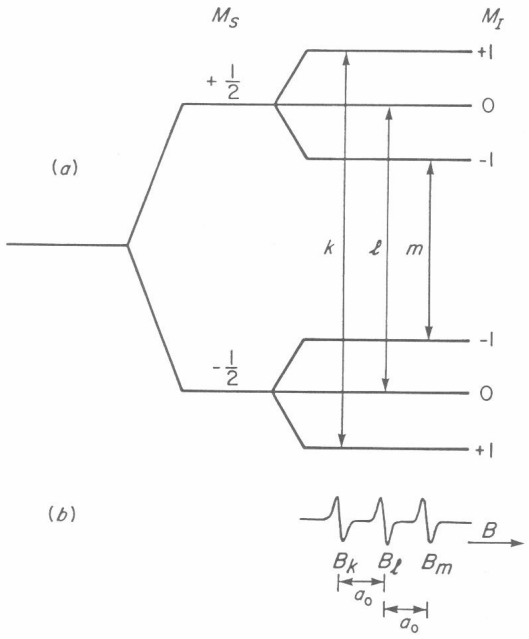

Figure 8. Energy levels of system with S = 1/2 and I = 1

(a) Energy levels and allowed EPR transitions at constant field for a system of S = ½ and I = 1. Energy levels are shown in horizontal lines marked with M_S and M_I value. The allowed EPR transitions between two different spin states are indicated by vertical arrows k, l m.

(b) Simulated EPR field-sweep spectrum. External fields B_k, B_l, B_m are the resonant fields corresponding to allowed transitions k, l, m respectively.

The ***g*** factor of the unpaired electron is de facto anisotropic due to the anisotropic environment provided by other electrons and nuclei in the magnetic species. Specifically, it is the admixture of the electron-spin angular momentum and a generally small amount of orbital angular momentum that gives rise to the anisotropy of the ***g*** factor. In the lab frame, the ***g*** tensor can be expressed as a 3×3 matrix. The ***g*** tensor can be diagonalized by an appropriate matrix transformation, which corresponds to a rotation of the axes. The new axes are called principal axes.

$$\boldsymbol{LgL^{-1}} = \boldsymbol{g}(diagonal) = \begin{bmatrix} g_{xx} & 0 & 0 \\ 0 & g_{yy} & 0 \\ 0 & 0 & g_{zz} \end{bmatrix}$$

The principal axes of nitroxide spin labels are generally well defined within the molecular frame of the nitroxide with g_{xx} along the N-O bond and g_{zz} perpendicular to the nearly planar nitroxide ring (Figure 9).

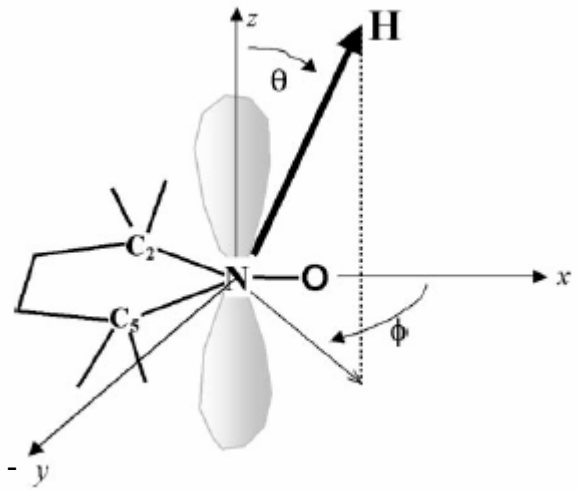

Figure 9. Geometry of the spin probe in the principal axes

H is the laboratory-frame magnetic field, oriented with spherical angles θ, φ with the nitroxide z axis (LaConte *et al.* 2002).

The anisotropy exists in the hyperfine splitting ***A*** as well as the Zeeman splitting ***g***. The interaction between an electron and nearby nuclear dipoles gives rise to the observed anisotropic component of hyperfine coupling. The dipolar interaction Hamiltonian is

$$\hat{\mathcal{H}}_{dipolar} = -\frac{\mu_0}{4\pi} g \beta_e g_n \beta_n \left[\frac{\hat{\boldsymbol{S}}^T \cdot \hat{\boldsymbol{I}}}{r^3} - \frac{3(\hat{\boldsymbol{S}}^T \cdot \boldsymbol{r})(\hat{\boldsymbol{I}}^T \cdot \boldsymbol{r})}{r^5} \right] \xrightarrow{\text{integrate over the spatial variables}} \hat{\boldsymbol{S}}^T \cdot \boldsymbol{T} \cdot \hat{\boldsymbol{I}}$$

The symmetric 3×3 matrix $\boldsymbol{T}$ can be diagonalized. For MTSSL, the diagonal elements correspond to the principal axes (Figure 9) due to the high local symmetry. The isotropic hyperfine term and anisotropic hyperfine term can be combined to generate the hyperfine tensor $\boldsymbol{A}$:

$$\boldsymbol{A} = A_0 \mathbf{1}_3 + \boldsymbol{T}$$

The complete spin Hamiltonian for the nitroxide spin label is

$$\hat{\mathcal{H}} = \beta_e \boldsymbol{B}^T \cdot \boldsymbol{g} \cdot \hat{\boldsymbol{S}} - g_n \beta_n \boldsymbol{B}^T \cdot \hat{\boldsymbol{I}} + \hat{\boldsymbol{S}}^T \cdot \boldsymbol{A} \cdot \hat{\boldsymbol{I}}$$

Electron spin-spin interaction

Two unpaired electrons in proximity interact with each other. The electron spin-spin interaction originates from electron-exchange interactions (through orbital overlap) and electron-electron dipole interactions (through space).

In a two-spin system, two angular momenta can be constructed in two equivalent ways, an uncoupled representation (S1, S2) and a coupled representation (S). There are four spin states for two unpaired electrons. In a paramagnetic center of moderate size, if two unpaired electrons interact appreciably, for example, the electron orbitals overlap, form a bond or rapidly collide with each other (Hustedt and Beth 1999), the system separates in energy into a triplet (S=1) and a singlet (S=0) state, represented by the spin Hamiltonian:

$$(\hat{\mathcal{H}}_{exch})_{iso} = J_0 \hat{\boldsymbol{S}}_1^T \cdot \hat{\boldsymbol{S}}_2$$

The exchange-energy operator J is a 3×3 matrix taking the electric (coulombic) interaction between the two unpaired electrons into account. In practice, only the isotropic part J_0 is considered important. The isotropic electron-exchange coupling

constant J_0 is the analog of the isotropic hyperfine coupling parameter A_0. The first approximation of J_0 is given by the exchange integral:

$$J_0 = -2 < \phi_a(1)\phi_b(2) \left| \frac{e^2}{4\pi\varepsilon_0 r} \right| \phi_a(2)\phi_b(1) > ,$$

where ϕ_a and ϕ_b are different normalized spatial molecular-orbital wavefunctions, evaluated while considering the electrons to be non-interacting, ε_0 is the permittivity of the vacuum.

The electron-electron dipole interaction is analogous to the anisotropic hyperfine interaction between electronic and nuclear magnetic dipoles. The magnetic dipole-dipole interaction is given by the Hamiltonian:

$$\hat{\mathcal{H}}_{ss}(\boldsymbol{r}) = \frac{\mu_0}{4\pi}\left[\frac{\hat{\boldsymbol{\mu}}_1^T \cdot \hat{\boldsymbol{\mu}}_2}{r^3} - \frac{3(\hat{\boldsymbol{\mu}}_1^T \cdot \boldsymbol{r})(\hat{\boldsymbol{\mu}}_2^T \cdot \boldsymbol{r})}{r^5}\right]$$

The spin Hamiltonian is given by replacing the magnetic-moment operators $\hat{\boldsymbol{\mu}} = g\beta\hat{\boldsymbol{S}}$

$$\hat{\mathcal{H}}_{ss}(\boldsymbol{r}) = \frac{\mu_0}{4\pi} g_1 g_2 \beta_e^2 \left[\frac{\hat{\boldsymbol{S}}_1^T \cdot \hat{\boldsymbol{S}}_2}{r^3} - \frac{3(\hat{\boldsymbol{S}}_1^T \cdot \boldsymbol{r})(\hat{\boldsymbol{S}}_2^T \cdot \boldsymbol{r})}{r^5}\right] = \hat{\boldsymbol{S}}_1^T \cdot \boldsymbol{D} \cdot \hat{\boldsymbol{S}}_2$$

As the $\boldsymbol{g}$ tensor and $\boldsymbol{A}$ tensor, the 3×3 matrix $\boldsymbol{D}$ can be diagonalized. Given that the interelectron distance is considerably larger than the size of the molecular orbital of the unpaired electron on the nitroxide, the $\boldsymbol{D}$ tensor is axially symmetric and the principle z-axis of the diagonalized $\boldsymbol{D}$ tensor aligns with the interelectron vector (Hustedt and Beth 1999). Interestingly, the electron spin-orbital coupling and generalized anisotropic exchange interaction give rise to the same form as $\boldsymbol{S} \cdot \boldsymbol{D} \cdot \boldsymbol{S}$.

Spin relaxation

In a two-level spin system, the ratio of α (upper level for electron Ms = +1/2) to β spins at thermal equilibrium follows Boltzmann's distribution:

$$\frac{N_\alpha}{N_\beta} = e^{-\frac{\Delta E}{kT}},$$

where $\Delta E = E_\alpha - E_\beta$ is the energy difference between the α and β states; k is the Boltzmann constant; and T is the absolute temperature at thermal equilibrium. The population difference between the two spin levels allows us to detect the resonance absorption.

Certain perturbations (for example the oscillating magnetic field B1) can shift the spin system away from thermal equilibrium. The spin system has the tendency to relax back to thermal equilibrium by transferring the excess energy to other degrees of freedom of the system. The rate of population change of the β state for this kinetic system is:

$$\frac{dN_\beta}{dt} = \frac{dn}{2dt} = N_\alpha W_{\alpha\beta} - N_\beta W_{\beta\alpha} = \frac{(N-n)}{2} W_{\alpha\beta} - \frac{(N+n)}{2} W_{\beta\alpha} = \frac{N(W_{\alpha\beta} - W_{\beta\alpha}) - n(W_{\alpha\beta} + W_{\beta\alpha})}{2}$$

where $N = N_\alpha + N_\beta$; $n = N_\beta - N_\alpha$; $W_{\alpha\beta}$ and $W_{\beta\alpha}$ is the downward and upward relaxation probabilities for electrons. The first-order kinetic equation may be rewritten as

$$\frac{dn}{dt} = \frac{N\left(\frac{W_{\alpha\beta} - W_{\beta\alpha}}{W_{\beta\alpha} + W_{\alpha\beta}}\right) - n}{\frac{1}{W_{\alpha\beta} + W_{\beta\alpha}}} = \frac{n_s - n}{T_1}, \text{ where } T_1 = \frac{1}{W_{\alpha\beta} + W_{\beta\alpha}}, \; n_s = N\left(\frac{W_{\alpha\beta} - W_{\beta\alpha}}{W_{\beta\alpha} + W_{\alpha\beta}}\right)$$

T_1 is called the spin-lattice relaxation time or longitudinal relaxation time. The solution of the differential equation $n(t) = n_0 + (n_s - n_0)(1 - e^{-\frac{t-t_0}{T_1}})$ describes the temporal decay of the excess energy, where the perturbation is applied along the arbitrary z direction at time t_0. The physical meaning of this solution lies in that n (and M_z, the bulk magnetization,

which is proportional to n) evolves exponentially from initial state n_0 toward steady state n_s ($\frac{dn}{dt} = 0$) with a rate constant $1/T_1$. T_1 is the time required for n to change by $(n_s-n_0)(1-e^{-1})$ and is related to the mean lifetime of a given spin-orientation state. The resulting lifetime broadening can be estimated from the uncertainty principle ($\Delta\omega\Delta t \approx 1$).

Other relaxation processes such as spin diffusion, characterized by T_2 (spin-spin relaxation time or transverse relaxation time) have the effect of varying the relative energies of the spin levels, rather than their lifetimes. In Cartesian space, T_2 can be used to describe the relaxation of the bulk magnetization M in the x-y plane (B is along the z axis. M_x and M_y usually relax with the same rate constant $1/T_2$). From Newton's Laws, the magnetic moment precessing in a magnetic field B will experience a torque T, $\hat{\boldsymbol{T}} = \hat{\boldsymbol{\mu}} \times \boldsymbol{B}$, $\because \frac{d\hat{\boldsymbol{L}}}{dt} = \frac{d\hat{\boldsymbol{S}}}{dt} = \hat{\boldsymbol{T}} = \hat{\boldsymbol{\mu}} \times \boldsymbol{B}$, $\therefore \frac{d\hat{\boldsymbol{\mu}}}{dt} = \gamma\hat{\boldsymbol{\mu}} \times \boldsymbol{B}$. This can be also deduced from quantum mechanics. Ensemble averaging of this equation ($\boldsymbol{M} = \frac{1}{V}\sum_i^N \boldsymbol{\mu}_i$) with relaxation effects leads to the fundamental Bloch equations. In a system where the sinusoidally oscillating magnetic field B1 ($B_{1x}=B_1\cos\omega t$; $B_{1y}=B_1\sin\omega t$; $B_{1z}=0$) is imposed in a direction perpendicular to the static magnetic field B (along z), the Bloch equations are

$$\begin{aligned}
\frac{dM_x}{dt} &= \gamma_e\left(BM_y - B_1 \sin\omega t\, M_z\right) - \frac{M_x}{T_2} \\
\frac{dM_y}{dt} &= \gamma_e\left(B_1 \cos\omega t\, M_z - BM_x\right) - \frac{M_y}{T_2} \\
\frac{dM_z}{dt} &= \gamma_e\left(B_1 \sin\omega t\, M_x - B_1 \cos\omega t\, M_y\right) - \frac{M_z - M_z^{\,0}}{T_1}
\end{aligned} \quad ,$$

where M_z^0 is the M_z value at thermal equilibrium only in the presence of B ($\frac{dM_z}{dt} = \frac{M_z^0 - M_z}{T_1} = 0,\ \boldsymbol{B_1} = 0$). To simplify the mathematical detail, it is convenient to visualize the time dependence of M in the rotating frame (Figure 10). The steady-state solutions of the Bloch equations in the rotating frame are:

$$M_{x\phi} = -M_z^0 \frac{\gamma_e B_1 (\omega_B - \omega) T_2^{\,2}}{1 + (\omega_B - \omega)^2 T_2^{\,2} + \gamma_e^{\,2} B_1^{\,2} T_1 T_2}$$

$$M_{y\phi} = M_z^0 \frac{\gamma_e B_1 T_2}{1 + (\omega_B - \omega)^2 T_2^{\,2} + \gamma_e^{\,2} B_1^{\,2} T_1 T_2} \quad ,$$

$$M_z = M_z^0 \frac{1 + (\omega_B - \omega) T_2^{\,2}}{1 + (\omega_B - \omega)^2 T_2^{\,2} + \gamma_e^{\,2} B_1^{\,2} T_1 T_2}$$

where $\omega_B = |\gamma_e B|$. For electrons ($M = \chi H = \chi B/\kappa\mu_0$), the dynamic magnetic susceptibilities can be defined via $\chi' = \kappa\mu_0 M_{x\phi} / B_1$ and $\chi'' = \kappa\mu_0 M_{y\phi} / B_1$. χ' and χ" represent the dispersion and absorption of the magnetic resonance transition. The actual spectrum is determined by the average power absorbed per cycle. Under field-sweep conditions, the absorption lineshape Y(B-Br) is a Lorentzian with half-width at half-height given by $\Gamma = \frac{1}{|\gamma_e| T_2} (1 + \gamma_e^{\,2} B_1^{\,2} T_1 T_2)^{1/2}$. The peak-to-peak width of the first-derivative equation Y' is $\frac{2}{\sqrt{3}}\Gamma$. When $\gamma_e^{\,2} B_1^{\,2} T_1 T_2 \ll 1$ (non-saturation), EPR central line width (ΔH_{pp}) is about $\frac{2}{\sqrt{3}|\gamma_e| T_2}$. For nitroxides, T_2 is in the 100-nanosecond range while T_1 is normally in the microsecond time range at ambient temperature, and therefore $T_2 < T_1$.

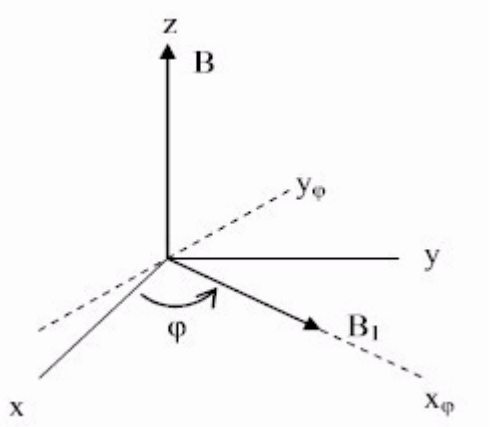

Figure 10. Rotating frame in relation to lab frame

The Cartesian coordinates (xyz) represent the lab frame. The static magnetic field **B** is along the z axis. The oscillating magnetic field $\mathbf{B_1}$, perpendicular to **B**, rotates about the **z** axis (azimuthal angle φ) in the x-y plane at the angular frequency ω. The rotating frame ($x_\varphi y_\varphi z$) also rotates at ω. Axis x_φ aligns with $\mathbf{B_1}$.

Spin dynamics

Any dynamic process (hindered rotation, molecular tumbling, chemical reaction, etc.) in and around the paramagnetic center can cause lineshape effects. Lineshape broadening can be classified into homogeneous broadening and inhomogeneous broadening. Homogeneous broadening arises from individual equivalent spins (a set of spins possess identical spin Hamiltonian parameters and identical time-averaged local fields over sufficiently short intervals). Spin lifetime (T_1), spin diffusion (T_2) and dynamic processes contribute to the homogeneous linewidth. Inhomogeneous broadening from nonequivalent spins is due to the variation of the external magnetic field and unresolved hyperfine structure.

Considering a simplified case of a dynamic process, a radical exists in either of two distinct forms or environments, $a \rightleftharpoons b$. Since the bulk magnetization M is proportional to the spin concentration, we can solve the generalized Bloch equations

containing first-order kinetic terms. Under the regimen of slow dynamics, average lifetime τ (>50ns) is longer than $\Delta\omega^{-1}$ ($\tau^{-1} = \tau_a^{-1}+\tau_b^{-1}$, $\tau_a = k_a^{-1}$, $\tau_b = k_b^{-1}$, k_a and k_b are the rate constants of the first-order kinetics, $\Delta\omega = |\omega_a-\omega_b| = |\gamma B_a-\gamma B_b|$, ω_a and ω_b are the Larmor frequencies of spin a and spin b, B_a and B_b are the corresponding resonance fields.) and we observe two separate lines. In the intermediate-rate region, as the lifetime decreases (5~50ns), the two lines are broadened and moving inward until merging into a single broad line. At the fast-rate limit, the lifetime τ is very short ($\tau\rightarrow 0$). According to the uncertainty principle $\Delta\omega\Delta t\approx 1$ (Δt represents the smallest average time period during which the state a and state b may be distinguished.), if the lifetime τ is less than Δt, then only one central line is observed since the two states cannot be distinguished. These dynamic lineshape effects can also be explained by spin density matrix. In general, dynamic fluctuations in the local field at the unpaired electron can cause lineshape effects. If the rate of the fluctuations is sufficiently slow, the EPR lines can be assigned to distinct spin species. Nevertheless, as the rate of the fluctuations increases, the EPR lines broaden and finally coalesce into a single narrowed line at the weighted-average frequency (Weil *et al.* 1994).

The conventional EPR operated in the 1 to 100 GHz frequency range is sensitive to dynamics on the nanosecond time scale. Fast motions (correlation time shorter than 1 ns, corresponding to sidechain motions of surface residues) effectively average the anisotropic magnetic interactions and give rise to sharp spectra. Intermediate motions (1 to 10 ns, corresponding to backbone motions of surface exposed loops and global tumbling of small globular protein (<20 kDa)) that partly average the anisotropic magnetic interactions lead to homogeneously broadened spectral features. Slow motions

(10 ns to 1μs, corresponding to global tumbling of large globular protein in solution) lead to resolution of the spectral features of the anisotropic magnetic interactions. Motions in the rigid limit (greater than 1 μs, corresponding to certain conformational changes in many proteins and global uniaxial rotational motions of transmembrane proteins in a lipid bilayer) result in powder spectra in CW EPR (Hustedt and Beth 1999). However, in biological systems, molecular motions in the proteins range from 10^{-14} s (bond vibration) to 10 s (local denaturation). Among these motions, most conformational changes directly coupled to the catalytic process occur on time scales longer than microseconds. For instance, allosteric transitions fall into an approximate time scale from 10^{-5} s to 1 s (Hammes 2002; Benkovic and Hammes-Schiffer 2003). Saturation transfer EPR (ST-EPR) spectroscopy has been employed to characterize the very slow motions from μs to ms. In ST-EPR, one narrow region of the inhomogeneously broadened EPR spectra is saturated. The recovery and spreading of the saturation via spin diffusion to the rest of the line is studied by monitoring secondary harmonic signals. The efficiency of the magnetization diffusion depends sensitively on the motional dynamics. Recent calculation shows that high field/high frequency (250 GHz) ST-EPR can increase the sensitivity to very slow rotational motions in the 1–100 ms time window (Hustedt and Beth 2004).

Pulsed EPR

In the presence of B and absence of B1 (see Figure 10), each individual electron spin magnetic moment undergoes the Larmor precession around the z direction in the "cone of uncertainty" at its Larmor frequency $\omega_B = 2\pi\upsilon_B = |\gamma_e B| = 2\pi g\beta B/h$. Considering a

set of independent electron spins, there is an excess number of electron spins (n) in the lower energy state ($|\beta\rangle$ Ms = -1/2) at thermal equilibrium, so the net bulk magnetization M is along the z axis. In the EPR experiment, circularly polarized B1 with a microwave frequency ω is applied perpendicular to B (in most cases, $|B_1| \ll |B|$). At resonance, $\omega_B = \omega$. By rotating the coordinate system at an angular frequency ω, B1 appears to be stationary (designated as the new x axis) and the Larmor precession around the z axis is seemingly absent. So B disappears in the rotating frame while M rotates about the x axis following the right hand rule at Rabi frequency $\omega_1 = |\gamma_e B_1|$. The rotation angle of M in the yz plane is depicted by the tip angle $\alpha = \omega_1 t_p = |\gamma_e B_1| t_p$, where t_p is the time length of applied B1 (Figure 11). In continuous wave EPR (CW-EPR), $t_p \rightarrow \infty$, B1 has the constant amplitude with time. B1 drives the spins back and forth between states Ms = ±1/2. If the T_1 relaxation process is adequate, n ($n = N_\beta - N_\alpha$) is maintained and a net absorption signal is observed. In pulsed EPR, t_p is in the range of several nanoseconds, excitation amplitude is time dependent $B_1(t)$. Pulses are often labeled by their tip angles such as π/2 pulse and π pulse. Different pulse sequences, a combination of different pulses at different time, can generate a wealth of information about the spin system. For example, the inversion recovery sequence (π-t-π/2-τ-π-τ) is used to measure T_1 and the spin echo sequence (π/2-t-π-t) is used to measure T_2 (Carrington and McLachlan 1967; Berliner and etc 1976; Weil *et al.* 1994; Levitt 2001).

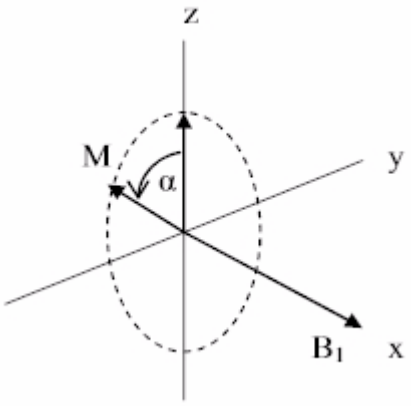

Figure 11. The tip angle of bulk magnetization M in the rotating frame

The oscillating magnetic field $\mathbf{B_1}$ is along the **x** axis (+x pulse). α is the tip angle of bulk magnetization **M**. The direction of the tip angle α follows the right hand rule.

Pulsed EPR greatly extends the realm of EPR studies, especially in biological sciences. As discussed above, pulsed experiments are powerful techniques to manipulate the spin system. Suppressing specific interactions and diluting the spectra in a multi-dimensional spectral space are of great advantage in revealing the information content of the spectra in complex spin systems (Prisner *et al.* 2001). Well-developed pulsed techniques include ESEEM (electron spin echo envelope modulation), DEER (double electron electron resonance) also called pulsed ELDOR (electron electron double resonance), DQC (double quantum coherence) and pulsed ENDOR (electron nuclear double resonance) etc. Four pulsed DEER will be introduced in the next section in detail.

Applications of SDSL in EPR

Site-directed spin labeling

EPR has been applied to study materials with electron spins such as metal ions and free radicals. Most free radicals are not very stable *in vivo* as they are susceptible to various redox reactions. Spin trap reagents and spin labels that are chemically stable are designed to solve this problem. In the case of MTSSL (methanethiosulfonate spin label), a pyrroline derivative, four methyl groups protect the unpaired electron in the pπ orbital of the nitroxide (Figure 12). Without these methyl groups, nitroxides can be easily reduced to the hydroxylamine by reducing agents such as ascorbic acid. In the regime of biological sciences, nitroxides can be covalently attached to different small molecules to serve as analogues of specific inhibitors, substrates, cofactors, agonists, antagonists, intermediate products, chemical modifiers and unnatural components (such as unnatural amino acids (Toniolo *et al.* 1995; McNulty *et al.* 2000)) of macromolecules. The spectral resolution can be enhanced by using isotopically substituted nitroxides (for example ^{15}N (I=1/2) with two hyperfine splitting peaks and deuteron ^{2}H (I=1) with a low magnetogyric ratio) (Hustedt and Beth 1999) or high field/high frequency which gives enhanced separation of the anisotropic $\boldsymbol{g}$ tensors. Nitroxides spin labels act as reporters that provide a wealth of structural and functional information of the free electron and its vicinity.

The development of molecular cloning and site-directed mutagenesis has greatly broadened the application of EPR in biophysical research. The basic strategy of SDSL (site-directed spin labeling) is mutating all the native nondisulfide bonded cysteine

residues to alanines or serines, replacing a native residue (or residues) at the desired position with cysteine, followed by modification of the reactive SH group with a selective nitroxide reagent (spin label). The widely used spin labels are the commercially available methanethiosulfonate derivatives that generate the disulfide-linked nitroxide side chains; for example, the unsaturated methanethiosulfonate spin label (MTSSL) produces the side chain R1 (Figure 12) (Hubbell and Altenbach 1994; Langen *et al.* 2000). SDSL has become a powerful technique to probe static and dynamic structural features of both water-soluble and membrane proteins.

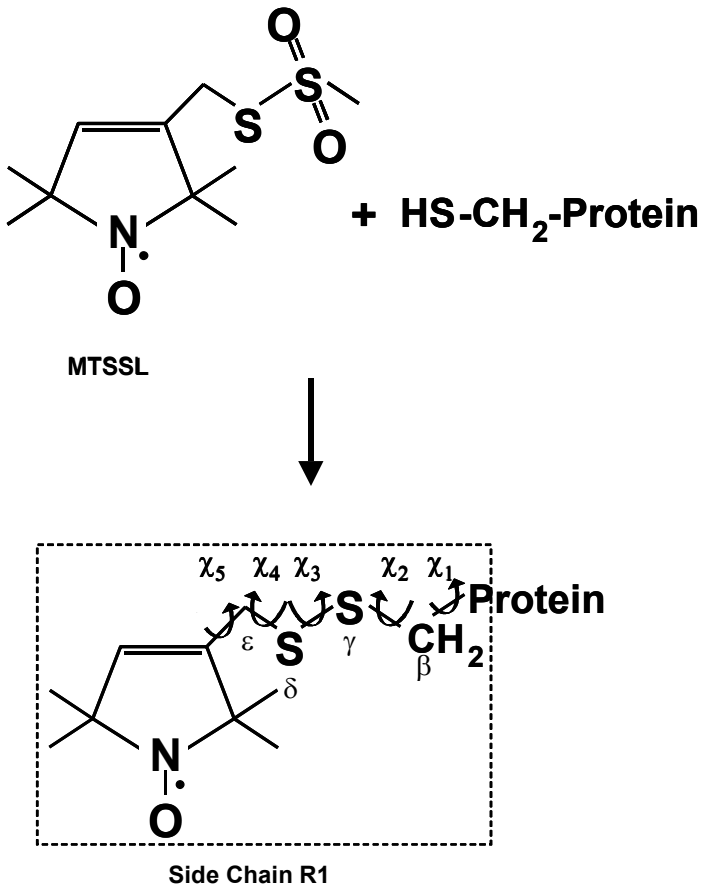

Figure 12. The reaction of the spin label with protein

The unsaturated methanethiosulfonate spin label reacts with a cysteine residue on a protein to generate the nitroxide side chain R1. Bond rotation angles $\chi 1$, $\chi 2$, $\chi 3$, $\chi 4$ and $\chi 5$ that relate the spin label to the Cα carbon of the protein are defined.

The effect of cysteine mutations on protein structure and function is potentially a significant perturbation and must be investigated on a case-by-case basis. However, nitroxide-derived spin labels are comparable in size to tryptophan and should have relatively trivial perturbation on protein structure and function, especially in most situations of labeling surface residues (Hubbell and Altenbach 1994). Buried sites may be less tolerant of spin labels and have low labeling efficiency, but some of them can accommodate the spin label in a well-constrained pocket. Mutations that affect protein function do not necessarily change the protein fold, so the overall protein structure is generally less affected than the protein function by spin labeling as long as the cysteine mutations do not affect protein folding. Since denatured proteins or aggregated proteins always have distinct EPR lineshapes, EPR lineshapes can in turn serve as an indication of protein native folding. In the vast majority of studies reported in the literature, cysteine substitution and subsequent spin-labeling with MTSSL has been minimally perturbing, particularly at surface exposed sites in a wide range of soluble and membrane bound proteins.

Side chain mobility

The CW-EPR lineshape is sensitive to dynamics on the nanosecond time scale. The sidechain mobility reflects the amplitude and the rate of constrained anisotropic rotational diffusion. The motions that affect the dynamics of the spin label moiety are the determinants of nitroxide sidechain mobility. The motion of free spin labels is mainly manifested by the rotational correlation time τ. Roughly speaking, τ measures the average lifetime of a particular spatial orientation of the nitrogen p orbital, and τ^{-1} is the rate of

the motion (Columbus and Hubbell 2002). As discussed in the spin dynamic theory, the exchange between different spin species can be viewed as a kinetic balance. Therefore, EPR lineshapes reflect rotational motions at different correlation times in solutions of different viscosity (Figure 13). When the spin label is tethered to a protein backbone (Figure 12), the motion of the nitroxide ring will have contributions from rotational diffusion of the protein, internal dynamic modes of the sidechain, tertiary interactions between the sidechain and its nearby groups, and local backbone fluctuations. The contribution of protein rotation and tumbling can be reduced by increasing solution viscosity without affecting the sidechain mobility relative to the protein at room temperature, for instance, 19 kDa T4L in 30% w/w sucrose (McHaourab *et al.* 1996). The χ_4/χ_5 model of R1 (Figure 12) on a helix, fully solvent-exposed with no contact with adjacent residues, has been proposed according to the data from crystallography, chemical modifications of R1 sidechain, and fitting of the spectra to models for the sidechain motion (McHaourab *et al.* 1996; Langen *et al.* 2000; Columbus *et al.* 2001). In this case, the internal anisotropic motion of the R1 sidechain is mainly limited to the torsional oscillation around dihedral angles χ_4/χ_5 since the S_δ sulfur atom forms a hydrogen bond with the C_α hydrogen atom (Langen *et al.* 2000). As a result, the motion of R1 is coupled to the motion of the backbone.

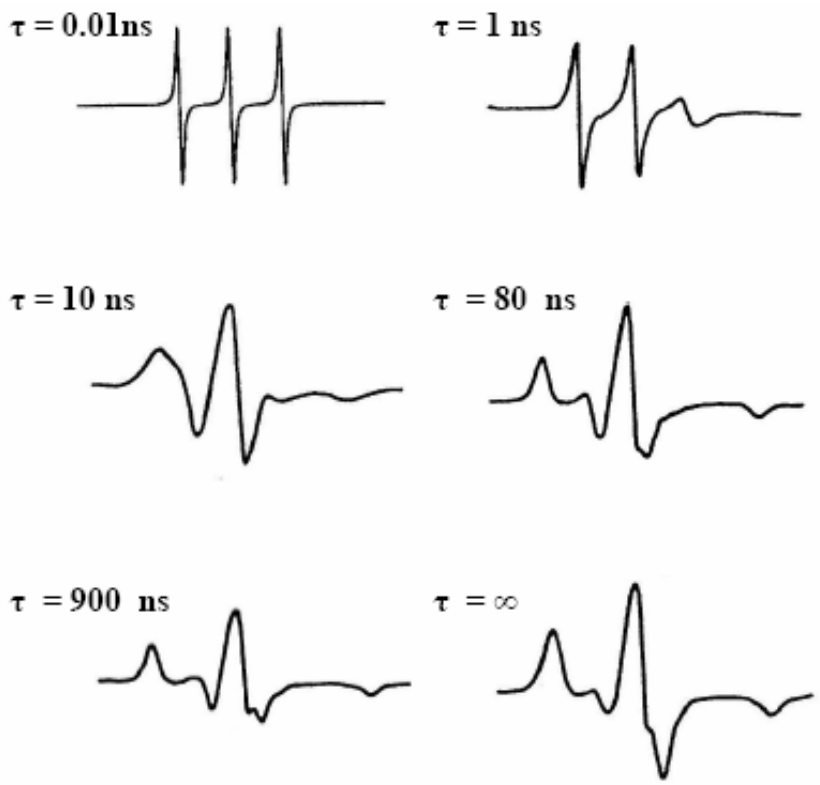

Figure 13. The effects of rotational motion on CW-EPR lineshapes

Simulated X-band CW-EPR lineshapes of a nitroxide spin label (^{14}N) at different isotropic rotation correlation times. Notice at the fast rotation limit ($\tau \rightarrow 0$), the first derivate EPR spectrum contains three sharp lines. (At high field resonance line, different spin species collapse into a single line.) As the rotation correlation time increases, the rate of motion decreases, both the central line and the overall spectrum are broadened. (At the intermediate correlation time $\tau \approx 10$ ns, the high field line is most broadened.) At the slow motion limit ($\tau = \infty$), the powder spectrum can be observed in a system of random oriented single crystals, where each of them experiences highly anisotropic motion. (At high field resonance line, different spin species are separated, and each of them is a single sharp line. In reality, we observe an inhomogeneously broadened packet.)

Completely parsing the movement of the nitrogen p orbital is of interest, especially the amplitudes and rates of the backbone fluctuation that are involved in protein function. Quantitative analysis of EPR spectra can be accomplished by spectra simulation, albeit there are limitations at the current stage, such as the difficulties of predicting the weak interactions between R1 and other neighboring groups without crystal structures of the spin-labeled protein. Hopefully this problem can be solved in the

near future through applying MD trajectory simulation and multi-frequency studies. Alternatively, semi-quantitative analysis of the EPR lineshape is very convenient and effective. The central line width ΔH_0 is the peak-to-peak first derivative width of the central resonance ($M_I = 0$). The spectral second moment $<H^2>$, calculated from

$$\langle \omega^2 \rangle = \int \omega^2 f(\omega) d\omega \Big/ \int f(\omega) d\omega$$ (Slichter 1980),

represents the breadth of the EPR spectra (Hubbell and Altenbach 1994; McHaourab *et al.* 1996; Columbus and Hubbell 2002). For highly disordered motion (high frequency and large amplitude), the EPR spectrum is three sharp lines similar to the spectrum of free spin labels at very short rotational correlation time τ. As the decrease in sidechain mobility and the increase in molecular ordering about any particular axis, both ΔH_0 and $<H^2>$ increase. When spectra contain multiple populations of mobility states, ΔH_0 is biased toward the mobile component whereas $<H^2>$ is biased toward the immobilized component. For highly ordered motion (low frequency and small amplitude, or large amplitude with extremely low frequency (the slow motion exceeds the EPR time window), or high frequency with extremely small amplitude (highly anisotropic motion)), the EPR spectrum resembles the spectrum of free spin labels at long rotational correlation time ($\tau > 80$ns). In the plot of the reciprocal second moment $<H^2>^{-1}$ versus the reciprocal central line width ΔH_0^{-1}, data points are roughly linear and clustered together according to the structural classes from the T4L crystal structure (Figure 14). The mobility decreases in the order from loop sites, helix surface sites, tertiary contact sites to buried sites, respectively. The loop sites are all located in the high mobility region, as expected for the disordered motion of R1 at such sites and the buried sites all have low mobility consistent with highly ordered motion of R1 in the densely packed interior. Overlaps

between tertiary interaction sites, helix surface sites and buried sites may partially be caused by the effects of backbone dynamics superimposed on the effects of tertiary interactions. ΔH_0 also shows periodic changes along elements of well-packed secondary structure. The periodicity, 3.6 for an α helix and 2 for a β strand, can be used to determine the secondary structure in combination with solvent accessibility data (see next section) (McHaourab *et al.* 1996). The sequence dependent mobility gradient may also distinguish propagated modulation of backbone dihedral angles from rigid body (collective modes) fluctuations in the backbone (Columbus and Hubbell 2002).

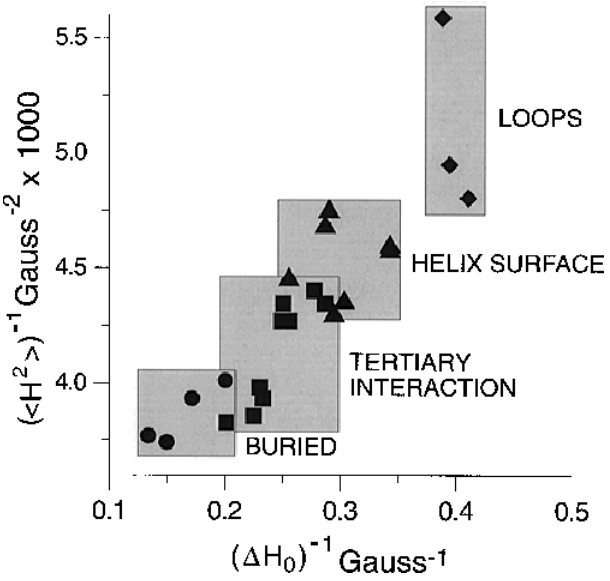

Figure 14. Correlation between sidechain mobility and protein structure

The reciprocal second moment $<H^2>^{-1}$ is plotted versus the reciprocal central line width ΔH_0^{-1} from the EPR spectra of selected non-terminal R1 sites on T4 lysozyme. Structural classes of buried sites, tertiary contact sites, helix surface sites and loop sites are represented by black circle, square, triangle and diamond respectively (McHaourab *et al.* 1996).

Solvent accessibility

The accessibility of side chain R1 to paramagnetic reagents is one of the most informative features of the protein fold. Solvent accessibility is determined from the collision frequency of the nitroxide with paramagnetic reagents such as O_2 and NiEDDA. The presence of the paramagnetic reagents provides an additional pathway for nitroxide spin relaxation, leading to a decreased spin-lattice relaxation time T_1. The change in T_1 of the nitroxide can be characterized by the rate of direct contact interaction between the nitroxide and the paramagnetic reagent, termed as the Heisenberg exchange rate, W_{ex}. In general, for exchange reagents with $T_{1R} < \tau_c$, where T_{1R} is the longitudinal relaxation time for the reagent R and τ_c is the encounter complex life time, Heisenberg exchange leads to equal changes in longitudinal relaxation time T_1 and transverse relaxation time T_2 of the nitroxide:

$$W_{ex} = \Delta(1/T_1) = \Delta(1/T_2) = 1/T_1 - 1/T_1^0,$$

where ^{0} indicates the absence of R.

The ideal exchange reagent R for determining solvent accessibility should have high solubility, should have limited accessibility to the interior of a well-packed protein, should be electrically neutral (EDDA forms a neutral chelate with Ni^{2+} at pH 7, whereas EDTA chelate has negative charges at pH 7), and should have similar size to the nitroxide itself. The exchange between the nitroxide and R should be in the strong exchange limit, where the rate is solely determined by the rate of diffusional encounter but not on details of the encounter complex. The only manifestation of the nitroxide/reagent interaction should be Heisenberg exchange, with little contribution from distance-dependent magnetic dipolar coupling. When $T_{1R} < \tau_c$, the nitroxide relaxation pathway from

nitroxide/reagent dipolar interaction can be ignored. Both O_2 and NiEDDA meet the above criteria as ideal exchange reagents (Altenbach *et al.* 2005).

For a bimolecular encounter between a small nitroxide N and an exchange reagent R in solution, the Heisenberg exchange frequency, W_{ex}, experienced by the nitroxide is given by

$$W_{ex} = k_{ex} C_R ,$$

where k_{ex} is the exchange rate constant, C_R is the concentration of R. In the strong exchange limit, where Heisenberg exchange is diffusion controlled,

$$W_{ex} = k_{ex} C_R = P_{\max} f k_D C_R = P_{\max} f 4\pi (N_A / 1000)(D_N + D_R) r_c C_R ,$$

where P_{max} is the maximum exchange efficiency (P_{max}=1, when strong exchange limit and $T_{1R} < \tau_c$ are satisfied), f is the steric factor, k_D is the diffusion-controlled rate constant, D_N and D_R are the diffusion constants for the nitroxide and reagent, respectively. The collision radius $r_c = r_N + r_R$, where r_N and r_R are the effective radii of the nitroxide and reagent respectively. For a nitroxide attached to a protein P, $D_N^P + D_R \approx D_R$, however, the nitroxide retains rotational degrees of freedom about the bonds of the tether. Since R and the nitroxide are still viewed as the colliding species, rather than R and the spin labeled protein, the definition of the collision radius, r_c, is retained. The local protein environment and interactions of the nitroxide with the protein may reduce the number of effective collisions below that characteristic of the free nitroxide in solution, and all such effects are collectively accounted for by the accessibility factor ρ. Thus, for a protein-attached nitroxide, W_{ex}^P in the strong exchange limit is

$$W_{ex}^P = k_{ex}^P C_R^P = \rho f k_D^P C_R = \rho f 4\pi (N_A / 1000) D_R r_c C_R$$

$$\rho = W_{ex}^P / (f k_D^P C_R) = (W_{ex}^P k_D) / (W_{ex} k_D^P) = (k_{ex}^P k_D) / (k_{ex} k_D^P) = [k_{ex}^P (D_R + D_N)] / (k_{ex} D_R)$$

For a small, electrically neutral but polar exchange reagent, ρ varies from 0 for a nitroxide buried in the protein interior to a limiting value of unity for a nitroxide at a completely exposed site on the protein surface.

Experimental determination of Heisenberg exchange rate W_{ex} can be based on the measurement of either T_2 or T_1. In the case of measuring the change of T_2, Heisenberg exchange leads to Lorentzian line broadening. The broadening can be determined as the width at half height of the Lorentzian line ($\Delta H_{1/2}$) that, when convoluted with the spectrum in the absence of collision, yields the interacting spectrum. Alternatively, the broadening can be directly measured as the increase in peak-to-peak central linewidth of the first derivative EPR spectrum ($\Delta\Delta H_{pp}$) under non-saturation condition.

$$\Delta H_{pp} = \frac{2}{\sqrt{3}|\gamma_e|T_2} = \frac{H_{1/2}}{\sqrt{3}}$$

$$W_{ex} = \Delta(1/T_2) = \gamma\Delta H_{1/2}/2 = \sqrt{3}\gamma\Delta\Delta H_{pp}/2$$

The convolution approach is more accurate for noisy spectra and small broadening. In the T_1-based methods, saturation recovery (SR) provides a direct determination of the nitroxide T_1 (Pyka *et al.* 2005) and CW saturation is an indirect way to detect the change of T_1. The inversion recovery pulse sequence (π-t-π/2-τ-π-τ) can also be used to measure T_1. In CW saturation EPR, the amplitude (A) of the first derivative central resonance (M_I=0) is measured as a function of microwave power (P), and the data fit to the function A(P)

$$A = \frac{cB_1}{(1+\gamma_e^2 T_1 T_2 B_1^2)^{\varepsilon}} = \frac{c\Lambda\sqrt{P}}{(1+\gamma_e^2 T_1 T_2 \Lambda^2 P)^{\varepsilon}} = \frac{I\sqrt{P}}{\left[1+\left(2^{1/\varepsilon}-1\right)P/P_{1/2}\right]^{\varepsilon}}$$

$$P_{1/2} = \frac{2^{1/\varepsilon}-1}{\Lambda^2\gamma_e^2 T_1 T_2}$$

Where c is an instrumental proportionality constant, B_1 is the microwave magnetic field component, γ_e is gyromagnetic ratio of the electron ($\gamma_e = 2\pi g\beta/h = g\beta/\hbar$), ε is a lineshape adjustment parameter (ranging from $\varepsilon = 1.5$ for the homogeneous saturation limit to $\varepsilon = 0.5$ for a completely inhomogeneous saturation limit), Λ is an instrumental factor ($B_1 = \Lambda P^{1/2}$), I is the scaling factor ($I = c\Lambda$), and $P_{1/2}$ is the half saturation power, which is the incident microwave power where the first derivative amplitude is reduced to half of its unsaturated value. For the common case where $W_{ex} << 1/T_2$, T_2 may be taken as a constant, and

$$\Delta P_{1/2} = P_{1/2} - P_{1/2}^0 = \frac{2^{1/\varepsilon}-1}{\Lambda^2\gamma_e^2}\left(\frac{1}{T_1T_2} - \frac{1}{T_1^0T_2^0}\right) = \frac{2^{1/\varepsilon}-1}{\Lambda^2\gamma_e^2T_2}\left(\frac{1}{T_1} - \frac{1}{T_1^0}\right) = \frac{2^{1/\varepsilon}-1}{\Lambda^2\gamma_e^2T_2}W_{ex},$$

$$\therefore \Delta P_{1/2} \propto W_{ex}/T_2 \propto W_{ex}\Delta H_{pp}$$

$$\therefore \Delta P_{1/2}/\Delta H_{pp} \propto W_{ex} \propto \rho$$

Although $\Delta P_{1/2} / \Delta H_{pp}$ is proportional to W_{ex}, it also depends on properties of the resonator through Λ. To reduce this dependency and standardize measurements from different resonators, a dimensionless accessibility parameter Π is defined as

$$\Pi = \frac{\Delta P_{1/2}/\Delta H_{pp}}{(P_{1/2}/\Delta H_{pp})_{DPPH}} = \alpha W_{ex}$$

DPPH is selected as the reference to normalize for variations in resonator efficiency. (Altenbach *et al.* 2005)

The local protein environment has a large effect on the collision frequency between the nitroxide and the exchange reagent. Therefore, sidechain solvent accessibility is very sensitive to the local environment of the nitroxide. For example, if an α helix or a β strand experiences amphipathic environments along its sequences in a

periodic pattern, the accessibility Π is likely to show an approximate periodicity of 3.6 or 2, respectively. Compared to buried sites, solvent exposed side chain R1 has high accessibility to a water-soluble paramagnetic reagent (Figure 15a) as well as possible high mobility. Interestingly, the nonpolar reagent O_2 has a gradient across the lipid bilayer with highest [O_2] at the middle of bilayer, while the polar reagent NiEDDA is membrane-impermeable. Thus oxygen accessibility of a transmembrane helix shows a 3.6 periodicity with the highest value in the middle of the bilayer, and NiEDDA accessibility is close to zero at sites buried in the bilayer (Figure 15b). When one face of an α helix is solvated by the aqueous environment (high Π_{NiEDDA}, low Π_{O2}), and the other face of the α helix is in contact with the hydrocarbon interior of the lipid bilayer (low Π_{NiEDDA}, high Π_{O2}), the sinusoidal curves of Π_{NiEDDA} and Π_{O2} are 180° out of phase (Figure 15b, c). The application of solvent accessibility is a powerful tool not only in probing the secondary structure, tertiary structure and protein folding such as water soluble protein α-crystallin (Berengian *et al.* 1997) and voltage dependent potassium channel KvAP (Cuello *et al.* 2004) (Figure 15), but also in detecting conformational changes in dynamic processes like receptor activation and channel gating, for instance, G protein coupled receptor rhodopsin (Farrens *et al.* 1996), pH gated K^+ channel KcsA (Perozo *et al.* 1999), vitamin B12 transporter BtuB (Merianos *et al.* 2000), mechanosensitive channel MscL (Perozo *et al.* 2002), and multidrug transporter MsbA(Dong *et al.* 2005).

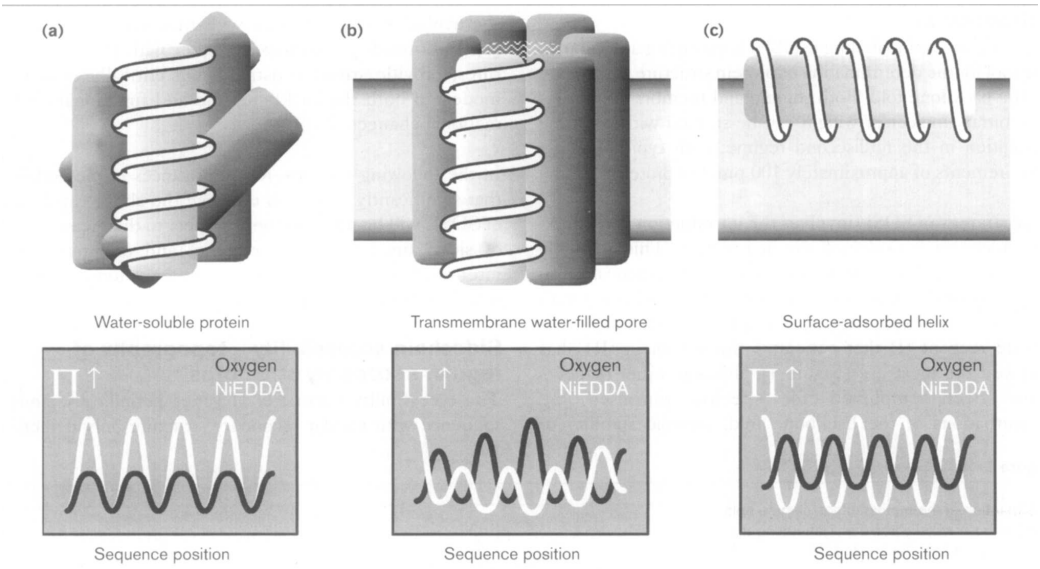

Figure 15. Solvent accessibility on model systems

(a): an α helix on the surface of a water soluble protein. Π parameters along the α helix repeat every 3.6 residues with maximal values at solvated sites and minimal values at buried sites. Π_{NiEDDA} (gray line) has stronger amplitude and is in phase with Π_{O2} (black line).

(b): a transmembrane α helix around a water-filled pore. O_2 is highly soluble in the membrane with a gradient towards the middle of the lipid bilayer. Thus besides the period of 3.6, Π_{O2} has another important signature: the maximal value at the middle of the membrane. Nitroxides exposed to solvent outside lipid bilayer have highest NiEDDA accessibility. When nitroxides are in the lipid environment, Π_{NiEDDA} is minimal (close to zero) since NiEDDA is polar and membrane-impermeable. At the portion of the α helix facing the water-filled pore, nitroxides experience intermediate NiEDDA accessibility and lowest O_2 accessibility. All of this information is valuable for determining the lipid-solvent interface and the orientation of the transmembrane helix.

(c): a horizontally surface-attached α helix. Nitroxides buried in the membrane have high Π_{O2} and low Π_{NiEDDA}, vise versa for the solvent-exposed sites. (Hubbell *et al.* 1998)

Spin-Spin distance

Modern EPR techniques can measure the distance between two spins from 8 Å up to 80 Å (Jeschke 2002b). CW-EPR can detect the electron spin-spin distance in the range of 8 Å to 25 Å where the spin-spin interactions are larger than the inhomogeneous linewidth of singly labeled samples. Pulsed EPR is able to cover the electron spin-spin

distance from 17 Å to 80 Å. The spin Hamiltonian for two interacting nixtroxide spin labels is given by

$$\hat{\mathcal{H}} = \beta_e \boldsymbol{H_0} \cdot \boldsymbol{g_1} \cdot \hat{\boldsymbol{S}}_1 + \beta_e \boldsymbol{H_0} \cdot \boldsymbol{g_2} \cdot \hat{\boldsymbol{S}}_2 - \omega_n (I_{z1} + I_{z2}) + \gamma_e \hat{\boldsymbol{I}}_1 \cdot \boldsymbol{A_1} \cdot \hat{\boldsymbol{S}}_1 + \gamma_e \hat{\boldsymbol{I}}_2 \cdot \boldsymbol{A_2} \cdot \hat{\boldsymbol{S}}_2 + \hat{\boldsymbol{S}}_1 \cdot \boldsymbol{D} \cdot \hat{\boldsymbol{S}}_2 + J \hat{\boldsymbol{S}}_1 \cdot \hat{\boldsymbol{S}}_2$$

where the pair of interacting nitroxides are labeled as 1 and 2, β_e is the Bohr magneton, $\boldsymbol{H_0}$ is the static external magnetic field, $\boldsymbol{g}$ is the Zeeman tensor defining the interaction of the electron spin of nitroxide $\boldsymbol{S}$ with the external magnetic field $\boldsymbol{H_0}$, ω_n is the Larmor frequency of the nitrogen nucleus, I_z is the z component of the spin angular momentum $\boldsymbol{I}$ of nitrogen nucleus, γ_e is the electron gyromagnetic ratio, $\boldsymbol{A}$ is the hyperfine tensor defining the interaction of the nitrogen nuclear spin $\boldsymbol{I}$ with electron spin $\boldsymbol{S}$, $\boldsymbol{D}$ is the dipolar coupling tensor of two electron spins, and J is the scalar of exchange interaction between two electron spins. In this Hamiltonian, the dominant localization of the unpaired electron density is to the N-O bond of the nitroxide (point dipole approximation). The principal axes of the $\boldsymbol{g}$ tensor and the $\boldsymbol{A}$ tensor of most nitroxides are essentially coincident in the molecular frame of the nitroxide due to the symmetric structure of the nitroxide ring (Figure 9). $\boldsymbol{D}$ is proportional to $1/\boldsymbol{R}^3$, where $\boldsymbol{R}$ is the inter-electron distance. Because the size of the molecular orbital of the unpaired electrons on the nitroxide is negligible compared to the inter-spin distance, the $\boldsymbol{D}$ tensor is axially symmetric and the principal z axis of the diagonalized $\boldsymbol{D}$ tensor is aligned along the inter-electron vector. J coupling may be only observable within 10 Å range, arising from the direct orbital overlap, the bond mechanism, or the exchange due to rapid collision.

In CW-EPR, spin-spin distances in the range 10-20 Å may produce dipolar splitting of 55 G to 7 G equivalent to frequencies of 150 MHz to 20 MHz. The observable dipolar splitting (the $\boldsymbol{D}$ tensor), similar to the $\boldsymbol{A}$ tensor and $\boldsymbol{g}$ tensor, will be partially

averaged by motions with correlation time 1-100 ns. Therefore, to obtain the inter-nitroxide distance, the relative orientation and their distributions, it is necessary to determine the global motion of the protein and the local motion of nitroxides. Specific cases can be categorized into three groups (Hustedt and Beth 1999).

Case 1: Statically arranged spins. The two nitroxides adopt a fixed distance and orientation and the protein has a global rotational correlation time ≥ 1 μs. Spin-labeled high affinity ligand rigidly bound to a large protein complex (Berliner and McConnell 1966; Beth *et al.* 1984; Philipp *et al.* 1984), nitroxide R1 sidechain within extensive tertiary contacts (near slow-motion limit) (McHaourab *et al.* 1996) and spin-labeled unnatural amino acid TOAC (Hanson *et al.* 1998; Monaco *et al.* 1999) in the backbone fall into this case.

Six independent parameters, the inter-nitroxide distance R, angles ζ, η relating the interelectron vector R, and angles α, β, γ relating the orientation of nitroxide 2 to nitroxide 1, define the steric geometry of the two probes. For a given set of 6 variables directly calculating the above Hamiltonian of two interacting spins can generate the EPR spectrum. The best fitting set to the experimental data is rigorously determined through global analysis that allows simultaneous nonlinear-least-squares analysis of multiple data sets from different microwave frequencies using the Marquardt-Levenberg algorithm. The multidimensional (one distance and five angles) χ^2 surface with multiple local minima can be explored by the simulated annealing minimization technique (Hustedt *et al.* 1997).

Case 2: Statically disordered spins. The nitroxides possess a static distribution of distances and orientations with respect to each other. Both the global rotation of the

protein and the local motion of the nitroxides occur on a timescale ≥ 1 μs. The applications under normal conditions in this case are limited. Nevertheless, at low temperatures or in viscous solutions, the sidechain dynamics and global rotation can be slowed down so that many examples under Case 3 below will meet the requirement of Case 2. Nitroxide sidechain R7 (4-Br derivative of R1) can also be introduced to restrict the amplitude of internal bond rotation in the sidechain. Combining viscous solutions and Br derived spin labels can make the real time detection of distance changes applicable for many biological studies at non-freezing temperature (Altenbach *et al.* 2001).

In a two-spin system, from the Hamiltonian electron dipole-dipole interaction

$$\hat{\mathcal{H}}_{ss}(\boldsymbol{r}) = \frac{\mu_0}{4\pi}\left[\frac{\hat{\boldsymbol{\mu}}_1{}^T \cdot \hat{\boldsymbol{\mu}}_2}{r^3} - \frac{3(\hat{\boldsymbol{\mu}}_1{}^T \cdot \boldsymbol{r})(\hat{\boldsymbol{\mu}}_2{}^T \cdot \boldsymbol{r})}{r^5}\right],$$

when only considering an isotropic Zeeman effect and electron dipolar coupling, the energies of the triplets under high external magnetic field are

$$\begin{aligned} U_{-1} &= -g_e\beta_e B - \tfrac{1}{4} g_e^2\beta_e^2 r^{-3}(3\cos^2\theta - 1) \\ U_0 &= \tfrac{1}{2} g_e^2\beta_e^2 r^{-3}(3\cos^2\theta - 1) \\ U_{+1} &= g_e\beta_e B - \tfrac{1}{4} g_e^2\beta_e^2 r^{-3}(3\cos^2\theta - 1) \end{aligned},$$

where θ is angle between the external magnetic field B and inter-spin vector r. Since the transitions from the triplets to the singlet are highly forbidden, the resonance absorption conditions for the perturbed system are $\Delta E_{\Delta M_S=1} = h\nu = g_e\beta_e B \pm \frac{3}{4} g_e^2\beta_e^2 r^{-3}(3\cos^2\theta - 1)$. When $\cos\theta = 1/\sqrt{3}$, $h\nu = g_e\beta_e B = g_e\beta_e B_0$, and θ = 54.7° known as the magic angle. So $\Delta B = B - B_0 = \pm\frac{3}{4} g_e\beta_e r^{-3}(3\cos^2\theta - 1)$. In crystalline powders (the statistically randomly oriented single crystals), each spin center (assuming isotropic g tensor) has virtually the identical properties such as hyperfine splitting and other zero-field splittings (ignored in

this case). However, the vector ***r*** may adopt all possible orientations relative to the direction of external magnetic field *B*. Considering a circumpolar infinitesimal area on the surface of a sphere, the fraction of the interspin vector occurring between angles θ and θ + dθ is $P(\theta)d\theta = 2\pi(r\sin\theta)(rd\theta)/(4\pi r^2) = \frac{1}{2}\sin\theta d\theta$. It is proportional to the probability $P(B)dB$ of a spin system experiencing a resonant field between B and B + dB,

$$P(\theta)d\theta = 2\pi(r\sin\theta)(rd\theta)/(4\pi r^2) = \tfrac{1}{2}\sin\theta d\theta \propto P(B)dB$$

$$\therefore P(B) \propto \sin\theta d\theta / dB \propto \sin\theta/(dB/d\theta) \propto \sin\theta/(2\cos\theta\sin\theta) \propto 1/\cos\theta$$

$$1/\cos\theta \propto (\Delta B/(\pm\tfrac{3}{4}g_e\beta_e r^{-3})+1)^{-\frac{1}{2}}$$

$$\therefore P(\Delta B) \propto (\Delta B/(+\tfrac{3}{4}g_e\beta_e r^{-3})+1)^{-\frac{1}{2}} \qquad \Delta B \in (-(+\tfrac{3}{4}g_e\beta_e r^{-3}), 2(+\tfrac{3}{4}g_e\beta_e r^{-3}))$$
$$+ (\Delta B/(-\tfrac{3}{4}g_e\beta_e r^{-3})+1)^{-\frac{1}{2}} \qquad \Delta B \in (-2(+\tfrac{3}{4}g_e\beta_e r^{-3}), (+\tfrac{3}{4}g_e\beta_e r^{-3}))$$

This is the well known Pake pattern, which is the sum of the spectra of individual crystallites that are randomly distributed in the sample. The EPR absorption lines are split by 2ΔB in the magnetic field $2\Delta B = \frac{3}{2}g_e\beta_e r^{-3}(3\cos^2\theta - 1)$. The maximal splitting is $2\Delta B_{\max} = \frac{3}{2}g_e\beta_e r^{-3}$ (Figure 16).

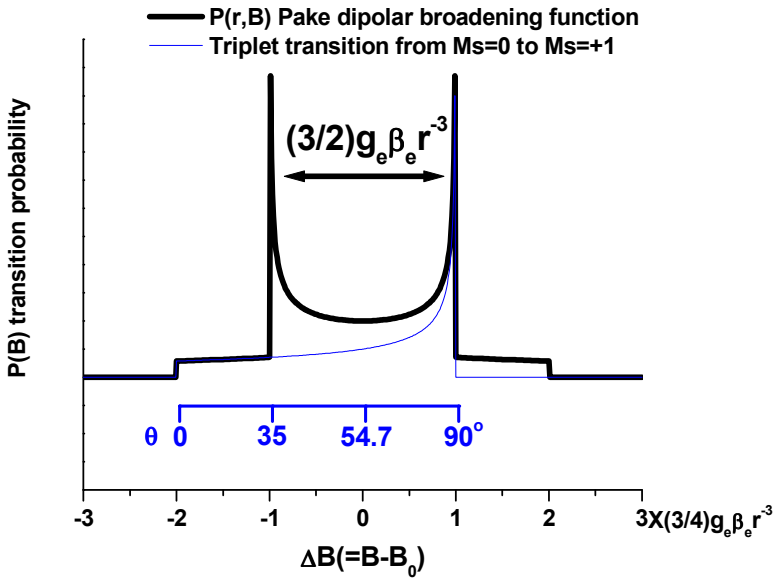

Figure 16. Pake pattern

The probability of one triplet transition is shown in blue. The angle θ between r and B is isotropically distributed. The absorption amplitude is proportional to 1/cosθ or $(\Delta B/(-\frac{3}{4}g_e\beta_e r^{-3})+1)^{-\frac{1}{2}}$. The turning points are labeled at 0˚ and 90˚. The black line represents the absorption lineshape of two dipolar coupled electron spins in crystalline powders (isotropic θ and g_e, omitting ω_n, $\boldsymbol{A}$ and $\boldsymbol{J}$). The maximal splitting is $2\Delta B_{\max} = \frac{3}{2}g_e\beta_e r^{-3}$. The magic angle is 54.7˚ where there is no splitting between two transitions (Pake 1948).

In practice, other interactions such as the hyperfine effect influence the EPR lineshape. The dipolar-coupled lineshape can be approximated by the convolution of the spectrum of the noninteracting nitroxides with a Pake broadening function averaged over a distribution of distances due to the tethering of the nitroxide sidechain and the conformational variation of proteins.

$$D(B) = S(B) \otimes M(B) = \int_{-\infty}^{\infty} S(B')M(B'-B)dB'$$

where D(B) is EPR spectrum for the two interacting nitroxides, S(B) is the average of two noninteracting EPR spectra S(B) = [S_1(B)+S_2(B)]/2, M(B) is the weighted sum of the

Pake pattern P(r, B) over the distance distribution σ(r, B), $M(B) = \sum_r \sigma(r) P(r, B)$.

According to the convolution theorem,

$$F(D) = F(S \otimes M) = F(S) \cdot F(M) \quad \therefore M = F^{-1}[F(D) / F(S)],$$

where F and F^{-1} are the forward and inverse Fourier transform operators, respectively. The average distance and distance distribution of the two nitroxides can be calculated from the average splitting <2ΔB> (Rabenstein and Shin 1995). Alternative to the deconvolution approach above, the experimental spectra can be fitted by a direct convolution approach using nonlinear least-squares methods to determine the best values of r and σ. The distribution in interspin distance can be obtained by averaging the Pake pattern function over a Gaussian distribution (Steinhoff *et al.* 1997).

Two fundamental assumptions are involved in the convolution-deconvolution methods. First, the Pake pattern of the dipolar broadening function requires neglecting the anisotropic effect of the ***g*** and ***A*** tensors. Second, the relative orientation of the two nitroxides and the orientation of the interelectron vector with respect to the nitroxides are randomly and isotropically distributed over a sphere. Especially the latter is not likely to be valid except for the most flexible small peptides. Each or both of the nitroxides will be restricted to some relative orientation relative to the interelectron vector because of the attachment to the protein backbone and the sidechain interaction. In the tether-in-a-cone simulation, recently developed by Hustedt and coworkers, the ***g*** tensors, hyperfine ***A*** tensors and the dipolar coupling ***D*** tensor of the spin Hamiltonian are all determined by a set of Euler angle transformations. The tethers adopt all possible angles within the cones of half width μmax resulting in the interspin distance distribution and orientation distribution. Indeed, the tether-in-a-cone model shows that simulated spectra are sensitive

to the relative orientation of the nitroxide cones, which are used to simplify $\chi 1$-$\chi 5$ bond rotations (strongly sensitive when the half-width of the cone is less than 40˚). (Hustedt *et al.* 2006).

Case 3: Dynamically disordered spins. The inter-nitroxide distance and orientation are averaged by fast motion. The local motions of the nitroxides or the global rotational diffusion of the protein take place on a timescale to which linear EPR is sensitive (τ in ns). Many applications belong to this case, such as nitroxide R1 sidechains on the surface of an α helix free of tertiary interactions.

In fast motion, if the reorientation of the dipolar interaction vector is high relative to the energy of interaction (in frequency units), the dipolar splitting is nearly averaged to zero. Based on fast-motion relaxation theory, the line broadening due to dipolar interaction (exchange interaction is small) is proportional to $1/r^6$ (also proportional to $1/T_2$). As distance increases, the broadening decreases much faster than Case 2 ($1/r^3$), and it becomes difficult to observe. So in practice, Case 3 may be converted to Case 2 by slowing the motion down using low temperatures or viscous solutions.

In theory, the spin-spin distance, distribution and relative orientation can be obtained by spectral simulation with the complete spin Hamiltonian and accurate dynamic models for all three cases. The time domain free induction decay (FID) can be calculated by solving the stochastic Liouville equation (the differential equation for the spin Hamiltonian whose molecular orientation variables are stochastically modulated according to dynamic models) using a rapid solution approach (Millhauser *et al.* 1989) or using a Monte Carlo approach to generate random molecular trajectories according to a classical Brownian isotropic rotational diffusion model. Fourier transform of the FID

(time domain) signal generates the dipolar coupled CW-EPR spectrum (frequency domain) (Robinson *et al.* 1992; Hustedt and Beth 1999).

The upper limit of CW-EPR distance measurement is 25 Å, as dictated by the inhomogeneous linewidth. A number of time-domain EPR techniques have been developed for measuring biradical spin-spin distances from 17 Å to 80 Å in the frozen state. Among them, double electron electron resonance (DEER) (Pannier *et al.* 2000) and double quantum coherence (DQC) (Borbat *et al.* 2002) techniques have been successfully applied to biological samples for measuring distance from 17Å to 70 Å. The upper limit of pulsed EPR is determined by the maximal evolution time, which is confined by the phase memory time or spin-spin relaxation time (T_2 is limited to approximate 4 μs for protonated nitroxides) of the nitroxide spin labels.

In DEER experiments, suppose that spin packet A is excited with a $\pi/2$ pulse (+x direction) of microwave frequency υ_A at time 0. The spin packet A is then tipped into the xy plane (-y direction) where it precesses with the angular rate ω_A, and magnetization along -y axis is oscillating as $M_{-y}=M\cos\omega_A t$ in the lab frame. Due to the field inhomogeneity such as unresolved couplings, spins in A under different local resonance field will rotate at slightly different angular rates (dephasing). Under homogeneous field, the spins in A interact with each other and undergo motional transitions, resulting in mutual and random spin flip-flops, hence, increased or decreased angular rates. For many spins, the x and y components of the magnetization tend to cancel out each other and decrease the net transverse magnetization, known as the free induction decay (FID). (The decay of the transverse magnetization from the inhomogeneous broadening mechanism is a non-exponential decay with a characteristic time constant T_2^*, resulting in a Gaussian

lineshape in the frequency domain. The decay of the transverse magnetization from the homogeneous broadening mechanism is in general an exponential decay: $M_{-y} = e^{\frac{-t}{T_2}}$ and $\frac{dM_{-y}}{dt} = -\frac{e^{\frac{-t}{T_2}}}{T_2} = -\frac{M_{-y}}{T_2}$, corresponding to a Lorentzian frequency spectrum. The FID contains all the frequency information of the EPR spectrum, thus a Fourier transform of the time domain FID gives rise to the frequency domain EPR spectrum.) In the rotating frame, the transverse magnetization fans out because some spins rotate faster than ω_A, some are slower in the lab frame. At time τ_1, the first π pulse imposed on spins A flips the magnetization 180˚ about the x axis. These spins still rotate in the same direction (right hand rule) and speed and finally refocus together creating a spin echo at time $2\tau_1$. Spins continue to process in the xy plane and the second π pulse at constant time $2\tau_1 + \tau_2$ on spins A can refocus the echo at time $2\tau_1 + 2\tau_2$, although with a smaller amplitude as the phase coherence is lost because of the transverse relaxation. (The $\pi/2$-π pulse generates a Hahn echo, the second π pulse is applied to avoid the signal distortion or dead time due to pulse overlap in a short time after the $\pi/2$ pulse.) The pumping pulses of υ_B are applied at time variables $(2\tau_1 + t)$, flipping spin packet B and therefore reversing the dipolar contribution of spin B at the location of spin A. As a result spins from packet A cannot be fully refocused and the intensity of the echo decreases. The extent of coherence loss is a function of the dipolar interaction strength ω_{AB} and t, the time difference spins A experienced $+1/2\omega_{AB}$ versus $-1/2\omega_{AB}$ (Figure 17 and Figure 18). The theory of the DEER experiment is explained in the following:

The simplified spin Hamiltonian for Spin A: $H = \omega_A S_A + \omega_{AB} S_B S_A = (\omega_A + \omega_{AB} S_B) S_A$

Angular rates of spin A:

after $\pi/2$ pulse at ν_A: $\omega_A+\omega_{AB}S_B$

after the first π pulse at ν_A: $-\omega_A-\omega_{AB}S_B$

after π pulse at ν_B: $-\omega_A+\omega_{AB}S_B$

after the second π pulse at ν_A: $\omega_A-\omega_{AB}S_B$

At time $2\tau_1+2\tau_2$, the phase angle for Spin A (constants $\tau_1\approx$120-200ns, $\tau_2\approx1\mu$s-6μs):

$(\omega_A+\omega_{AB}S_B)\tau_1+(-\omega_A-\omega_{AB}S_B)(\tau_1+t)+(-\omega_A+\omega_{AB}S_B)(\tau_2-t)+(\omega_A-\omega_{AB}S_B)\tau_2$

$= -\underline{\omega_A}t-\omega_{AB}S_Bt-\omega_A\tau_2+\underline{\omega_A}t+\omega_{AB}S_B\tau_2-\omega_{AB}S_Bt+\omega_A\tau_2-\omega_{AB}S_B\tau_2= -2\omega_{AB}S_Bt= -\omega_{AB}t$

Thus, $M_y = M_{y0}\cos(-\omega_{AB}t)$. The echo amplitude of spin A oscillates with $\cos\omega_{AB}t$. This modulation of the echo as the pumping π pulse is swept between the two observing π pulses is the DEER signal. Qualitatively, fast decay of the initial echo and higher frequency of DEER echo modulation reflect shorter interspin distance. The more oscillations the DEER signal has, the narrower the distance distribution is. Like the quantitative analysis of dipolar coupled CW-EPR spectra, the information of interspin distance and distance distribution can be obtained from the DEER signal via deconvolution methods (Fourier transform of the DEER signal generates the Pake doublet) and data fitting methods (single or two Gaussian distribution is assumed).

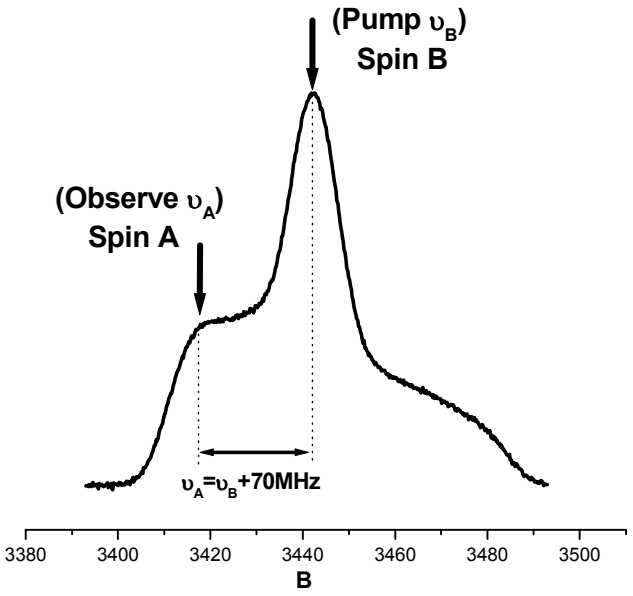

Figure 17. Excitation profiles of the MW pulses in the DEER experiment

The field sweep of cdb3_290_MTSSL in an over-coupled resonator. Black arrows indicate the pumping pulse at υ_B and the observing pulse at υ_A.

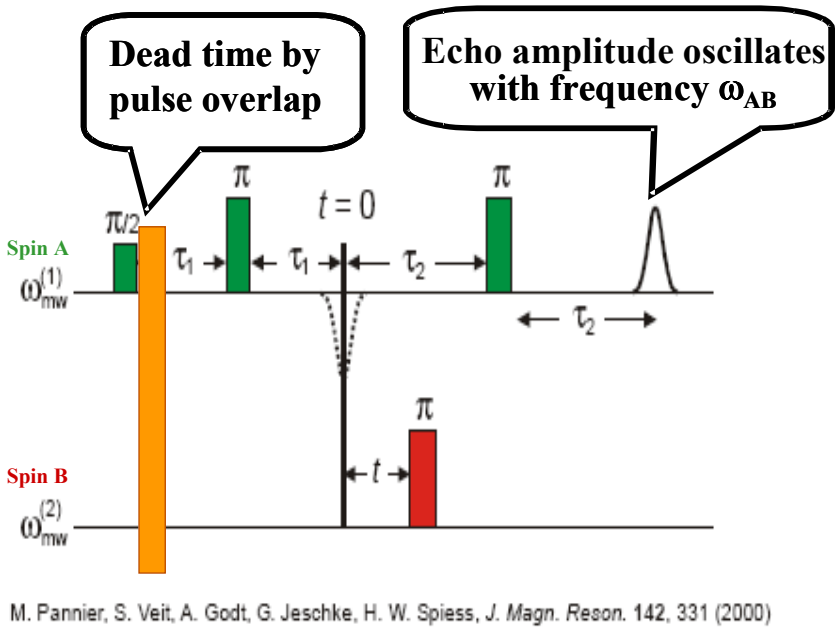

Figure 18. 4-pulse DEER sequence

Spin A is excited by the observing pulse (green bars) and spin B is excited by the pumping pulse (red bar). The orange bar represents the dead time. If spin B is close to spin A, spin A senses the excited spin B and the echo amplitude of spin A is affected by the manipulation of spin B (π pulse at υ_B inverts the local dipolar field at the position of spin A). When the pumping pulse of spin B is applied at variable time t, the echo intensity of spin A oscillates with ω_{AB} (Pannier *et al.* 2000).

Double quantum coherence (DQC) EPR utilizes a DQC pulse sequence to preserve the contribution to the double quantum echo signal solely from the dipolar interaction between the two spins. The intensity of the echo is recorded as a function of time and a Fourier transform of the echo generates the dipolar coupled Pake pattern spectrum, which is directly related to the distance between the two spin labels. One advantage of DQC is that in theory, DQC excites more spins than DEER under the same spin concentration giving rise to higher signal-to-noise ratio (Recall that DEER only excites part of the field sweep spectrum) (Borbat *et al.* 2001). All of the experiments reported in this work were preformed using he 4-pulse DEER sequence described in Figure 18.

CHAPTER III

GENERAL EXPERIMENTAL METHODS

Circular Dichroism

CD spectra were recorded on a Jasco J-810 system (Easton, MD) at room temperature in a 0.1 cm path-length cell. All spectra were obtained on samples in buffer containing 10 mM NaH_2PO_4, 1 mM EDTA, pH 7.4. The data were collected from 190 to 260 nm at a scan speed of 10 nm/min. The raw data, in degrees θ, were converted to molar ellipticity [θ] using the relationship:

$$[\theta] = (100 \times \theta)/(n \times c \times l),$$

where n is the number of amino acid residues, c is the protein concentration in mM, and l is the path length in cm.

Differential Scanning Calorimetry

DSC measurements were carried out on a MicroCalorimetry VP-DSC instrument (Northampton, MA) at a protein concentration of 1-2 mg/mL. The samples were prepared in 10 mM NaH_2PO_4, 1 mM EDTA, pH 7.4. The sample and buffer were degassed for 5 minutes at 20° C before being loaded into the tantalum sample cell and reference cell, respectively. The data were collected in the range of 20-100°C at a scan rate of 1.5°C/min.

CW-EPR Measurements

X-band (9.8 GHz) CW-EPR spectra were collected using a Bruker EMX spectrometer equipped with a TM_{110} cavity (BrukerBiospin, Billerica, MA) at room temperature. Samples prepared at 100 μM spin concentration were drawn into 50 μL glass capillaries (VWR, West Chester, PA) and sealed with Critoseal sealant (Fisher, Pittsburgh, PA). Samples for distance measurements by CW-EPR spectroscopy were prepared in 50% sucrose (w/w) and controlled at 2 ˚C by a standard Bruker variable-temperature unit. CW-EPR spectra were acquired at 5 mW microwave power using a 100 Gauss sweep width. All spectra contained 1024 data points collected at 100 kHz Zeeman field modulation frequency of 1.25 Gauss amplitude (peak-to-peak) and a 42 second sweep time. The second moment was calculated by

$$\langle \omega^2 \rangle = \int \omega^2 f(\omega) d\omega \Big/ \int f(\omega) d\omega ,$$

as a measure of the breadth of the EPR spectra (Slichter 1980; Hubbell and Altenbach 1994). Distances between spin-labeled sites in some samples were determined from fitting of CW-EPR spectra either using a tether-in-a-cone model (Hustedt *et al.* 2006) or by spectral convolution assuming a Gaussian distance distribution (Rabenstein and Shin 1995; Steinhoff *et al.* 1997) as defined in the table and figure legends.

Solvent Accessibility

Solvent accessibility of individual spin-labeled residues was measured on samples diluted to 100 μM spin concentration in 20 mM NaH_2PO_4, 100 mM NaCl, pH 6.8. NiEDDA was added at a final concentration of 5 mM. Samples were purged of molecular oxygen by flowing nitrogen gas over the sample contained in a TPX capillary for 15

minutes prior to and during measurements. A TM_{110} cavity or an ER4123D dielectric resonator was utilized in different experiments as indicated in figure legends. A 25 Gauss scan of the central resonance line for each mutant was carried out using a 1 Gauss modulation amplitude of 100 kHz frequency. A total of 24 scans were separately recorded at microwave powers ranging from 1 mW to 200 mW (1 dB attenuation/step). Data were analyzed by non-linear least squares curve fitting using Origin 6.1 software (OriginLab Corporation, Northampton, MA) of the spectral amplitude (A_0) versus the square root of microwave power ($\sqrt{P_0}$) using the equation:

$$A_0 = \frac{c\Lambda\sqrt{P_0}}{\left[1+\left(2^{1/\varepsilon}-1\right)P_0/P_{1/2}\right]^{\varepsilon}},$$

where A_0 is the peak-to-peak amplitude of the first derivative spectrum, c is the instrumental proportionality constant, Λ is the instrumental factor, P_0 is the input power, ε is the lineshape adjustment parameter and $P_{1/2}$ is the half saturation power. The NiEDDA accessibility was calculated by the following equation:

$$\mathrm{Ac(NiEDDA)} = \frac{P_{1/2}\left(\mathrm{NiEDDA}\right) - P_{1/2}\left(\mathrm{N_2}\right)}{\Delta H_0},$$

where Ac is the accessibility, $P_{1/2}$ (NiEDDA) is the half saturation power in the presence of 5 mM NiEDDA, $P_{1/2}$ (N_2) is the half saturation power in the absence of NiEDDA, and ΔH_0 is the central line width (Subczynski and Hyde 1981; Altenbach *et al.* 1989).

DEER Measurements

Long-range nitroxide-nitroxide distances were measured by double electron electron resonance (DEER) spectroscopy. DEER experiments were performed at X-band using a Bruker E680 X/W-band pulsed EPR instrument (Bruker Spectrospin, Billerica, Mass.) at the National High Magnetic Field Laboratory (Tallahassee, FL) using a 4-pulse sequence (Pannier *et al.* 2000). For DEER measurements, spin-labeled cdb3 dimer samples were approximately 300 μM in spin concentration as measured by the doubly integrated intensity of the room temperature CW-EPR spectrum in comparison to a standard of known spin concentration. All samples contained 30% (w/w) glycerol. All DEER experiments were performed at 65°K using a 1 msec shot repetition time and a 16 nsec 90° pulse width in an over-coupled dielectric resonator (ER 4118X-MD5, Bruker Biospin, Billerica, MA). The 180° ELDOR pulse was 32 nsec wide at 70 MHz frequency offset. DEER data were analyzed using the DeerPackage 2002.1 software made available by G. Jeschke (Max Planck Institute for Polymer Research, Mainz, Germany; (Jeschke 2002b; Jeschke 2002a; Jeschke *et al.* 2002)) assuming a single Gaussian distance distribution.

Fluorescence Measurements

Intrinsic tryptophan fluorescence and badan (6-bromoacetyl-2-(dimethylamino) naphthalene) fluorescence were measured on a PTI Quantamaster 2000-7SE fluorometer (Photon Technology International, Lawrenceville, NJ) at room temperature, using a quartz cuvette (200 μl, 1 cm path length). Detailed sample preparations and machine settings are described in Chapter 4 and Chapter 6.

CHAPTER IV

SOLUTION STRUCTURE OF CDB3

Introduction

The crystal structure of the cdb3 dimer (55-356) at 2.6 Å resolution was determined at pH 4.8 (Figure 4 and Table 1) by Dr. Low's group. Each monomer contains a large peripheral globular domain, a dimerization arm, and unresolved N (1-54) and C (357-379) termini. Two dimerization arms, one per monomer, interdigitate into each other. The total interacting surface area between two monomers is approximately 5200 $Å^2$ with 3700 $Å^2$ of the buried surface associated with nonpolar sidechains. There are 8 backbone-to-backbone hydrogen bonds contributed in part by the two antiparallel β strands (Leu319Val320Leu321 from each monomer) and a hydrophobic core of 9 interacting leucine residues among the extensive intermonomeric interactions (Leu319, 321, 332, 333, 335 from one monomer chain P and Leu319, 321, 332, 335 from another monomer chain Q). This compact homodimer has an axial ratio of 1.9:1 (Zhang *et al.* 2000).

A 10:1 axial ratio was predicted in previous work from analytical ultracentrifuge analysis of the cdb3 dimer separated from the tdb3 (Colfen *et al.* 1996). This result indicated a highly asymmetric, elongated conformation (Appell and Low 1981), consistent with early data on cdb3 in full length band 3 in the red blood cell membrane (Weinstein *et al.* 1978). Furthermore, a reversible pH-dependent conformational change was reported by several biophysical and biochemical experiments (Appell and Low 1981;

Low *et al.* 1984; Low 1986; Thevenin *et al.* 1994; Salhany *et al.* 1998). Three conformations may exist with transition points at pH 7.2 and 9.2 (Zhou and Low 2001). The prevailing model of cdb3 throughout the 1980's and 1990's was that the cdb3 dimer folded into a rod-like domain that extended into the cytosolic compartment of the erythrocyte with the N-termini far from the cytoplasmic surface of the membrane. Consequently, it was a major surprise when the X-ray crystal structure of cdb3 (residues 55-356) showed a compact quasi-symmetric dimer. Equally as surprising, the unresolved N- and C-termini did not exit the dimer on opposite surfaces, a geometry that would seem reasonable for optimal exposure of the N-terminus for binding to intracellular proteins (Zhang *et al.* 2000). Due to these contradictions, expansion of the cdb3 dimer at elevated pH has been proposed (Figure 19) (Zhou and Low 2001). Since the globular domain and the dimerization arm are tightly folded, the short segments between them (Glu291-Gln302) might be a possible hinge which allows a pivoting motion while maintaining the secondary structure (Appell and Low 1981; Low *et al.* 1984) and the dimer configuration through the intact dimerization arms. This model could reconcile the difference between the low pH conformation and the high pH conformation, specifically, only at low pH, the Trp fluorescence quenching by a H bond between Trp105 of one subunit to Asp316 of the other subunit, ankyrin binding to cdb3 (Thevenin and Low 1990; Low *et al.* 1991), preventing the formation of a intermonomer disulfide bond of Cys201-Cys317, hemoglobin binding and moving toward the bilayer (Salhany *et al.* 1998).

In this chapter, a series of site-directed spin labeling studies, in combination with CW-EPR and DEER experiments, have been carried out to address the question of how the structure of cdb3 at neutral pH compares with the crystal structure determined at pH

4.8. The significance of this work lies in establishing the structure of cdb3 at physiological pH in solution and providing a new starting point to characterize structural details of the protein-protein interactions that maintain the structure and function of the erythrocyte membrane, ranging from control of red blood cell shape, mechanical stability (Low *et al.* 1991; Peters *et al.* 1996; Southgate *et al.* 1996), flexibility and viscoelasticity (Moriyama *et al.* 1992; Schofield *et al.* 1992; Blackman *et al.* 2001), to mediation of anion transport (Malik *et al.* 1993), regulation of glucose metabolism (Low *et al.* 1993; Weber *et al.* 2004) and governing red cell life span (Kannan *et al.* 1991).

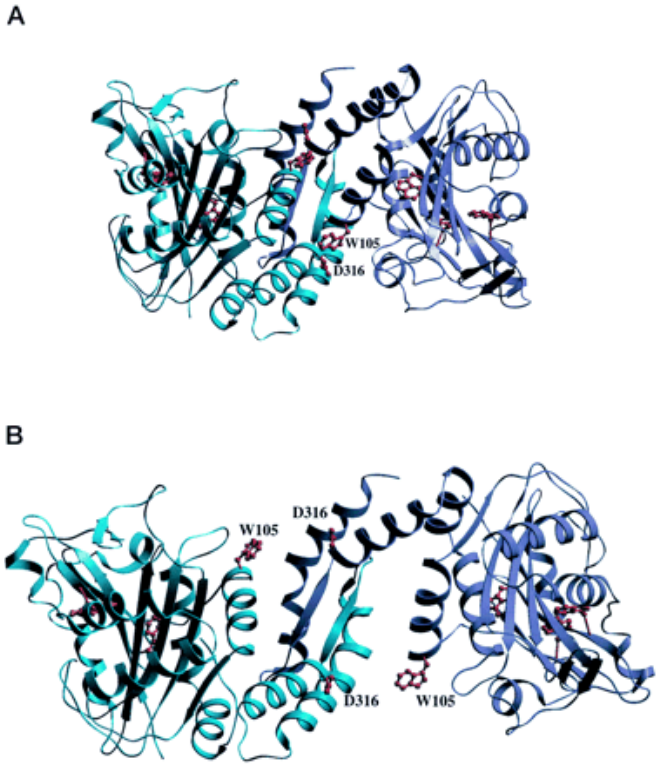

Figure 19. Hypothetical structure model of cdb3 dimer at high pH

Panel A. The crystal structure of cdb3 from crystals grown at pH 4.8. One subunit is represented in cyan color. The other subunit is in blue. All 8 tryptophan residues are shown in red. Aspartic acid 316 of one monomer forms a hydrogen bond with tryptophan 105 from the other pairing monomer, which quenches the intrinsic tryptophan fluorescence.

Panel B. The hypothetical structure of the cdb3 dimer at high pH. The two globular domains rotate away from the shared dimerization domain at glycine 305 in the hinge region. The Trp105-Asp316 H bond is broken (Zhou and Low 2001).

Experimental Methods

Cloning and site-directed mutagenesis

The full length human AE1 cDNA was kindly provided by Dr. Robert Gunn (Emory University). The segment of the cDNA encoding residues 1-379 of AE1 was amplified using Pfu DNA polymerase (Stratagene, La Jolla, CA) with the N-terminal (forward) primer

5'ACGGGAATTCCATATGGAGGAGCTGCAGGATGATTATG

and the C-terminal (reverse) primer

5'TCACACCGCTCGAGTTATTAGAAGAGCTGGCCTGTCTGCTG

(IDT DNA, Coraville, IA). The PCR product was cloned into the pET-19b vector (Novagen, Madison, WI) between the NdeI and XhoI sites, and designated as pZZ3_WT. The cysteineless mutant (pZZ3) and single cysteine mutants were constructed by using the QuikChange® Site-Directed Mutagenesis Kit (Stratagene, La Jolla, CA). The sequences of all mutants were confirmed by DNA sequencing.

Protein preparation

pZZ3 plasmids were transformed into BL21 Gold (DE3) *E. coli* competent cells (Stratagene, La Jolla, CA). Expression of cdb3 was followed by the auto-induction protocol developed by Dr. F. William Studier (Brookhaven National Laboratory) (Studier 2005). Briefly, overnight starter cultures were grown in PAG at 37˚C and 200 μL of the starter cultures were used to inoculate 200 mL ZYP-5052 for overnight auto-induction (14 hours). Typically, saturation (A_{600} = 4.8~7.0) was reached in about 10 hours at 37˚C.

Additional incubation for 4 hours maximized lactose auto-induction. His-tagged cdb3 purification was carried out using Ni-NTA resin as described by the manufacturer (Qiagen, Valencia, CA). For some mutants, the N-terminal His tag was cleaved via the Enterokinase Cleavage Capture Kit (Novagen, Madison, WI). For certain mutants, gel filtration was performed on an HPLC TSK G3000SW column (TosoHaas, Montgomeryville, PA). Protein concentration was determined by UV absorption at 280 nm using an extinction coefficient of 33,000 $M^{-1}cm^{-1}$. Purity of the expressed proteins was at least 95%, as determined by SDS-PAGE (Laemmli 1970). Single cysteine mutants were spin-labeled with a 10-fold molar excess of 1-oxyl-2,2,5,5-tetramethyl-Δ3-pyrroline-3methyl methanethiosulfonate spin label (MTSSL; Toronto Research Chemicals, North York, ON Canada) in the dark at room temperature for 2 hours and then at 4˚C overnight in a buffer containing 50 mM NaH_2PO_4, 300 mM NaCl, and 200 mM imidazole, pH 8.0. In order to singly spin label the cdb3 dimer, MTSSL and a non-paramagnetic label (1-acetyl-2,2,5,5-tetramethyl-Δ3-pyrroline-3-methyl) methanethiosulfonate; (Toronto Research Chemicals, North York, ON Canada) were used at a 1:5 molar ratio. Unreacted label was removed from all samples by dilution and reconcentrating 4 times (1:50 v/v) in an Amicon Ultra-4 Centrifugal Filter Device (30 kDa nominal molecular weight limit, Millipore, Bedford, MA) with a buffer containing 20 mM NaH_2PO_4, 100 mM NaCl, 1 mM EDTA, pH 6.8. All EPR and DEER measurements reported were collected with the spin-labeled samples in this buffer at pH 6.8. Identical spectral results were obtained on samples recorded in this same buffer at pH 8.0 (data not shown). The disulfide bond between the spin label and the cysteine side

chain is more stable at the lower pH thereby facilitating the storage and shipping of samples for recording DEER data at the National High Magnetic Field Laboratory.

Intrinsic tryptophan fluorescence

Purified cysless-cdb3 and wt-cdb3 were concentrated and buffer-exchanged into a pH 7.0 phosphate-borate buffer (50 mM sodium phosphate, 50 mM boric acid, 70 mM NaCl, 2 mM EDTA). Tryptophan fluorescence emission spectra were collected on 150 μL samples of wt-cdb3 and cysless-cdb3 diluted to a final concentration of 50 μg/mL (5 mg/mL stock solutions, diluted 100x in buffer of the desired pH). Identical experimental results were also obtained on samples in a phosphate-citrate buffer over the same pH range (20 mM sodium phosphate, 20 mM citric acid, 2 mM EDTA; data not shown). The emission spectra were collected on a PTI Quantamaster 2000-7SE fluorometer (Photon Technology International, Lawrenceville, NJ) at room temperature, using an excitation wavelength of 290 nm and collecting fluorescence emission from 300 – 400 nm (both excitation and emission slit widths were set at 2 nm). Data are presented as the center of mass wavelength of the emission spectra (i.e., the spectral midpoint wavelength where half of the total emission is above and half is below).

Molecular modeling

Molecular models of the spin-labeled cdb3 mutants were manually constructed from the known crystal structure of cdb3 (PDB ID: 1HYN; (Zhang *et al.* 2000)) using the molecular graphics program PSSHOW. Estimates of the distance between spin labels were obtained using the $\chi_4\chi_5$ model (Figure 12; (Langen *et al.* 2000; Columbus *et al.*

2001)). The torsion angles of the first three bonds between Cα of the spin-labeled cysteine and the nitroxide ring were fixed to χ_1= -60°, χ_2= -60°, and χ_3= -90° respectively, while χ_4 and χ_5 were iteratively rotated in steps of 30° within NAB (Macke and Case 1998). After each rotation, the distance between the spin labels was measured from points equidistant between the nitrogen and oxygen atoms of the nitroxides. The distance was rejected if the orientation of the spin label resulted in overlap with any other atom in the structure greater than 0.4 times the sum of the van der Waals radii. The average and standard deviation of the accepted distances were then computed.

Experimental Results

Characterization of recombinant cdb3

Recombinant wt-cdb3, cysless-cdb3, and all single cysteine mutants of cdb3 in the cysless background were expressed and purified as described in Methods. The purity of cdb3 was greater than 95% as determined by SDS-PAGE for all samples used in this work (Figure 20). A single dominant band was observed in native gel electrophoresis and a single peak eluted from size exclusion chromatography, suggesting that recombinant cdb3 adopts a single size (data not shown). The position of the eluted peak, in comparison with molecular weight standards, confirmed that recombinant wt-cdb3 and all mutants examined exist as dimers in solution at neutral pH. More evidence of a dimeric structure will be discussed in the following sections. Circular dichroism (CD) was employed to evaluate the secondary structure of recombinant cdb3. The CD spectrum from recombinant wt-cdb3 (Figure 21) exhibited a crossover point near 198 nm,

a negative extremum at 207 nm, and a shoulder at 222 nm and was indistinguishable from the CD spectrum reported for cdb3 isolated from human erythrocytes (Appell and Low 1981). The melting temperature (T_m) of wt-cdb3, as monitored by differential scanning calorimetry (DSC), was 70°C at pH 7.4 (Figure 22), close to the value of 68°C reported previously for erythrocyte cdb3 (Appell and Low 1981). Collectively, these data indicate that the construct of wt-cdb3 containing a His_9 tag at the N-terminus that was expressed and purified from *E. coli* exhibited essentially the same secondary and quaternary structure and essentially the same thermal stability as wt-cdb3 that was isolated from the erythrocyte membrane. The EPR data obtained from His_9-cdb3 was indistinguishable from the data obtained following cleavage of the His_9 tag from the N-terminus (data not shown). Therefore, all spectra presented were obtained from His_9-cdb3.

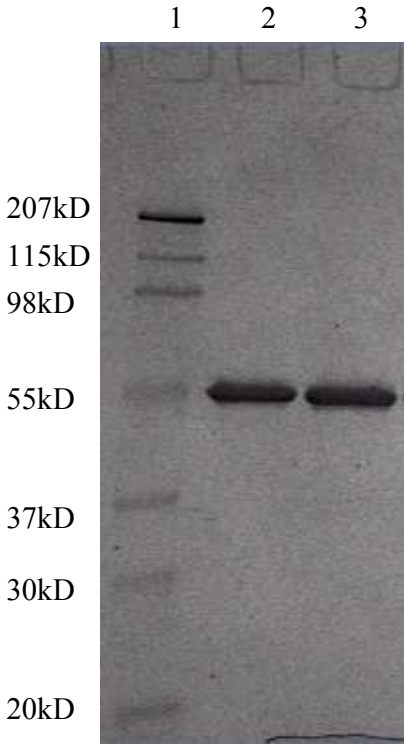

Figure 20. SDS-PAGE of cdb3
Molecular weight markers are shown in lane 1. About 1 μg wt-cdb3 (1 μl~20 μM) and cysless-cdb3 were loaded on lane 2 and 3, respectively. A single dominant band in each lane can be seen through Coomassie staining from either wt or cysless-cdb3.

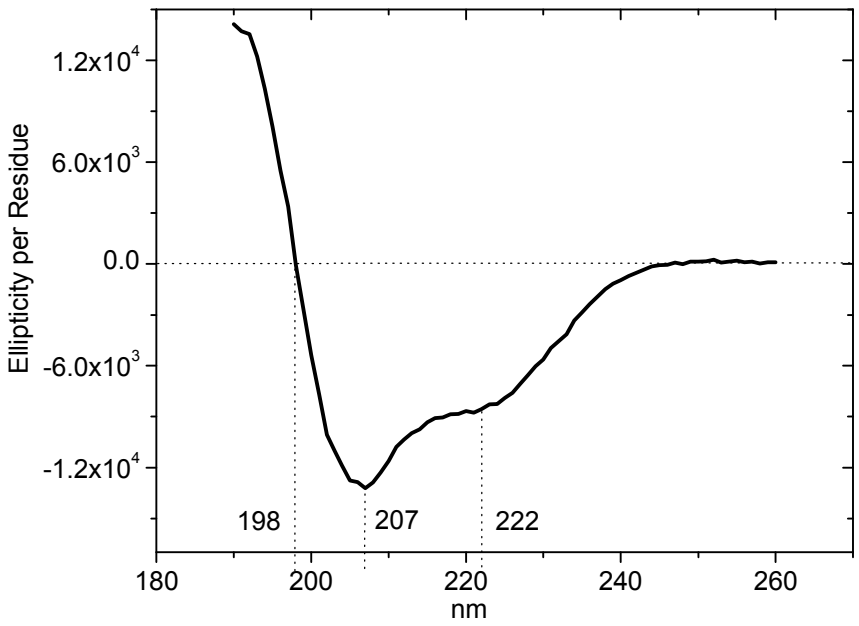

Figure 21. Circular dichroism of cdb3

The CD spectrum of recombinant wt-cdb3. Three signature points are shown: the crossover point at 198 nm, the negative extremum at 207 nm and the shoulder at 222 nm.

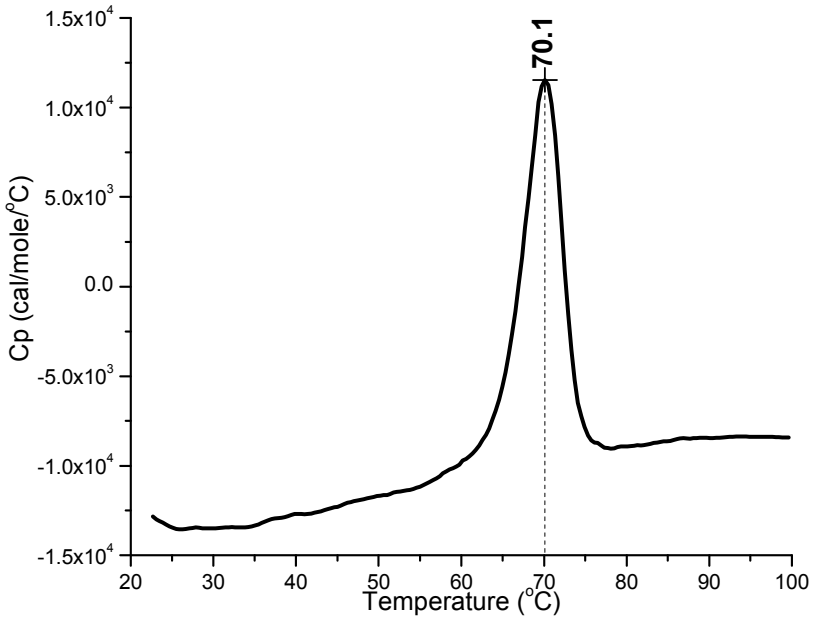

Figure 22. Differential scanning calorimetry of cdb3

The first up scan of wt-cdb3 is shown. The melting temperature 70˚C is indicated by the vertical black dashed line. The unfolding enthalpy was not determined due to only 50% reversibility.

Intrinsic tryptophan fluorescence in recombinant wt-cdb3 and cysless-cdb3

Previous work has shown that wt-cdb3 undergoes two fully reversible pH-dependent conformational changes in the range from 6 to 10 (Appell and Low 1981; Low *et al.* 1984; Thevenin *et al.* 1994; Zhou and Low 2001). These studies have provided strong evidence that cdb3 can exist in three different conformations with the mid-points for the transitions at pH 7.2 and 9.2, that the transitions do not involve changes in the secondary structure of cdb3, and that there is an increase in molecular asymmetry and segmental dynamics as the pH is increased (Low *et al.* 1984; Thevenin *et al.* 1994; Zhou and Low 2001). Previous work (Zhou and Low 2001) has shown that recombinant cdb3 (residues 1-379) undergoes the same conformational transitions as cdb3 isolated from erythrocyte membranes. However, other work indicated that chemical modification or cross-linking of the two endogenous cysteine residues of wt-cdb3 led to a merging of the two structural transitions into a single transition with a midpoint at pH 8.7 (Low *et al.* 1984). Since one of the main goals of this work was to compare the solution structure of cdb3 at neutral pH with the crystal structure determined at pH 4.8, and since the two endogenous cysteines were mutated to alanines prior to introduction of a single cysteine at a selected position for site-directed spin labeling, it was important to compare the magnitude of the change in tryptophan fluorescence in recombinant wt-cdb3 with recombinant cysless-cdb3. As shown in Figure 23, similar changes in tryptophan fluorescence were observed as a function of pH indicating that very similar conformational changes were occurring in both proteins. The two midpoints around pH 7 and 9 of wt-cdb3 reported in the literature are not as prominent for cysless cdb3, but the overall magnitude of change is comparable.

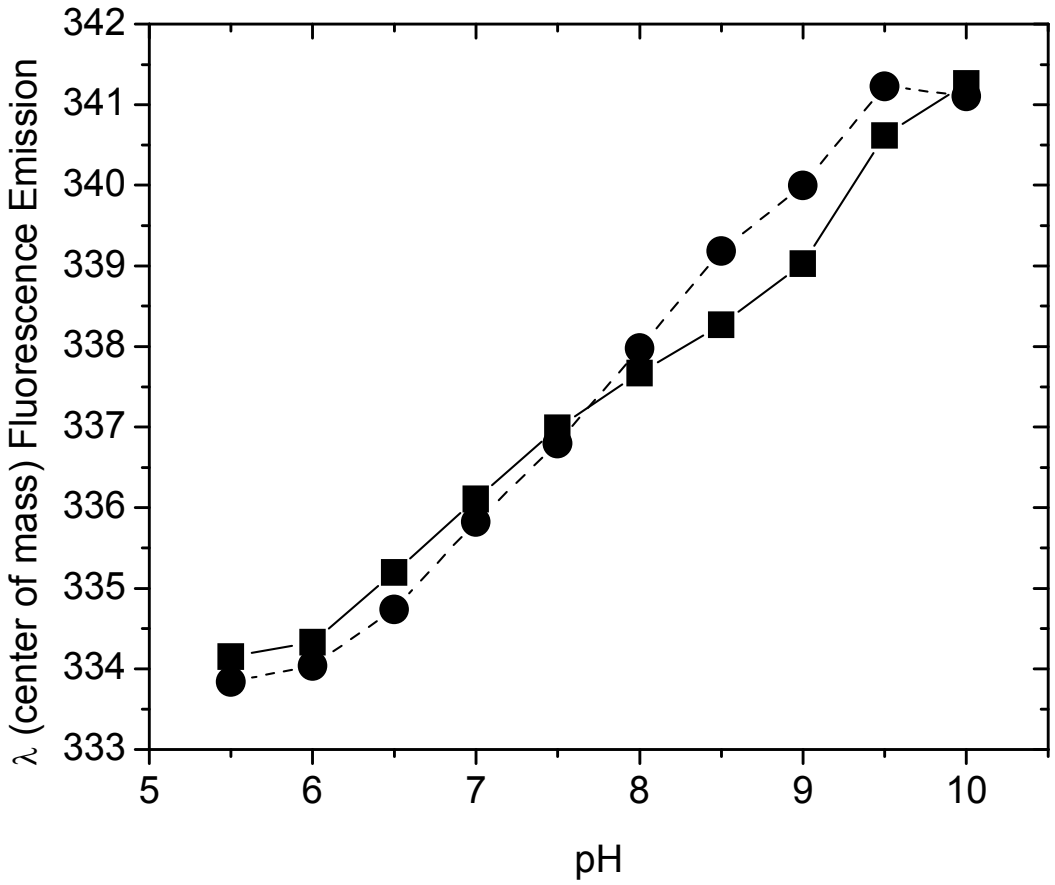

Figure 23. Intrinsic tryptophan fluorescence of cdb3

The filled squares are from wt-cdb3 and the filled circles are from cysless-cdb3. The data are plotted as the wavelength (λ) at the center of mass of the tryptophan fluorescence emission spectrum versus pH.

Structure and packing of residues 127-137 in the peripheral domain of cdb3

Residues 127 to 137 form an α-helix in the crystal structure at pH 4.8 with one surface of the helix packed against the central β-sheet and the opposite surface exposed to solvent. To assess whether this structural feature was preserved at neutral pH, each residue from 127 to 137 was mutated to cysteine, one at a time. The proteins were expressed, purified, and spin labeled with MTSSL to yield the spin-labeled side chain denoted R1 (Figure 12). The EPR spectrum at each position is shown in Figure 24.

Solvent accessibility was measured for each of these spin-labeled proteins using NiEDDA as a water soluble paramagnetic broadening agent using a TM_{110} cavity (Farahbakhsh *et al.* 1992; Hubbell *et al.* 1996) as shown in Figure 25. These data show a sinusoidal change in accessibility to NiEDDA with a period of approximately 3.6 residues, which is characteristic of an α-helix with one surface exposed to solvent and the opposite surface buried in a structured region of the protein. Residues 128, 131, 132, and 135 are the least accessible to the aqueous paramagnetic broadening agent in complete agreement with the packing of the same surface of this α-helix against the β-sheet as determined in the crystal structure (Figure 25). The rotational mobility of the spin-labeled side chains at each of these buried positions was also hindered relative to the adjacent surface exposed sites on the opposite face of the helix as shown in Figure 25 by the inverse second moment of the EPR spectrum (Hubbell *et al.* 1996). Together, these results provide strong evidence that the structure of this surface helix, and by inference, the surrounding protein structure in the peripheral domain of cdb3, is the same in solution at neutral pH as it is in the crystal lattice at pH 4.8.

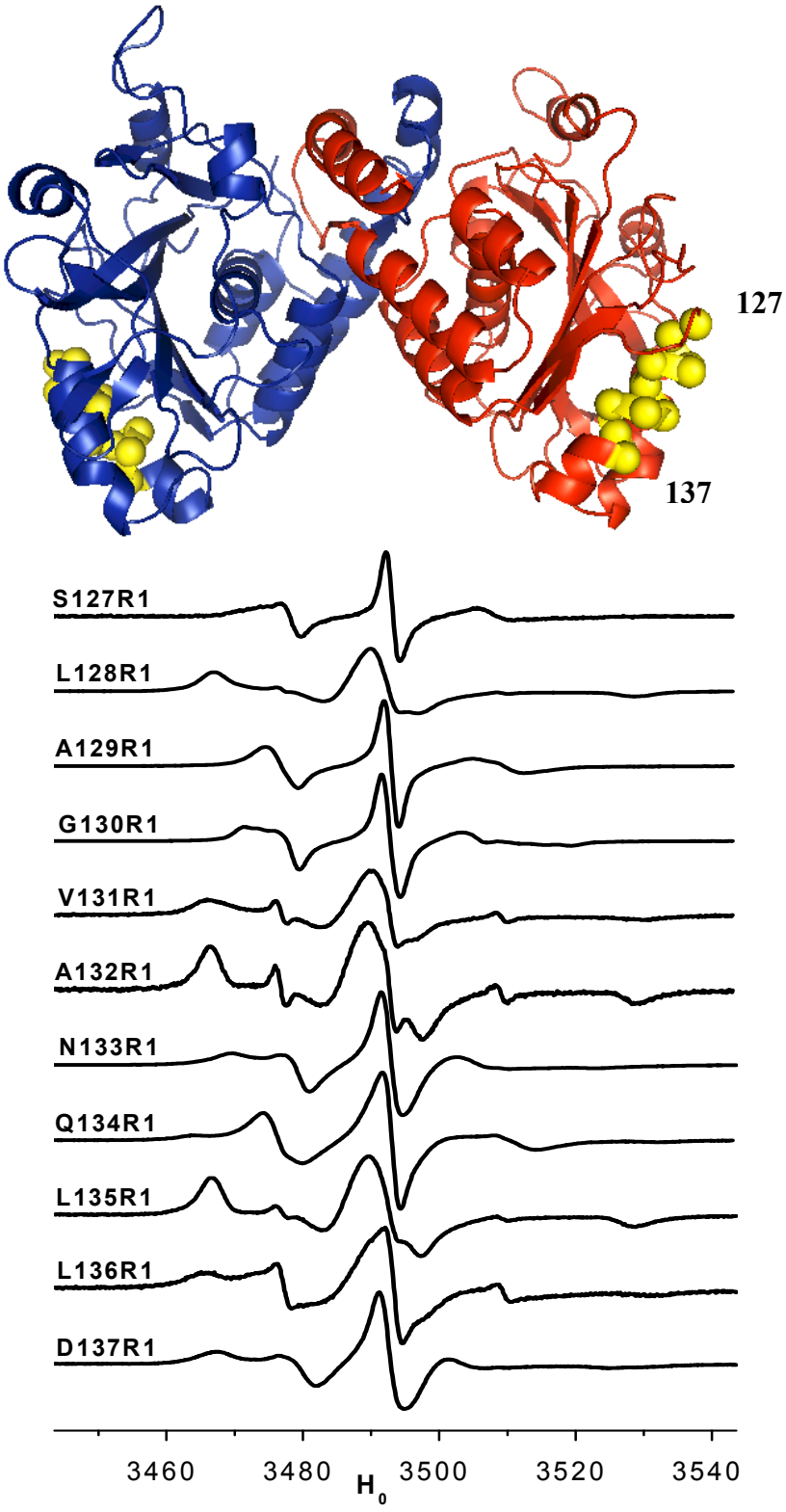

Figure 24. CW-EPR characterization of residues 127-137 on a surface helix

The upper panel shows the structure and location of residues 127-137 in the crystal structure (yellow) on the ribbon diagram of the cdb3 dimer (blue and red). The conventional CW-EPR spectrum at each position is shown in the lower panel normalized to the same amplitude and with a total scan width of 100 Gauss.

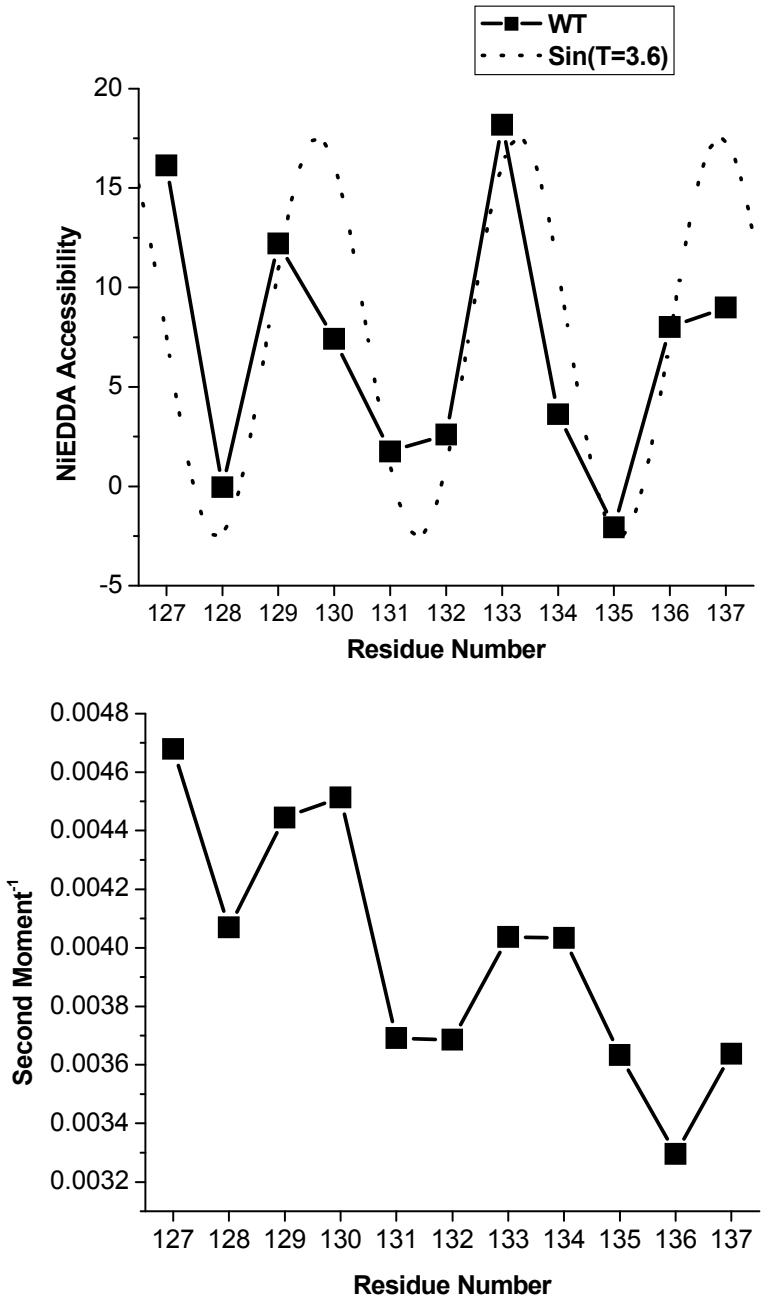

Figure 25. Parameterized EPR data from residues 127-137

The upper panel shows a plot of the accessibility of the R1 side chain at each indicated residue to NiEDDA using P1/2 data obtained in a TM_{110} cavity. The dotted line represents a sinusoid with a period of 3.6 residues per turn. The lower panel shows a plot of the inverse second moment of the conventional CW-EPR spectrum (Figure 24) at each residue. The parameters were calculated from the EPR data as described in Methods.

Structure of the dimer interface in cdb3

The high stability of the cdb3 dimer can be explained by the extensive interactions between the "dimerization arms" of each monomer observed in the crystal structure (Zhang *et al.* 2000). The dimerization arms of each monomer (residues 314-344) are composed of helix $\alpha 9^{304\text{-}316}$, beta strand $\beta 11^{318\text{-}323}$, and helix $\alpha 10^{328\text{-}347}$. The close packing of residues of cdb3 around helix 9 and beta strand 11 in the crystal structure suggested that these regions might be difficult to characterize by site-directed spin labeling given the lack of contrast (i.e. limited solvent exposure) and potential difficulty in stoichiometric spin labeling of introduced cysteine residues in these secondary structure elements. However, based on the static structure, helix 10 was predicted to be an attractive and informative segment for SDSL characterization. Hence, the structure and packing of the C-terminal portion of helix 10 (residues 337-348) was investigated as shown by the EPR spectra in Figure 26. Accessibility to NiEDDA obtained from EPR spectra recorded in a TM_{110} cavity showed a periodicity of approximately 3.6 residues with local minima in the accessibility profile at residues 339, 342, 345, and 346 as shown in Figure 27. The same experiment has been repeated using a new dielectric cavity (see next Chapter). The accessibility data are in close agreement with side-chain mobility measurements which showed local minima at residues 339, 342, and 346 as revealed by the inverse second moment of the EPR spectrum (Figure 27). The data in Figure 27 also suggest that there is a monotonic increase in average accessibility and side chain mobility in progressing from residue 337 to 348. These findings are all consistent with residues 337 to 348 forming an α-helix with greater solvent exposure at the C-terminal end and

with the same face of the helix packed in the interior of the cdb3 dimer, as predicted by the crystal structure determined at pH 4.8 (Zhang *et al.* 2000).

The EPR spectrum observed with the R1 side chain at residue 339 gives a highly resolved dipolar coupling between the spin labels on each monomer. The magnitude of this inter-subunit dipolar coupling provides a direct measure of the distance between these two spin-labeled side chains in the cdb3 dimer (Rabenstein and Shin 1995; Hustedt *et al.* 1997; Hustedt and Beth 1999; Hustedt and Beth 2000; Stein *et al.* 2004). The data in Figure 28 show the spectral effects of the intersubunit dipolar coupling (compare the double labeled and the single labeled samples). Analysis of the double labeled spectrum using a tether-in-a-cone model (Stein *et al.* 2004) yielded an interprobe distance of 14.7 Å. As discussed more fully below, this distance is very close to the distance predicted from the static crystal structure with a spin-labeled cysteine residue modeled at position 339 in place of the normal wild-type glutamine residue.

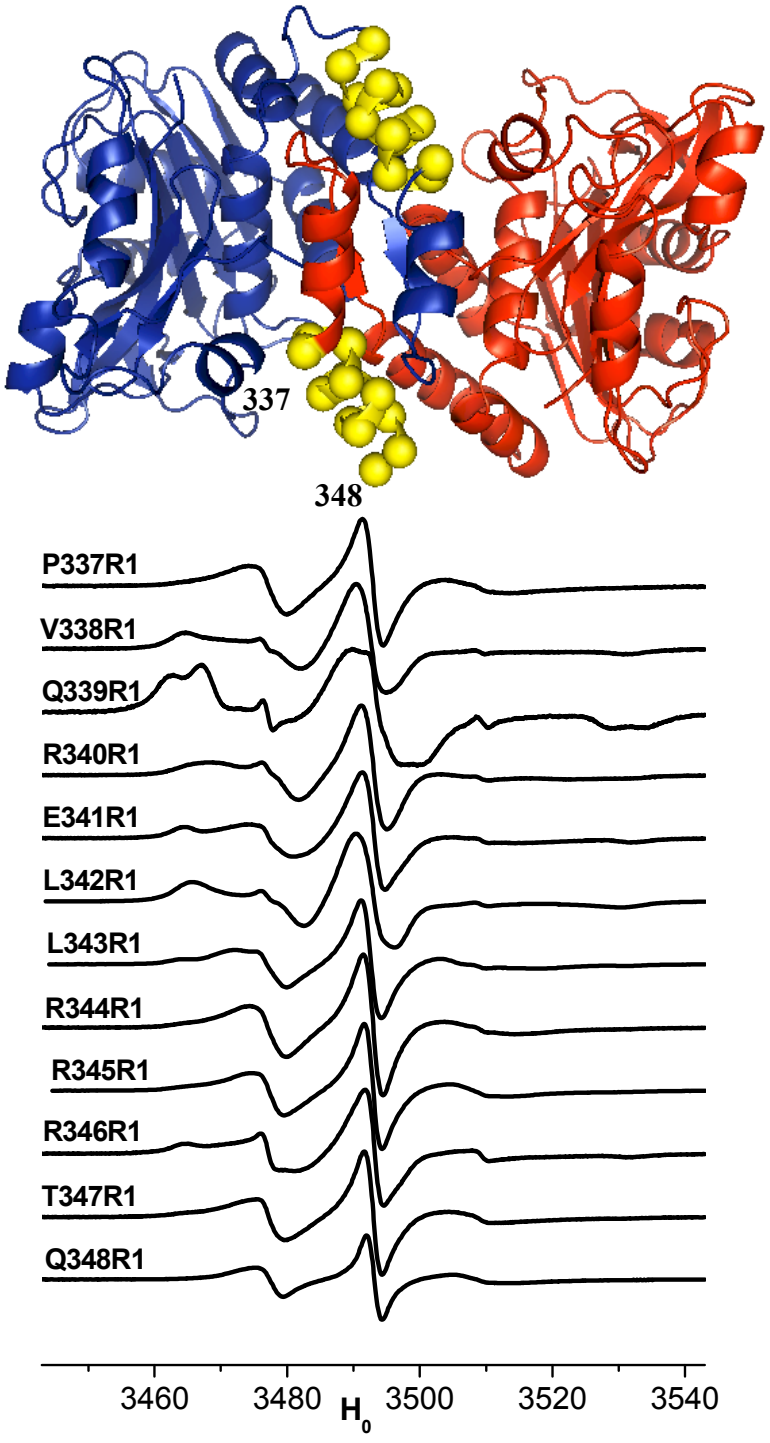

Figure 26. CW-EPR characterization of residues 337-348 on the dimerization arm

The upper panel shows the structure and location of residues 337-348 in the crystal structure (yellow) on the ribbon diagram of the two subunits of the cdb3 dimer (blue and red). The conventional CW-EPR spectrum at each position is shown in the lower panel normalized to the same amplitude and with a total scan width of 100 Gauss.

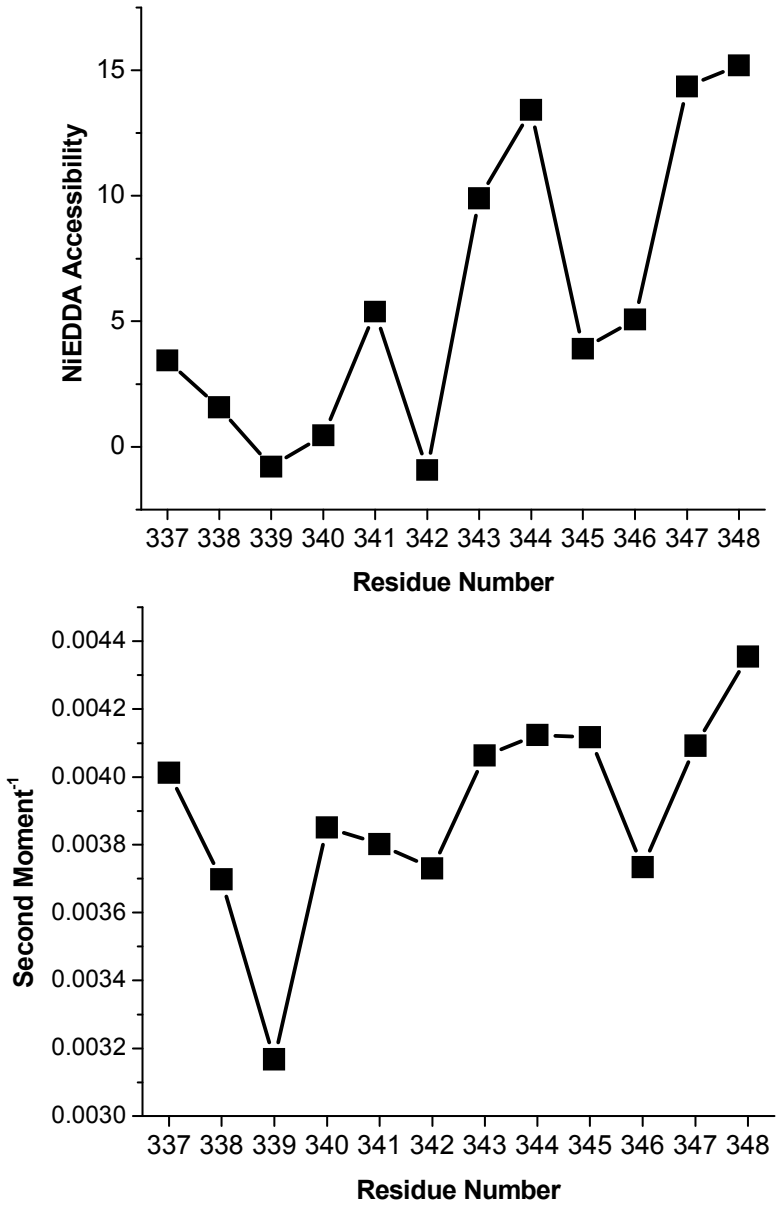

Figure 27. Parameterized EPR data from residues 337-348

The upper panel shows a plot of the accessibility of the R1 side chain at each indicated residue to NiEDDA using P1/2 data obtained from a TM_{110} cavity. The lower panel shows a plot of the inverse second moment of the conventional CW-EPR spectrum (Figure 26) at each residue. The parameters were calculated from the EPR data as described in Methods. At residue 339, the second moment was calculated from the EPR spectrum obtained after single labeling (see Figure 28, lower panel) thereby excluding the contributions of dipolar coupling.

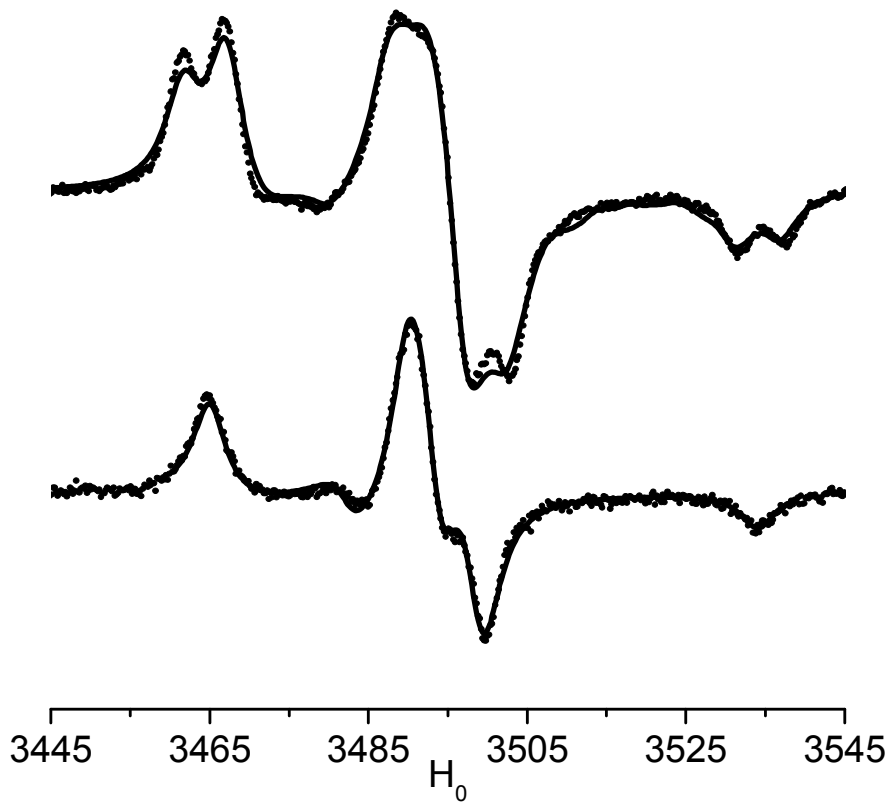

Figure 28. Analysis of EPR spectra at residue 339 using tether-in-a-cone model

The experimental EPR spectra under conditions of double labeling (R1 side chain incorporated in both subunits; upper) and single labeling (R1 side chain in only a fraction of sites in one subunit; lower) are shown as dots. The best-fit computer simulations for each spectrum are shown as solid lines. Analysis of the lower single labeled spectrum (Hustedt *et al.* 1993) allowed determination of the principal elements of the A and G tensors: g_{xx} = 2.0079; g_{yy} = 2.0062; g_{zz} = 2.0024; A_{xx} = 7.82 Gauss; A_{yy} = 2.81 Gauss; and A_{zz} = 34.51 Gauss. These values were used as input parameters for fitting the upper double labeled spectrum using a tether-in-a-cone model (Hustedt *et al.* 2006), which gave an average interprobe separation (14.7 Å) and the width of the distance distribution (0.4 Å).

Intersubunit distances between residues 340-345 of the dimerization arm

To more fully characterize the spatial arrangement of the dimerization arms of the two monomers in the cdb3 dimer, pulsed Double Electron Electron Resonance (DEER) measurements were carried out with spin-labeled cysteine residues in positions 340 through 345. Representative data are shown in Figure 29. DEER is a pulsed EPR technique that extends the maximum inter-probe distance that can be measured from the

20 to 25 Å range by CW-EPR methods (Rabenstein and Shin 1995; Hustedt *et al.* 1997; Hustedt and Beth 1999; Hustedt and Beth 2000) out to the 40 to 50 Å range (reviewed in (Jeschke *et al.* 2000), see introduction to EPR distance measurement on pages 65-77). The sensitivity to long distances permit placing spin label probes at sequential positions that are not likely to disrupt the structure of the dimer interface due to changes in packing of side chains in the interior of the protein while still providing direct information on the spatial arrangement of the dimerization arms. The data in Figure 30 show that the interprobe distances measured from CW-EPR (residue 339; Figure 28) and DEER (residues 340-345; Figure 29; data from all sites compiled in Table 3) experiments followed the same trend as the Cα-Cα distances measured from the corresponding residues in the crystal structure at pH 4.8.

Also shown in Figure 30 are the predicted average distances between the unpaired electrons of the two spin labels from molecular modeling of the R1 side-chain at each site based on the static crystal structure. The results of these modeling experiments, which were carried out to approximate contributions from the dimensions and flexibility of the R1 side chain as described in Methods (see (Poirier *et al.* 1998; Borbat *et al.* 2002; Sale *et al.* 2002; Schiemann *et al.* 2004) for additional discussion), are in reasonable agreement with the interprobe distances that were obtained from the experimental measurements. When combined with the data in Figure 27, which showed that residues 339-346 form a continuous α-helix, these long-range distance constraints show that the spatial arrangement of these two helices in the cdb3 dimer is very similar, if not identical, to their spatial arrangement in the crystal structure at pH 4.8.

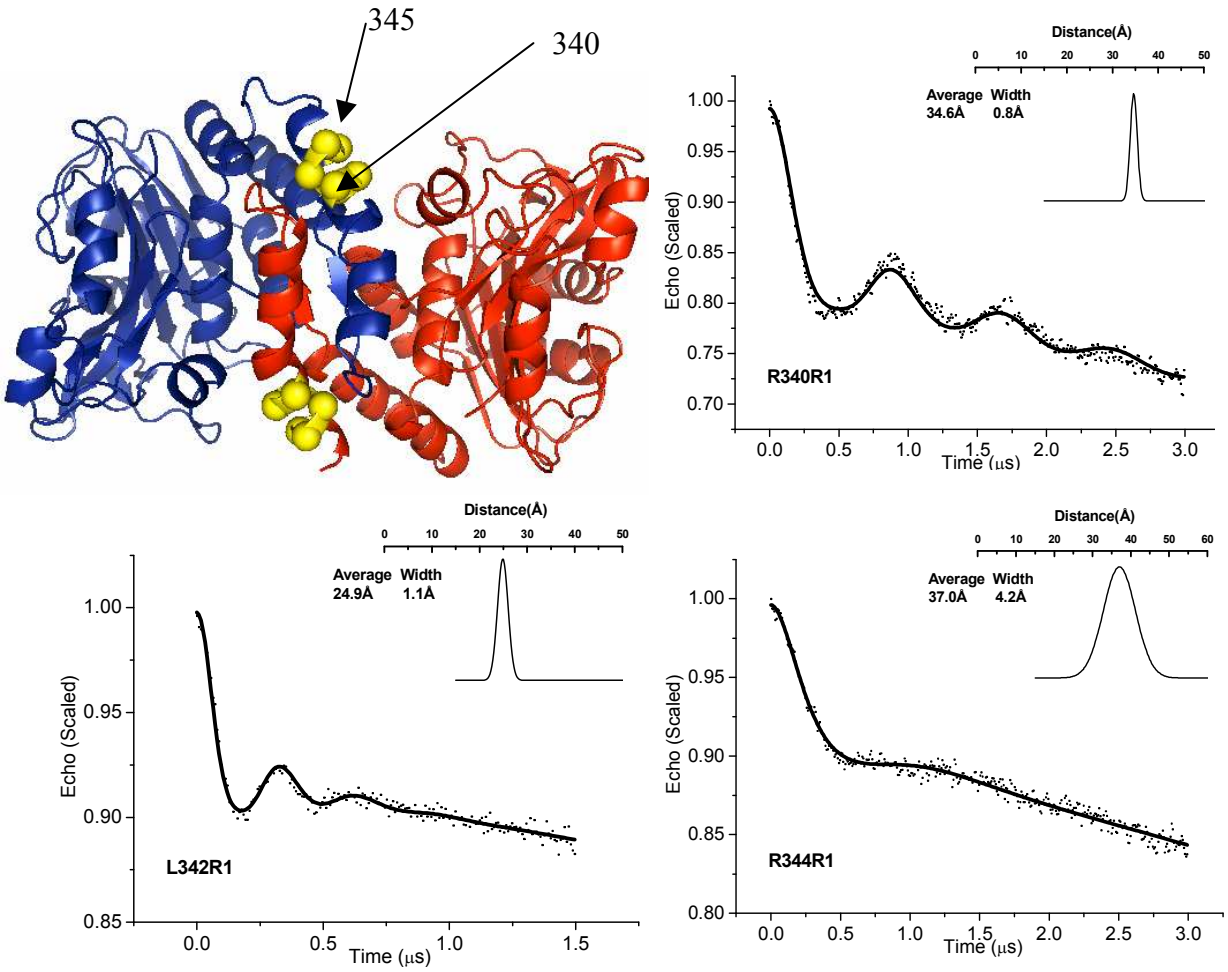

Figure 29. DEER characterization of intersubunit distances between residues 340-345 in the dimerization arm

The upper left panel shows the structure and location of residues 340-345 in the crystal structure (yellow) on the ribbon diagram of the two subunits of the cdb3 dimer (blue and red). The scaled echo amplitude (shown as dots, normalized to 1) is plotted as a function of time in a 4-pulse DEER experiment with the R1 side chain at positions 340 (upper right), 342 (lower left), and 344 (lower right). The solid line is the best fit of the scaled echo amplitude versus time using DeerPackage 2002.1 as described in Methods. The insets in the upper right of each DEER spectrum show the average interprobe distance and the distribution of distances from fitting the experimental data. Tabular data for residues 341, 343 and 345 (DEER data not shown) are listed in Table 3.

Table 3. Interresidue distance in the dimerization arm of cdb3

Residue #	339	340	341	342	343	344	345
R (Å)	14.7[a]	34.6	31.9	24.9	34.0	37.0	35.5
σ (Å)	0.4[a]	0.8	3.6	1.1	2.3	4.2	6.6

[a]The values for R and σ at residue 339 were obtained by fitting the CW-EPR data to a tether-in-a-cone model (Hustedt *et al.* 2006). The values for R and σ at positions 340 through 345 were determined by fitting the corresponding DEER data to a single Gaussian distribution of interspin distances as described in Methods.

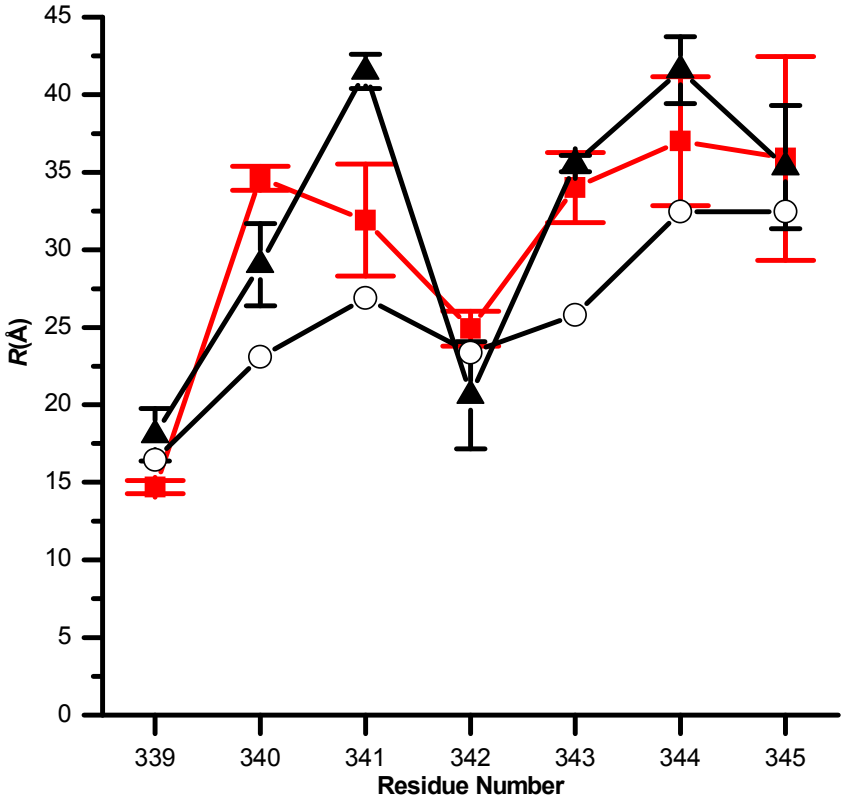

Figure 30. Comparison of calculated and experimentally determined interprobe distances in the dimerization arm

The open circles show the C_α-C_α distances from the crystal structure. The filled squares (red) are the experimentally determined inter-R1 distances determined from fitting the CW-EPR data (339) or the DEER data (340-345). The vertical bars are the widths of the distance distributions determined from fitting the experimental data (σ in the Gaussian function is the standard deviation). The filled triangles are the predicted average distances and the widths of the distance distributions that were calculated by modeling the R1 side chain into the crystal structure at each position (see the method section). The widths of the distance distributions were calculated by positioning the spin label at all allowed orientations (no steric clashes with nearby residues) by rotation about dihedral angles χ_4 and χ_5 (Figure 12).

Intersubunit distances at additional sites away from dimerization arm

Previous studies have provided compelling evidence that the Stokes radius of cdb3 reversibly increases from 55 to 66 Å as the pH is raised in the range of 6 to 10 with the most dramatic increase (~80%) occurring between pH 8 and 10 (Low *et al.* 1984; Zhang *et al.* 2000; Zhou and Low 2001). Based on the crystal structure, it has been hypothesized that cdb3 could form elongated structures without an overall change in secondary structure, by rotations about residues G305 (Figure 19) or E291 (Zhang *et al.* 2000). To test whether cdb3 exhibited a significantly elongated structure at neutral pH relative to the static crystal structure, 11 different sites on the side of the compact peripheral domain of each monomer that is proximal to the dimer interface were chosen for measurement of interprobe distances as shown in Figure 31. Following expression, purification, and spin labeling of each of these 11 single cysteine mutants, EPR or DEER experiments were carried out and analyzed to determine the average interprobe separation distance and the distribution of interprobe distances (Table 4). Figure 31 demonstrates that the average distances from these measurements agree extremely well with the Cα-Cα distances measured from the crystal structure but do not agree well, either in general trend or in magnitude, with the two elongated models that were generated by rotations about E291 or about G305.

Table 4. Interresidue distances between selected sites away from dimerization arm

Residue #	84	96	105	108	112	116	142	199	208	277	290
R (Å)	27.2	32.6	15.4	6.2[a]	18.0[a]	17.4	32.1	36.2	47.7	29.8	38.4
σ (Å)	2.5	5.0	3.7	4.4[a]	6.9[a]	3.1	3.1	5.0	13.2	3.4	0.5

[a]The values for R and σ at positions 108 and 112 were determined by fitting the CW-EPR data with a convolution method assuming a single Gaussian distribution of distances (Rabenstein and Shin 1995). The values at all other residues were determined by fitting the corresponding DEER data to a single Gaussian distribution of distances as described in Methods.

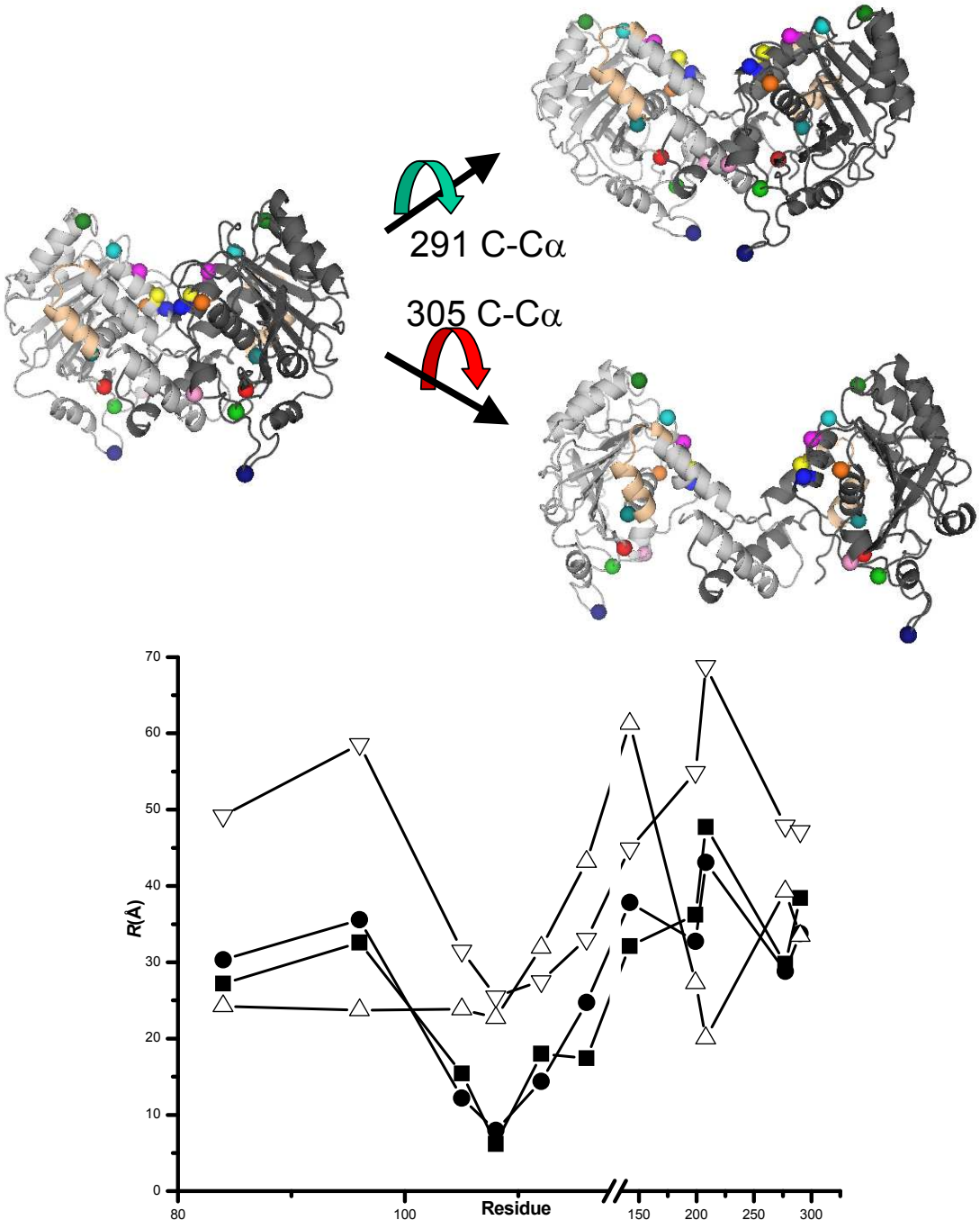

Figure 31. Comparison of interprobe distances for three structural models of cdb3
The ribbon structure on the left from the crystal structure shows 11 residues that were converted to the R1 side chain for interprobe distance measurements. The structure in the upper right was generated by a single 30° rotation about the C-C_α bond of Glu 291. The structure in the lower right was generated by a single 30° rotation about the C-C_α bond of Gly 305. The plot in the lower panel shows the experimentally determined interprobe distances at residues 84 (red), 96 (green), 105 (dark blue), 108 (yellow), 112 (purple), 116 (light blue), 142 (dark green), 199 (pink), 208 (blue), 277 (orange), and 290 (medium blue) as filled squares. The filled circles are the C_α-C_α distances from the crystal structure on the left. The open triangles are the C_α-C_α distances from the structural model in the upper right. The inverted open triangles are the C_α-C_α distances from the structural model in the lower right.

Structure of the N-terminus of cdb3

N-terminal residues 1-54 were not resolved in the crystal structure of cdb3, presumably due to this region of the protein being disordered (either static or dynamic) in the crystal lattice (Zhang *et al.* 2000). Given the central role that the N-terminus plays in binding several intracellular proteins, it is important to determine the structure and dynamics of this region. Toward this goal, single cysteine residues were introduced into cdb3 at positions 2, 15, 16, 34-38, 45, 46 and 48-56, spin labeled, and the CW-EPR spectra were recorded at each of these positions as shown in Figure 32. At sites 2, 15, 16, 34-38, 45, and 46 the EPR spectra were indicative of fast, relatively unrestricted motion as would be expected for a dynamically disordered peptide lacking stable secondary structure in solution. From residues 46 to 56 there was a monotonic decrease in mobility until residues 54 through 56, where the EPR spectra were characteristic of a spin-labeled side-chain in a structured environment in tertiary contact with nearby elements of secondary structure (Hubbell *et al.* 1996). These data, which are consistent with the boundary between structured and disordered domains in the crystal structure, demonstrate that the N-terminus of cdb3 lacks stable secondary structure and exists in solution as a highly flexible and dynamic structure on the nanosecond time scale that is capable of accessing the full range of available conformational states.

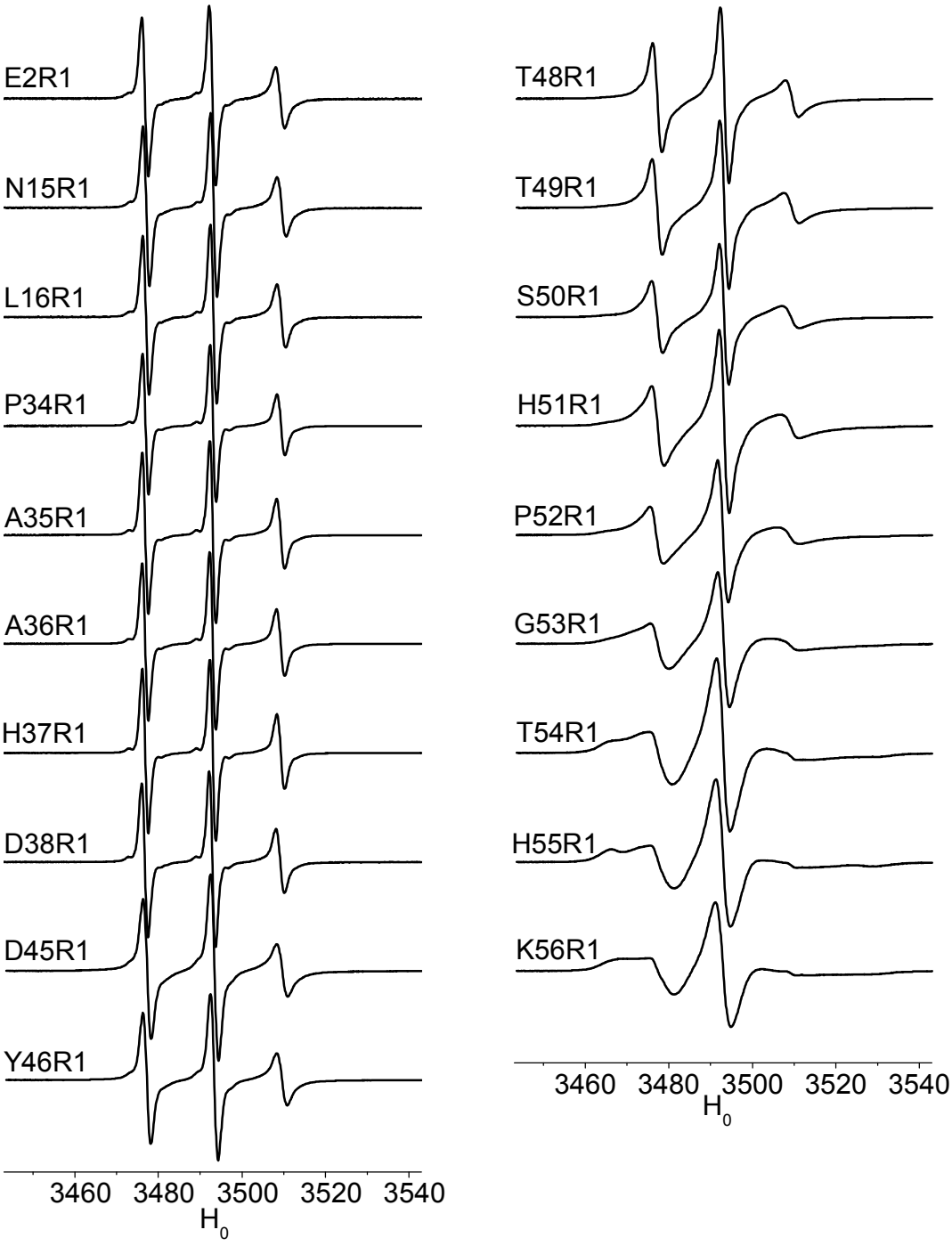

Figure 32. EPR characterization of the structure and dynamics of the N-terminus

The conventional CW-EPR spectra at selected residues in the N-terminus of cdb3 are shown as 100 Gauss displays normalized to the same amplitude.

Structure of the C-terminus of cdb3

The structure of the C-terminus of cdb3 is of considerable interest since this segment forms the physical link with the transmembrane domain of AE1. Previous work has suggested that there is a flexible linkage between the two independent domains of AE1 (Blackman *et al.* 2001) and that this flexibility may be critical for maintenance of the unusual mechanical properties of the erythrocyte membrane (Moriyama *et al.* 1992; Schofield *et al.* 1992; Wang 1994). Single cysteine residues were introduced at positions 357, 358, 361, 364, 368, 372, 376, and 378, spin labeled, and the EPR spectra recorded as shown in Figure 33. At all of these positions, the EPR spectra were indicative of relatively unrestricted motion as would be expected for peptide lacking stable secondary structure in solution.

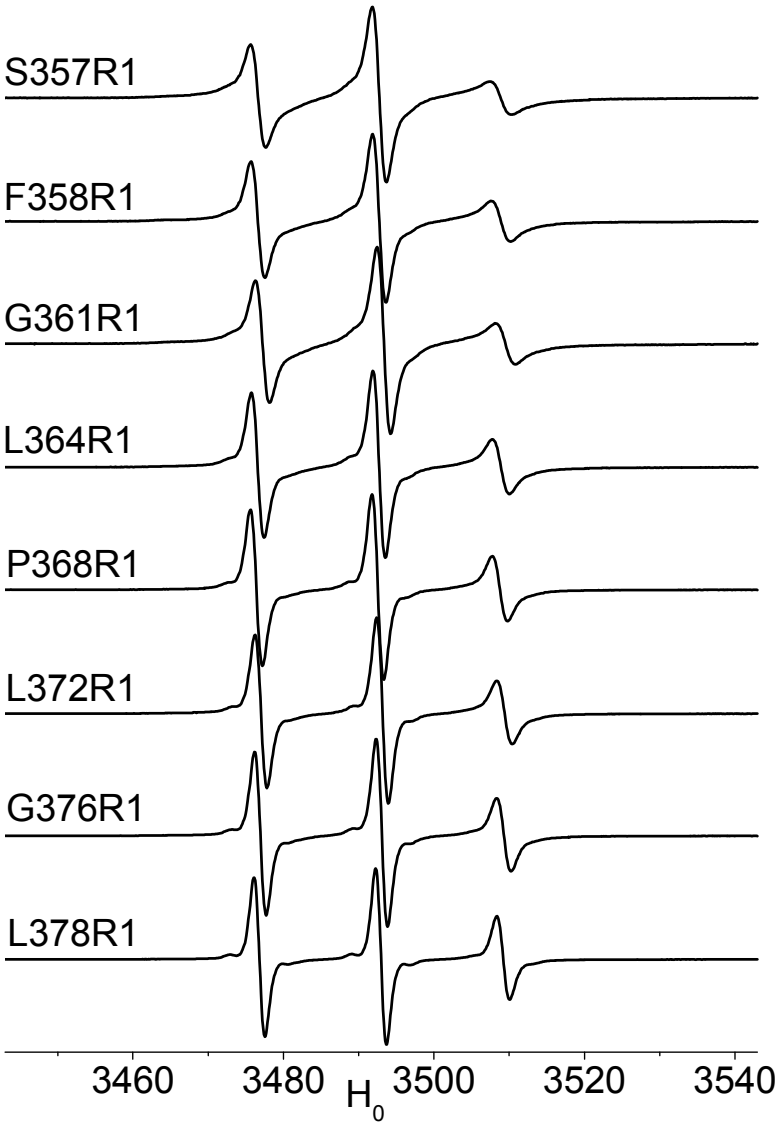

Figure 33. EPR characterization of the structure and dynamics of the C-terminus

The conventional CW-EPR spectra at selected residues in the C-terminus of cdb3 are shown as 100 Gauss displays normalized to the same amplitude.

Discussion

Significance

Recent progress in determination of the atomic resolution structures of cdb3 (Zhang *et al.* 2000) and a large fragment of ankyrin (Michaely *et al.* 2002) has enabled the design of new experiments aimed at assembling atomic, or near atomic, resolution models of the complex of proteins that are known to stabilize the erythrocyte membrane. An essential starting point for establishing these models is an accurate knowledge of the solution structure of cdb3 at physiological pH. For many proteins, determination of the atomic resolution structure at a non-physiological pH would be adequate. However, for cdb3, previous hydrodynamic studies (Appell and Low 1981; Colfen *et al.* 1996) had suggested a highly elongated structure that was quite different than the compact globular structure that was determined in the crystal lattice. The hydrodynamic studies, coupled with the knowledge that intrinsic tryptophan fluorescence (e.g. (Zhou and Low 2001)), thermal stability (Appell and Low 1981), stokes radius (Low *et al.* 1984), and segmental dynamics (Thevenin *et al.* 1994) all exhibited significant changes as a function of pH in the range from 6 to 10, provided suggestions that the structure of cdb3 could be significantly different at pH 4.8 than in the physiological 7.2 to 7.4 range.

In addition to raising concerns about the magnitude of structural changes that occur as a function of pH, previous studies had not led to a clear elucidation of the structure and dynamics of the N- and C-terminal segments of cdb3. Neither of these regions was resolved in the crystal structure. However, they both play key roles in the overall function of cdb3 with the N-terminus serving as a critical organizing center for

binding to a number of intracellular proteins (reviewed in (Low 1986)) and the C-terminus forming a physical link to the transmembrane domain of AE1. To address the magnitude of structural changes that occur as a function of pH and to elucidate the structure and dynamics of the N- and C-terminal segments, the two endogenous cysteines in cdb3 were mutated to alanine and a unique cysteine was introduced at selected positions, spin labeled, and characterized using established approaches of site-directed spin labeling and EPR to elucidate secondary structure, tertiary structure contacts, solvent accessibility, and local side-chain dynamics (reviewed in (Hubbell and Altenbach 1994; Hubbell *et al.* 1996; Hubbell *et al.* 1998); (Feix and Klug 1998). Similarly, the quaternary structure of the cdb3 dimer was investigated using the recently developed pulsed EPR method, DEER. Collectively, this study has provided strong evidence that the structure of the central core of cdb3 at physiological pH is indistinguishable, within the limits of current resolution, from that reported for the crystal structure at pH 4.8. Additional studies have shown that the N- and C-termini of cdb3 are dynamically disordered.

Evaluation of the pH dependent conformational changes

The phosphate, bicarbonate, bisulphate ions and proteins constitute a very effective buffering system so that the pH changes within a circulating red blood cell are very restricted (pH 7.3 ± 0.1). Interestingly solid experimental evidence has shown that cdb3 undergoes reversible conformational rearrangements as a function of pH (e.g. tryptophan fluorescence (Zhou and Low 2001), thermal stability (Appell and Low 1981), Stokes radius (Low *et al.* 1984), and segmental dynamics (Thevenin *et al.* 1994)). For example, as pH is increased from 6.0 to 10.0, the Stokes radius increases from 55 to 66 Å

(Low *et al.* 1984) or from 51 to 62 Å (Zhou and Low 2001). Simultaneously, the intrinsic tryptophan fluorescence intensity at fixed wavelength increases from highly quenched by the W105-D316 hydrogen bond to more than doubling in value (Zhou and Low 2001). However, the largest changes appear to occur in the pH range from 8 to 10, which is well outside the normal intracellular pH range of 7.2 to 7.4 for a human erythrocyte. Initial spin-labeling studies that have been carried out in the pH 8.5-10 range have yielded EPR spectral changes at these higher pH values (data not shown; (Cobb *et al.* 2003; Cobb *et al.* 2004)). Future studies can be focused on analyzing these data to develop a structural model that may provide insights into the increased hydrodynamic radius, decreased thermal stability, increased dynamics, and decreased and shifted tryptophan fluorescence that have previously been reported. However, the most pressing question is: what is the structure of cdb3 under conditions that approximate the physiological pH environment within the erythrocyte? Therefore, this work is focused on answering the fundamental question of how the structure of cdb3 at neutral pH compares with the crystal structure determined from crystals grown at pH 4.8. It should be noted that it was not possible to compare EPR and DEER data from spin-labeled samples at neutral pH with the corresponding data obtained at pH 4.8 due to the tendency of many of the single cysteine mutants of cdb3 to aggregate (~100 μM) at the lower pH. This aggregation, which was almost immediate for some samples, produced spectral shifts that masked any structural changes that might have occurred.

Structure of the peripheral $\alpha^{+}\beta$-fold domain

The crystal structure of cdb3 showed that the peripheral protein binding domain was composed of a compact $\alpha^{+}\beta$-fold with the central β-sheet packed on both faces against α-helices. In order to assess the effect of pH on the global structure of the peripheral protein binding domain, residues (127-137), which comprise a major portion of the $\alpha 2^{128\text{-}141}$ surface exposed helix, were individually mutated to the R1 side chain and characterized by EPR as shown in Figures 24 and 25. The parameterized data in Figure 25 are consistent with an α-helix with one surface exposed to the water soluble paramagnetic broadening agent NiEDDA and the opposite face packed against the interior of the protein and inaccessible to NiEDDA. Likewise, the second moments of the EPR spectra, which provide a measure of the restriction of R1 side chain motion (e.g. (Hubbell *et al.* 1996)), are also consistent with residues 127-137 forming a standard α-helix. The data in Figure 25 (lower) are plotted as the inverse second moment so that the phase of the side chain mobility data is the same as the accessibility data (i.e. the least restricted R1 side chains with the largest inverse second moments have the highest exposure to water and the greatest accessibility to NiEDDA). The parameterized data in Figure 25 are all consistent with the structure and packing of this α-helix that was determined in the crystal structure. While these data do not rule out subtle structural rearrangements of the peripheral protein binding domain in solution at neutral pH, they do provide solid evidence that the local structure in, and around, the α2-helix is preserved. This observation, coupled with the compact globular nature of this domain with an extensive hydrophobic core, strongly suggests that the reported pH dependent conformational changes in cdb3 do not result from major changes in the structure of the

peripheral protein binding domain in agreement with previous predictions (Zhang *et al.* 2000).

Structure of the dimer interface in cdb3

The crystal structure of cdb3 revealed extensive interactions, consisting of eight intermonomeric hydrogen bonds and a hydrophobic core of nine leucine residues, between the dimerization arms (residues 314-344) of each monomer (Zhang *et al.* 2000). These multiple interactions, coupled with the fact that cdb3 is a stable dimer throughout the pH range where structural transitions have been observed, suggested that the local structure in the dimer interface was preserved at neutral pH. As a direct test of this tenet, residues 337 to 348 were individually converted to the R1 side chain and the EPR spectra characterized as shown in Figures 26 and 27. The parameterized data in Figure 27 show that these residues are contained in an α-helix (NiEDDA and inverse second moment show sinusoidal trends with an approximate periodicity of 3.6 residues) and the same surfaces of the helix are exposed to water and buried as reported in the crystal structure at pH 4.8 (Zhang *et al.* 2000). These data provide solid indications that the local structure in, and around, helix 10 is the same at neutral pH as reported in the crystal structure.

The EPR spectrum at residue 339 (Q339R1; Figure 26) showed classic characteristics of a resolved intersubunit dipole-dipole interaction between the R1 side chains on adjacent monomers. Such highly resolved dipolar couplings are only seen in conventional continuous wave EPR spectra when the two spin label probes are separated by 18 Å or less (see (Hustedt and Beth 1999); (Hustedt and Beth 2000)). Analysis of the EPR spectrum at this position, using a newly developed tether-in-a-cone model (Stein *et*

al. 2004), yielded an interprobe distance of 14.7 Å (Figure 28). This is very close to the average predicted distance of 18.1 Å between the R1 side chains based on the static crystal structure and molecular modeling as shown in Figure 30.

The structure of the dimer interface was more fully characterized by DEER measurements at positions 340-345 as shown in Figure 29. The conventional EPR spectral shapes and linewidths at each of these positions were characteristic of spatially isolated spin labels (Figure 26), indicating a separation of 25 Å (Rabenstein and Shin 1995; Hustedt *et al.* 1997; Hustedt and Beth 1999; Hustedt and Beth 2000). However, as shown in Figure 29 and in Table 3, the interprobe distances were readily measured using DEER. As shown in Figure 30, the experimentally determined distances were in reasonable agreement with the average distances predicted from molecular modeling of allowed probe orientations. It is important to emphasize that the trend of measured intersubunit distances followed the Cα-Cα distances calculated from the crystal structure throughout this region. The important points to be made in regard to this work are that the experimental data in Figures 26 and 27 indicate that residues 337-348 are contained within a continuous α-helix and that the intersubunit (interhelical) distances between residues in the two helices in the cdb3 dimer (Figures 28-30) indicate that their spatial arrangement is the same, within the limits of current resolution, as reported in the crystal lattice. While it is not possible to absolutely rule out a subtle 1 to 2 Å rigid body change in helix position, it would be difficult to reconcile the entire body of experimental data in Figures 26, 27, 28, 29, and 30 with a larger change in position or relative orientation.

An important consideration in evaluating structural models that are derived or refined based on interprobe distance constraints obtained from conventional or pulsed

EPR methods is how accurate these distances are. Accordingly, several studies have appropriately been devoted to making measurements on well-defined model systems using both continuous wave EPR (e.g. (Rabenstein and Shin 1995; Hustedt *et al.* 1997; Kim *et al.* 2004)) or pulsed EPR techniques including double quantum coherence (DQC; (Borbat *et al.* 2002; Borbat *et al.* 2004)) and DEER (e.g. (Jeschke *et al.* 2000; Jeschke 2002b)). Collectively, these studies have provided solid indications that average interprobe distances in the 8-50 Å range can be measured with accuracies on the order of ± 2 Å when the distribution of distances are accurately taken into account. The greatest uncertainty remains how to accurately model the distribution of interprobe distances between the R1 side chains that reliably accounts for its inherent dimensions, flexibility, dynamics, and interactions as well as the dynamic contributions from backbone fluctuations or domain motions. Several recent studies have explored different ways of relating the experimentally determined average interprobe distances and distance distributions back to the local structure and dynamics of the protein including static modeling approaches (e.g. (Borbat *et al.* 2002; Borbat *et al.* 2004)), combined Monte Carlo and molecular dynamics approaches (e.g. (Sale *et al.* 2002)), and pure molecular dynamics approaches (e.g. (Poirier *et al.* 1998; Fu *et al.* 2003; Schiemann *et al.* 2004)). In this work, the dimensions and accessible conformational space for the R1 side chain was modeled based on the local environment in the static crystal structure. Molecular dynamics simulations (not shown) were also explored in these studies and found to give reasonable results for buried, motionally constrained sites (e.g. residues 339, 342, and 343) but much less realistic sampling at surface exposed sites (e.g. sites 344 and 345) where short (2 nsec) simulations in vacuum greatly underestimated the distribution of

distances recovered from fitting the DEER data and the apparent accessible space from the crystal structure. More extensive molecular dynamics simulations including longer trajectories using both continuum and explicit solvent models may eventually prove to be an effective method for characterizing the conformational space of the R1 side chain including the effects of local backbone fluctuations. Further development of robust methods for relating the average distances and the distribution of distances for interactions between R1 side chains remains an active area of investigation in site-directed spin labeling.

Current efforts are also being directed toward improving the methods for recovering the true distribution of distances from experimental DEER and DQC data (e.g. refs (Bowman *et al.* 2004; Jeschke *et al.* 2004; Chiang *et al.* 2005)). The implementation of these newer methods, along with obtaining experimental data at a variety of microwave frequencies, should provide the capability to more rigorously evaluate more complex distance distribution models (e.g. bimodal or multimodal) in future studies.

Quaternary structure of the cdb3 dimer at neutral pH

Based upon the crystal structure at pH 4.8, it was hypothesized that the pH dependent changes in cdb3 that had been reported in the literature did not involve changes in the peripheral protein binding domain nor in the dimer interface but that it might involve changes in the positioning of these two domains relative to each other (Zhang *et al.* 2000). Specifically, plausible models for the expansion or elongation of the cdb3 dimer could be generated by single rotations about glutamic acid 291, located between helices α7 and α8, or about glycine 305, located between helices α8 and α9. The

resulting families of structures could be generated without any significant changes in the secondary structure of the cdb3 dimer. Figure 31 shows two elongated structures that were generated either by a 30° rotation about the C-Cα bond of Glu291 (upper right) or by a 30° rotation about the C-Cα bond of Gly305 (lower right). The graphical data show that experimental intersubunit distance measurements agree very well with the Cα-Cα distances calculated from the crystal structure (R.M.S. deviation of 4.1 Å) but do not agree in magnitude or trend with the Cα-Cα distances calculated from the model generated by rotation about Glu 291 (R.M.S. deviation of 16.8 Å) or by rotation about Gly305 (R.M.S. deviation of 17.6 Å). Given the excellent agreement in overall trend of distances and the extensive coverage of labeling, it is reasonable to conclude that the tertiary structure of the cdb3 dimer at neutral pH is remarkably similar to the structure reported in the crystal lattice at pH 4.8.

This conclusion is compatible with a recent study that utilized luminescence resonance energy transfer to measure the distance between Cys201 residues on adjacent monomers of the isolated cdb3 dimer (Pal *et al.* 2005b). Specifically, this study reported a small 2 Å change in interprobe separation between pH 5 and 8 and a large 8 Å change between pH 8 and 10. The small 2 Å change between pH 5 and 8, which might be due in part to the breaking of a hydrogen bond between aspartic acid 316 (Asp316) and tryptophan 105 (Trp105) as previously hypothesized (Zhang *et al.* 2000), cannot be ruled out based on the current data. Interestingly, this study did report an 8 Å change in interprobe separation between pH 5 and 8 when measurements were carried out on full length AE1 in KI-stripped inside out vesicles prepared from erythrocyte membranes. Obviously, this structural rearrangement should be under serious consideration of the size

of the donor molecule (TbM, terbium chelate maleimide) and the acceptor molecule (FM, fluorescein 5-maleimide) as well as the number of distance constraints available to build the distance geometry. This interesting preliminary observation, which could indicate that the pH dependent structural transitions of the cytoplasmic domain are quite different in full length AE1, merits further investigation once high level expression and purification of the full length protein is accomplished.

Another possibility that should be considered is whether cdb3 adopts the same structure in the crystal lattice from crystals grown at pH 4.8 as it does in solution at pH 4.8. It is entirely possible that crystal packing forces could select for a conformation of cdb3 that is similar, or the same, as its conformation in solution at neutral pH. Along these lines, it is interesting to note that there was some asymmetry between the two monomers in the crystal structure and that the N- and C-termini were resolved to different residues in the two monomers in the crystal lattice. Examination of the crystal lattice suggests that these differences may be due to crystal packing interactions. This idea is supported by the current EPR data which do not give any indications (e.g. two-component spectra or unusual spectral broadening) of differences in dynamics or ordering of the two N- or two C-termini in the cdb3 dimer in those regions near the boundary of resolved residues in the crystal structure, suggesting that the asymmetry observed in the crystal structure does not exist in solution.

Structure and dynamics of the N- and C-termini of cdb3

The N- and C-termini of cdb3 both play important roles in the human erythrocyte with the N-terminus serving as a site for binding of several intracellular proteins

(reviewed in (Low 1986)) and the C-terminus providing a physical link between the membrane skeleton-ankyrin-cdb3 complex and the transmembrane domain of AE1. Though previous work had provided indications that the N-terminus of cdb3 binds aldolase (Schneider and Post 1995) and hemoglobin (Walder *et al.* 1984) in an extended conformation, and it would be difficult to bind these peripheral proteins to a compact and highly structured N-terminus without steric interference from the lipid bilayer (Zhang *et al.* 2000), little direct evidence for its structure has been reported. The data in Figure 32 provide compelling evidence that the entire N-terminus lacks stable secondary structure and that it is highly dynamic on the EPR (nanosecond) timescale. Using an average value of 3.5 Å for the length of a single amino acid, the N-terminal methionine of cdb3 (residues 1-54) could be located 189 Å away from the point of entry into the structured central core in its fully extended conformation. The ability of the N-terminus to exist in such an extended conformation could explain how the highly acidic distal region can bind to a wide range of rather large intracellular proteins without interference from the cytoplasmic surface of the bilayer.

It is possible that the highly acidic N-terminus could interact with the globular core of cdb3 in a pH dependent manner. Changes in the nature and extent of such interactions could contribute, in part, to the observed changes in intrinsic tryptophan fluorescence and to the increase in radius of the protein at higher pH. Additional studies will be required to test these possibilities.

Several lines of experimental evidence have suggested that at least a portion of the C-terminal segment of cdb3 is flexible and possibly lacks secondary structure ((Steck *et al.* 1976; Nigg and Cherry 1980; Blackman *et al.* 2001); reviewed in (Wang 1994)).

The data in Figure 33 show that in the isolated cdb3 dimer, residues 357-378 are indeed dynamic on the nanosecond time scale and lacking in stable secondary structure. While these data do not prove that this region is likewise unstructured in full length AE1, they are consistent with many experimental observations in the full length protein including the high degree of susceptibility to proteolysis at residue 379 (Steck *et al.* 1976), the limited restriction of rotational motion of the transmembrane domain of that subpopulation of AE1 that is bound to the membrane skeleton via ankyrin (Nigg and Cherry 1980; Blackman *et al.* 2001), and the structural and functional independence of the two domains.

Conclusions

The body of site-directed spin labeling data reported in this chapter indicates that the solution structure of the central core of cdb3 at neutral pH is remarkably similar to the structure previously reported from crystals grown at pH 4.8. While the resolution currently available from these EPR studies is not sufficient to rule out small structural differences, it is significant that the entire body of data obtained from 34 different sites in the central core domain is remarkably consistent with the static crystal structure. The results further suggest that the structural changes that have been detected in the pH 5 to 8 range using techniques such as intrinsic tryptophan fluorescence are likely due to localized changes and not to large global changes in the structure of cdb3. The N- and C-termini of cdb3 are very dynamic on the nanosecond time scale and do not exhibit detectable regions of stable secondary structure. These latter observations explain a number of previous observations including the ability of the N-terminus to bind relatively

large intracellular proteins and the limited motional coupling between the cytoplasmic and transmembrane domains of full length AE1.

CHAPTER V

STRUCTURE OF CDB3 HEREDITARY SPHEROCYTIC VARIANT: P327R

Introduction

Hereditary spherocytosis (HS) is a congenital disorder of the red blood cell membrane that is clinically associated with hemolytic anemia (See HS section for details). In HS, the erythrocytes appear as different degrees of spherical shape with decreased cell size instead of the normal biconcave-disk shape. The primary cellular dysfunction in HS is destabilization of the lipid bilayer, resulting in the budding of membrane as microvesicles and the decrease in surface area relative to volume (sphere shape). These spherical red cells become more osmotically fragile, less able to deform, and consequently sequestered in the narrow passages of the spleen (cordal-sinus junction). The splenic destruction of the trapped spherocytes is the main cause of the hemolytic anemia. HS is associated with gene SPTA1, SPTB, ANK1, EPB42 and SLC4A1, which encodes spectrin α-chain, spectrin β-chain, ankyrin, protein 4.2, and anion exchanger 1 (AE1 or band 3), respectively. These HS inducing genes are essential for the interactions between the erythrocyte membrane skeleton and the lipid bilayer (Gallagher and Ferriera 1997; Tanner 1997; Eber and Lux 2004). The incidence of HS is one family out of 2,000-3,000. Among Caucasians, band 3 defects account for approximately 15-20% of HS cases (Delaunay 2002).

Band 3 is the most abundant integral membrane protein in human erythrocytes (Fairbanks *et al.* 1971) (Refer to the AE1 section). It consists of two structurally and

functionally distinct domains (Steck *et al.* 1976; Tanner *et al.* 1988; Lux *et al.* 1989). The C-terminal transmembrane domain of band 3 exchanges bicarbonate and chloride anions across the membrane (Lepke and Passow 1976; Grinstein *et al.* 1978; Tanner 1997) whereas the N-terminal cytoplasmic domain of band 3 (cdb3) functions as an anchoring component for other membrane-associated proteins (Low 1986). The protein complex of cdb3, ankyrin (Bennett and Stenbuck 1980), protein 4.2 (Bennett and Stenbuck 1980; Rybicki *et al.* 1996), protein 4.1 (Pasternack *et al.* 1985) together with the spectrin-actin cytoskeleton network play important roles in maintaining red blood cell shape and mechanical stability (Low *et al.* 1991; Peters *et al.* 1996; Southgate *et al.* 1996) and providing flexibility and viscoelasticity for erythrocytes (Moriyama *et al.* 1992; Schofield *et al.* 1992).

A considerable number of band 3 mutations (more than 40) associated with HS have been identified and sequenced including missense mutation, nonsense mutation, frameshift, insertion and deletion. Most of them are sporadic mutations and dominantly inherited (Gallagher and Forget 1997; Tanner 1997; Delaunay 2002). The deletion of 9 amino acid residues in band 3, at the junction of the cytoplasmic and transmembrane domains, causes Southeast Asian ovalocytosis (SAO) (Jarolim *et al.* 1991; Wrong *et al.* 2002). In addition, mutations in kAE1, a band 3 isoform normally expressed at the basolateral surface of the proton-secreting α-intercalated cells in the kidney cortical collecting ducts, cause distal renal tubular acidosis (dRTA) (Eber and Lux 2004). Among these mutations, band 3 Tuscaloosa (P327R) is very intriguing with regards to structural biology. The clinical phenotype of the patient with heterozygous P327R was a typical HS with moderate hemolytic anemia. The red blood cell membrane from the patient showed

a partial (29% ± 5%) deficiency of protein 4.2. The binding of ankyrin to inside-out vesicles (IOVs) prepared from peripheral venous blood was in the normal range. In contrast, the predicted maximal binding capacity of these IOVs for protein 4.2 decreased about 20% to 33% (Jarolim *et al.* 1992). The crystal structure of wt-cdb3 (residues 55-356) has been determined at pH 4.8 (Zhang *et al.* 2000). Work presented in the previous chapter showed that the structure at low pH agreed very well with the structure at pH 7 studied by site directed spin labeling (Zhou *et al.* 2005b). The cdb3 structure at atomic resolution greatly facilitates localization of cdb3 HS mutations, which particularly have normal expression levels but abnormal structures and functions (Low *et al.* 2001). Proline 327 is situated in the loop region on the highly conserved dimerization arm (304-357) (Zhang *et al.* 2000). Open questions are whether the substitution of a basic arginine residue for proline 327 dissociates the cdb3 dimer and whether P327R causes secondary and tertiary structure perturbations (Low *et al.* 2001).

To address these questions, site directed spin labeling (SDSL) studies utilizing a combination of conventional CW-EPR and advanced pulsed-EPR (DEER) experiments were conducted on cysteineless cdb3 background with or without the P327R mutation. In this chapter, data show that substitution of arginine for proline 327 destabilizes cdb3 without inducing dimer dissociation. Structural disturbances caused by the P327R mutation localize to the adjacent region of the two 327 sites for the cdb3 dimer and the C-terminal end of the dimerization arms. No dramatic global conformation changes are detected using the biophysical tools that are currently available.

Experimental Methods

Native gel electrophoresis

Samples were prepared in the 1X loading buffer containing 31.2 mM Tris-HCl pH 6.8, 20% glycerol (V/V) and 0.005% (g/ml) bromophenol blue. The 1X native PAGE running buffer was composed of 25 mM Tris-base, 192 mM glycine, pH adjusted to 8.3. Electrophoresis was conducted on a precast gel (12% resolving gel, Bio-Rad, Hercules, CA) under constant current 10mA, about 100V in the cold room (4 °C) surrounded by ice or at room without temperature control.

Molecular cloning and protein purification

Dr. Robert Gunn (Emory University) kindly provided the full length human AE1 DNA. The segment of the cDNA encoding residues 1-379 of AE1 was amplified using Pfu DNA polymerase (Stratagene, La Jolla, CA) with the N-terminal (forward) primer

5'ACGGGAATTCCATATGGAGGAGCTGCAGGATGATTATG

and the C-terminal (reverse) primer

5'TCACACCGCTCGAGTTATTAGAAGAGCTGGCCTGTCTGCTG

(IDT DNA, Coraville, IA). The PCR product was cloned into the pET-19b vector (Novagen, Madison, WI) between the NdeI and XhoI sites, and designated as pZZ3_WT. P327R was introduced into the pZZ3_WT construct using a pair of primers:

5'CCACCGATGCCCGCTCCGAGCAGGC

5'GCCTGCTCGGAGCGGGCATCGGTGG

and designated as pZZ4_WT. The cysteineless mutants (pZZ3 and pZZ4) and single cysteine mutants were constructed by using the QuikChange® Site-Directed Mutagenesis Kit (Stratagene, La Jolla, CA). The sequences of all mutants were confirmed by DNA sequencing. Protein purification and other experimental methods are described in Chapter 3 and 4. 3D structures were visualized in PyMOL 0.97 (DeLano Scientific LLC, San Carlos, CA) and Chimera beta version 1 (UCSF, San Francisco, CA).

CD melting experiment

CD spectra were recorded as described in Chapter 3. CD melting studies were conducted on a Jasco J-810 CD spectropolarimeter equipped with a Peltier temperature controller. Samples were prepared in a 0.1 cm path-length cell with a buffer containing 10 mM NaH_2PO_4, 1 mM EDTA, pH 7.4. Temperature scans were from 30 °C to 95 °C with a slope of 40 °C/hour and a data pitch of 1 °C. Spectral changes were monitored at 222 nm using a slit width of 1 nm.

Experimental Results

P327R still forms a stable dimer

The crystal structure provided an atomic description of the cdb3 dimeric conformation (Zhang *et al.* 2000), which was confirmed by our recent studies of the solution structure at neutral pH (Zhou *et al.* 2005b). The dimerization arms, consisting of α-helix 9 (304-316), β-strand 11 (318-323), α-helix 10 (328-347) and residues connecting these secondary elements in each subunit, interlock two monomers by

extensive interactions (Zhang *et al.* 2000). Along the highly homologous dimerization arm, four proline residues at positions 322, 323, 327 and 337 are perfectly conserved in chicken, rat, mouse and human erythrocyte band 3 (Jarolim *et al.* 1992). One direct consequence of substituting an arginine for one of the well-conserved prolines might be the dissociation of the cdb3 dimer (Low *et al.* 2001). To analyze the oligomer state of the P327R mutant, wild type cdb3 and the P327R mutant were expressed and purified as described in the materials and methods section. SDS-PAGE showed that protein purity was greater than 95% for both samples (data not shown). Circular dichroism (CD) spectra of wt cdb3 and the P327R mutant are almost superimposable with characteristic crossover points at 198 nm, negative extremum at 207 nm and a shoulder at 222 nm (Figure 34, upper panel), which are consistent with isolated erythrocyte cdb3 (Appell and Low 1981). WT cdb3 and P327R show identical migration patterns on native gel electrophoresis at 4°C (Figure 34, lane 1 and 2 of the lower panel). Single peaks were eluted from a size exclusion column at the same retention time compared with molecular weight standards (data not shown). All of this evidence suggests that both wt cdb3 and the P327R variant exist as dimers in solution at neutral pH. More evidence on the dimeric structure of the P327R mutant will be further examined in the following SDSL studies. Collectively, the P327R mutant exhibits a conformation that is similar to wt cdb3 and does not dissociate the cdb3 dimer.

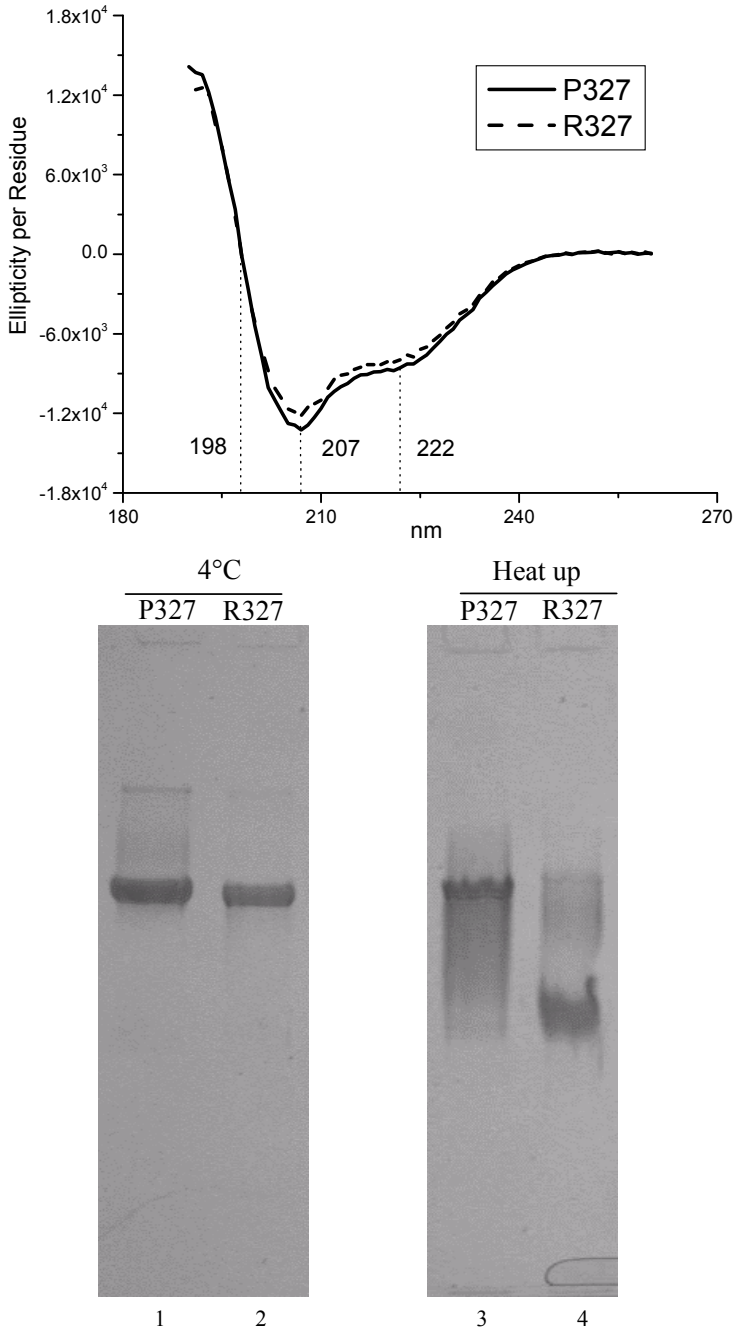

Figure 34. Comparison of the global conformation of recombinant wild type cdb3 and P327R mutant

Upper Panel: Circular dichroism spectra of the recombinant wt cdb3 (solid line) and the P327R mutant (dash line). Three vertical dot lines indicate the identical characteristic marks of wt cdb3 and P327R, crossover points at 198 nm, negative extremum at 207 nm and a shoulder at 222 nm. CD spectra of wt cdb3 and P327R overlaid with each other, indicating similar secondary structure.

Lower Panel: Native gel electrophoresis of wt cdb3 and P327R. Lanes 1 and 2 are the electrophoresis patterns at 4°C, loaded with wt cdb3 and P327R, respectively. Lanes 3 and 4 were loaded with wt cdb3 and P327R while the gel heated up during the electrophoresis at room temperature.

P327R decreases melting temperature

An interesting finding was that the P327R mutant migrated faster than wt cdb3 and formed an new band of lower molecular weight on native gel electrophoresis without temperature control (Figure 34, lane 3 and 4 of the lower panel); per contra, wt cdb3 and P327R ran to the same position on SDS-PAGE (data not shown) and on native gel electrophoresis with temperature control (4°C), suggesting the same molecular weight as a monomer and comparable conformation as a dimer of wt cdb3 and P327R (Figure 34, lane 1 and 2 of the lower panel). The specific electrophoretic patterns of wt cdb3 and P327R indicate the replacement of proline 327 with arginine may decrease the thermal stability of cdb3, which prompted a more stringent study of the stability of cdb3 by means of differential scanning calorimetry (DSC). Indeed, the calorimetric scans of wt cdb3 and the P327R mutant confirm this prediction (Figure 35). The P327R mutation decreases the melting temperature about 7°C. This result was confirmed in a CD melting experiment where the thermal transition of P327R shifts to lower temperature in comparison with wt cdb3 (Figure 35, lower panel). Even though the unusual elevation of the baseline at pretransition temperatures of erythrocyte cdb3 is eliminated in the DSC experiments of recombinant cdb3, we still could not calculate accurate enthalpies due to the poor reversibility (less than 50%), in contrast to the total irreversible transition observed from erythrocyte cdb3 (Appell and Low 1981). Taken together, these results from thermal stability experiments provide the first biophysical evidence towards understanding the molecular mechanism of the band 3 Tuscaloosa (P327R) phenotype (Zhou *et al.* 2005a).

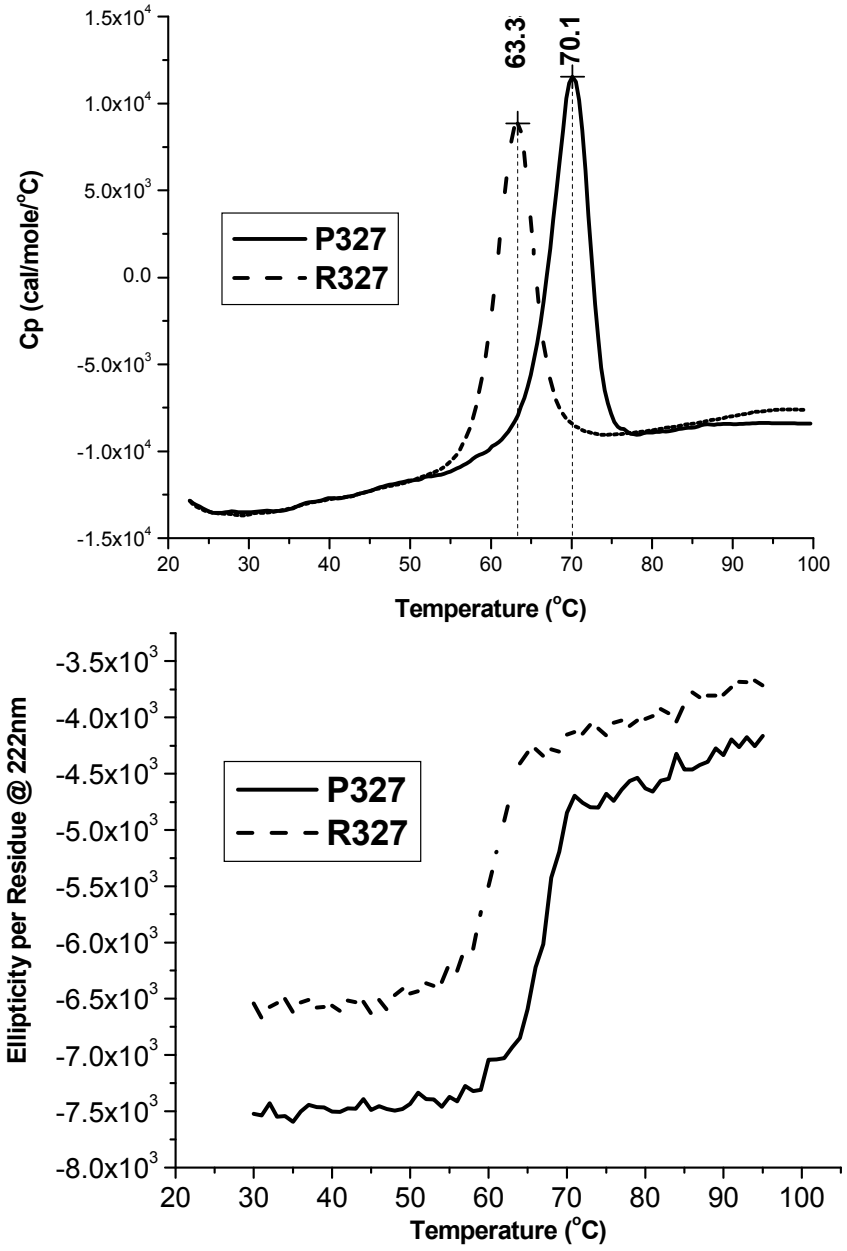

Figure 35. Thermal stability of wt cdb3 and P327R mutant

Upper Panel: Differential scanning calorimetry of wt cdb3 (solid line) and P327R (dash line). The heat capacity is plotted as a function of temperature. The melting temperature (Tm) of each sample is labeled at the transition peak, 70.1 °C for wt cdb3 and 63.3°C for P327R mutant.

Lower Panel: Circular dichroism melting experiment of wt cdb3 (solid line) and P327R (dash line). The ellipticity per residue at 222 nm is plotted versus temperature.

Structural rearrangement of the P327R mutant in the dimerization arms

Although the P327R mutation does not disrupt the dimer configuration of cdb3, the arginine residue is quite distinct from proline in terms of sidechain steric effects and electrostatic properties. Furthermore, the arginine can form relatively flexible φ, ψ dihedral angles in comparison with the restricted φ-ψ space of proline. Based on these considerations, the replaced arginine might allow the continuation of α-helix 10 (328-347) (Low *et al.* 2001) and/or perturb the dimer interface. To investigate the effect of the P327R substitution on the backbone of the dimer interface, site directed spin labeling coupled with electron paramagnetic resonance (SDSL-EPR) was employed on the cysless-cdb3 background with or without the P327R mutation. A series of single cysteine mutants were expressed, purified and spin labeled with MTSSL (Figure 12) designated as side chain R1 (McHaourab *et al.* 1996). The protein purity was monitored by SDS-PAGE for all the mutants used in this work (greater than 95%). Double integration of EPR signals from spin labeled cysless-cdb3 was less than 5% of that from spin labeled single cysteine mutants (data not shown).

From the crystal structure of wt cdb3, two major interactions at the dimer interface exist. Two β-strands 11 (318-323), one from each monomer, form an antiparallel β-sheet, which contributes 8 intermonomeric backbone-to-backbone hydrogen bonds. A hydrophobic core of 9 interacting leucine residues (from α-helices 10, β-strands 11) also stabilizes the dimer configuration (Zhang *et al.* 2000). In previous work, we have shown that the solution structure of the cdb3 dimerization arm at neutral pH is indistinguishable from the crystal structure at pH 4.8 (Zhou *et al.* 2005b). The spectra of L321R1 on P327 and R327 backgrounds are more than 200G broadened

(Figure 36), a characteristic of strong spin-spin interaction between two nitroxides at the dimer interface. Different degrees of spectral broadening are also observed at position 329R1, 332R1 and 333R1 on both backgrounds (Figure 36). These observations provide direct structural evidence that the P327R mutant still dimerizes in solution and the important backbone-to-backbone hydrogen bonds and hydrophobic interactions at the dimer interface are not totally disturbed by the P327R mutation. EPR lineshapes from R1 sidechains in the N terminal end of the dimerization arm of cdb3 (312R1 is marked as a magenta sphere and 313 is in hot pink) are superimposed on P327R lineshapes at corresponding sites (see Figure 36). EPR lineshape changes between the P327 and R327 proteins can be detected at sites 321R1, 329R1, 332R1, and 333R1. According to crystal structure of wt cdb3, Cα-Cα distances between P327 and E312, G313, L321, E329, L332, L333 in one subunit are about 32 Å, 30 Å, 13 Å, 6 Å, 9 Å, 10 Å, respectively. The α carbons of E312 and G313 are closer to the α carbon of P327 from another monomer with distances of 24 Å and 21 Å. These data suggest that the perturbation of making the P327R mutation localizes at the surroundings of site 327 (about a radius of 10-12 Å) in the dimerization arm.

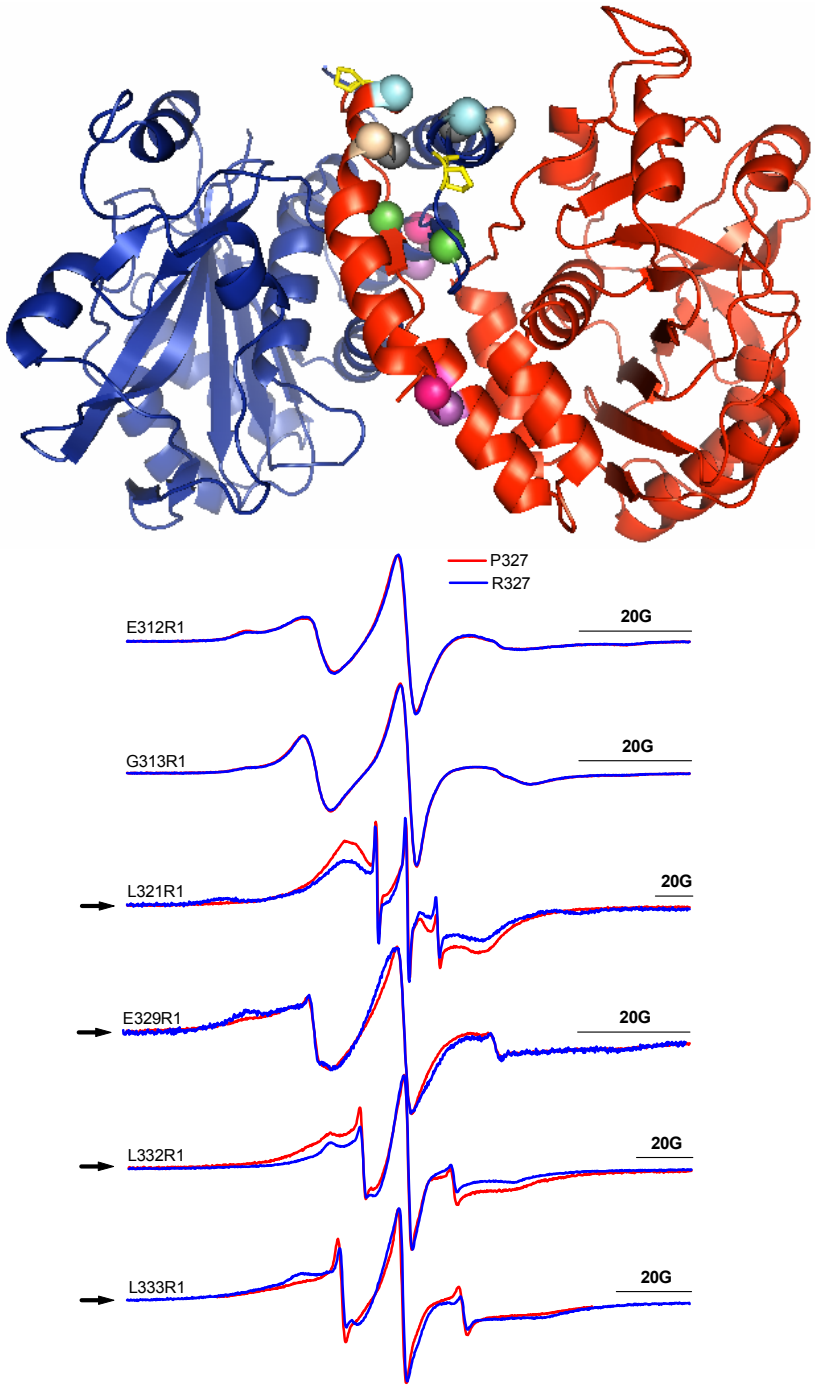

Figure 36. EPR spectra of P327 cdb3 and R327 mutant at indicated sites of dimerization arms

Top Panel: Ribbon structure of the cdb3 dimer. R1 sites are highlighted as spheres on the α-carbons: 312 (magenta), 313 (hot pink), 321 (green), 329 (cyan), 332 (black), 333 (wheat). P327 is shown in yellow stick.

Bottom Panel: EPR lineshapes of P327 cdb3 (red line) and R327 mutant (blue line). The spectra are normalized to the same amplitude for ease of comparison. The scale of 20 G field width is indicated in each spectrum. Black arrows indicate observable EPR lineshape differences between wt cdb3 and P327R.

It has been demonstrated that the packing of the C-terminal portion of α-helix 10 (residues 337-348) in solution is in good agreement with the prediction of the crystal structure (Zhou *et al.* 2005b). Further SDSL-EPR studies were carried out to characterize the effect of the P327R mutation on the C-terminal α-helix of the dimerization arm. Significant EPR lineshape changes caused by the P327R mutation are observed at position Q339R1, R340R1, L343R1 and R346R1 (pink balls, Figure 37), which are located on the same face of the α-helix that faces the other monomer and follow an i to i + 3, i + 4 pattern. Cα distances between these residues in one subunit and P327 from the other subunit are about 10 Å, 10 Å, 12 Å, and 16 Å, respectively. Accessibility to collision with the water-soluble paramagnetic agent NiEDDA was measured at each R1 site from residue 337 to 348 using a dielectric resonator (Farahbakhsh *et al.* 1992; Hubbell *et al.* 1996). Solvent accessibility from P327 and R327 backgrounds are plotted as a function of residue number (Figure 38). The common characteristics of accessibility plots from P327 and R327 include: a) an approximate periodicity of 3 or 4, suggesting that α-helix 10 retains its backbone integrity; b) a very similar trend of collision frequency to the aqueous paramagnetic broadening agent from 337R1 to 342R1, indicating that the overall tertiary environment of this helical region is the same, that is, one surface is exposed to solvent and the opposite surface is buried in the dimer interface; c) a universal increase in average accessibility in progressing from residue 337R1 to 348R1 with the least accessibility at position 339R1 and 342R1, consistent with an α-helix with greater solvent exposure at the C-terminal end as exiting the compact dimer interface. It should be noticed that there is no complete buried site similar to Q339 or L342 along residues 343-348 (Figure 39). The decreased accessibility value at 343R1 and

the increased accessibility value at 346R1 after the replacement of P327 with arginine are in agreement with the increased immobilized component of the 343R1 lineshape and the increased mobile component of the 346R1 lineshape (Figure 37 and Figure 38). In the crystal structure of wt cdb3, the L343 (magenta), R346 (cyan), and Y347 (wheat) sidechains adopt an orientation relatively tangent to the boundary of protein and aqueous solvent while the adjacent R344, R345, Q348 sidechains (green) are sticking out of the protein surface and L342 is deeply buried inside (Figure 39). This half-buried and half-exposed conformation may render 343R1, 346R1, 347R1 multiple rotamer configurations, as seen in EPR lineshapes (Figure 37). A slight disturbance due to the P327R mutation may cause one or several favorable conformations of the nitroxide sidechain. As a result of the P327R substitution, 343R1 (magenta) becomes less accessible to NiEDDA, 346R1 (cyan) experiences higher collision frequency to NiEDDA and the NiEDDA accessibility of 347R1 (wheat) decreases (Figure 38 and Figure 39). One reasonable explanation for these data is that this segment of helix 10 rotates a small angle clockwise viewed from the C terminal end to N terminus if assuming that the R1 sidechain follows the same orientation of original sidechain. Thus previously exposed 343R1 and 347R1 sidechains of wt cdb3 may be partially inserted into the protein interior in the P327R protein, and simultaneously, 346R1 becomes more accessible to the broadening agent. Molecular dynamics simulation of the P327R mutant is consistent with the prediction from the NiEDDA accessibility data (data not shown). To evaluate this model, absolute Heisenberg exchange rates need to be determined since the NiEDDA accessibility, calculated by dividing the central linewidth, may be misrepresented in the case of the dimerization arm. Along this region, the EPR lineshapes at several sites

(340R1, 341R1, 343R1, 346R1) have multiple components. Direct measurement of T_1 by pulsed EPR or saturation recovery EPR may avoid the overweight on fast motion components. Molecular dynamics simulations of each spin labeled position on the P327R background can also facilitate the analysis of the EPR constraints.

We also measured EPR lineshapes from 338R1 to 345R1 under the background of the double mutation P327R and K56E. The K56E mutation, also known as band 3 Memphis, has trivial structural effects on the conformation of band 3 Tuscaloosa (P327R) since the EPR lineshapes of R1 from the double mutant (P327R, K56E) match those from the single mutant (P327R) very well (data not shown). Combined with accessibility constraints and lineshape comparison, SDSL-EPR studies reveal that the dimerization arm is not completely impaired in band 3 Tuscaloosa, the effect of P327R mutation propagates mostly along the C-terminal end of the dimerization arm, and at least the fragment 343-348 of helix 10 in the dimerization arm undergoes some extent of rigid body movements.

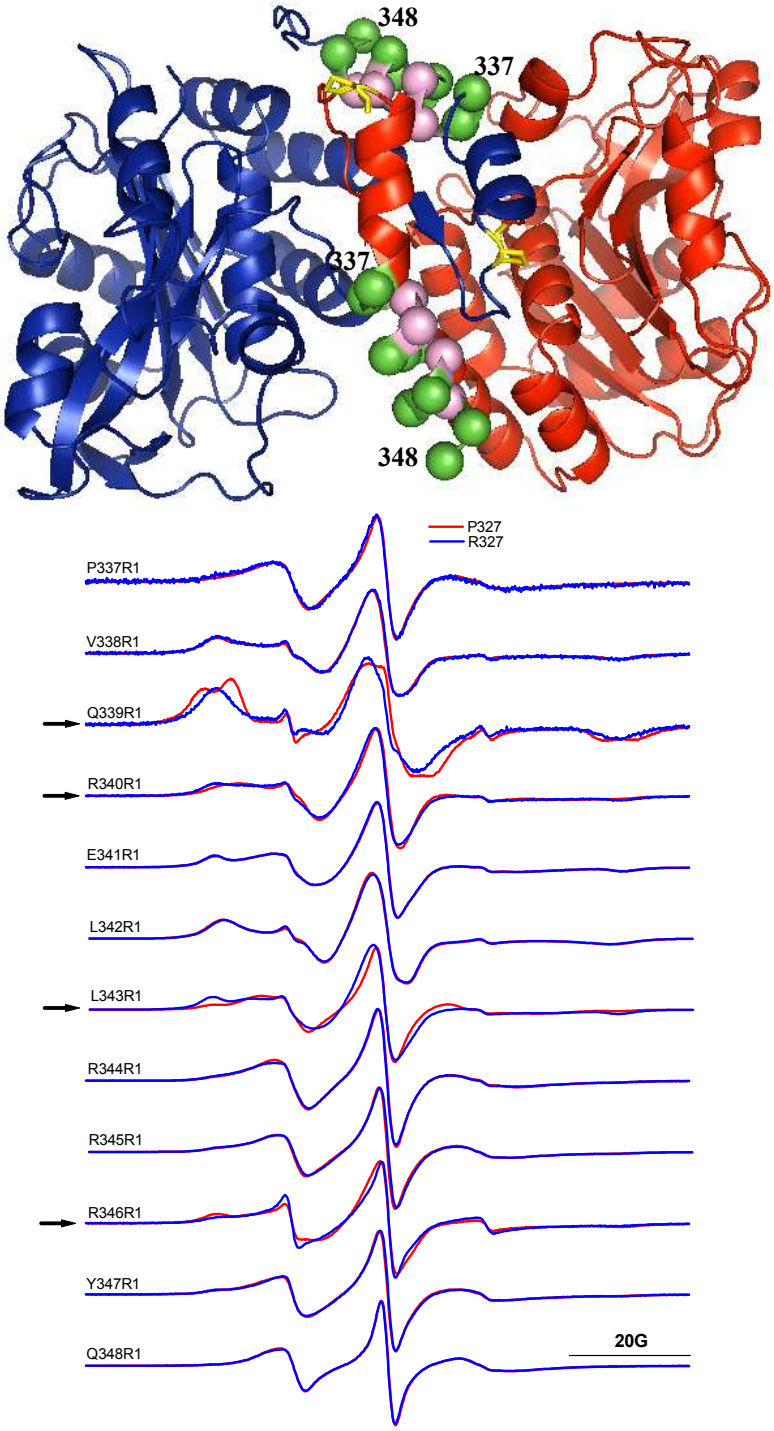

Figure 37. EPR spectra of P327 cdb3 and R327 mutant at residues 337-348 of dimerization arms

Upper panel: Ribbon diagram of the cdb3 dimer. R1 sites at 339, 340, 343, and 346 are marked as pink spheres on the α-carbons. Other labeled sites are in green spheres. P327 is shown in yellow stick.
Lower panel: EPR lineshapes of P327 cdb3 (red line) and R327 mutant (blue line) with 100 G scan width. The spectra are normalized to the same amplitude. Black arrows indicate the sites where the EPR lineshapes have significant difference between P327 cdb3 and R327 mutant. Black arrows indicate the EPR lineshape changes between wt cdb3 and P327R.

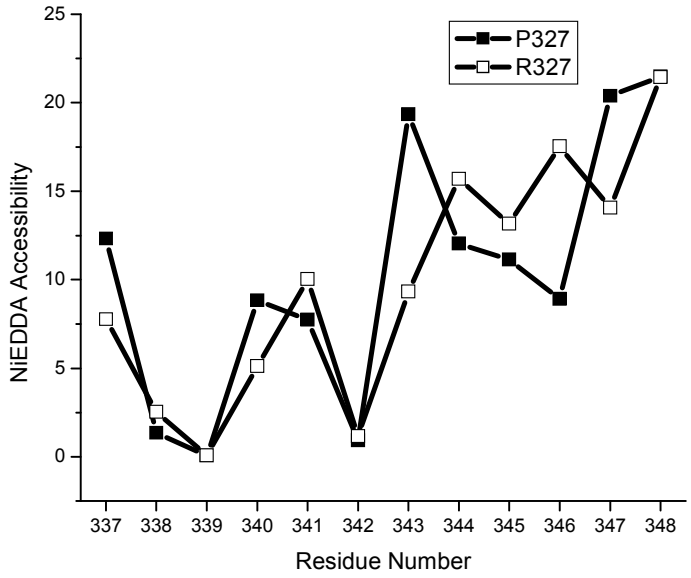

Figure 38. NiEDDA accessibility of the R1 sidechain from site 337 to 348

Filled squares represent the NiEDDA accessibility of wt cdb3 from 337R1 to 348R1. Open squares are the NiEDDA accessibility of P327R mutant from 337R1 to 348R1.

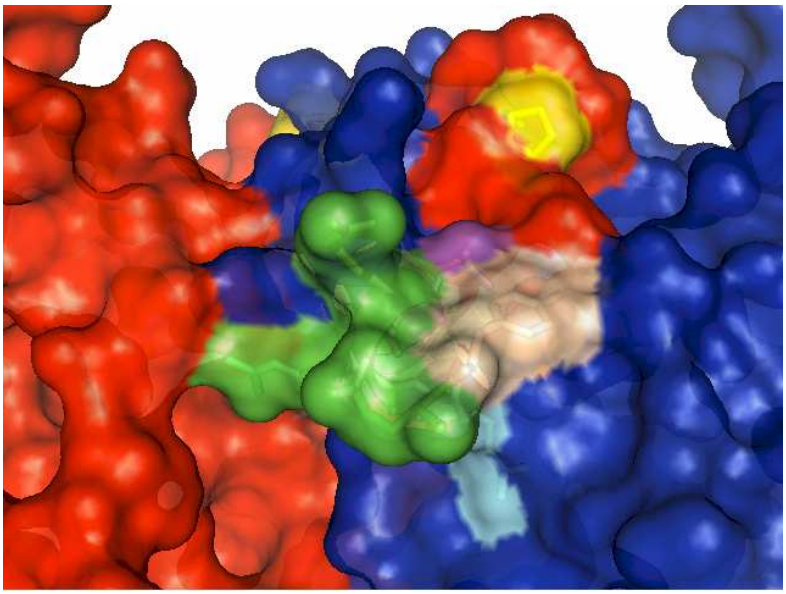

Figure 39. Surface view of C terminus of wt cdb3

The surface of cdb3 dimer is shown in red (Q chain) and blue (P chain). P327 is represented in yellow stick and surface. Notice the sidechains of R344, R345, Q348 (green) protrude out of the backbone surface and the sidechains of L343 (magenta), R346 (cyan), and Y347 (wheat) are lying on the surface parallel to the protein backbone.

The data in Figure 34 suggest that the P327R mutation does not change the conformation of wt cdb3 at the level of secondary structure and oligomeric state. The global effects of the P327R mutation were tested by means of designing 11 R1 sidechains distributed around the peripheral globular domain (Figure 40). The spectral signatures of most sites are remarkably similar between P327 and R327 backgrounds with regards to sidechain mobility, lineshape components and splitting. For instance, the fast motion spectra of 208R1, which is located on a highly flexible loop region free of tertiary contact; the immobilized lineshapes of 290R1, which occupies a interior pocket (on α-helix 7, facing towards the central β sheet); two components of 199R1 (one fast motion and one intermediate motion), which resides on a 1.7 turn α-helix 5 (196-201) in the middle of a long loop; the 150G broadening and three-peak splitting at 108R1 due to strong spin-spin interactions. Only at 84R1 in a loop of a β-turn, the ratio of the immobilized component to the intermediate component increases after mutating P327 to arginine. Close examination of the crystal lattice reveals that the α carbon of L84 is relatively close (12 Å) to the α carbon of P327 from the other monomer (Figure 42). These data provide more evidence that the majority of tested R1 nitroxides are in an indistinguishable local environment under two backgrounds and most regions of the globular domain are not affected by the P327R mutation.

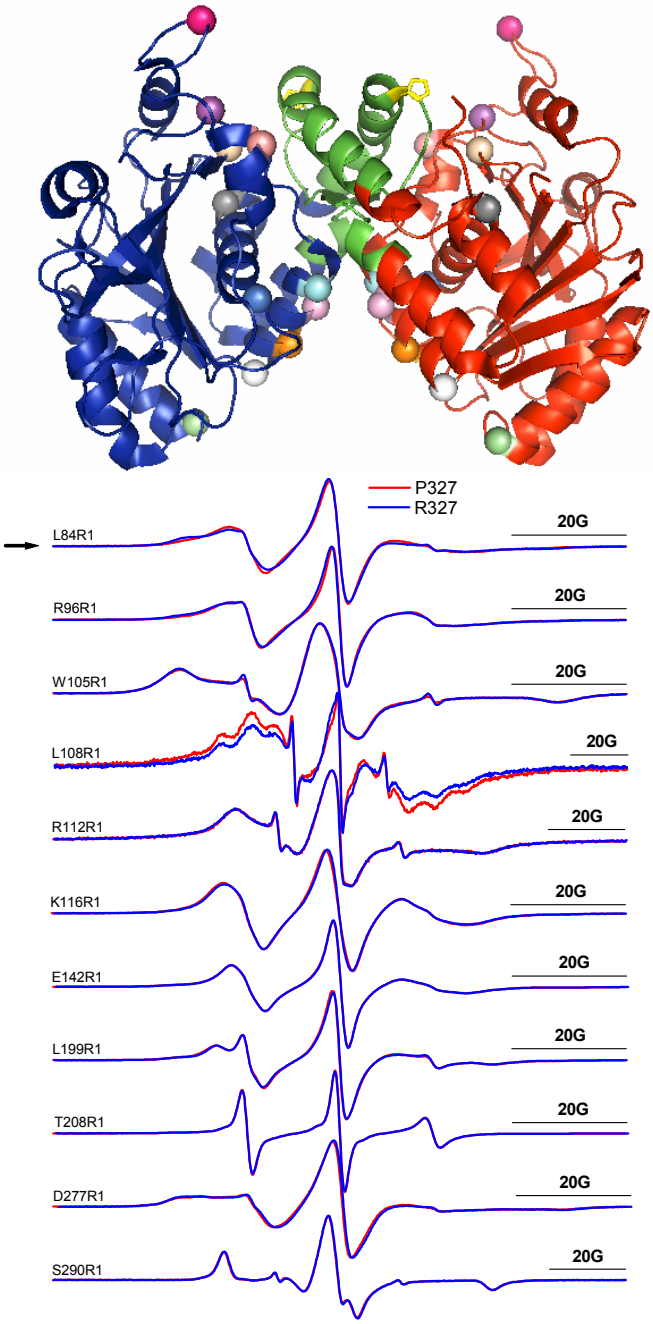

Figure 40. EPR lineshapes of P327 and R327 at various residues away from dimerization arms

Upper panel: Ribbon diagram of the cdb3 dimer. P327 is shown in yellow stick. Dimerization arms are highlighted in green ribbon. R1 sidechain at position 84 (wheat), 96 (magenta), 105 (cyan), 108 (pink), 112 (orange), 116 (white), 142 (lime), 199 (salmon), 208 (hot pink), 277 (marine), and 290 (black) are marked as spheres on the α-carbons.

Bottom Panel: EPR lineshapes of P327 cdb3 (red line) and R327 mutant (blue line). The spectra are normalized to the same amplitude for easy comparison. The scale of 20 G field width is indicated in each spectrum. The black arrow indicates the EPR lineshape changes between wt cdb3 and P327R.

Intermonomer distances of P327R mutant at dimer interface

P327 is located in loop region (324-327), which connects β-strand 11 (318-323) and α-helix 10 (328-347) at the dimer interface. It has been hypothesized that the P327R mutation could allow the continuation of α-helix 10 (Low *et al.* 2001). If the loop region (324-327) builds an extra turn of α-helix, the α-helices 10 from the two monomers are more likely to have relative movement. On the contrary, two β-strands 11 from two monomers may remain the original conformation due to their involvement in the large-scale hydrogen bonds and hydrophobic interactions. To further characterize the possible corresponding movement of the C-terminus of the dimerization arm caused by P327R, DEER spectroscopy was employed to measure the intermonomeric nitroxide distances ranging from ~20 Å to 50 Å (Pannier *et al.* 2000). The data in Figure 41 show the summary of DEER distance constraints of residues 340R1-345R1 along the dimerization arms and various paired sites apart from the dimerization arms (142R1, 312R1, 96R1, 105R1, 116R1, 199R1, 208R1, 227R1, 290R1) under P327 and R327 backgrounds. We detect very similar intermonomeric distances and distance distributions at positions residing in the globular domain between P327 and R327 backgrounds. The interprobe distances obtained from residues 340-345 within the dimerization arm on the R327 background follow the same trend as the spin-spin distances measured from the P327 background. No consistent monotonic distance increase or decrease is detected at those sites (340R1-345R1), which suggests there is no significant relative movement between the two α-helices 10 of the two monomers. Surprisingly, R1 distance distributions of 340R1, 342R1, and 345R1 are distinct between P327 and R327 background (Figure 41, lower panel). This unorganized distance distribution of R327 may provide a plausible

explanation of the decreased thermal stability of cdb3 Tuscaloosa. According to the NiEDDA accessibility data (Figure 38), the C-terminal part of the dimerization arm also undergoes a small rigid body movement (rotation and/or translation) coupled to the P327R mutation. The quantification of this motion is still uncertain under the current resolution of DEER experiments. More powerful molecular modeling methods will be needed essential to construct the distance geometry from the distance constraints obtained from DEER experiments.

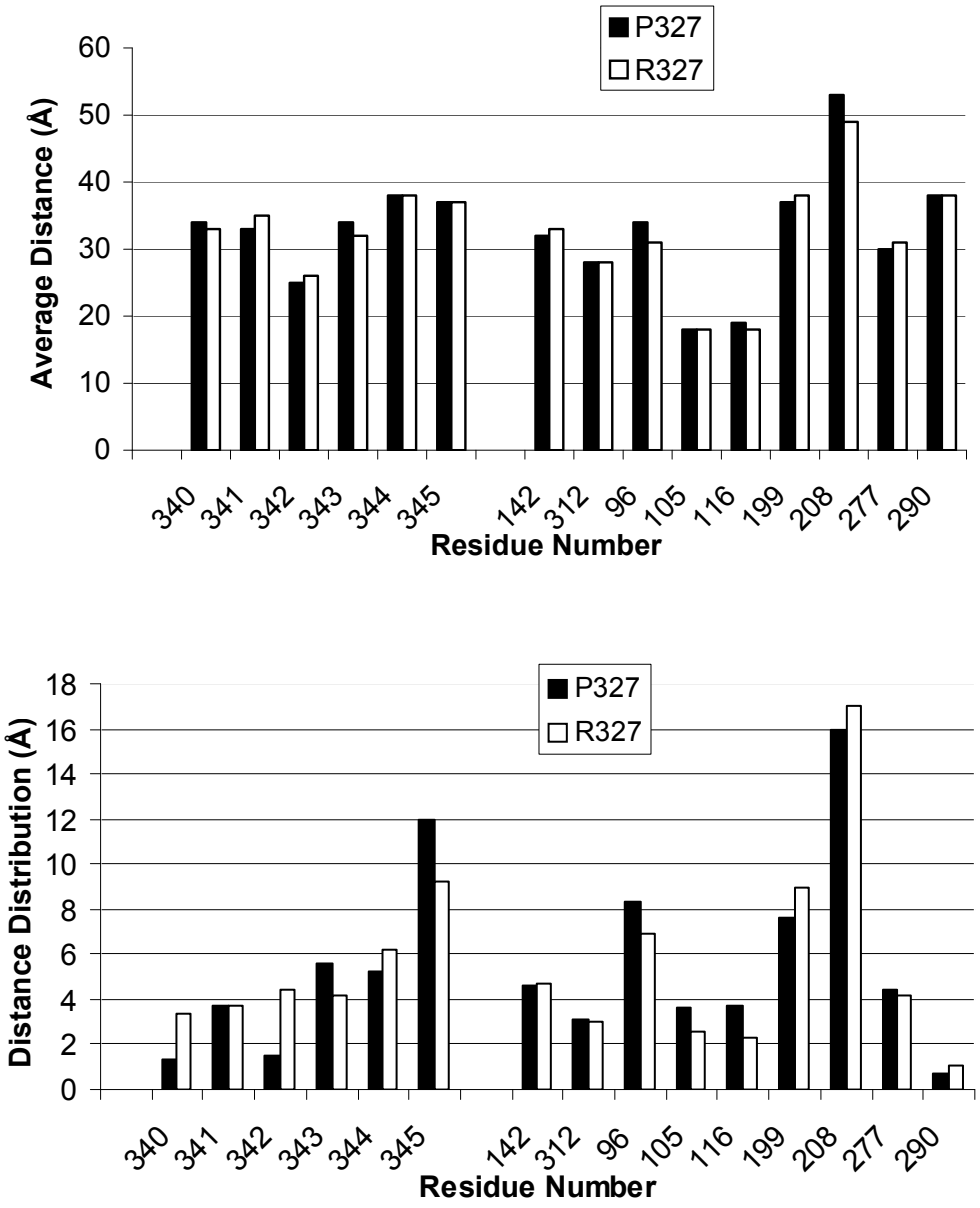

Figure 41. Comparison of DEER results between wt cdb3 and P327R

Upper panel: Intermonomeric spin-spin distances measured from DEER experiments along dimerization arm 340-345 and from various paired sites in the dimer interface are indistinguishable between wt cdb3 (filled square: P327) and the P327R mutant (open square: R327).

Lower panel: Significant difference in distance distribution is detected at sites within dimerization arm, such as residues 340 and 342, which may be consistent with the decreased stability of the P327R mutant compared to wt CDB3, however, the overall dimer conformation of the P327R mutant remains similar to wt CDB3.

Discussion

Significance

Aside from polymorphic variants in the human genome, pathogenic mutations are closely linked to human diseases. Like most disease-causing mutations, AE1 mutations may affect protein function in several ways: abnormal biosynthesis levels, trafficking to an incorrect target location, misfolding, altered stability, functional defects, etc. AE1 mutations are responsible for HS, SAO and dRTA (distal renal tubular acidosis). The important roles of cdb3 in organizing protein-protein interactions, sustaining membrane stability and maintaining cellular deformability are reflected by the mutations that cause certain diseases (HS, SAO) associated with membrane defects. The crystal structure of cdb3 at atomic resolution (Zhang *et al.* 2000) and the SDSL-EPR structure of cdb3 in solution (Zhou *et al.* 2005b) enable us to localize the structurally important mutations that result in abnormal red blood cell shape but not alter band 3 expression. Replacement of P327 with arginine (designated as Band 3 Tuscaloosa) occurs at a critical turning loop of the highly conserved dimerization arm, which lead to the prediction of changes in secondary structure (Jarolim *et al.* 1992; Low *et al.* 2001). The consequent oligomer state of band 3 and the change in structure of the membrane protein complex were previously unknown. The molecular modeling of the P327R mutation mutant at the turning loop that connects the β-strand 11 and α-helix 10 is thought to be difficult. Moreover, the crystallization of the P327R mutant would be refractory since this mutation decreases the thermal stability of cdb3 dimer demonstrated by Reithmeier's group (Bustos and Reithmeier 2006) and us (Zhou *et al.* 2005a) independently. Low-resolution data from

CD spectra, native gel electrophoresis and size exclusion chromatography of wt cdb3 and P327R substituted cdb3 indicate the mutation does not dissociate the cdb3 dimer.

For the purpose of studying structural rearrangements at higher resolution caused by the P327R mutation, site-directed spin labeling and EPR strategies were utilized to compare solvent accessibility, sidechain mobility, and distance distribution at various sites of cdb3 with P327 and R327 backgrounds. These selected positions are primarily located along the dimerization arm or scattered in the globular domain. Collectively, the multiple structural constraints demonstrate the similarity in the secondary structure and global conformation of wt cdb3 and the P327R mutant. The structural variations resulting from the replacement of P327R are localized to the C terminal end of the dimerization arm and regions close to position 327. These sites are the probable candidate areas where cdb3 physically contacts protein 4.2. Our data provide strong evidence that P327R neither causes the misfolding of cdb3 dimer nor rearranges the secondary structure of the dimerization arm, but rather leads to small perturbation in the dimer interface. The highlights of this study are the extensive long distance constraints obtained from DEER in biological samples and the initiatives towards the molecular and structural pathophysiology of hereditary spherocytosis.

The effects of P327R mutation on cdb3

Proline has very unique φ (~ -60˚), ψ (two regions on the Ramachandran plot, one in the α-helical region centered around -45˚ and one in the β-strand region centered near +135˚) angles and is known to be a helix breaker (Richardson 1981) due to the rotational restriction of N-Cα bond, the steric effect of the pyrroline ring and lack of the amide NH

hydrogen bond donor. However, proline has a high propensity as a helix capping residue at both ends (Aurora and Rose 1998) as well as a connecting residue in β-turns and in loop regions (Gellman 1998; Crespo *et al.* 2004). P327, functioning as the N-terminal cap for α-helix 10, is located at the loop region, which connects β-strand 11 and α-helix 10 at the dimer interface of cdb3. As shown in the crystal structure, the A326/P327 peptide bond is in the trans conformation and the φ, ψ dihedral angles for P327 are -59° (N-Cα) and 110° (Cα-C), respectively. The trans configuration of peptide bonds involving the imino nitrogen of proline is slightly more favorable in energy than the cis conformation (Zimmerman and Scheraga 1976). Replacement of proline 327 with a positively charged arginine may change the electrostatic feature and destabilize α-helix 10, thereby altering the local structure. 312R1 and 313R1 are on the α-helix 9, close to N-terminus of β-strand 11. The β-strands 11 from both monomers form an antiparallel β-sheet, which constructs the central core of intermonomeric interactions. This stable structure probably blocks the propagation of the effect of the P327R mutation along the N-terminus of P327R. However, the positive charge and the steric effect of the arginine sidechain may influence the neighboring group of position 327. Moreover, the relatively unrestrained N-Cα bond of the arginine may impart extra flexibility of the downstream helix 10 in solution. The dynamic feature of the C-terminal dimerization arm could contribute to the destabilization of the cdb3 dimer. Whether the amide H of the arginine forms a hydrogen bond is beyond the resolution of SDSL. Nevertheless, the multiple constraints (distance, distance distribution, accessibility and mobility) from various sites obtained in this work are in good agreement with the above-mentioned possible effects of P327R mutation and unquestionably exclude the possibility of drastic changes in the backbone structure of the

dimerization arm, such as the extension and relocation of helix 10. For simplicity, only R1 sites with obvious EPR lineshape changes from Figure 36, 37, and 40 are summarized in Figure 42. Most of the examined positions (green ribbons) are insensitive to the P327R mutation. EPR spectral changes at 84R1 (cyan balls) probably result from the spatial and/or electrostatic impact of the R327 sidechain. This sidechain effect of R327 and/or rotational effect of its N-Cα bond may cause small lineshape deviations (Figure 42). The overall consequence of the P327R mutation is a slight destabilization of the cdb3 dimer.

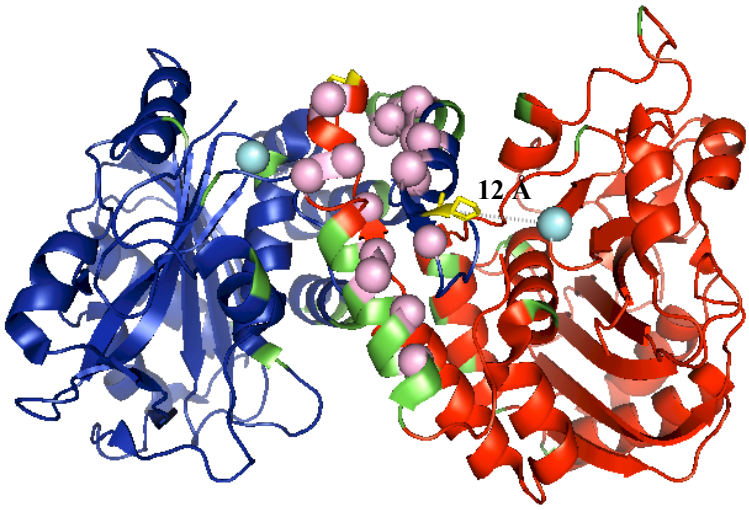

Figure 42. Mapping the sites of EPR lineshape changes (P327 vs R327) onto the crystal structure

P327 is shown in yellow stick. Green ribbons highlight the tested residues by SDSL. Pink or cyan balls represent the positions where EPR lineshapes of R1 sidechains in wt cdb3 are different from R327 background. 321R1, 329R1, 332R1, 333R1, 339R1, 340R1, 343R1, 346R1 are in pink. Cyan balls are the two 84R1 sidechains in the cdb3 dimer. Dashed line labels the average Cα-Cα distance (12 Å) between P327 from one monomer and L84 from the other monomer.

Protein 4.2 binding sites on cdb3

Three naturally occurring cdb3 mutations (Glu40Lys (Rybicki *et al.* 1993), Gly130Arg (Inoue *et al.* 1998), Pro327Arg (Jarolim *et al.* 1992)) are associated with

different degrees of protein 4.2 deficiency and HS. Protein 4.2 is another important component of the red blood cell membrane skeletal network and interacts with cdb3 and ankyrin (Korsgren and Cohen 1986; Korsgren and Cohen 1988). A recent study showed that protein 4.2 increased DNDS-sensitive Cl^- influx in *Xenopus* oocytes (Toye *et al.* 2005). However the precise functions and interactions of protein 4.2 remain unknown, partially due to the aggregation of purified protein 4.2 and protein 4.2 fragments (Toye *et al.* 2005). The further investigation of the aforementioned mutations may shed light on the study of the cdb3-protein 4.2 interaction. E40K resides in the N-terminal unstructured region (Zhang *et al.* 2000), which is highly dynamically disordered in solution at neutral pH (Zhou *et al.* 2005b). G130R of α-helix 2 is located on the surface of the globular domain of cdb3 (Zhang *et al.* 2000) and also in the hypothesized cdb3-ankyrin interaction interface (Davis *et al.* 1989; Michaely *et al.* 2002). Proline has very specific dihedral angles and the P327R mutation occurs in the loop region that connects β-strand 11 (318-323) and α-helix 10 (328-347) of the highly conserved dimerization arm (304-357) (Zhang *et al.* 2000). The results of this work clearly show that the P327R mutation lowers cdb3 melting temperature about 7°C and subtly alters protein structure in the vicinity of 327 and the C terminal end of the dimerization arm. Therefore, the deficiency of protein 4.2 in band 3 Tuscaloosa may be due to the destabilization of cdb3 dimer caused by the P327R substitution. Another possibility is that the highly conserved P327 and/or its proximity and/or C terminal end of cdb3 directly contact protein 4.2. The other possibilities lie in the allosteric effect of P327R mutation in vivo, which may induce the conformational change at the cdb3-protein 4.2 interface. To answer these questions, high-resolution structures of cdb3-protein 4.2 complex and function studies are indispensable.

The effect of band 3 Memphis (K56E) on band 3 Tuscaloosa (P327R)

Band 3 Memphis (Mueller and Morrison 1977) is a silent band 3 polymorphism with Lys56 to Glu56 substitution (Yannoukakos *et al.* 1991), which is a widespread band 3 variant with a different frequency in each population (Ranney *et al.* 1990). K56E appears not to affect the normal functions of band 3 (Bruce and Tanner 1996). No recognized clinical or hematological abnormalities were observed in individuals having the band 3 Memphis allele (Ranney *et al.* 1990). Biochemical evidence showed that protein 4.2 content of a band 3 Memphis carrier was normal (Mueller and Morrison 1977). The transport rates of inorganic phosphate (Ideguchi *et al.* 1992) and chloride anion (Retelewska *et al.* 1991) of band 3 Memphis were almost identical to wt band 3. No lineshape differences between the P327R background and the double mutation background (P327R, K56E) were observed from our site directed spin labeling study on a number of R1 sidechains (338R1-345R1), suggesting that K56E has no significant impact on the C termini of the dimerization arms (data not shown). Three sharpe lines were detected when introducing 34R1 or 35R1 sidechain to the double-mutatnt background, in agreement with the highly dynamic structure of the flexible N terminus on the EPR (nanosecond) timescale (data not shown). Similar intermonomer distances were still obtained from DEER experiments at residues 343R1 and 344R1 under the double mutation background. However, SAO mutation and band 3 Tuscaloosa are associated in cis with band 3 Memphis in all reported patients. K56E alone showed an increased membrane binding of hemoglobin under low ionic strength and low pH and an increased membrane binding of aldolase under physiological ionic strength (Retelewska *et al.* 1991). The transport rate of phosphoenolpyruvate (PEP) in homozygous K56E

erythrocytes was decreased 20% relative to normal erythrocytes. These results suggested that a single charge in the cytoplasmic domain might affect certain peripheral protein binding and anion transport (Ideguchi *et al.* 1992). Thus, we cannot completely exclude the effect of band 3 Memphis (K56E) on band 3 Tuscaloosa (P327R). A three dimentional structure of the double mutant and/or longer molecular dynamics simulation may provide more structural information about whether a salt bridge can be formed between R327-E56 or between R327 and any of the N terminal acidic residues. Our data indicate that the salt bridges, if formed, may not totally disrupt the dimer interface. As aspects of functional studies, the recent established Xenopus oocyte expression system for protein 4.2 and band 3 (Toye *et al.*) may elucidate the importance of K56E in the band 3 Tuscaloosa patient.

The flexible linker between cdb3 and tdb3

Red blood cells are exposed to a pressure gradient and shearing force in blood flow. The remarkable deformability of erythrocytes allows them to pass through the microcirculation and spleen filter intact (Skalak and Branemark 1969). Band 3 is crucial for the visoelastic properties of the red blood cell since it is one major connecting point between the lipid bilayer and the membrane skeleton network. The vital linkage resides in the C-terminal segment of cdb3 around the inner membrane surface. This region is susceptible to mild protease digestion at Tyr359, Lys360 and Arg379 (Lepke and Passow 1976; Grinstein *et al.* 1978), and flexible to the restricted rotational motion of the transmembrane domain (32˚) when cdb3 is bound to the membrane skeleton through ankyrin (Blackman *et al.* 2001). The deletion of codons 400-408 in SAO patients

increases membrane rigidity and inhibits the stretching of the membrane skeleton (Jarolim *et al.* 1991; Wang 1994). In recombinant cdb3 (1-379), the C-terminus is dynamically disordered (Zhou *et al.* 2005b). Changes of EPR lineshape, sidechain mobility, solvent accessibility and distance distribution at the C-terminal end of cdb3 due to the P327R mutation have been detected in this work. It is valuable to test whether this point mutation can modify the flexibility of the linkage between the cytoplasmic domain and transmembrane domain in full length AE1. In vivo, these minor structural variations caused by autosomal dominant P327R mutation and/or K56E may affect three quarters of the total band 3 pool if assuming that both alleles have identical chances to transcribe, and that the functional unit of band 3 is a dimer. However, the functional effects of P327R are probably underestimated in this way. If the tetramer of band 3 upon ankyrin binding requires all four normal subunits to be functioning correctly, the probability of fully competent band 3 decreases exponentially $(1/2)^4$. The normal red blood cell is even scarce considering that about 28% band 3 is bound to the membrane skeleton as a entire network (Blackman *et al.* 1998). The underlying molecular mechanism of this amplifying cascade is that one P327R mutation disturbs its adjacent groups on both subunits of the cdb3 dimer and these affected positions may alter the binding capacity and affinity of cdb3 and protein 4.2.

Conclusions

Based on the previous clinical and biochemical studies of band 3 Tuscaloosa that suggested the normal expression and correct distribution of band 3 to the red blood cell membrane (Jarolim *et al.* 1992), we independently report that the P327R mutation

destabilizes the cdb3 dimer with a decreased melting temperature of 7°C (Zhou *et al.* 2005a), which is also observed by Reithmeier and coworkers (Bustos and Reithmeier 2006). The structural effects of this mutation have been evaluated by SDSL-EPR techniques. The strong spin-spin interaction at certain sites like 108R1, 112R1, 321R1 and 332R1, along with the extensive long-range distance constrains from CW-EPR and DEER are solid evidence that the global conformation of the P327R mutant is a very similar to the wt cdb3 dimer. The differences in EPR lineshapes, sidechain mobility, solvent accessibility and distance distribution between P327 and R327 allow localization of the perturbation of P327R to the proximity of position 327 and the C terminal end of the dimerization arm, which may be a portion of the 'hot spots' interacting with protein 4.2. These biophysical data undoubtedly rule out the models of misfolding, dimer dissociation and repacking of the secondary structure of the dimerization arm concerning the P327R mutation. This work is a valuable application of EPR technology to biological samples and an important step toward the understanding of the molecular mechanisms of hereditary spherocytosis.

CHAPTER VI

ANKYRIN-CDB3 INTERACTION

Introduction

Ankyrins are ubiquitously expressed adaptor proteins that interact with spectrin-actin based cytoskeletons and a variety of membrane associated proteins in metazoans. These broad-spectrum interactions can be classified into four major groups. Depending upon cell type, ankyrins interact with ion transporters/channels including anion exchangers AE1 (Bennett and Stenbuck 1979b; Bennett and Stenbuck 1979a), AE2 (Jons and Drenckhahn 1998), AE3 (Morgans and Kopito 1993), Na^+/Ca^{2+} exchanger (Li *et al.* 1993), voltage-dependent Na^+ channels (Srinivasan *et al.* 1988; Malhotra *et al.* 2000), Na^+/K^+ ATPase (Nelson and Veshnock 1987; Koob *et al.* 1988; Morrow *et al.* 1989), H^+/K^+ ATPase (Smith *et al.* 1993; Festy *et al.* 2001), and ammonia transporter RhBG (Lopez *et al.* 2005). Ankyrins also associate with receptor mediated Ca^{2+} release channels such as the ryanodine receptor (Bourguignon *et al.* 1995; Tuvia *et al.* 1999), the IP_3 receptor (Bourguignon *et al.* 1993; Joseph and Samanta 1993; Tuvia *et al.* 1999) and the IP_3R-3/Sig-1R complex (Hayashi and Su 2001). Cell adhesion molecules (CAM) including CD44 (Kalomiris and Bourguignon 1988; Lokeshwar *et al.* 1994), and L1 CAM family (L1/neurofascin/NrCAM/CHL1/NgCAM) (Lundberg *et al.* 1992; Davis *et al.* 1993; Davis and Bennett 1994a; Dubreuil *et al.* 1996; Hortsch *et al.* 1998; Zhang *et al.* 1998a; Bouley *et al.* 2000) also bind to ankyrins. Ankyrins link to various cytoplasmic proteins such as β-spectrin (Bennett and Stenbuck 1979a), tubulin (Bennett and Davis

1981; Davis and Bennett 1984; Davis *et al.* 1991), the vesicle coating protein clathrin (Michaely *et al.* 1999), the molecular co-chaperone Hdj1/Hsp40, the Rho-GEF proteins obscurin (Bagnato *et al.* 2003; Kontrogianni-Konstantopoulos *et al.* 2003) and Tiam-1 (Bourguignon *et al.* 2000), and the death receptor Fas (Del Rio *et al.* 2004; Mohler and Bennett 2005b). Through these diversified interactions, ankyrins may anchor their binding partners to specialized membrane domains in both the plasma membrane and the endoplasmic reticulum.

Mammals have three ankyrin genes, ANK1, ANK2 and ANK3, encoding three groups of proteins, ankyrinR, ankyrinB and ankyrinG, respectively. A large number of isoforms are derived from alternative splicing ranging from 26 kDa to 480 kDa. Canonical ankyrins (190-220 kDa) consist of a membrane-binding domain (24 ANK repeats are divided into 4 subdomains and each subdomain is composed of 6 ANK repeats), a spectrin-binding domain, a death domain and a regulatory domain. An extraordinary characteristic of ankyrins is that they are able to interact with proteins of unrelated sequence and diverse structure via the ANK repeats (Bennett and Baines 2001). ANK repeats are widely distributed in hundreds of proteins such as the adaptor protein ankyrins, the transcription regulators GABPβ and Iκ-B, the tumor suppressors p16 and p53BP2, and the TRP calcium channels, etc. Ankyrins contain 24 ANK repeats that are further divided into four subdomains (D1, D2, D3 and D4) according to proteolytic maps (Michaely and Bennett 1993). The ANK repeat motif, a 33-residue sequence, is a helix-loop-helix-β-hairpin/loop fold forming a L-shaped structure (Figure 5 in Chapter 1). The stacking of multiple ANK repeats give rise to an elongated, curved surface for protein recognition. Current data from co-crystals suggest that the primary binding surface is

made up of the inner short helices and/or β-hairpin/loop regions of the ANK repeats (Figure 43) (Mosavi *et al.* 2004).

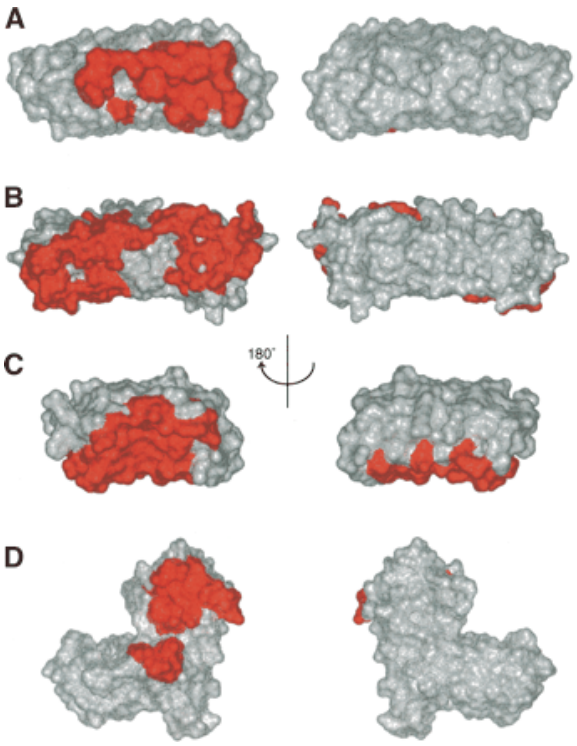

Figure 43. Interaction interface in different ANK repeat co-crystal structures

The structures of proteins containing ANK repeats are illustrated in gray surface. Red surface represents the residues involved in the interaction with protein partners. In left panels, the β-hairpin/loop region is pointing outward. The right panels are the views from 180˚ rotation of the left panels along a vertical axis. In right panels, the β-hairpin/loop region is pointing away from the reader.

(*A*) The interface between GABP-β (four and half ANK repeats) and GABP-α from the co-crystal structure 1AWC (Batchelor *et al.* 1998)
(*B*) The interface between Iκ-Bα (six ANK repeats) and NFκ-B from the co-crystal structure 1NFI (Jacobs and Harrison 1998)
(*C*) The interface between p16 (four ANK repeats), an INK family member, and Cdk6 from the co-crystal structure 1BI7 (Russo *et al.* 1998)
(*D*) The interface between p53BP2 (four ANK repeats) and p53 from the co-crystal structure 1YCS. Note that the lower red patch is the ankyrin repeat interface, while the upper patch is the SH3 domain interface (Gorina and Pavletich 1996; Mosavi *et al.* 2004).

In erythrocytes, the major role of ankyrinR is bridging the cytoplasmic domain of band 3 (cdb3) to the spectrin-based membrane skeleton. Band 3 (anion exchanger 1 or

AE1) is a highly expressed integral membrane protein comprising one quarter of the total membrane protein of the red blood cell (Fairbanks *et al.* 1971). Cdb3, in addition to binding to glycolytic enzymes, hemoglobin and protein kinase (Tanner 1997), is an important organizing center of protein-protein interactions in the red blood cell membrane. The membrane skeleton is responsible for maintaining the mechanical support of the erythrocyte membrane bilayer. The linkage of ankyrin between AE1 and the spectrin based membrane skeleton is vital to the deformability and required viscoelestic properties of red blood cells (Bennett and Baines 2001). Biochemical data have suggested that ankyrinR may interact with two distinct regions of cdb3, one required region near residues 175-185 and one accessorial region close to the N terminus (Davis *et al.* 1989; Willardson *et al.* 1989; Chang and Low 2003).

The full-length structure of band 3 or ankyrin or their complex is not available. However, the structures of two domains, one in band 3 and another in ankyrin, have been determined in separate crystallographic studies. The cytoplasmic domain of band 3 is structurally and functionally independent from the transmembrane domain (Lepke and Passow 1976; Grinstein *et al.* 1978). The crystal structure of cdb3 at pH 4.8 (Zhang *et al.* 2000) is indistinguishable from its structure in solution at neutral pH (Zhou *et al.* 2005b) and therefore may closely represent the physiological conformation at neutral pH that binds to ankyrin (Low *et al.* 1991). The dimerization arms from both monomers interlock two peripheral domains into a compact dimeric structure (75×55×45 Å) (Figure 4) with highly dynamic disordered N-termini (possibly up to 190 Å long). The critical ankyrin-binding fragment, comprised of residues 175-185, has been mapped to a β-hairpin loop structure of the peripheral globular domain of cdb3 (Chang and Low 2003). The repeat

subdomains 3 and 4 (ANK_D34) of the ankyrin family are known to interact with band 3 (Michaely and Bennett 1995a), clathrin heavy chain (Michaely *et al.* 1999), Na^+/K^+ ATPase (Thevananther *et al.* 1998), L1 CAM family proteins (Michaely and Bennett 1995b), and voltage-dependent and amorilide-sensitive Na channel (Srinivasan *et al.* 1992; Michaely *et al.* 2002). Each repeat (33 amino acid residues) in ANK_D34 adopts the typical L-shaped structure and the 12 ANK repeats (ANK repeat 13-24) stack one against another to form a 125 Å long, left-handed superhelix. The concave curvature of the ankyrin groove is the result of relatively tight packing of the inner row helices (Figure 5). Based on these domain structures, a cdb3-ANK_D34 complex model has been proposed using the protein-docking program suite, 3D-Dock (Figure 44) (Michaely *et al.* 2002). However, there are currently no structural data to verify this docking model or build a novel configuration of this complex. The open questions include where the precise contact sites and the interface are located, how ankyrinR promotes the formation of an AE1 tetramer, and why ankyrins are capable of interacting with various proteins that share neither apparent sequence homology nor convergent structure.

The goal of this chapter is to investigate the interaction interface of cdb3 and ANK_D34 when complexed based on their atomic resolution structures. A series of site directed fluorescence labeling (SDFL) experiments have been carried out on both cdb3 and ANK_D34 using the environment sensitive probe badan (Figure 46). By monitoring the maximum emission wavelength shift at certain sites upon complex formation, it has been possible to map the interface of cdb3-ANK_D34 interaction experimentally. This study is an important advance towards the complete assembly of the AE1-ankyrin

complex and should be a valuable application in the broader context where the docking of two proteins with known structures is involved.

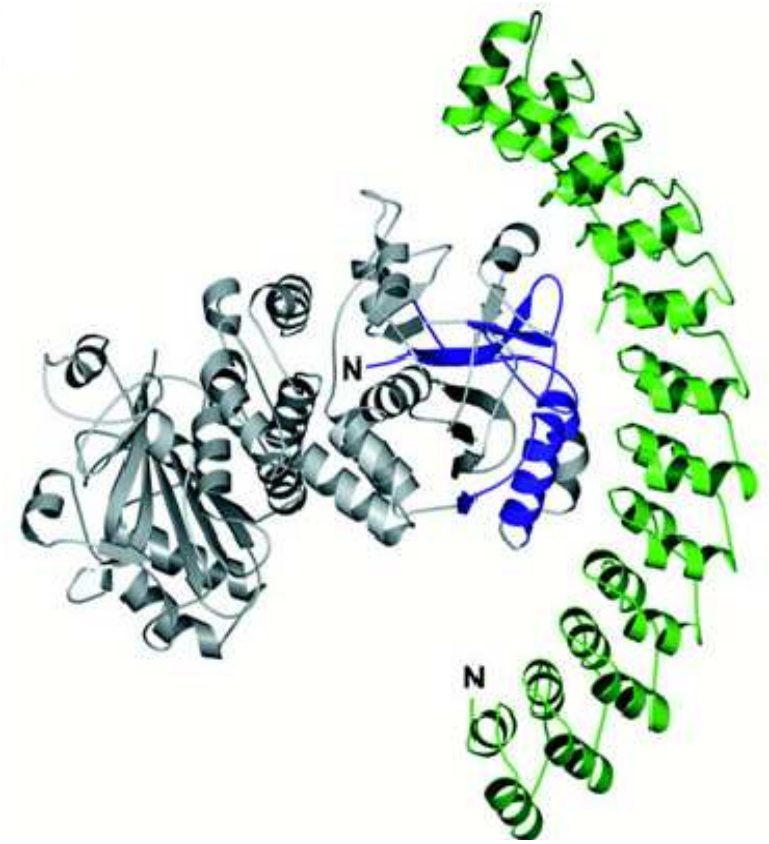

Figure 44. The docking model of cdb3-ANK_D34 complex

Ankyrin repeat domains 3 and 4 (ANK_D34) are shown in green ribbon. Cdb3 is in light gray. Blue color highlights the residues involved in ankyrin binding predicted from a protein-docking program, 3D-Dock (Michaely *et al.* 2002).

Experimental Methods

Cloning and site-directed mutagenesis

The cDNA encoding the ankyrinR membrane-binding domain 3 and 4 (residues 403-827) was generously provided by Dr. Peter Michaely (University of Texas

Southwestern Medical Center). This cDNA was re-amplified using Pfu DNA polymerase (Stratagene, La Jolla, CA) with the N-terminal (forward) primer

5' ACTCGCGGATCCTCTGGCCTGACACCTCTCCACGTG

and the C-terminal (reverse) primer

5' CGGAATTCGAAGCTGATGAGTTCTTCCCCTTCATCTTCC

(IDT DNA, Coraville, IA). The PCR product was cloned into the pGEX-2T vector (GE Healthcare, Piscataway, NJ) between the HindIII and EcoRI sites, and designated as pZZ9_WT. The single cysteine mutants pZZ9_C476C and pZZ9_C531C were constructed by the replacement of original C531 and C476 to serine and alanine respectively using the QuikChange® Site-Directed Mutagenesis Kit (Stratagene, La Jolla, CA). The sequences of all mutants were confirmed by DNA sequencing.

Protein preparation and on-column labeling

pZZ9 plasmids were transformed into BL21 Gold (DE3) *E. coli* competent cells (Stratagene, La Jolla, CA). ANK_D34 was expressed following the auto-induction protocol developed by Dr. F. William Studier (Brookhaven National Laboratory) (Studier 2005). Briefly, overnight starter cultures were grown in PAG at 37 ˚C and 1 mL of the starter cultures were used to inoculate 1 L ZYP-5052 for overnight auto-induction (14 hours). Typically, saturation (A_{600} = 4.8~7.0) was reached in about 11 hours at 37 ˚C. Additional incubation for 3 hours maximized lactose auto-induction. GST-tagged ANK_D34 was purified using glutathione sepharose as described by the manufacturer (GE Healthcare, Piscataway, NJ). For the wild type ANK_D34, the N-terminal GST tag was removed via thrombin on-column cleavage in a PBS buffer containing 140 mM

NaCl, 2.7 mM KCl, 10 mM NaH_2PO_4, 1.8 mM KH_2PO_4, 1 mM EDTA, pH 7. The thrombin was captured by benzamidine sepharose. For single cysteine mutants, on-column labeling with a 10-fold molar excess of badan (6-bromoacetyl-2-(dimethylamino)naphthalene; Invitrogen, Carlsbad, CA) was carried out in a PBS buffer at pH 7.3 in the dark at room temperature for 2 hours and then at 4 ˚C overnight. Unreacted label was removed from all samples by washing the resin 4 to 5 times (1:20 v/v) with a PBS buffer (pH 7) before thrombin cleavage. Protein concentration of the wt ANK_D34 was determined by UV absorption at 280 nm using an extinction coefficient of 16,000 $M^{-1}cm^{-1}$. Purity of the expressed proteins was at least 95%, as determined by SDS-PAGE (Laemmli 1970) and gel filtration column. Wild type cdb3 and single cysteine mutants were expressed and purified as described in Chapter 4 and in previous work (Zhou *et al.* 2005b).

Steady-state badan fluorescence

A 1 μM badan labeled cdb3 single cysteine mutant with/without 10 μM ANK_D34 or a 2 μM badan labeled ANK_D34 single cysteine mutant with/without 20 μM cdb3 in a final volume of 150 μL PBS buffer (pH 7) was incubated on a nutator at 4˚C in the dark overnight. The emission spectra were collected on a PTI Quantamaster 2000-7SE fluorometer (Photon Technology International, Lawrenceville, NJ) at room temperature, using an excitation wavelength of 387 nm and collecting fluorescence emission from 420 – 620 nm. The excitation slit was kept at 10 nm while the emission slit was set at 1 nm to maximize the resolution in emission data (Mansoor *et al.* 1999). The

wavelength at maximal emission was determined from the zero crossing point of the first derivative of the background corrected spectrum.

Experimental Results

Expression and purification of recombinant ANK_D34

Recombinant wild type ANK_D34 and two single cysteine mutants were expressed and purified as described previously (Michaely *et al.* 2002) and in experimental methods. The purity of ANK_D34 was greater than 95% as determined by SDS-PAGE for all samples used in this work (Figure 45, lane 2 and 3 of right panel). A single dominant band was observed in native gel electrophoresis and a single peak eluted from size exclusion chromatography, suggesting that recombinant ANK_D34 adopts a homogenous conformation (data not shown). During the purification trials of single cysteine mutants, one of the two original cysteines (C531) appeared to be very conserved and important for protein expression. When C531 was mutated to alanine, the production of the single cysteine mutant ANK_D34_C476C_C531A was seriously impaired. Interestingly, serine at position 531 rescued the protein yield of mutant ANK_D34_C476C_C531S (data not shown).

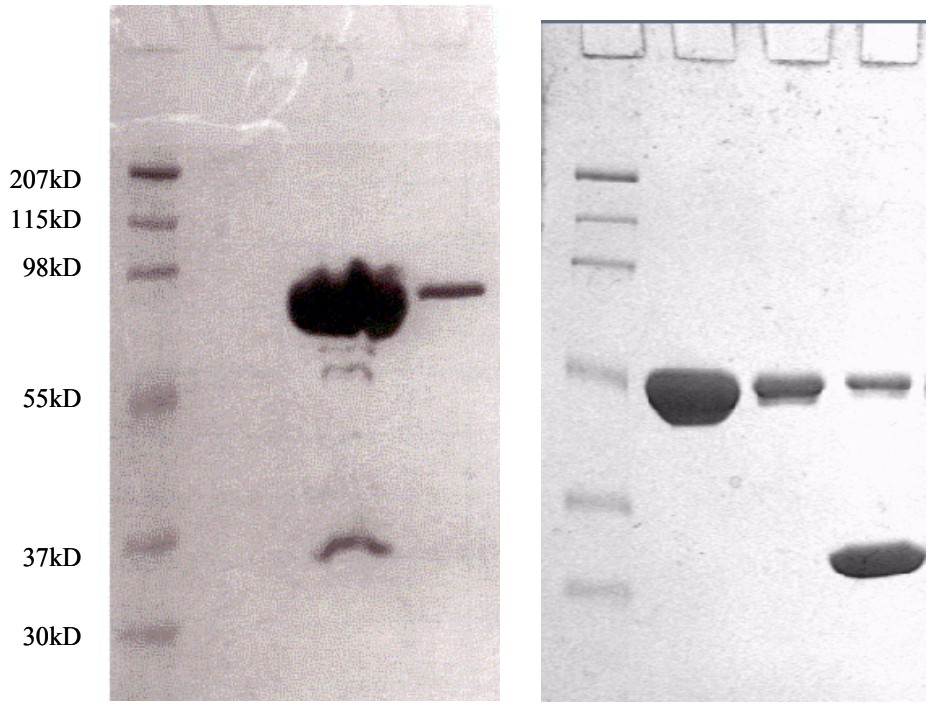

Figure 45. SDS-PAGE of ANK_D34 constructs

Molecular weight markers are labeled on the left. Two protein lanes in the left panel were loaded with elution 1 and 2 of GST-ANK_D34 protein (72 kD). The products after thrombin cleavage are shown in the right panel. The three lanes are ANK_D34 (46 kD) flowthrough 1, flowthrough 2 from benzamidine sepharose, and eluted GST tag (24 kD) from glutathione sepharose, respectively.

Effects of cdb3-ANK_D34 binding on badan-cdb3 fluorescence

Previous studies have suggested that the both mid-region (155-195 (Ding *et al.* 1996), 174-186 (Davis *et al.* 1989), 190-203 (Willardson *et al.* 1989)) and the N-terminus (1-65) (Willardson *et al.* 1989; Ding *et al.* 1994; Wang *et al.* 1995) of cdb3 are involved in ankyrin binding. In view of the high-resolution cdb3 structure, the critical 175-185 fragment forms a β-hairpin loop, which resembles the structure of the ankyrin-binding motif in the Na^+/K^+-ATPase (Zhang *et al.* 1998b). Nevertheless, the flexible N-terminus may not be crucial for ankyrin interaction since cdb3 lacking the entire N-terminus (1-50) displayed a similar binding affinity for intact ankyrin and GST-tagged 46.5 kDa ankyrin

(Chang and Low 2003). A careful examination of the surface of the peripheral domain suggests that the exterior curvature of the ankyrin-binding loop (between β-strand 6 (176-180) and β-strand 7 (182-185)), α-helix 2 (128-141) and α-helix 3 (146-158) may fit in the ankyrin groove (Figure 47, the green arc of left upper panel). To investigate the probable interface between cdb3 and ANK_D34, a group of positions on cdb3 were selected to construct single cysteine mutations on the cysless background. These cdb3 mutants were expressed, purified and badan (Figure 46) labeled as described in the experimental methods. The emission spectra were collected in the absence or in the presence of a 10-fold molar excess of wild type ANK_D34. As shown in the lower right panel of Figure 47, a distinct 25 nm blue shift of the maximum emission wavelength (λmax) and an 80% increase in fluorescence intensity are observed at position 152 of α-helix 3 upon addition of ANK_D34. The λmax of cdb3_180_badan residing on the ankyrin-binding loop red-shifts about 6 nm after ANK_D34 binding, at the same time, the emission intensity decreases by 35%. In comparison, site 208, which is at the cdb3 dimer interface, no obvious λmax shift is detected. All the maximum emission wavelength and λmax shift data are summarized in Table 5.

The λmax shifts at all tested sites were mapped onto the three-dimensional structure of the cdb3 dimer as shown in Figure 48. Blue and red shifts can be clearly viewed on the curved surface of the ankyrin-binding loop, α-helix 2 and α-helix 3 (Figure 48, upper panel). It is interesting to note that the ankyrin-binding hairpin loop contains two colors, a blue shift on one side (β-strand 7) and a red shift on the other side (β-strand 6). This bicolor configuration may indicate the importance of the hairpin loop: β-strand 7 is in a more nonpolar environment and β-strand 6 changes to a more polar environment

upon ankyrin binding. In contrast to the surface of the peripheral globular domain opposite the dimer interface, the λmax at control sites of 96 (the dimer-interface side of the globular domain), 208 (the dimer-interface side of the globular domain), and 344 (the dimerization arm) are almost unchanged after adding ANK_D34 to badan-labeled cdb3 (Table 5 and Figure 48 lower panel), suggesting that these positions are far away from the cdb3-ankyrin interface. Collectively, the SDFL studies on cdb3 upon ANK_D34 binding provide strong experimental evidence that the surface of the cdb3 globular domain opposite the dimer interface contacts ankyrin.

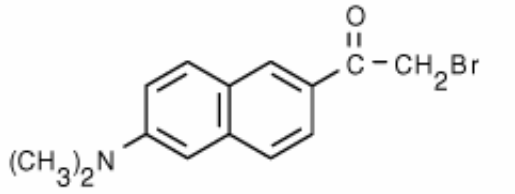

Figure 46. Chemical structure of badan

Table 5. λmax shift upon ANK_D34 binding to cdb3

Residue #	127	133	137	148	151	152	155	156
λ_{cdb3} (nm)	536	531	526	531	521	524	527	503
$\lambda_{cdb3+ANK\_D34}$ (nm)	516	527	514	531	512	499	525	499
$\Delta\lambda max = \lambda_{cdb3} - \lambda_{cdb3+ANK\_D34}$	20	4	12	0	9	25	2	4

Residue #	179	180	181	183	96	208	344
λ_{cdb3} (nm)	515	526	530	530	516	516	516
$\lambda_{cdb3+ANK\_D34}$ (nm)	522	532	533	523	516	515	517
$\Delta\lambda max = \lambda_{cdb3} - \lambda_{cdb3+ANK\_D34}$	-7	-6	-3	7	0	1	-1

The maximum emission wavelength (λmax) is summarized in the table. Δλmax is defined as the difference between $\lambda_{cdb3+ANK\_D34}$ and λ_{cdb3}. This leads to a positive sign for a blue shift and a negative sign for a red shift.

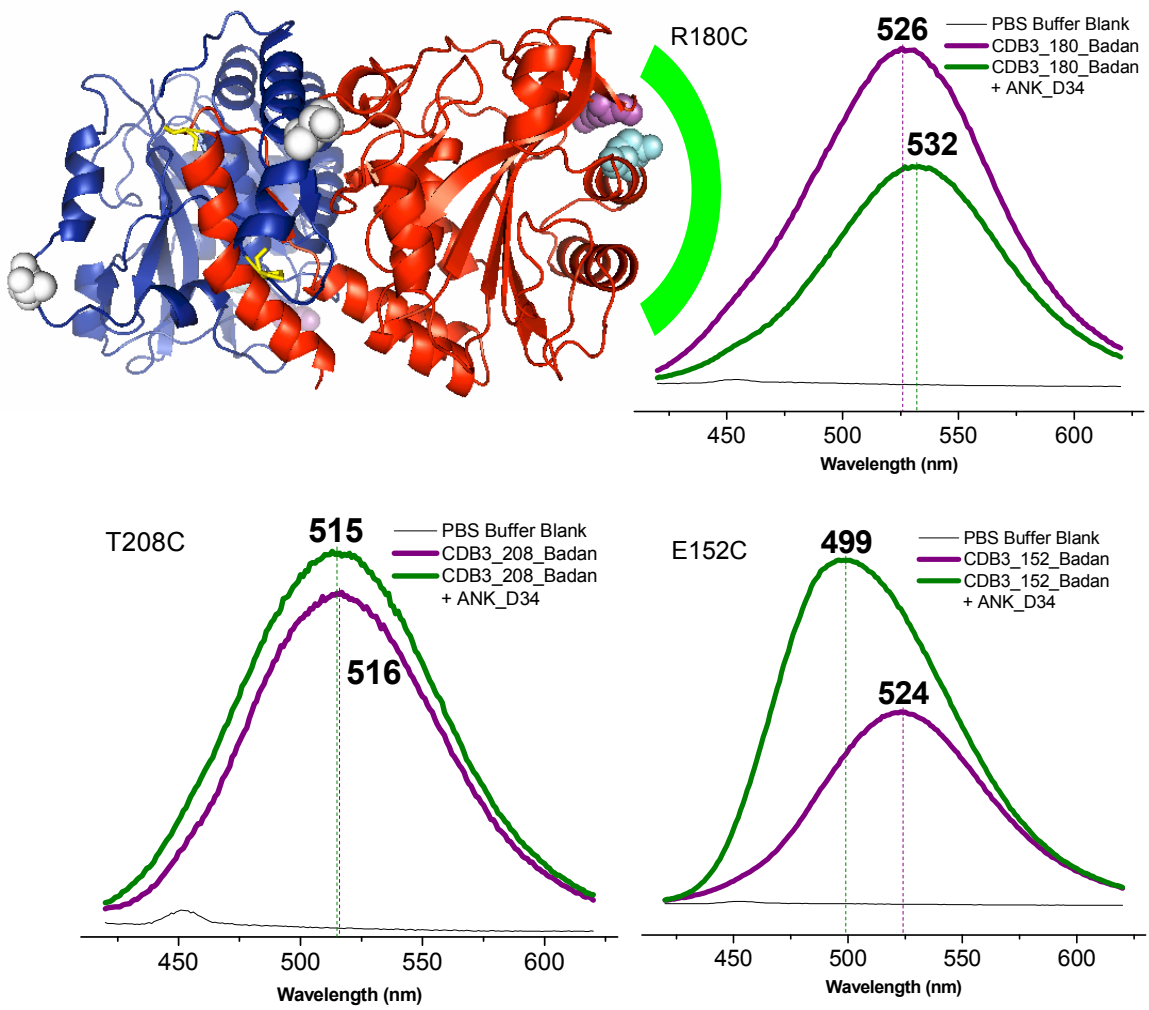

Figure 47. The effect of ANK_D34 binding to cdb3

The upper left panel shows a ribbon diagram of the cdb3 dimer (Zhang *et al.* 2000). Purple, cyan and white spheres represent site 180, 152 and 208, respectively. The surface curvature of the hypothesized cdb3-ankyrin interface is highlighted in green. Three experiments corresponding to three selected sites are shown here. Upper right: cdb3_180_badan; lower left: cdb3_208_badan; lower right: cdb3_152_badan. Purple lines are the emission spectra of 1 μM cdb3 labeled with badan. Green lines are the emission spectra after addition of 10 μM wt ANK_D34. Black lines are the PBS buffer controls. The maximum emission wavelength (λmax) is indicated on each spectrum.

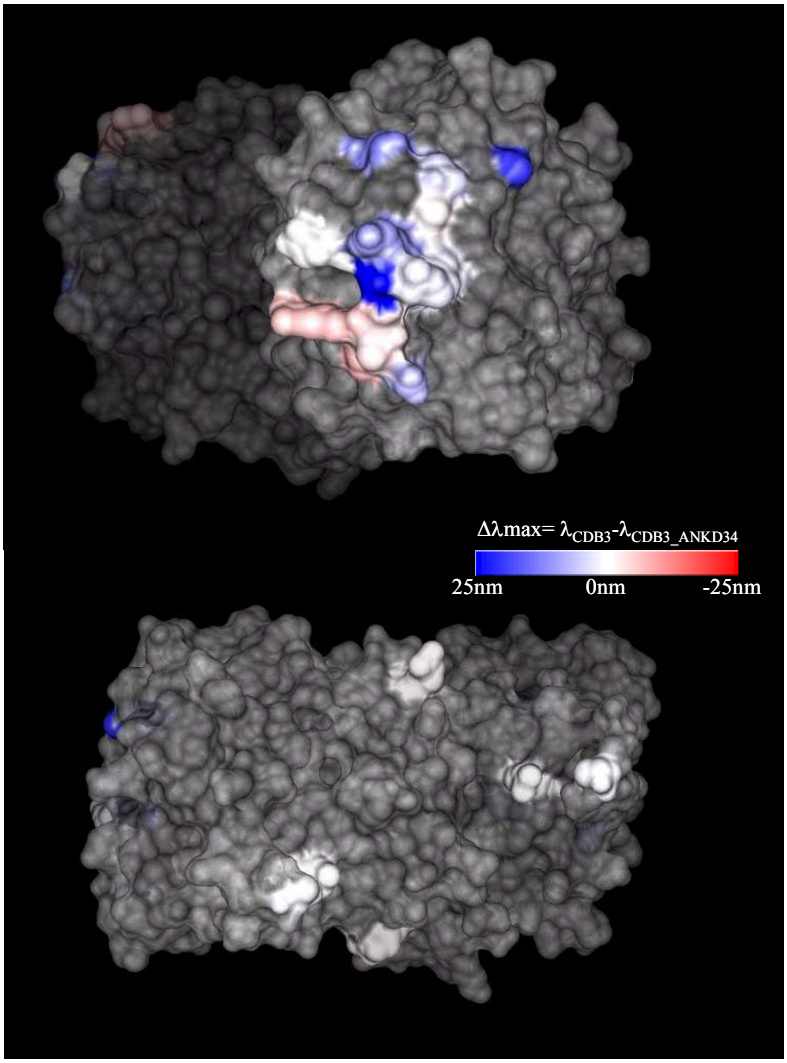

Figure 48. Mapping the ankyrin-binding interface on the cdb3 dimer

The cdb3 dimer structure is shown in gray surface with 20% transparency (Zhang *et al.* 2000). Tested positions are indicated in solid color. Colored legend bar is the linear-gradient scale of blue or red shift of the maximum emission wavelength (λmax) upon ankyrin binding. Top panel: viewing the surface of the cdb3 globular domain. Tested positions are mainly focused on α-helix 2, α-helix 3 and β strands 6, 7 (hairpin) and highlighted in solid color according to the values of Δλmax (Table 5). Note the bicolor mode of the hypothesized ankyrin-binding hairpin loop. Lower panel: the 'back' view of control sites after rotating the cdb3 dimer in the top panel about 135˚ along the vertical axis.

Effects of cdb3-ANK_D34 binding on badan-ANK_D34 fluorescence

Ideally, the SDFL experiments could be conducted at various positions of the ankyrin repeat domains 3 and 4 to study ANK_D34_badan binding to wild type cdb3.

However, C531 seems quite conserved and we failed to express the C531A mutant at high level. This is probably due to misfolding and/or aggregation. Fortunately, the yield of mutant C531S can reach 3 μM concentration in 1 mL volume from 1 L culture which is enough for fluorescence experiments. Then each of the two original cysteines on ANK_D34 was labeled with badan in two separate experiments. The emission spectra were recorded in the absence or in the presence of 10-fold excess of wild type cdb3. At position 531 of ankyrin repeat 16 (red sphere in Figure 49, top cartoon), a 4 nm blue shift of maximum emission wavelength (λmax) is detected together with a 50% increase in fluorescence intensity after adding wild type cdb3 into badan labeled ANK_D34_C531C (Figure 49, bottom left panel). When wild type cdb3 binds to ANK_D34_C476C (yellow sphere highlighting position 476 of ankyrin repeat 15 in top carton of Figure 49), we observe an apparent 16 nm blue shift of λmax and a 1.6-fold increase in fluorescence intensity (Figure 49, bottom left panel). These fluorescence data support the predication that the ankyrin groove is the de facto boundary in the band 3-ankyrin complex. Given that the first 11 amino acid residues (802-812) of the 62 kDa spectrin-binding domain stick on the ankyrin groove of C terminal repeats (20-24) in the crystal structure (Figure 49, upper panel) (Michaely *et al.* 2002), the blue shifts shown at sites 476 and 531 suggest that the cdb3 docking loci may be closer to the N terminal stacking of the ANK repeats.

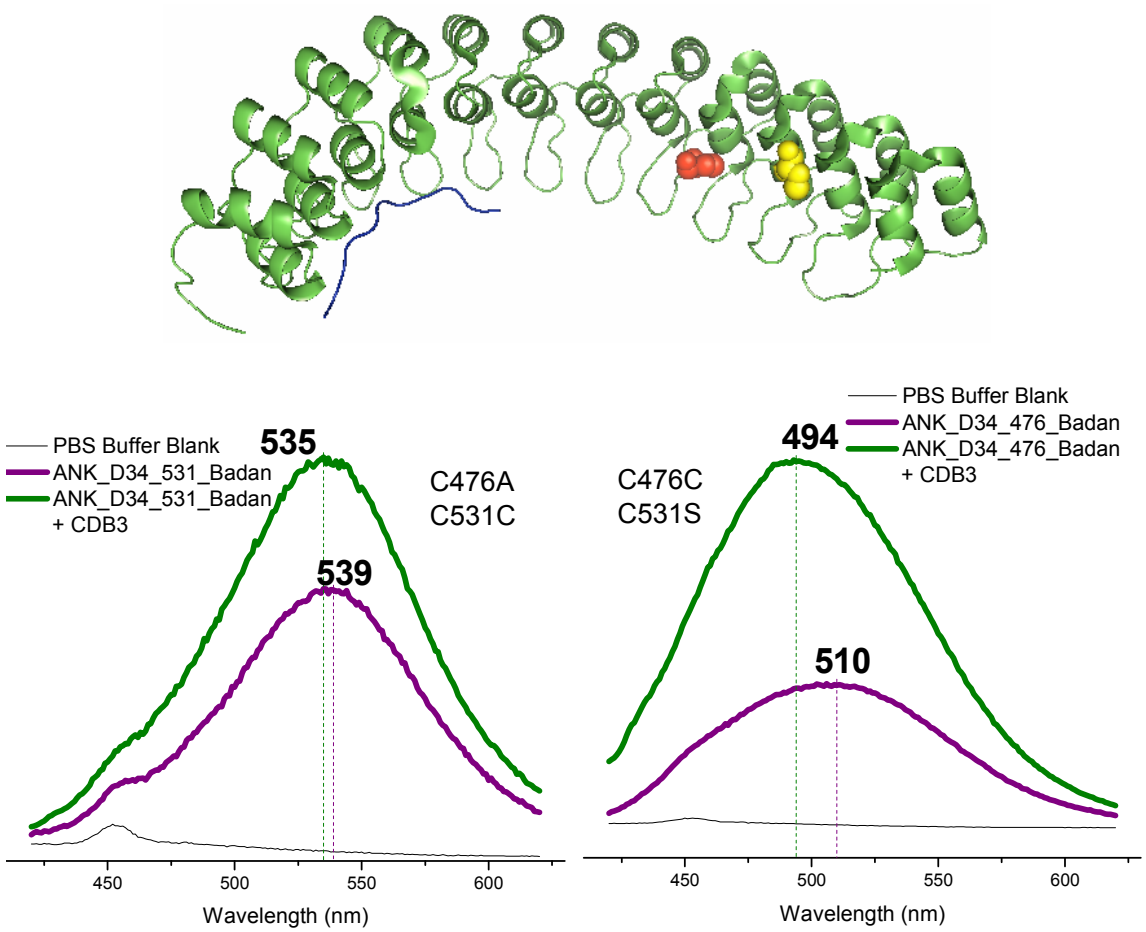

Figure 49. The effect of cdb3 binding to ANK_D34

The upper panel is a ribbon structure of ANK_D34. Yellow and red spheres represent site 476 and 531 respectively. The blue loop represents the fragment of the spectrin-binding domain (802-812) that binds to the ANK repeat 20-24 stack (Michaely *et al.* 2002). Lower right shows the fluorescence experiment on ANK_D34_476_badan; lower left shows the fluorescence experiment on ANK_D34_531_badan. Purple lines are the emission spectra of 2 μM ANK_D34 labeled with badan. Green lines are the emission spectra after addition of 20 μM wt cdb3. Black lines are the PBS buffer controls. The maximum emission wavelength (λmax) is indicated on the top of each spectrum.

Discussion

Significance

As more three-dimensional structures of biomolecules are becoming available, it is crucial to determine how they interact with each other. Gathering structural

information on the organization and communication among individual components is the first step towards fully elucidating biological functions. Stable complexes can potentially be studied by X-ray crystallography and cryo-electron microscopy (cryo-EM). Different conditions or mutations can be screened to reduce the dynamics of transient complexes. Nevertheless, the task of assembling interaction partners with known structures still requires a painstaking procedure. Environment-sensitive fluorescence probes have been proven to be sensitive to changes in the polarity of their surroundings (Mansoor *et al.* 1999). The secondary structure elements and binding interfaces determined from environmentally sensitive probes along with distances calculated from FRET between donor and acceptor are valuable to construct complexes with dynamic characteristics or low expression levels. Here we utilize a classical spectroscopic approach combined with site-directed mutagenesis to investigate a hypothesized interface between cdb3 and ankyrinR.

In the red blood cell, the bridging protein ankyrinR links the cytoplasmic domain of anion exchanger 1 to the spectrin-based membrane skeleton, which sustains the fundamental mechanical support of the lipid bilayer. The connection of cdb3 to ankyrin, one major linkage between the bilayer and the membrane skeleton, has been shown to be important for the stability, integrity, flexibility and deformability of the erythrocyte membrane as demonstrated by a whole range of studies including knockout animal models (Peters *et al.* 1996; Southgate *et al.* 1996) and natural-occurring mutations in humans (Gallagher and Forget 1997; Eber and Lux 2004). Although the atomic resolution structures of one domain from band 3 (cdb3) and one fragment from ankyrinR (subdomain 3 and 4 of the ANK repeat domain) have been determined, the precise

interface between these two fragments is still unknown, chiefly due to the difficulties in the formation of co-crystals ($K_d \approx 0.4$ μM) and intermediate molecular weight with asymmetrical structure. The map of interaction 'hot spots' generated from our SDFL data suggests that the ankyrin groove loops around the peripheral domain on the side opposite the cdb3 dimer interface. This result provides an important insight into the assembly of the full-length band 3 and ankyrin complex. The current results support the concept that the grooved surface of ANK repeats in many scaffold proteins is a primary docking site for their diverse binding targets.

Direct binding vs allosteric effects

Upon the formation of the ANK_D34-cdb3 complex, the badan fluorescence λmax at various positions displayed dramatic changes ranging from a 7 nm red shift to a 25 nm blue shift (Table 5). The local polarity variations can be supported as these sidechains being directly coupled to the binding interface. An alternative explanation is that the badan emission changes are due to an allosteric transition. If the colored surface of cdb3 in Figure 48 is the allosteric site, there must be an authentic ankyrin binding site at the distal region and a signal pathway between the binding site and the allosteric site involved. The extra energy expenditure might be unfavorable in the case of a scaffold protein binding to its target as a basic architecture in the membrane skeleton network. When perturbing one part of the allosteric site, the binding affinity should be retained, at least to some degree. This deduction, however, directly contradicts with the experimental observation that the cdb3 mutant with β-hairpin loop (175-185) deletion exhibited no ankyrin binding affinity (Chang and Low 2003). Therefore, the colored surface of cdb3

(Figure 48, upper panel) is unlikely an allosteric site. However, we cannot exclude the possibility that this region may be along the signaling pathway between the true binding site and the allosteric site. In terms of the attachment site of cdb3 on ANK_D34, only two native cysteines (C476 and C531) were tested because of the conserved C531. In spite of very limited information on the band 3-ankyrinR interface, eight co-crystal structures containing ANK repeats have been reported. The contacting surface of the ANK repeats to their partners are exclusively located on the grooved surface comprised of the inner short helices and the β-hairpin/loops (Figure 43) (Mosavi *et al.* 2004). Since the 62 kDa spectrin-binding domain occupies the inner concave surface of the C terminal repeats (at least repeats 20-24) (Figure 49, top panel) (Michaely *et al.* 2002), and a relatively large area of cdb3 (a β-hairpin loop and two surface α-helices, Figure 48) is involved in ankyrin association, the straightforward predication is that ANK repeats 15 (containing C476) and 16 (accommodating C531) may contact cdb3 in a direct manner or may be very close to the direct interacting site. All the experimental evidence and theoretical calculations to date are consistent with the idea that polarity changes at abovementioned sites result from physical interaction rather than allosteric effects giving rise to the observed spectral shifts.

Band 3-ankyrin interface

It has been suggested that ankyrin contains two anchoring sites for cdb3, one lies in ANK repeat subdomain 2 (repeats 7-12) and the other requires ANK repeat subdomains 3 and 4 (repeats 13-24) (Michaely and Bennett 1995a). ANK_D34 alone is capable of binding cdb3 with high affinity and promoting the formation of an AE1

tetramer (Davis and Bennett 1990; Van Dort *et al.* 1998). The area of the interaction surface is more than 1500 $Å^2$ from a cdb3-ANK_D34 model generated by the 3D-Dock program (Michaely *et al.* 2002). Although it is almost impossible to determine the relative orientations of these two proteins without distance constraints, the SDFL results enable us to dissect the binding site at the resolution of individual residues. More detailed information about the interface may be available if the whole ANK repeat domain or the full-length ankyrin can be enriched to homogeneity at μM concentration.

The λmax shift data support the hypothesis that the β-hairpin loop (175-185) and nearby residues on the surface of the cdb3 globular domain interact with ankyrin. The N terminus was thought to be the second ankyrin-binding site on cdb3 mainly because kidney cdb3, lacking N terminal residues 1-65, does not interact with ankyrin (Ding *et al.* 1994; Wang *et al.* 1995). The unresolved N terminus (1-54) of cdb3 in the crystal lattice is disordered and EPR studies have shown that it is highly dynamic in solution at neutral pH. However, residues 57-66, forming β-strand 1 in the central β sheet of the globular domain, are also absent in kidney band 3 due to alternative splicing (Zhang *et al.* 2000). Removing this central β-strand may well affect the global folding of the cdb3 dimer, hence altering the binding affinity to ankyrin. Indeed, reevaluation of the cdb3 N terminus in ankyrin association showed that cdb3 lacking residues 1-50 exhibited the similar binding affinity to ankyrin (Chang and Low 2003). Considering that ankyrin binding inhibits the phosphorylation of tyrosine 8 on cdb3 and antibodies against N terminus of cdb3 obstruct ankyrin association (Willardson *et al.* 1989), the N terminus may be adjacent to the ankyrin-binding site (Chang and Low 2003). More experiments are needed to evaluate the possibility that the highly flexible N terminus of cdb3 becomes

more ordered after ankyrin binding or changes from an extended conformation to more compact conformation adjacent to the globular domain upon interaction with ankyrin.

ANK repeats

The ANK repeat motif has been found in protein databases with very high frequency. The canonical ANK repeat exhibits a well-defined helix-loop-helix-β-hairpin/loop fold. Multiple repeats stack together to form a portion of a superhelix, which would require 28-32 repeats to complete one turn (Figure 49 top panel) (Michel *et al.* 2001; Michaely *et al.* 2002). The difference in helix length in one repeat (inner helix is shorter than the outer helix) and the packing interaction of the inter-repeat contribute to the slight curvature of the stacking surface. The consensus residues define the overall structure of the ANK repeat. The diversity of ANK repeat interactions with various proteins mostly arise from variation of residues in the ankyrin groove, different insertions in the loop region, and alternative splicing without altering the integrity of the ANK repeat stack (Michaely *et al.* 2002; Mosavi *et al.* 2004). It is not surprising that the mutant C531A of ankyrinR_D34 failed to express while the replacement of C531 with serine recovers the expression to a reasonable level since C531 is located at the loop region of repeat 16 that is involved in intra-repeat interaction with S528. The SH group of C531 appears to donate a proton to the carbonyl oxygen of S528 to form an intra-repeat H bond. The serine mutation at position 531, but not the alanine mutation, can serve as a surrogate for cysteine by providing a proton at the space close to CO of S528. C531 is situated at position 30 of ankyrinR repeat 16, nevertheless, alanine frequently occurs at position 30 in other repeats (repeat 14, 17, 19, 21, 22), which was the primary reason that

alanine substitution was initially chosen at this position. In most ANK repeats, the carbonyl oxygen of non-polar residues at position 30 makes a H-bond with the side chain proton from His at position 27. These observations exemplify the structure complexity of the ANK repeat and the difficulties of 3-D structure prediction based solely on the analysis of sequence homology.

Conclusions

The ankyrin linkage between an integral membrane protein and the cytoskeleton probably endures certain stress during mechanical deformation in the whole cell lifespan. In the light of atomic resolution structures obtained from fragments of band 3 and ankyrin, here we report a SDFL approach to examine the band 3-ankyrin interface to circumvent the limitations of crystallography and NMR. SDFL does not require the formation of co-crystals and has no size limitations. Our results suggest that the ankyrin groove of ANK_D34 surrounds the peripheral domain of cdb3 and are consistent with the idea that full-length ankyrin is capable of associating with band 3 tetramer beneath the erythrocyte membrane. The α-helix 2, α-helix 3 and β strands 6, 7 (hairpin) of cdb3 may bind to ankyrin directly.

CHAPTER VII

SUMMARY AND PERSPECTIVES

Summary

This dissertation work addresses three aspects of structure-function relationships in a biological system: the evaluation of an atomic resolution structure that was determined under non-physiological conditions, the perturbation of the known structure of a protein that leads to abnormal function, and the extension of individual domain structures into the structure of the complex.

First, the multiple SDSL-EPR distance constraints (8~25 Å from CW-EPR and 17~50 Å from DEER) on the dimerization arm and the peripheral domain of cdb3 acquired at physiological pH have shown the solution structure of cdb3 to be indistinguishable from the structure of cdb3 obtained from crystals grown at a non-physiological pH 4.8. Prior to this work, there was a controversy regarding the compact dimer configuration in comparison with previous hydrodynamic studies that had indicated an elongated structure with a 10:1 axial ratio. The mobility and accessibility data of cdb3 in solution are totally consistent with the static crystal structure. EPR lineshapes of the N terminus indicate the dynamic features of this region that can adopt a wide range of conformations and thereby dock a variety of cytoplasmic proteins to the inner surface of the red blood cell membrane. Similar disorder is detected at the C terminus of cdb3, which may represent the relatively flexible linker that connects the erythrocyte membrane and the membrane skeleton network. Determining the structure of

cdb3 in solution at physiological pH is a necessary step in characterizing cdb3 functions, especially the cdb3-protein interactions that stabilize the red blood cell membrane.

Second, based upon the validated solution structure, a pathogenetic mutation P327R (band 3 Tuscaloosa) has been studied by a series of biochemical and biophysical experiments. DSC shows that the P327R mutation decreases the melting temperature of the cdb3 dimer by 7°C. A large body of EPR constraints (distance, mobility, accessibility) indicates that the additional modest effects of the P327R substitution are localized in the vicinity of the mutated residue and its C-terminal downstream region. No evidence has been obtained that suggests the cdb3 dimers dissociation, rearranging secondary structure or structurally misfolding. This work sheds light on our understanding of the subtleties in structure that can result in the hereditary spherocytosis phenotype. Although most identified HS defects are caused by single point mutations, certain mutations may share similar features in biochemical and/or structural defects. (Each individual kindred has a unique mutation in the current database (Gallagher and Ferriera 1997).) In the case of band 3 Tuscaloosa, P327R may belong to a group of variants, which decrease protein 4.2 binding and/or destabilized the cdb3 dimer and/or change the flexibility of the linkage between cdb3 and tdb3.

Finally, the band 3-ankyrin complex has been extensively studied. Recently, the crystal structures of cdb3 and ANK_D34 have been reported thereby enabling studies aimed at elucidating the structure and dynamics of the complex. Studies using site directed fluorescence labeling have now been conducted on both cdb3 and ANK_D34. The badan emission spectra shifts at specific sites show that upon formation of the cdb3-ANK_D34 complex, the peripheral domain of cdb3 (α-helix 2, α-helix 3 and a β hairpin

strands composed of β strands 6, 7) binds to the ankyrin groove of ANK_D34. The ankyrin binding interface on cdb3 is located on the surface of the globular domain opposite the dimer interface. It is the first experimental data to associate these two important membrane skeletal components, which construct a framework for more docking targets and building a molecular model of the supercomplex.

In summary, this dissertation has thoroughly described the solution structure of cdb3, clearly demonstrated structural effects of the P327R mutation on the cdb3 dimer, and mapped the interaction interface between cdb3 and ANK_D34. These studies show that spectroscopic approaches, in combination with the powerful site-directed mutagenesis, can not only complement the classical techniques in structure biology, but also provide valuable structural information towards the eventual goal of fully understanding the structure and function of biomolecules.

Temperature Concern Regarding DEER Experiments

Temperature is important to any dynamic process according to the third law of thermodynamics. At absolute zero temperature, there is zero thermal energy or heat, thus there should be no molecular motion at all. The DEER experiments have been conducted at the very low temperature of 60~66K. Lowering temperature reduces the overall dynamics of the molecule, increases T_1 (1-100 ms) and T_2 (1-2 μs) relaxation times, and enhances the population difference of the Boltzmann distribution at thermal equilibrium. A long spin-spin relaxation time, T_2, lengthens the spin coherence and allows a long evolution time. In turn, a long evolution time facilitates the measurement of weak dipolar interactions. The increased net magnetization also strengthens the intensity of the spin

echo. However, the long spin-lattice relaxation time T_1 hinders the speed of data averaging. Since the echo in the DEER experiment is collected at constant time, the quality of DEER signals is proportional to the signal to noise ratio. The S/N of one complete DEER experiment is given by

$$S/N = S_0\sqrt{t_c/SRT} = kC(1-e^{-SRT/T_1})e^{-\tau/T_2}\sqrt{t_c/SRT},$$

where S_0 represents the signal from a four-pulse DEER sequence, k is an instrumental constant, C is the spin concentration, τ is the time of one DEER sequence from the $\pi/2$ pulse to the echo detection, t_c is the total collection time, and SRT is the shot repetition time, which is the time between individual 4-pulse experiments to allow the magnetization to recover to equilibrium. As T↓, T1 and T2↑, $e^{-\tau/T2}$↑ while $(1-e^{-SRT/T1})$↓. So the optimal temperature 60K is a tradeoff between the echo strength and the pulse repetition rate to achieve maximal S/N during the same experiment time. Another acceptable compromise is the SRT = 1.2T1. SRT = 4.7T1 guarantees 99% recovery of the z magnetization, but the number of experiments is much fewer than with shorter SRT.

When intramolecular spin-spin distance is of interest, the spin concentration should not exceed an upper boundary, beyond which the contribution from intermolecular spin-spin interaction cannot be ignored. Normally, a protein concentration of less than 500 μM can be tolerated. However, the freezing of aqueous solutions tends to exclude macromolecules from ice crystals causing very high local protein concentration. In DEER, cryogenic protection of higher than 50% sucrose or higher than 30% glycerol is utilized to form glass solutions and prevent ice formation. One drawback of glycerol is that it can potentially alter protein-protein interfaces resulting in the dissociation of protein complexes.

In the EPR field, it is still controversial about the effects of low temperature on average distances and distance distributions. At room temperature, the high mobility of one or both nitroxides may cause a wide distribution of interspin distances. During the DEER experiment at very low temperature (60K), this correlation still holds in most cases, that is to say, nitroxides with low mobility at room temperature tend to have a narrow distance distribution obtained from DEER (Compare CW-EPR lineshape and DEER distribution of P3_208, P3_84, P3_290). However, in some special cases, nitroxides with narrow distance distribution at low temperature can be relatively mobile and disordered at room temperature (See P3_340, which shows an intermediate mobility from CW-EPR while has 0.8 Å distance distribution from DEER). In the cone model, distance distribution between two spin labels is orientation dependent while the mobility of each spin label is involved in the amplitude (the cone width) and rate of the motion. Assuming identical cone widths, two cones with the overlapping axes aligned to the base vector (head to head or head to tail or tail to tail) tend to possess narrower distance distribution than two cones whose axes are not aligned to the base vector. Another potential explanation for this apparent inconsistency lies in the freezing procedure. Ideally, fast freezing should not only reduce the rate of nitroxide motion to near zero but also capture all of the conformations of the nitroxides at room temperature. In reality, however, the freezing rate (10ms to 10s) is much slower than the nitroxide motion at room temperature (ns to μs). Consequently, certain conformations may be energetically favorable at low temperature. The main factors that define the conformational space are the local minima and energy barriers at low temperatures rather than the motional restrictions at room temperature. If the energy profile is smooth, the cooling will lead to a

single rotamer with the lowest energy even if relatively the high mobility at room temperature was caused by more rotamers. On the other hand, an immobilized CW-EPR lineshape at room temperature is not necessarily an indication for a narrow distance distribution from DEER because ordered nitroxides may have several rotamers. DEER at low temperature tends to report the distance distributions closer to or narrower than the physiological condition. As mentioned in the sidechain mobility section of Chapter 2, the nitroxide motions come from sidechain dynamics, tertiary contact, backbone fluctuation and protein tumbling. The first three factors contribute most to the distance distribution. Since it is the motion and distance distribution of the original sidechains and the motion of the backbone that is of biological significance, various spin labels with distinct chemical structure may be used to test the effect of the nitroxide sidechain.

Outlook of SDSL-EPR Application in Biomedical Research

Site-directed spin labeling (SDSL) coupled with electron paramagnetic resonance (EPR) has become a powerful tool for monitoring the structure and dynamics of soluble and membrane proteins, and for connecting structure and function of these biomolecules. The advanced development of SDSL-EPR includes incorporating nitroxides into the protein backbone (Toniolo *et al.* 1995; McNulty *et al.* 2000), synthesizing new spin labels with reduced internal sidechain motion, increasing spectra resolution with high field/high frequency EPR (Hustedt and Beth 2004), optimizing simulation programs (Hustedt *et al.* 2006) and data analysis (Hustedt *et al.* 1997), applying pulsed EPR techniques in biological system, and so on. After the completion of genomic projects of human and other model organisms, structural genomics is emerging as a research goal.

With more and more protein structures becoming available at atomic resolution, the requirement for understanding the relationship between structure and function becomes more clear and present. In general terms, conformational changes in the microsecond to millisecond range and local backbone fluctuations in the picosecond and microsecond range are of functional significance. Static crystal structures can provide clues to conformation switches because sometimes molecules are trapped in an asymmetric unit or have different crystal forms and the B factor reflects the spatial disorder. Nuclear magnetic resonance (NMR) is mostly applicable to small soluble proteins (<35 kDa). Cryo-electron microscopy (Cryo-EM) is preferred for structural determination of supramolecular complexes. SDSL-EPR is one of the promising approaches to elucidate protein dynamics in solution without size limits at the corresponding time window (ps~μs for CW-EPR) (Columbus and Hubbell 2002).

Given a high-resolution structure as a starting point, if we can biochemically enrich certain conformations from the ensemble of all conformations, for example, changing pH or binding to substrate, SDSL-EPR can be applied to study the conformation changes between two states including domain movements, rigid body motions and changes in secondary structure. Successful examples include the tilting and rotating motion of rhodopsin transmembrane helices due to light activation (Farrens *et al.* 1996), the gating of pH dependent potassium channel KcsA (Liu *et al.* 2001), the pore opening of mechanosensitive channel MscL (Perozo *et al.* 2002), the local unfolding in transporter BtuB upon binding vitamin B12 substrate (Merianos *et al.* 2000), the transporter opening (helix tilting on two monomers of the multidrug transporter dimer) of MsbA upon binding non-hydrolyzable ATP analog (Dong *et al.* 2005), etc. Theoretically,

the structure of the 'end state' can be solved if sufficient numbers of distance constraints are obtained from CW-EPR and/or pulsed EPR at multiple frequencies and distance geometry is therefore constructed from the 'start state' using molecular simulation. More intriguing, we can 'watch' how proteins work in real time when combining EPR and stop-flow techniques (Hubbell *et al.* 1996).

The overall motion of the nitroxide is strongly coupled to backbone motions on the nanosecond time scale. The CW-EPR lineshape is very sensitive to dynamics in the same time range. Semi-quantitative analysis of spin label mobility may provide information to map dynamic regions that are functionally relevant. It is possible to determine backbone fluctuations quantitatively by fitting multifrequency EPR data. In principle, high field / high frequency (250GHz) saturation transfer-EPR (ST-EPR) can extend the sensitivity limit to very slow rotational motions in the 1–100 ms time window. At the higher microwave frequency, ST-EPR spectra are also more sensitive to the anisotropic characteristics and small constraints of the motion (Hustedt and Beth 2004). Suppose a transmembrane protein that undergoes uniaxial rotational diffusion (URD) in the lipid bilayer with a correlation time of 1 ms. Some of its helices may rotate and/or tilt at much faster rate (1 μs) to transport substrates or transduce signals. CW-EPR spectra cannot distinguish the substrate-transporting or signal-transducing helices from surrounding helices while high field/high frequency ST-EPR spectra can give a direct answer. This method may be especially useful in cases when no distinct environment difference exists, such as a water-filled pore or the lack of a convenient way to trap one conformation.

In summary, SDSL-EPR has been proven to be an advantageous method to understand the structure, dynamics and function of soluble and membrane proteins. The future advance of this technique is highlighted in constructing the distance geometry from long range distance constraints and broadening the sensitivity timescale to ns~ms, which overlaps the time window of various biological processes through multifrequency approaches.

The Structure and Function of kAE1

kAE1 is highly expressed in the basolateral membrane of the α–intercalated cell in kidney. In comparison with eAE1, the translation of kAE1 initiates from exon 5 due to alternative splicing (Kollert-Jons *et al.* 1993; Sahr *et al.* 1994). The truncated AE1 is missing residues 1-65 of eAE1. The deletion of the N-terminal fragment may have two major impacts. First, kidney cdb3 does not interact with intracellular glycolytic enzymes (Wang *et al.* 1995) since the dynamically disordered N terminus (1-54) of erythrocyte cdb3 is responsible for docking glycolytic enzymes to the inner layer of membrane. Second, the deletion of a central β-strand (57-66) in the core of the cdb3 monomer (Zhang *et al.* 2000) may lead to a distinct fold, therefore destroying the ankyrin binding surface (Ding *et al.* 1994; Wang *et al.* 1995). The trafficking and targeting of kAE1 to the basolateral membrane is very intriguing. Kanadaptin (kidney anion exchanger adaptor protein) binds and colocalizes with kAE1 only in cytoplasmic vesicles of intercalated cells in the collecting tubule, but not in the basolateral membrane (Chen *et al.* 1998). Mutations of AE1 with deficient anion exchange kinetics, impaired trafficking (Quilty *et al.* 2002) or mis-targeting kAE1 to the apical membrane may seriously impact both the

retrieval of bicarbonate from renal tubules and the tubular acid excretion, thus causing dRTA (Wrong *et al.* 2002; Eber and Lux 2004). Interestingly, interaction with ankyrinG is required for the ammonium transporter RhBG, a nonerythroid Rh member, to target at the basolateral membrane of the connecting tubule and collecting duct cells (Lopez *et al.* 2005). Knowing whether different ankyrin isoforms are involved in kAE1 sorting and anchoring to the basolateral membrane in polarized cells is crucial to the understanding of the mechanism and regulation of the pH homeostasis and HCO_3^-/Cl^- transport in the distal nephron.

REFERENCES

Agre, P., E. P. Orringer and V. Bennett (1982) Deficient red-cell spectrin in severe, recessively inherited spherocytosis. *N Engl J Med* **306**(19): 1155-61.

Alper, S. L., R. B. Darman, M. N. Chernova and N. K. Dahl (2002) The AE gene family of Cl/HCO3- exchangers. *J Nephrol* **15 Suppl 5**: S41-53.

Alper, S. L., H. Rossmann, S. Wilhelm, A. K. Stuart-Tilley, B. E. Shmukler and U. Seidler (1999) Expression of AE2 anion exchanger in mouse intestine. *Am J Physiol* **277**(2 Pt 1): G321-32.

Alper, S. L., A. Stuart-Tilley, C. F. Simmons, D. Brown and D. Drenckhahn (1994) The fodrin-ankyrin cytoskeleton of choroid plexus preferentially colocalizes with apical Na+K(+)-ATPase rather than with basolateral anion exchanger AE2. *J Clin Invest* **93**(4): 1430-8.

Altenbach, C., S. L. Flitsch, H. G. Khorana and W. L. Hubbell (1989) Structural studies on transmembrane proteins. 2. Spin labeling of bacteriorhodopsin mutants at unique cysteines. *Biochemistry* **28**(19): 7806-12.

Altenbach, C., W. Froncisz, R. Hemker, H. McHaourab and W. L. Hubbell (2005) Accessibility of nitroxide side chains: absolute Heisenberg exchange rates from power saturation EPR. *Biophys J* **89**(3): 2103-12.

Altenbach, C., K. J. Oh, R. J. Trabanino, K. Hideg and W. L. Hubbell (2001) Estimation of inter-residue distances in spin labeled proteins at physiological temperatures: experimental strategies and practical limitations. *Biochemistry* **40**(51): 15471-82.

An, X. L., Y. Takakuwa, W. Nunomura, S. Manno and N. Mohandas (1996) Modulation of band 3-ankyrin interaction by protein 4.1. Functional implications in regulation of erythrocyte membrane mechanical properties. *J Biol Chem* **271**(52): 33187-91.

Ango, F., G. di Cristo, H. Higashiyama, V. Bennett, P. Wu and Z. J. Huang (2004) Ankyrin-based subcellular gradient of neurofascin, an immunoglobulin family protein, directs GABAergic innervation at purkinje axon initial segment. *Cell* **119**(2): 257-72.

Appell, K. C. and P. S. Low (1981) Partial structural characterization of the cytoplasmic domain of the erythrocyte membrane protein, band 3. *J Biol Chem* **256**(21): 11104-11.

Askin, D., G. B. Bloomberg, E. J. Chambers and M. J. Tanner (1998) NMR solution structure of a cytoplasmic surface loop of the human red cell anion transporter, band 3. *Biochemistry* **37**(33): 11670-8.

Aurora, R. and G. D. Rose (1998) Helix capping. *Protein Sci* **7**(1): 21-38.

Bagnato, P., V. Barone, E. Giacomello, D. Rossi and V. Sorrentino (2003) Binding of an ankyrin-1 isoform to obscurin suggests a molecular link between the sarcoplasmic reticulum and myofibrils in striated muscles. *J Cell Biol* **160**(2): 245-53.

Bahar, S., C. T. Gunter, C. Wu, S. D. Kennedy and P. A. Knauf (1999) Persistence of external chloride and DIDS binding after chemical modification of Glu-681 in human band 3. *Am J Physiol* **277**(4 Pt 1): C791-9.

Batchelor, A. H., D. E. Piper, F. C. de la Brousse, S. L. McKnight and C. Wolberger (1998) The structure of GABPalpha/beta: an ETS domain- ankyrin repeat heterodimer bound to DNA. *Science* **279**(5353): 1037-41.

Benkovic, S. J. and S. Hammes-Schiffer (2003) A perspective on enzyme catalysis. *Science* **301**(5637): 1196-202.

Bennett, V. and A. J. Baines (2001) Spectrin and ankyrin-based pathways: metazoan inventions for integrating cells into tissues. *Physiol Rev* **81**(3): 1353-92.

Bennett, V. and J. Davis (1981) Erythrocyte ankyrin: immunoreactive analogues are associated with mitotic structures in cultured cells and with microtubules in brain. *Proc Natl Acad Sci U S A* **78**(12): 7550-4.

Bennett, V. and P. J. Stenbuck (1979a) Identification and partial purification of ankyrin, the high affinity membrane attachment site for human erythrocyte spectrin. *J Biol Chem* **254**(7): 2533-41.

Bennett, V. and P. J. Stenbuck (1979b) The membrane attachment protein for spectrin is associated with band 3 in human erythrocyte membranes. *Nature* **280**(5722): 468-73.

Bennett, V. and P. J. Stenbuck (1980) Association between ankyrin and the cytoplasmic domain of band 3 isolated from the human erythrocyte membrane. *Journal of Biological Chemistry* **255**(13): 6424-32.

Berengian, A. R., M. P. Bova and H. S. McHaourab (1997) Structure and function of the conserved domain in alphaA-crystallin. Site-directed spin labeling identifies a beta-strand located near a subunit interface. *Biochemistry* **36**(33): 9951-7.

Berliner, L. J. and etc (1976) Spin Labeling: Theory and Applications. New York, Academic Press.

Berliner, L. J. and H. M. McConnell (1966) A spin-labeled substrate for alpha-chymotrypsin. *Proc Natl Acad Sci U S A* **55**(4): 708-12.

Beth, A. H., B. H. Robinson, C. E. Cobb, L. R. Dalton, W. E. Trommer, J. J. Birktoft and J. H. Park (1984) Interactions and spatial arrangement of spin-labeled NAD+ bound to glyceraldehyde-3-phosphate dehydrogenase. Comparison of EPR and X-ray modeling data. *J Biol Chem* **259**(15): 9717-28.

Birkenmeier, C. S. and J. E. Barker (2004) Hereditary haemolytic anaemias: unexpected sequelae of mutations in the genes for erythroid membrane skeletal proteins. *J Pathol* **204**(4): 450-9.

Blackman, S. M., E. J. Hustedt, C. E. Cobb and A. H. Beth (2001) Flexibility of the cytoplasmic domain of the anion exchange protein, band 3, in human erythrocytes. *Biophys J* **81**(6): 3363-76.

Blackman, S. M., D. W. Piston and A. H. Beth (1998) Oligomeric state of human erythrocyte band 3 measured by fluorescence resonance energy homotransfer. *Biophys J* **75**(2): 1117-30.

Borbat, P. P., A. J. Costa-Filho, K. A. Earle, J. K. Moscicki and J. H. Freed (2001) Electron spin resonance in studies of membranes and proteins. *Science* **291**(5502): 266-9.

Borbat, P. P., J. H. Davis, S. E. Butcher and J. H. Freed (2004) Measurement of large distances in biomolecules using double-quantum filtered refocused electron spin-echoes. *J Am Chem Soc* **126**(25): 7746-7.

Borbat, P. P., H. S. McHaourab and J. H. Freed (2002) Protein structure determination using long-distance constraints from double-quantum coherence ESR: study of T4 lysozyme. *J Am Chem Soc* **124**(19): 5304-14.

Bork, P. (1993) Hundreds of ankyrin-like repeats in functionally diverse proteins: mobile modules that cross phyla horizontally? *Proteins* **17**(4): 363-74.

Boron, W. F. (2001) Sodium-coupled bicarbonate transporters. *Jop* **2**(4 Suppl): 176-81.

Bouley, M., M. Z. Tian, K. Paisley, Y. C. Shen, J. D. Malhotra and M. Hortsch (2000) The L1-type cell adhesion molecule neuroglian influences the stability of neural ankyrin in the Drosophila embryo but not its axonal localization. *J Neurosci* **20**(12): 4515-23.

Bourguignon, L. Y., A. Chu, H. Jin and N. R. Brandt (1995) Ryanodine receptor-ankyrin interaction regulates internal Ca2+ release in mouse T-lymphoma cells. *J Biol Chem* **270**(30): 17917-22.

Bourguignon, L. Y., H. Jin, N. Iida, N. R. Brandt and S. H. Zhang (1993) The involvement of ankyrin in the regulation of inositol 1,4,5-trisphosphate receptor-mediated internal Ca2+ release from Ca2+ storage vesicles in mouse T-lymphoma cells. *J Biol Chem* **268**(10): 7290-7.

Bourguignon, L. Y., H. Zhu, L. Shao and Y. W. Chen (2000) Ankyrin-Tiam1 interaction promotes Rac1 signaling and metastatic breast tumor cell invasion and migration. *J Cell Biol* **150**(1): 177-91.

Bowman, M. K., A. G. Maryasov, N. Kim and V. J. DeRose (2004) Visualization of distance distribution from pulsed double electron-electron resonance data. *Applied Magnetic Resonance* **26**(1-2): 23-39.

Bruce, L. J., R. Beckmann, M. L. Ribeiro, L. L. Peters, J. A. Chasis, J. Delaunay, N. Mohandas, D. J. Anstee and M. J. Tanner (2003) A band 3-based macrocomplex of integral and peripheral proteins in the RBC membrane. *Blood* **101**(10): 4180-8.

Bruce, L. J. and M. J. Tanner (1996) Structure-function relationships of band 3 variants. *Cellular & Molecular Biology* **42**(7): 953-73.

Burley, S. K. (2000) An overview of structural genomics. *Nat Struct Biol* **7 Suppl**: 932-4.

Bustos, S. P. and R. A. Reithmeier (2006) Structure and stability of hereditary spherocytosis mutants of the cytosolic domain of the erythrocyte anion exchanger 1 protein. *Biochemistry* **45**(3): 1026-34.

Cabantchik, Z. I. and A. Rothstein (1972) The nature of the membrane sites controlling anion permeability of human red blood cells as determined by studies with disulfonic stilbene derivatives. *J Membr Biol* **10**(3): 311-30.

Cabantchik, Z. I. and A. Rothstein (1974) Membrane proteins related to anion permeability of human red blood cells. I. Localization of disulfonic stilbene binding sites in proteins involved in permeation. *J Membr Biol* **15**(3): 207-26.

Carlile, G. W., D. H. Smith and M. Wiedmann (2004) Caspase-3 has a nonapoptotic function in erythroid maturation. *Blood* **103**(11): 4310-6.

Carrington, A. and A. McLachlan (1967) Introduction to Magnetic Resonance. New York, Harper & Row.

Carugo, K. D., S. Banuelos and M. Saraste (1997) Crystal structure of a calponin homology domain. *Nat Struct Biol* **4**(3): 175-9.

Casey, J. R. and R. A. Reithmeier (1991) Analysis of the oligomeric state of Band 3, the anion transport protein of the human erythrocyte membrane, by size exclusion

high performance liquid chromatography. Oligomeric stability and origin of heterogeneity. *J Biol Chem* **266**(24): 15726-37.

Chang, S. H. and P. S. Low (2001) Regulation of the glycophorin C-protein 4.1 membrane-to-skeleton bridge and evaluation of its contribution to erythrocyte membrane stability. *J Biol Chem* **276**(25): 22223-30.

Chang, S. H. and P. S. Low (2003) Identification of a critical ankyrin-binding loop on the cytoplasmic domain of erythrocyte membrane band 3 by crystal structure analysis and site-directed mutagenesis. *J Biol Chem* **278**(9): 6879-84.

Chen, J., S. Vijayakumar, X. Li and Q. Al-Awqati (1998) Kanadaptin is a protein that interacts with the kidney but not the erythroid form of band 3. *J Biol Chem* **273**(2): 1038-43.

Cherry, L., N. Menhart and L. W. Fung (1999) Interactions of the alpha-spectrin N-terminal region with beta-spectrin. Implications for the spectrin tetramerization reaction. *J Biol Chem* **274**(4): 2077-84.

Chiang, Y. W., P. P. Borbat and J. H. Freed (2005) The determination of pair distance distributions by pulsed ESR using Tikhonov regularization. *J Magn Reson* **172**(2): 279-95.

Cobb, C. E., M. Dixit, S. Brandon, E. J. Hustedt and A. H. Beth (2003) Investigation of pH-induced structural changes of cdb3 by site-directed spin labeling. *Biophys J* **84**: 496a (abstract).

Cobb, C. E., M. Silvestry, Z. Zhou, A. Camarata, M. Dixit, S. Brandon, E. J. Hustedt and A. H. Beth (2004) Investigation of the structure and stability of cdb3 by site-directed spin labeling and intrinsic tryptophan fluorescence. *Biophys J* **86**: 100a (abstract).

Colfen, H., S. E. Harding, J. M. Boulter and A. Watts (1996) Hydrodynamic examination of the dimeric cytoplasmic domain of the human erythrocyte anion transporter, band 3. *Biophys J* **71**(3): 1611-5.

Columbus, L. and W. L. Hubbell (2002) A new spin on protein dynamics. *Trends Biochem Sci* **27**(6): 288-95.

Columbus, L., T. Kalai, J. Jeko, K. Hideg and W. L. Hubbell (2001) Molecular motion of spin labeled side chains in alpha-helices: analysis by variation of side chain structure. *Biochemistry* **40**(13): 3828-46.

Conboy, J., N. Mohandas, G. Tchernia and Y. W. Kan (1986) Molecular basis of hereditary elliptocytosis due to protein 4.1 deficiency. *N Engl J Med* **315**(11): 680-5.

Crespo, M. D., G. W. Platt, R. Bofill and M. S. Searle (2004) Context-dependent effects of proline residues on the stability and folding pathway of ubiquitin. *Eur J Biochem* **271**(22): 4474-84.

Cuello, L. G., D. M. Cortes and E. Perozo (2004) Molecular architecture of the KvAP voltage-dependent K+ channel in a lipid bilayer. *Science* **306**(5695): 491-5.

Davis, J. Q. and V. Bennett (1984) Brain ankyrin. A membrane-associated protein with binding sites for spectrin, tubulin, and the cytoplasmic domain of the erythrocyte anion channel. *J Biol Chem* **259**(21): 13550-9.

Davis, J. Q. and V. Bennett (1994a) Ankyrin binding activity shared by the neurofascin/L1/NrCAM family of nervous system cell adhesion molecules. *J Biol Chem* **269**(44): 27163-6.

Davis, J. Q., T. McLaughlin and V. Bennett (1993) Ankyrin-binding proteins related to nervous system cell adhesion molecules: candidates to provide transmembrane and intercellular connections in adult brain. *J Cell Biol* **121**(1): 121-33.

Davis, L., S. E. Lux and V. Bennett (1989) Mapping the ankyrin-binding site of the human erythrocyte anion exchanger. *J Biol Chem* **264**(16): 9665-72.

Davis, L. H. and V. Bennett (1990) Mapping the binding sites of human erythrocyte ankyrin for the anion exchanger and spectrin. *J Biol Chem* **265**(18): 10589-96.

Davis, L. H. and V. Bennett (1994b) Identification of two regions of beta G spectrin that bind to distinct sites in brain membranes. *J Biol Chem* **269**(6): 4409-16.

Davis, L. H., J. Q. Davis and V. Bennett (1992) Ankyrin regulation: an alternatively spliced segment of the regulatory domain functions as an intramolecular modulator. *J Biol Chem* **267**(26): 18966-72.

Davis, L. H., E. Otto and V. Bennett (1991) Specific 33-residue repeat(s) of erythrocyte ankyrin associate with the anion exchanger. *J Biol Chem* **266**(17): 11163-9.

Del Rio, M., A. Imam, M. DeLeon, G. Gomez, J. Mishra, Q. Ma, S. Parikh and P. Devarajan (2004) The death domain of kidney ankyrin interacts with Fas and promotes Fas-mediated cell death in renal epithelia. *J Am Soc Nephrol* **15**(1): 41-51.

Delaunay, J. (2002) Molecular basis of red cell membrane disorders. *Acta Haematol* **108**(4): 210-8.

Devarajan, P., P. R. Stabach, A. S. Mann, T. Ardito, M. Kashgarian and J. S. Morrow (1996) Identification of a small cytoplasmic ankyrin (AnkG119) in the kidney and

muscle that binds beta I sigma spectrin and associates with the Golgi apparatus. *J Cell Biol* **133**(4): 819-30.

Ding, Y., J. R. Casey and R. R. Kopito (1994) The major kidney AE1 isoform does not bind ankyrin (Ank1) in vitro. An essential role for the 79 NH2-terminal amino acid residues of band 3. *J Biol Chem* **269**(51): 32201-8.

Ding, Y., S. Kobayashi and R. Kopito (1996) Mapping of ankyrin binding determinants on the erythroid anion exchanger, AE1. *J Biol Chem* **271**(37): 22494-8.

Discher, D. E. (2000) New insights into erythrocyte membrane organization and microelasticity. *Curr Opin Hematol* **7**(2): 117-22.

Discher, D. E., D. H. Boal and S. K. Boey (1998) Simulations of the erythrocyte cytoskeleton at large deformation. II. Micropipette aspiration. *Biophys J* **75**(3): 1584-97.

Discher, D. E., N. Mohandas and E. A. Evans (1994) Molecular maps of red cell deformation: hidden elasticity and in situ connectivity. *Science* **266**(5187): 1032-5.

Dong, J., G. Yang and H. S. McHaourab (2005) Structural basis of energy transduction in the transport cycle of MsbA. *Science* **308**(5724): 1023-8.

Dubreuil, R. R., G. MacVicar, S. Dissanayake, C. Liu, D. Homer and M. Hortsch (1996) Neuroglian-mediated cell adhesion induces assembly of the membrane skeleton at cell contact sites. *J Cell Biol* **133**(3): 647-55.

Eber, S. and S. E. Lux (2004) Hereditary spherocytosis--defects in proteins that connect the membrane skeleton to the lipid bilayer. *Semin Hematol* **41**(2): 118-41.

Fairbanks, G., T. L. Steck and D. F. Wallach (1971) Electrophoretic analysis of the major polypeptides of the human erythrocyte membrane. *Biochemistry* **10**(13): 2606-17.

Farahbakhsh, Z. T., C. Altenbach and W. L. Hubbell (1992) Spin labeled cysteines as sensors for protein-lipid interaction and conformation in rhodopsin. *Photochem Photobiol* **56**(6): 1019-33.

Farrens, D. L., C. Altenbach, K. Yang, W. L. Hubbell and H. G. Khorana (1996) Requirement of rigid-body motion of transmembrane helices for light activation of rhodopsin. *Science* **274**(5288): 768-70.

Feix, J. B. and C. S. Klug (1998) Site-directed spin labeling of membrane proteins and membrane interactions. Biological Magnetic Resonance. New York, Plenum Press. **14:** 251-281.

Feo, C. J., S. Fischer, J. P. Piau, M. J. Grange and G. Tchernia (1980) [1st instance of the absence of an erythrocyte membrane protein (band 4(1)) in a case of familial elliptocytic anemia]. *Nouv Rev Fr Hematol* **22**(4): 315-25.

Festy, F., J. C. Robert, R. Brasseur and A. Thomas (2001) Interaction between the N-terminal domain of gastric H,K-ATPase and the spectrin binding domain of ankyrin III. *J Biol Chem* **276**(11): 7721-6.

Fowler, V. M. and V. Bennett (1984) Erythrocyte membrane tropomyosin. Purification and properties. *J Biol Chem* **259**(9): 5978-89.

Fransen, E., V. Lemmon, G. Van Camp, L. Vits, P. Coucke and P. J. Willems (1995) CRASH syndrome: clinical spectrum of corpus callosum hypoplasia, retardation, adducted thumbs, spastic paraparesis and hydrocephalus due to mutations in one single gene, L1. *Eur J Hum Genet* **3**(5): 273-84.

Frohlich, O. and R. B. Gunn (1986) Erythrocyte anion transport: the kinetics of a single-site obligatory exchange system. *Biochim Biophys Acta* **864**(2): 169-94.

Fu, Z., E. Aronoff-Spencer, J. M. Backer and G. J. Gerfen (2003) The structure of the inter-SH2 domain of class IA phosphoinositide 3-kinase determined by site-directed spin labeling EPR and homology modeling. *Proc Natl Acad Sci U S A* **100**(6): 3275-80.

Furuya, W., T. Tarshis, F. Y. Law and P. A. Knauf (1984) Transmembrane effects of intracellular chloride on the inhibitory potency of extracellular H2DIDS. Evidence for two conformations of the transport site of the human erythrocyte anion exchange protein. *J Gen Physiol* **83**(5): 657-81.

Gallagher, P. G. and J. D. Ferriera (1997) Molecular basis of erythrocyte membrane disorders. *Curr Opin Hematol* **4**(2): 128-35.

Gallagher, P. G. and B. G. Forget (1997) Hematologically important mutations: band 3 and protein 4.2 variants in hereditary spherocytosis. *Blood Cells Mol Dis* **23**(3): 417-21.

Gardner, K. and V. Bennett (1987) Modulation of spectrin-actin assembly by erythrocyte adducin. *Nature* **328**(6128): 359-62.

Gargaro, A. R., G. B. Bloomberg, C. E. Dempsey, M. Murray and M. J. Tanner (1994) The solution structures of the first and second transmembrane-spanning segments of band 3. *Eur J Biochem* **221**(1): 445-54.

Gellman, S. H. (1998) Minimal model systems for beta sheet secondary structure in proteins. *Curr Opin Chem Biol* **2**(6): 717-25.

Gilligan, D. M., L. Lozovatsky, B. Gwynn, C. Brugnara, N. Mohandas and L. L. Peters (1999) Targeted disruption of the beta adducin gene (Add2) causes red blood cell spherocytosis in mice. *Proc Natl Acad Sci U S A* **96**(19): 10717-22.

Gorina, S. and N. P. Pavletich (1996) Structure of the p53 tumor suppressor bound to the ankyrin and SH3 domains of 53BP2. *Science* **274**(5289): 1001-5.

Grinstein, S., S. Ship and A. Rothstein (1978) Anion transport in relation to proteolytic dissection of band 3 protein. *Biochim Biophys Acta* **507**(2): 294-304.

Grum, V. L., D. Li, R. I. MacDonald and A. Mondragon (1999) Structures of two repeats of spectrin suggest models of flexibility. *Cell* **98**(4): 523-35.

Gunn, R. B. and O. Frohlich (1979) Asymmetry in the mechanism for anion exchange in human red blood cell membranes. Evidence for reciprocating sites that react with one transported anion at a time. *J Gen Physiol* **74**(3): 351-74.

Hall, T. G. and V. Bennett (1987) Regulatory domains of erythrocyte ankyrin. *J Biol Chem* **262**(22): 10537-45.

Hammes, G. G. (2002) Multiple conformational changes in enzyme catalysis. *Biochemistry* **41**(26): 8221-8.

Hanson, P., D. J. Anderson, G. Martinez, G. Millhauser, F. Formaggio, M. Crisma, C. Toniolo and C. Vita (1998) Electron spin resonance and structural analysis of water soluble, alanine-rich peptides incorporating TOAC. *Molecular Physics* **95**(5): 957-966.

Harrison, M. L., C. C. Isaacson, D. L. Burg, R. L. Geahlen and P. S. Low (1994) Phosphorylation of human erythrocyte band 3 by endogenous p72syk. *J Biol Chem* **269**(2): 955-9.

Hayashi, T. and T. P. Su (2001) Regulating ankyrin dynamics: Roles of sigma-1 receptors. *Proc Natl Acad Sci U S A* **98**(2): 491-6.

Hortsch, M., D. Homer, J. D. Malhotra, S. Chang, J. Frankel, G. Jefford and R. R. Dubreuil (1998) Structural requirements for outside-in and inside-out signaling by Drosophila neuroglian, a member of the L1 family of cell adhesion molecules. *J Cell Biol* **142**(1): 251-61.

Hubbell, W. L. and C. Altenbach (1994) Investigation of structure and dynamics in membrane proteins using site-directed spin labeling. *Current Opinion in Structural Biology* **4**(4): 566-573.

Hubbell, W. L., A. Gross, R. Langen and M. A. Lietzow (1998) Recent advances in site-directed spin labeling of proteins. *Current Opinion in Structural Biology* **8**(5): 649-656.

Hubbell, W. L., H. S. McHaourab, C. Altenbach and M. A. Lietzow (1996) Watching proteins move using site-directed spin labeling. *Structure* **4**(7): 779-83.

Hunter, M. J. (1971) A quantitative estimate of the non-exchange-restricted chloride permeability of the human red cell. *J Physiol* **218**(1): 49P-50P.

Hustedt, E. J. and A. H. Beth (1995) Analysis of saturation transfer electron paramagnetic resonance spectra of a spin-labeled integral membrane protein, band 3, in terms of the uniaxial rotational diffusion model. *Biophys J* **69**(4): 1409-23.

Hustedt, E. J. and A. H. Beth (1999) Nitroxide spin-spin interactions: applications to protein structure and dynamics. *Annu Rev Biophys Biomol Struct* **28**: 129-53.

Hustedt, E. J. and A. H. Beth (2000) Structural information from cw-EPR spectra of dipolar coupled nitroxide spin labels. Biological Magnetic Resonance. New York, Kluwer Academic/Plenum Publishers. **19:** 155-184.

Hustedt, E. J. and A. H. Beth (2004) High field/high frequency saturation transfer electron paramagnetic resonance spectroscopy: increased sensitivity to very slow rotational motions. *Biophys J* **86**(6): 3940-50.

Hustedt, E. J., C. E. Cobb, A. H. Beth and J. M. Beechem (1993) Measurement of rotational dynamics by the simultaneous nonlinear analysis of optical and EPR data. *Biophys J* **64**(3): 614-21.

Hustedt, E. J., A. I. Smirnov, C. F. Laub, C. E. Cobb and A. H. Beth (1997) Molecular distances from dipolar coupled spin-labels: the global analysis of multifrequency continuous wave electron paramagnetic resonance data. *Biophys J* **72**(4): 1861-77.

Hustedt, E. J., R. A. Stein, L. Sethaphong, S. Brandon, Z. Zhou and S. C. Desensi (2006) Dipolar coupling between nitroxide spin labels: the development and application of a tether-in-a-cone model. *Biophys J* **90**(1): 340-56.

Ideguchi, H., K. Okubo, A. Ishikawa, Y. Futata and N. Hamasaki (1992) Band 3-Memphis is associated with a lower transport rate of phosphoenolpyruvate. *British Journal of Haematology* **82**(1): 122-5.

Inaba, M., A. Yawata, I. Koshino, K. Sato, M. Takeuchi, Y. Takakuwa, S. Manno, Y. Yawata, A. Kanzaki, J. Sakai, A. Ban, K. Ono and Y. Maede (1996) Defective anion transport and marked spherocytosis with membrane instability caused by hereditary total deficiency of red cell band 3 in cattle due to a nonsense mutation. *J Clin Invest* **97**(8): 1804-17.

Inoue, T., A. Kanzaki, M. Kaku, A. Yawata, M. Takezono, N. Okamoto, H. Wada, T. Sugihara, O. Yamada, Y. Katayama, N. Nagata and Y. Yawata (1998) Homozygous missense mutation (band 3 Fukuoka: G130R): a mild form of hereditary spherocytosis with near-normal band 3 content and minimal changes of membrane ultrastructure despite moderate protein 4.2 deficiency. *Br J Haematol* **102**(4): 932-9.

Jacobs, M. D. and S. C. Harrison (1998) Structure of an IkappaBalpha/NF-kappaB complex. *Cell* **95**(6): 749-58.

Jarolim, P., J. Palek, D. Amato, K. Hassan, P. Sapak, G. T. Nurse, H. L. Rubin, S. Zhai, K. E. Sahr and S. C. Liu (1991) Deletion in erythrocyte band 3 gene in malaria-resistant Southeast Asian ovalocytosis. *Proc Natl Acad Sci U S A* **88**(24): 11022-6.

Jarolim, P., J. Palek, H. L. Rubin, J. T. Prchal, C. Korsgren and C. M. Cohen (1992) Band 3 Tuscaloosa: Pro327----Arg327 substitution in the cytoplasmic domain of erythrocyte band 3 protein associated with spherocytic hemolytic anemia and partial deficiency of protein 4.2. *Blood* **80**(2): 523-9.

Jenkins, J. D., D. P. Madden and T. L. Steck (1984) Association of phosphofructokinase and aldolase with the membrane of the intact erythrocyte. *J Biol Chem* **259**(15): 9374-8.

Jenkins, S. M. and V. Bennett (2001) Ankyrin-G coordinates assembly of the spectrin-based membrane skeleton, voltage-gated sodium channels, and L1 CAMs at Purkinje neuron initial segments. *J Cell Biol* **155**(5): 739-46.

Jennings, M. L. (1982) Stoichiometry of a half-turnover of band 3, the chloride transport protein of human erythrocytes. *J Gen Physiol* **79**(2): 169-85.

Jennings, M. L. (1989) Structure and function of the red blood cell anion transport protein. *Annu Rev Biophys Biophys Chem* **18**: 397-430.

Jennings, M. L. and J. S. Nicknish (1985) Localization of a site of intermolecular cross-linking in human red blood cell band 3 protein. *J Biol Chem* **260**(9): 5472-9.

Jennings, M. L., J. Whitlock and A. Shinde (1998) Pre-steady state transport by erythrocyte band 3 protein: uphill countertransport induced by the impermeant inhibitor H2DIDS. *Biochem Cell Biol* **76**(5): 807-13.

Jeschke, G. (2002a) Determination of the nanostructure of polymer materials by electron paramagnetic resonance spectroscopy. *Macromolecular Rapid Communications* **23**: 227-246.

Jeschke, G. (2002b) Distance measurements in the nanometer range by pulse EPR. *Chemphyschem* **3**(11): 927-32.

Jeschke, G., A. Koch, U. Jonas and A. Godt (2002) Direct conversion of EPR dipolar time evolution data to distance distributions. *J Magn Reson* **155**(1): 72-82.

Jeschke, G., G. Panek, A. Godt, A. Bender and H. Paulsen (2004) Data analysis procedures for pulse ELDOR measurements of broad distance distributions. *Applied Magnetic Resonance* **26**(1-2): 223-244.

Jeschke, G., M. Pannier and H. W. Spiess (2000) Double electron-electron resonance. Biological Magnetic Resonance. New York, Kluwer Academic/Plenum Publishers. **19:** 493-512.

Jons, T. and D. Drenckhahn (1998) Anion exchanger 2 (AE2) binds to erythrocyte ankyrin and is colocalized with ankyrin along the basolateral plasma membrane of human gastric parietal cells. *Eur J Cell Biol* **75**(3): 232-6.

Joseph, S. K. and S. Samanta (1993) Detergent solubility of the inositol trisphosphate receptor in rat brain membranes. Evidence for association of the receptor with ankyrin. *J Biol Chem* **268**(9): 6477-86.

Kalomiris, E. L. and L. Y. Bourguignon (1988) Mouse T lymphoma cells contain a transmembrane glycoprotein (GP85) that binds ankyrin. *J Cell Biol* **106**(2): 319-27.

Kannan, R., J. Yuan and P. S. Low (1991) Isolation and partial characterization of antibody- and globin-enriched complexes from membranes of dense human erythrocytes. *Biochem J* **278 (Pt 1)**: 57-62.

Kennedy, S. P., S. L. Warren, B. G. Forget and J. S. Morrow (1991) Ankyrin binds to the 15th repetitive unit of erythroid and nonerythroid beta-spectrin. *J Cell Biol* **115**(1): 267-77.

Kenwrick, S., A. Watkins and E. De Angelis (2000) Neural cell recognition molecule L1: relating biological complexity to human disease mutations. *Hum Mol Genet* **9**(6): 879-86.

Kim, N. K., A. Murali and V. J. DeRose (2004) A distance ruler for RNA using EPR and site-directed spin labeling. *Chem Biol* **11**(7): 939-48.

Knauf, P. A., G. F. Fuhrmann, S. Rothstein and A. Rothstein (1977) The relationship between anion exchange and net anion flow across the human red blood cell membrane. *J Gen Physiol* **69**(3): 363-86.

Knauf, P. A., L. J. Spinelli and N. A. Mann (1989) Flufenamic acid senses conformation and asymmetry of human erythrocyte band 3 anion transport protein. *Am J Physiol* **257**(2 Pt 1): C277-89.

Kobayashi, S., C. W. Morgans, J. R. Casey and R. R. Kopito (1994) AE3 anion exchanger isoforms in the vertebrate retina: developmental regulation and differential expression in neurons and glia. *J Neurosci* **14**(10): 6266-79.

Kollert-Jons, A., S. Wagner, S. Hubner, H. Appelhans and D. Drenckhahn (1993) Anion exchanger 1 in human kidney and oncocytoma differs from erythroid AE1 in its NH2 terminus. *Am J Physiol* **265**(6 Pt 2): F813-21.

Kontrogianni-Konstantopoulos, A., E. M. Jones, D. B. Van Rossum and R. J. Bloch (2003) Obscurin is a ligand for small ankyrin 1 in skeletal muscle. *Mol Biol Cell* **14**(3): 1138-48.

Koob, R., M. Zimmermann, W. Schoner and D. Drenckhahn (1988) Colocalization and coprecipitation of ankyrin and Na+,K+-ATPase in kidney epithelial cells. *Eur J Cell Biol* **45**(2): 230-7.

Kopito, R. R., B. S. Lee, D. M. Simmons, A. E. Lindsey, C. W. Morgans and K. Schneider (1989) Regulation of intracellular pH by a neuronal homolog of the erythrocyte anion exchanger. *Cell* **59**(5): 927-37.

Kopito, R. R. and H. F. Lodish (1985) Primary structure and transmembrane orientation of the murine anion exchange protein. *Nature* **316**(6025): 234-8.

Kordeli, E., S. Lambert and V. Bennett (1995) AnkyrinG. A new ankyrin gene with neural-specific isoforms localized at the axonal initial segment and node of Ranvier. *J Biol Chem* **270**(5): 2352-9.

Korsgren, C. and C. M. Cohen (1986) Purification and properties of human erythrocyte band 4.2. Association with the cytoplasmic domain of band 3. *Journal of Biological Chemistry* **261**(12): 5536-43.

Korsgren, C. and C. M. Cohen (1988) Associations of human erythrocyte band 4.2. Binding to ankyrin and to the cytoplasmic domain of band 3. *J Biol Chem* **263**(21): 10212-8.

Koury, M. J., S. T. Sawyer and S. J. Brandt (2002) New insights into erythropoiesis. *Curr Opin Hematol* **9**(2): 93-100.

Krauss, S. W., A. J. Lo, S. A. Short, M. J. Koury, N. Mohandas and J. A. Chasis (2005) Nuclear substructure reorganization during late-stage erythropoiesis is selective and does not involve caspase cleavage of major nuclear substructural proteins. *Blood* **106**(6): 2200-5.

Kuhn, H., J. Belkner, R. Wiesner and A. R. Brash (1990) Oxygenation of biological membranes by the pure reticulocyte lipoxygenase. *J Biol Chem* **265**(30): 18351-61.

Kuma, H., A. A. Shinde, T. R. Howren and M. L. Jennings (2002) Topology of the anion exchange protein AE1: the controversial sidedness of lysine 743. *Biochemistry* **41**(10): 3380-8.

LaConte, L. E., V. Voelz, W. Nelson, M. Enz and D. D. Thomas (2002) Molecular dynamics simulation of site-directed spin labeling: experimental validation in muscle fibers. *Biophys J* **83**(4): 1854-66.

Laemmli, U. K. (1970) Cleavage of structural proteins during the assembly of the head of bacteriophage T4. *Nature* **227**(5259): 680-5.

Lambert, S. and V. Bennett (1993) Postmitotic expression of ankyrinR and beta R-spectrin in discrete neuronal populations of the rat brain. *J Neurosci* **13**(9): 3725-35.

Lambert, S., H. Yu, J. T. Prchal, J. Lawler, P. Ruff, D. Speicher, M. C. Cheung, Y. W. Kan and J. Palek (1990) cDNA sequence for human erythrocyte ankyrin. *Proc Natl Acad Sci U S A* **87**(5): 1730-4.

Langen, R., K. J. Oh, D. Cascio and W. L. Hubbell (2000) Crystal structures of spin labeled T4 lysozyme mutants: implications for the interpretation of EPR spectra in terms of structure. *Biochemistry* **39**(29): 8396-405.

Lee, G., K. Abdi, Y. Jiang, P. Michaely, V. Bennett and P. E. Marszalek (2006) Nanospring behaviour of ankyrin repeats. *Nature*.

Lemieux, M. J., R. A. Reithmeier and D. N. Wang (2002) Importance of detergent and phospholipid in the crystallization of the human erythrocyte anion-exchanger membrane domain. *J Struct Biol* **137**(3): 322-32.

Lepke, S. and H. Passow (1976) Effects of incorporated trypsin on anion exchange and membrane proteins in human red blood cell ghosts. *Biochim Biophys Acta* **455**(2): 353-70.

Letunic, I., L. Goodstadt, N. J. Dickens, T. Doerks, J. Schultz, R. Mott, F. Ciccarelli, R. R. Copley, C. P. Ponting and P. Bork (2002) Recent improvements to the SMART domain-based sequence annotation resource. *Nucleic Acids Res* **30**(1): 242-4.

Levitt, M. H. (2001) Spin Dynamics: Basics of Nuclear Magnetic Resonance. New York, John Wiley & Sons, Inc.

Li, X. and V. Bennett (1996) Identification of the spectrin subunit and domains required for formation of spectrin/adducin/actin complexes. *J Biol Chem* **271**(26): 15695-702.

Li, Z. P., E. P. Burke, J. S. Frank, V. Bennett and K. D. Philipson (1993) The cardiac Na+-Ca2+ exchanger binds to the cytoskeletal protein ankyrin. *J Biol Chem* **268**(16): 11489-91.

Linn, S. C., K. E. Kudrycki and G. E. Shull (1992) The predicted translation product of a cardiac AE3 mRNA contains an N terminus distinct from that of the brain AE3 Cl-/HCO3- exchanger. Cloning of a cardiac AE3 cDNA, organization of the AE3 gene, and identification of an alternative transcription initiation site. *J Biol Chem* **267**(11): 7927-35.

Liu, S. C., L. H. Derick and J. Palek (1987) Visualization of the hexagonal lattice in the erythrocyte membrane skeleton. *J Cell Biol* **104**(3): 527-36.

Liu, Y. S., P. Sompornpisut and E. Perozo (2001) Structure of the KcsA channel intracellular gate in the open state. *Nat Struct Biol* **8**(10): 883-7.

Lokeshwar, V. B., N. Fregien and L. Y. Bourguignon (1994) Ankyrin-binding domain of CD44(GP85) is required for the expression of hyaluronic acid-mediated adhesion function. *J Cell Biol* **126**(4): 1099-109.

Lopez, C., S. Metral, D. Eladari, S. Drevensek, P. Gane, R. Chambrey, V. Bennett, J. P. Cartron, C. Le Van Kim and Y. Colin (2005) The ammonium transporter RhBG: requirement of a tyrosine-based signal and ankyrin-G for basolateral targeting and membrane anchorage in polarized kidney epithelial cells. *J Biol Chem* **280**(9): 8221-8.

Low, P. S. (1986) Structure and function of the cytoplasmic domain of band 3: center of erythrocyte membrane-peripheral protein interactions. *Biochim Biophys Acta* **864**(2): 145-67.

Low, P. S., P. Rathinavelu and M. L. Harrison (1993) Regulation of glycolysis via reversible enzyme binding to the membrane protein, band 3. *Journal of Biological Chemistry* **268**(20): 14627-31.

Low, P. S., M. A. Westfall, D. P. Allen and K. C. Appell (1984) Characterization of the reversible conformational equilibrium of the cytoplasmic domain of erythrocyte membrane band 3. *J Biol Chem* **259**(21): 13070-6.

Low, P. S., B. M. Willardson, N. Mohandas, M. Rossi and S. Shohet (1991) Contribution of the band 3-ankyrin interaction to erythrocyte membrane mechanical stability. *Blood* **77**(7): 1581-6.

Low, P. S., D. Zhang and J. T. Bolin (2001) Localization of mutations leading to altered cell shape and anion transport in the crystal structure of the cytoplasmic domain of band 3. *Blood Cells Mol Dis* **27**(1): 81-4.

Lundberg, S., V. P. Lehto and L. Backman (1992) Characterization of calcium binding to spectrins. *Biochemistry* **31**(24): 5665-71.

Lux, S. E., K. M. John and V. Bennett (1990) Analysis of cDNA for human erythrocyte ankyrin indicates a repeated structure with homology to tissue-differentiation and cell-cycle control proteins. *Nature* **344**(6261): 36-42.

Lux, S. E., K. M. John, R. R. Kopito and H. F. Lodish (1989) Cloning and characterization of band 3, the human erythrocyte anion- exchange protein (AE1). *Proc Natl Acad Sci U S A* **86**(23): 9089-93.

Macke, T. and D. A. Case (1998) Modeling unusual nucleic acid structures. Molecular Modeling of Nucleic Acids. N. B. Leontes and J. J. SantaLucia. Washington, DC, American Chemical Society**:** 379-393.

Malhotra, J. D., K. Kazen-Gillespie, M. Hortsch and L. L. Isom (2000) Sodium channel beta subunits mediate homophilic cell adhesion and recruit ankyrin to points of cell-cell contact. *J Biol Chem* **275**(15): 11383-8.

Malik, S., M. Sami and A. Watts (1993) A role for band 4.2 in human erythrocyte band 3 mediated anion transport. *Biochemistry* **32**(38): 10078-84.

Mansoor, S. E., H. S. McHaourab and D. L. Farrens (1999) Determination of protein secondary structure and solvent accessibility using site-directed fluorescence labeling. Studies of T4 lysozyme using the fluorescent probe monobromobimane. *Biochemistry* **38**(49): 16383-93.

Marfatia, S. M., R. A. Leu, D. Branton and A. H. Chishti (1995) Identification of the protein 4.1 binding interface on glycophorin C and p55, a homologue of the Drosophila discs-large tumor suppressor protein. *J Biol Chem* **270**(2): 715-9.

Markovich, D. (2001) Physiological roles and regulation of mammalian sulfate transporters. *Physiol Rev* **81**(4): 1499-533.

Martinez-Anso, E., J. E. Castillo, J. Diez, J. F. Medina and J. Prieto (1994) Immunohistochemical detection of chloride/bicarbonate anion exchangers in human liver. *Hepatology* **19**(6): 1400-6.

McHaourab, H. S., M. A. Lietzow, K. Hideg and W. L. Hubbell (1996) Motion of spin-labeled side chains in T4 lysozyme. Correlation with protein structure and dynamics. *Biochemistry* **35**(24): 7692-704.

McNulty, J. C., J. L. Silapie, M. Carnevali, C. T. Farrar, R. G. Griffin, F. Formaggio, M. Crisma, C. Toniolo and G. L. Millhauser (2000) Electron spin resonance of TOAC labeled peptides: folding transitions and high frequency spectroscopy. *Biopolymers* **55**(6): 479-85.

Merianos, H. J., N. Cadieux, C. H. Lin, R. J. Kadner and D. S. Cafiso (2000) Substrate-induced exposure of an energy-coupling motif of a membrane transporter. *Nat Struct Biol* **7**(3): 205-9.

Michaely, P. and V. Bennett (1993) The membrane-binding domain of ankyrin contains four independently folded subdomains, each comprised of six ankyrin repeats. *J Biol Chem* **268**(30): 22703-9.

Michaely, P. and V. Bennett (1995a) The ANK repeats of erythrocyte ankyrin form two distinct but cooperative binding sites for the erythrocyte anion exchanger. *J Biol Chem* **270**(37): 22050-7.

Michaely, P. and V. Bennett (1995b) Mechanism for binding site diversity on ankyrin. Comparison of binding sites on ankyrin for neurofascin and the Cl-/HCO3- anion exchanger. *J Biol Chem* **270**(52): 31298-302.

Michaely, P., A. Kamal, R. G. Anderson and V. Bennett (1999) A requirement for ankyrin binding to clathrin during coated pit budding. *J Biol Chem* **274**(50): 35908-13.

Michaely, P., D. R. Tomchick, M. Machius and R. G. Anderson (2002) Crystal structure of a 12 ANK repeat stack from human ankyrinR. *Embo J* **21**(23): 6387-96.

Michel, F., M. Soler-Lopez, C. Petosa, P. Cramer, U. Siebenlist and C. W. Muller (2001) Crystal structure of the ankyrin repeat domain of Bcl-3: a unique member of the IkappaB protein family. *Embo J* **20**(22): 6180-90.

Millhauser, G. L., A. A. Carter, D. J. Schneider, J. H. Freed and R. E. Oswald (1989) Rapid Singular Value Decomposition for Time-Domain Analysis of Magnetic-Resonance Signals by Use of the Lanczos-Algorithm. *Journal of Magnetic Resonance* **82**(1): 150-155.

Mohler, P. J. and V. Bennett (2005a) Ankyrin-based cardiac arrhythmias: a new class of channelopathies due to loss of cellular targeting. *Curr Opin Cardiol* **20**(3): 189-93.

Mohler, P. J. and V. Bennett (2005b) Defects in ankyrin-based cellular pathways in metazoan physiology. *Front Biosci* **10**: 2832-40.

Mohler, P. J., A. O. Gramolini and V. Bennett (2002) The ankyrin-B C-terminal domain determines activity of ankyrin-B/G chimeras in rescue of abnormal inositol 1,4,5-

trisphosphate and ryanodine receptor distribution in ankyrin-B (-/-) neonatal cardiomyocytes. *J Biol Chem* **277**(12): 10599-607.

Mohler, P. J., J. A. Hoffman, J. Q. Davis, K. M. Abdi, C. R. Kim, S. K. Jones, L. H. Davis, K. F. Roberts and V. Bennett (2004a) Isoform specificity among ankyrins. An amphipathic alpha-helix in the divergent regulatory domain of ankyrin-b interacts with the molecular co-chaperone Hdj1/Hsp40. *J Biol Chem* **279**(24): 25798-804.

Mohler, P. J., I. Rivolta, C. Napolitano, G. LeMaillet, S. Lambert, S. G. Priori and V. Bennett (2004b) Nav1.5 E1053K mutation causing Brugada syndrome blocks binding to ankyrin-G and expression of Nav1.5 on the surface of cardiomyocytes. *Proc Natl Acad Sci U S A* **101**(50): 17533-8.

Mohler, P. J., J. J. Schott, A. O. Gramolini, K. W. Dilly, S. Guatimosim, W. H. duBell, L. S. Song, K. Haurogne, F. Kyndt, M. E. Ali, T. B. Rogers, W. J. Lederer, D. Escande, H. Le Marec and V. Bennett (2003) Ankyrin-B mutation causes type 4 long-QT cardiac arrhythmia and sudden cardiac death. *Nature* **421**(6923): 634-9.

Mohler, P. J., I. Splawski, C. Napolitano, G. Bottelli, L. Sharpe, K. Timothy, S. G. Priori, M. T. Keating and V. Bennett (2004c) A cardiac arrhythmia syndrome caused by loss of ankyrin-B function. *Proc Natl Acad Sci U S A* **101**(24): 9137-42.

Mohler, P. J., W. Yoon and V. Bennett (2004d) Ankyrin-B targets beta2-spectrin to an intracellular compartment in neonatal cardiomyocytes. *J Biol Chem* **279**(38): 40185-93.

Monaco, V., F. Formaggio, M. Crisma, C. Toniolo, P. Hanson and G. L. Millhauser (1999) Orientation and immersion depth of a helical lipopeptaibol in membranes using TOAC as an ESR probe. *Biopolymers* **50**(3): 239-53.

Moores, C. A., N. H. Keep and J. Kendrick-Jones (2000) Structure of the utrophin actin-binding domain bound to F-actin reveals binding by an induced fit mechanism. *J Mol Biol* **297**(2): 465-80.

Morgans, C. W. and R. R. Kopito (1993) Association of the brain anion exchanger, AE3, with the repeat domain of ankyrin. *J Cell Sci* **105 (Pt 4)**: 1137-42.

Moriyama, R., H. Ideguchi, C. R. Lombardo, H. M. Van Dort and P. S. Low (1992) Structural and functional characterization of band 3 from Southeast Asian ovalocytes. *Journal of Biological Chemistry* **267**(36): 25792-7.

Morrow, J. S., C. D. Cianci, T. Ardito, A. S. Mann and M. Kashgarian (1989) Ankyrin links fodrin to the alpha subunit of Na,K-ATPase in Madin-Darby canine kidney cells and in intact renal tubule cells. *J Cell Biol* **108**(2): 455-65.

Mosavi, L. K., T. J. Cammett, D. C. Desrosiers and Z. Y. Peng (2004) The ankyrin repeat as molecular architecture for protein recognition. *Protein Sci* **13**(6): 1435-48.

Mueller, T. J. and M. Morrison (1977) Detection of a variant of protein 3, the major transmembrane protein of the human erythrocyte. *Journal of Biological Chemistry* **252**(19): 6573-6.

Murthy, S. N., T. Liu, R. K. Kaul, H. Kohler and T. L. Steck (1981) The aldolase-binding site of the human erythrocyte membrane is at the NH2 terminus of band 3. *J Biol Chem* **256**(21): 11203-8.

Nelson, W. J. and P. J. Veshnock (1987) Ankyrin binding to (Na+ + K+)ATPase and implications for the organization of membrane domains in polarized cells. *Nature* **328**(6130): 533-6.

Nigg, E. and R. J. Cherry (1979) Dimeric association of band 3 in the erythrocyte membrane demonstrated by protein diffusion measurements. *Nature* **277**(5696): 493-4.

Nigg, E. A. and R. J. Cherry (1980) Anchorage of a band 3 population at the erythrocyte cytoplasmic membrane surface: protein rotational diffusion measurements. *Proc Natl Acad Sci U S A* **77**(8): 4702-6.

Otto, E., M. Kunimoto, T. McLaughlin and V. Bennett (1991) Isolation and characterization of cDNAs encoding human brain ankyrins reveal a family of alternatively spliced genes. *J Cell Biol* **114**(2): 241-53.

Pake, G. E. (1948) Nuclear Resonance Absorption in Hydrated Crystals: Fine Structure of the Proton Line. *The Journal of Chemical Physics* **16**(4): 327-336.

Pal, P., B. Holmberg, J. Lesiione and P. A. Knauf (2005a) Effects of pH and peripheral protein binding on the structure of the cytoplasmic domain of AE1 observed by resonance energy transfer. *Biophys J* **88**: 47a (abstract).

Pal, P., B. E. Holmberg and P. A. Knauf (2005b) Conformational changes in the cytoplasmic domain of human anion exchanger 1 revealed by luminescence resonance energy transfer. *Biochemistry* **44**(42): 13638-49.

Pannier, M., S. Veit, A. Godt, G. Jeschke and H. W. Spiess (2000) Dead-time free measurement of dipole-dipole interactions between electron spins. *Journal of Magnetic Resonance* **142**(2): 331-40.

Pasternack, G. R., R. A. Anderson, T. L. Leto and V. T. Marchesi (1985) Interactions between protein 4.1 and band 3. An alternative binding site for an element of the membrane skeleton. *J Biol Chem* **260**(6): 3676-83.

Paw, B. H., A. J. Davidson, Y. Zhou, R. Li, S. J. Pratt, C. Lee, N. S. Trede, A. Brownlie, A. Donovan, E. C. Liao, J. M. Ziai, A. H. Drejer, W. Guo, C. H. Kim, B. Gwynn, L. L. Peters, M. N. Chernova, S. L. Alper, A. Zapata, S. N. Wickramasinghe, M. J. Lee, S. E. Lux, A. Fritz, J. H. Postlethwait and L. I. Zon (2003) Cell-specific mitotic defect and dyserythropoiesis associated with erythroid band 3 deficiency. *Nat Genet* **34**(1): 59-64.

Pawloski, J. R., D. T. Hess and J. S. Stamler (2001) Export by red blood cells of nitric oxide bioactivity.[see comment]. *Nature* **409**(6820): 622-6.

Pawloski, J. R. and J. S. Stamler (2002) Nitric oxide in RBCs.[comment]. *Transfusion* **42**(12): 1603-9.

Perozo, E., D. M. Cortes and L. G. Cuello (1999) Structural rearrangements underlying K+-channel activation gating. *Science* **285**(5424): 73-8.

Perozo, E., D. M. Cortes, P. Sompornpisut, A. Kloda and B. Martinac (2002) Open channel structure of MscL and the gating mechanism of mechanosensitive channels. *Nature* **418**(6901): 942-8.

Perry, C. and H. Soreq (2002) Transcriptional regulation of erythropoiesis. Fine tuning of combinatorial multi-domain elements. *Eur J Biochem* **269**(15): 3607-18.

Peters, L. L., K. M. John, F. M. Lu, E. M. Eicher, A. Higgins, M. Yialamas, L. C. Turtzo, A. J. Otsuka and S. E. Lux (1995) Ank3 (epithelial ankyrin), a widely distributed new member of the ankyrin gene family and the major ankyrin in kidney, is expressed in alternatively spliced forms, including forms that lack the repeat domain. *J Cell Biol* **130**(2): 313-30.

Peters, L. L., R. A. Shivdasani, S. C. Liu, M. Hanspal, K. M. John, J. M. Gonzalez, C. Brugnara, B. Gwynn, N. Mohandas, S. L. Alper, S. H. Orkin and S. E. Lux (1996) Anion exchanger 1 (band 3) is required to prevent erythrocyte membrane surface loss but not to form the membrane skeleton. *Cell* **86**(6): 917-27.

Philipp, R., J. O. McIntyre, B. H. Robinson, H. Huth, W. Trommer and S. Fleischer (1984) The synthesis of 15N- and deuterium-substituted, spin-labeled analogues of NAD+ and their use in EPR studies of dehydrogenases. *Biochim Biophys Acta* **790**(3): 251-8.

Poirier, M. A., W. Xiao, J. C. Macosko, C. Chan, Y. K. Shin and M. K. Bennett (1998) The synaptic SNARE complex is a parallel four-stranded helical bundle. *Nat Struct Biol* **5**(9): 765-9.

Popov, M., L. Y. Tam, J. Li and R. A. Reithmeier (1997) Mapping the ends of transmembrane segments in a polytopic membrane protein. Scanning N-

glycosylation mutagenesis of extracytosolic loops in the anion exchanger, band 3. *J Biol Chem* **272**(29): 18325-32.

Prisner, T., M. Rohrer and F. MacMillan (2001) Pulsed EPR spectroscopy: biological applications. *Annu Rev Phys Chem* **52**: 279-313.

Pyka, J., J. Ilnicki, C. Altenbach, W. L. Hubbell and W. Froncisz (2005) Accessibility and dynamics of nitroxide side chains in T4 lysozyme measured by saturation recovery EPR. *Biophys J* **89**(3): 2059-68.

Quilty, J. A., E. Cordat and R. A. Reithmeier (2002) Impaired trafficking of human kidney anion exchanger (kAE1) caused by hetero-oligomer formation with a truncated mutant associated with distal renal tubular acidosis. *Biochem J* **368**(Pt 3): 895-903.

Rabenstein, M. D. and Y. K. Shin (1995) Determination of the distance between two spin labels attached to a macromolecule. *Proc Natl Acad Sci U S A* **92**(18): 8239-43.

Ranney, H. M., G. H. Rosenberg, M. Morrison and T. J. Mueller (1990) Frequencies of Band 3 variants of human red cell membranes in some different populations. *British Journal of Haematology* **75**(2): 262-7.

Retelewska, W., M. Gaczynska, G. Bartosz and L. Judkiewicz (1991) Consequences of the presence of elongated variant of the major transmembrane protein (Band 3 protein) in the human erythrocyte. *Clinica Chimica Acta* **198**(3): 255-60.

Richardson, J. S. (1981) The anatomy and taxonomy of protein structure. *Adv Protein Chem* **34**: 167-339.

Rief, M., J. Pascual, M. Saraste and H. E. Gaub (1999) Single molecule force spectroscopy of spectrin repeats: low unfolding forces in helix bundles. *J Mol Biol* **286**(2): 553-61.

Robinson, B. H., L. J. Slutsky and F. P. Auteri (1992) Direct Simulation of Continuous Wave Electron-Paramagnetic Resonance-Spectra from Brownian Dynamics Trajectories. *Journal of Chemical Physics* **96**(4): 2609-2616.

Rogalski, A. A., T. L. Steck and A. Waseem (1989) Association of glyceraldehyde-3-phosphate dehydrogenase with the plasma membrane of the intact human red blood cell. *J Biol Chem* **264**(11): 6438-46.

Russo, A. A., L. Tong, J. O. Lee, P. D. Jeffrey and N. P. Pavletich (1998) Structural basis for inhibition of the cyclin-dependent kinase Cdk6 by the tumour suppressor p16INK4a. *Nature* **395**(6699): 237-43.

Rybicki, A. C., J. J. Qiu, S. Musto, N. L. Rosen, R. L. Nagel and R. S. Schwartz (1993) Human erythrocyte protein 4.2 deficiency associated with hemolytic anemia and a homozygous 40glutamic acid-->lysine substitution in the cytoplasmic domain of band 3 (band 3Montefiore). *Blood* **81**(8): 2155-65.

Rybicki, A. C., R. S. Schwartz, E. J. Hustedt and C. E. Cobb (1996) Increased rotational mobility and extractability of band 3 from protein 4.2-deficient erythrocyte membranes: evidence of a role for protein 4.2 in strengthening the band 3-cytoskeleton linkage. *Blood* **88**(7): 2745-53.

Sahr, K. E., W. M. Taylor, B. P. Daniels, H. L. Rubin and P. Jarolim (1994) The structure and organization of the human erythroid anion exchanger (AE1) gene. *Genomics* **24**(3): 491-501.

Sale, K., C. Sar, K. A. Sharp, K. Hideg and P. G. Fajer (2002) Structural determination of spin label immobilization and orientation: a Monte Carlo minimization approach. *J Magn Reson* **156**(1): 104-12.

Salhany, J. M. and R. Cassoly (1989) Kinetics of p-mercuribenzoate binding to sulfhydryl groups on the isolated cytoplasmic fragment of band 3 protein. Effect of hemoglobin binding on the conformation. *J Biol Chem* **264**(3): 1399-404.

Salhany, J. M., K. A. Cordes and R. L. Sloan (1998) Characterization of the pH dependence of hemoglobin binding to band 3. Evidence for a pH-dependent conformational change within the hemoglobin- band 3 complex. *Biochim Biophys Acta* **1371**(1): 107-13.

Schiemann, O., N. Piton, Y. Mu, G. Stock, J. W. Engels and T. F. Prisner (2004) A PELDOR-based nanometer distance ruler for oligonucleotides. *J Am Chem Soc* **126**(18): 5722-9.

Schneider, M. L. and C. B. Post (1995) Solution structure of a band 3 peptide inhibitor bound to aldolase: a proposed mechanism for regulating binding by tyrosine phosphorylation. *Biochemistry* **34**(51): 16574-84.

Schofield, A. E., M. J. Tanner, J. C. Pinder, B. Clough, P. M. Bayley, G. B. Nash, A. R. Dluzewski, D. M. Reardon, T. M. Cox and R. J. Wilson (1992) Basis of unique red cell membrane properties in hereditary ovalocytosis. *Journal of Molecular Biology* **223**(4): 949-58.

Schott, J. J., F. Charpentier, S. Peltier, P. Foley, E. Drouin, J. B. Bouhour, P. Donnelly, G. Vergnaud, L. Bachner, J. P. Moisan and et al. (1995) Mapping of a gene for long QT syndrome to chromosome 4q25-27. *Am J Hum Genet* **57**(5): 1114-22.

Schultz, J., F. Milpetz, P. Bork and C. P. Ponting (1998) SMART, a simple modular architecture research tool: identification of signaling domains. *Proc Natl Acad Sci U S A* **95**(11): 5857-64.

Scotland, P., D. Zhou, H. Benveniste and V. Bennett (1998) Nervous system defects of AnkyrinB (-/-) mice suggest functional overlap between the cell adhesion molecule L1 and 440-kD AnkyrinB in premyelinated axons. *J Cell Biol* **143**(5): 1305-15.

Sedgwick, S. G. and S. J. Smerdon (1999) The ankyrin repeat: a diversity of interactions on a common structural framework. *Trends Biochem Sci* **24**(8): 311-6.

Skalak, R. and P. I. Branemark (1969) Deformation of red blood cells in capillaries. *Science* **164**(880): 717-9.

Slichter, C. P. (1980). Principles of Magnetic Resonance. Berlin Heidelberg New York, Springer-Verlag**:** 69.

Smith, P. R., A. L. Bradford, E. H. Joe, K. J. Angelides, D. J. Benos and G. Saccomani (1993) Gastric parietal cell H(+)-K(+)-ATPase microsomes are associated with isoforms of ankyrin and spectrin. *Am J Physiol* **264**(1 Pt 1): C63-70.

Southgate, C. D., A. H. Chishti, B. Mitchell, S. J. Yi and J. Palek (1996) Targeted disruption of the murine erythroid band 3 gene results in spherocytosis and severe haemolytic anaemia despite a normal membrane skeleton. *Nat Genet* **14**(2): 227-30.

Srinivasan, Y., L. Elmer, J. Davis, V. Bennett and K. Angelides (1988) Ankyrin and spectrin associate with voltage-dependent sodium channels in brain. *Nature* **333**(6169): 177-80.

Srinivasan, Y., M. Lewallen and K. J. Angelides (1992) Mapping the binding site on ankyrin for the voltage-dependent sodium channel from brain. *J Biol Chem* **267**(11): 7483-9.

Staros, J. V. and B. P. Kakkad (1983) Cross-linking and chymotryptic digestion of the extracytoplasmic domain of the anion exchange channel in intact human erythrocytes. *J Membr Biol* **74**(3): 247-54.

Steck, T. L. (1972) Cross-linking the major proteins of the isolated erythrocyte membrane. *J Mol Biol* **66**(2): 295-305.

Steck, T. L., B. Ramos and E. Strapazon (1976) Proteolytic dissection of band 3, the predominant transmembrane polypeptide of the human erythrocyte membrane. *Biochemistry* **15**(5): 1153-61.

Stein, R. A., S. Brandon and E. J. Hustedt (2004) Dipolar coupling between nitroxide spin labels: the development of a tether in a cone model. *Biophys J* **86**: 484a (abstract).

Steiner, J. P. and V. Bennett (1988) Ankyrin-independent membrane protein-binding sites for brain and erythrocyte spectrin. *J Biol Chem* **263**(28): 14417-25.

Steiner, J. P., H. T. Walke, Jr. and V. Bennett (1989) Calcium/calmodulin inhibits direct binding of spectrin to synaptosomal membranes. *J Biol Chem* **264**(5): 2783-91.

Steinhoff, H. J., N. Radzwill, W. Thevis, V. Lenz, D. Brandenburg, A. Antson, G. Dodson and A. Wollmer (1997) Determination of interspin distances between spin labels attached to insulin: comparison of electron paramagnetic resonance data with the X-ray structure. *Biophys J* **73**(6): 3287-98.

Sterling, D. and J. R. Casey (2002) Bicarbonate transport proteins. *Biochem Cell Biol* **80**(5): 483-97.

Sterling, D., R. A. Reithmeier and J. R. Casey (2001) A transport metabolon. Functional interaction of carbonic anhydrase II and chloride/bicarbonate exchangers. *J Biol Chem* **276**(51): 47886-94.

Stuart-Tilley, A., C. Sardet, J. Pouyssegur, M. A. Schwartz, D. Brown and S. L. Alper (1994) Immunolocalization of anion exchanger AE2 and cation exchanger NHE-1 in distinct adjacent cells of gastric mucosa. *Am J Physiol* **266**(2 Pt 1): C559-68.

Studier, F. W. (2005) Protein production by auto-induction in high-density shaking cultures. *Protein Expr Purif* **41**(1): 207-234.

Subczynski, W. K. and J. S. Hyde (1981) The diffusion-concentration product of oxygen in lipid bilayers using the spin-label T1 method. *Biochim Biophys Acta* **643**(2): 283-91.

Tang, X. B. and J. R. Casey (1999) Trapping of inhibitor-induced conformational changes in the erythrocyte membrane anion exchanger AE1. *Biochemistry* **38**(44): 14565-72.

Tanner, M. J. (1993) Molecular and cellular biology of the erythrocyte anion exchanger (AE1). *Semin Hematol* **30**(1): 34-57.

Tanner, M. J. (1997) The structure and function of band 3 (AE1): recent developments (review). *Mol Membr Biol* **14**(4): 155-65.

Tanner, M. J., P. G. Martin and S. High (1988) The complete amino acid sequence of the human erythrocyte membrane anion-transport protein deduced from the cDNA sequence. *Biochemical Journal* **256**(3): 703-12.

Tchernia, G., N. Mohandas and S. B. Shohet (1981) Deficiency of skeletal membrane protein band 4.1 in homozygous hereditary elliptocytosis. Implications for erythrocyte membrane stability. *J Clin Invest* **68**(2): 454-60.

Thevananther, S., A. H. Kolli and P. Devarajan (1998) Identification of a novel ankyrin isoform (AnkG190) in kidney and lung that associates with the plasma membrane and binds alpha-Na, K-ATPase. *J Biol Chem* **273**(37): 23952-8.

Thevenin, B. J. and P. S. Low (1990) Kinetics and regulation of the ankyrin-band 3 interaction of the human red blood cell membrane. *J Biol Chem* **265**(27): 16166-72.

Thevenin, B. J., N. Periasamy, S. B. Shohet and A. S. Verkman (1994) Segmental dynamics of the cytoplasmic domain of erythrocyte band 3 determined by time-resolved fluorescence anisotropy: sensitivity to pH and ligand binding. *Proc Natl Acad Sci U S A* **91**(5): 1741-5.

Toniolo, C., E. Valente, F. Formaggio, M. Crisma, G. Pilloni, C. Corvaja, A. Toffoletti, G. V. Martinez, M. P. Hanson, G. L. Millhauser and et al. (1995) Synthesis and conformational studies of peptides containing TOAC, a spin-labelled C alpha, alpha-disubstituted glycine. *J Pept Sci* **1**(1): 45-57.

Toye, A. M., S. Ghosh, M. T. Young, G. K. Jones, R. B. Sessions, M. Ramauge, P. Leclerc, J. Basu, J. Delaunay and M. J. Tanner (2005) Protein 4.2 association with band 3 (AE1, SLCA4) in Xenopus oocytes: effects of three natural protein 4.2 mutations associated with hemolytic anemia. *Blood*.

Trapp, B. D., J. Peterson, R. M. Ransohoff, R. Rudick, S. Mork and L. Bo (1998) Axonal transection in the lesions of multiple sclerosis. *N Engl J Med* **338**(5): 278-85.

Tschopp, J., F. Martinon and K. Hofmann (1999) Apoptosis: Silencing the death receptors. *Curr Biol* **9**(10): R381-4.

Tse, W. T., M. C. Lecomte, F. F. Costa, M. Garbarz, C. Feo, P. Boivin, D. Dhermy and B. G. Forget (1990) Point mutation in the beta-spectrin gene associated with alpha I/74 hereditary elliptocytosis. Implications for the mechanism of spectrin dimer self-association. *J Clin Invest* **86**(3): 909-16.

Tse, W. T. and S. E. Lux (1999) Red blood cell membrane disorders. *Br J Haematol* **104**(1): 2-13.

Tuvia, S., M. Buhusi, L. Davis, M. Reedy and V. Bennett (1999) Ankyrin-B is required for intracellular sorting of structurally diverse Ca2+ homeostasis proteins. *J Cell Biol* **147**(5): 995-1008.

Tyler, J. M., B. N. Reinhardt and D. Branton (1980) Associations of erythrocyte membrane proteins. Binding of purified bands 2.1 and 4.1 to spectrin. *J Biol Chem* **255**(14): 7034-9.

Van Dort, H. M., R. Moriyama and P. S. Low (1998) Effect of band 3 subunit equilibrium on the kinetics and affinity of ankyrin binding to erythrocyte membrane vesicles. *J Biol Chem* **273**(24): 14819-26.

van Leyen, K., R. M. Duvoisin, H. Engelhardt and M. Wiedmann (1998) A function for lipoxygenase in programmed organelle degradation. *Nature* **395**(6700): 392-5.

Walder, J. A., R. Chatterjee, T. L. Steck, P. S. Low, G. F. Musso, E. T. Kaiser, P. H. Rogers and A. Arnone (1984) The interaction of hemoglobin with the cytoplasmic domain of band 3 of the human erythrocyte membrane. *J Biol Chem* **259**(16): 10238-46.

Wang, C. C., R. Moriyama, C. R. Lombardo and P. S. Low (1995) Partial characterization of the cytoplasmic domain of human kidney band 3. *J Biol Chem* **270**(30): 17892-7.

Wang, D. N. (1994) Band 3 protein: structure, flexibility and function. *FEBS Lett* **346**(1): 26-31.

Wang, D. N., W. Kuhlbrandt, V. E. Sarabia and R. A. Reithmeier (1993) Two-dimensional structure of the membrane domain of human band 3, the anion transport protein of the erythrocyte membrane. *Embo J* **12**(6): 2233-9.

Wang, D. N., V. E. Sarabia, R. A. Reithmeier and W. Kuhlbrandt (1994) Three-dimensional map of the dimeric membrane domain of the human erythrocyte anion exchanger, Band 3. *Embo J* **13**(14): 3230-5.

Wang, D. S. and G. Shaw (1995) The association of the C-terminal region of beta I sigma II spectrin to brain membranes is mediated by a PH domain, does not require membrane proteins, and coincides with a inositol-1,4,5 triphosphate binding site. *Biochem Biophys Res Commun* **217**(2): 608-15.

Waugh, S. M. and P. S. Low (1985) Hemichrome binding to band 3: nucleation of Heinz bodies on the erythrocyte membrane. *Biochemistry* **24**(1): 34-9.

Weber, A., C. R. Pennise, G. G. Babcock and V. M. Fowler (1994) Tropomodulin caps the pointed ends of actin filaments. *J Cell Biol* **127**(6 Pt 1): 1627-35.

Weber, R. E., W. Voelter, A. Fago, H. Echner, E. Campanella and P. S. Low (2004) Modulation of red cell glycolysis: interactions between vertebrate hemoglobins and cytoplasmic domains of band 3 red cell membrane proteins. *American*

Journal of Physiology - Regulatory Integrative & Comparative Physiology **287**(2): R454-64.

Weil, J. A., J. R. Bolton and J. E. Wertz (1994) Electron Paramagnetic Resonance: Elementary Theory and Practical Applications. New York, John Wiley & Sons, Inc.

Weinstein, R. S., J. K. Khodadad and T. L. Steck (1978) Fine structure of the band 3 protein in human red cell membranes: freeze-fracture studies. *J Supramol Struct* **8**(3): 325-35.

Wieth, J. O., O. S. Andersen, J. Brahm, P. J. Bjerrum and C. L. Borders, Jr. (1982) Chloride--bicarbonate exchange in red blood cells: physiology of transport and chemical modification of binding sites. *Philos Trans R Soc Lond B Biol Sci* **299**(1097): 383-99.

Willardson, B. M., B. J. Thevenin, M. L. Harrison, W. M. Kuster, M. D. Benson and P. S. Low (1989) Localization of the ankyrin-binding site on erythrocyte membrane protein, band 3. *J Biol Chem* **264**(27): 15893-9.

Wrong, O., L. J. Bruce, R. J. Unwin, A. M. Toye and M. J. Tanner (2002) Band 3 mutations, distal renal tubular acidosis, and Southeast Asian ovalocytosis. *Kidney Int* **62**(1): 10-9.

Yannoukakos, D., C. Vasseur, C. Driancourt, Y. Blouquit, J. Delaunay, H. Wajcman and E. Bursaux (1991) Human erythrocyte band 3 polymorphism (band 3 Memphis): characterization of the structural modification (Lys 56----Glu) by protein chemistry methods. *Blood* **78**(4): 1117-20.

Zermati, Y., C. Garrido, S. Amsellem, S. Fishelson, D. Bouscary, F. Valensi, B. Varet, E. Solary and O. Hermine (2001) Caspase activation is required for terminal erythroid differentiation. *J Exp Med* **193**(2): 247-54.

Zhang, D., A. Kiyatkin, J. T. Bolin and P. S. Low (2000) Crystallographic structure and functional interpretation of the cytoplasmic domain of erythrocyte membrane band 3. *Blood* **96**(9): 2925-33.

Zhang, X., J. Q. Davis, S. Carpenter and V. Bennett (1998a) Structural requirements for association of neurofascin with ankyrin. *J Biol Chem* **273**(46): 30785-94.

Zhang, Z., P. Devarajan, A. L. Dorfman and J. S. Morrow (1998b) Structure of the ankyrin-binding domain of alpha-Na,K-ATPase. *J Biol Chem* **273**(30): 18681-4.

Zhou, D., S. Lambert, P. L. Malen, S. Carpenter, L. M. Boland and V. Bennett (1998) AnkyrinG is required for clustering of voltage-gated Na channels at axon initial segments and for normal action potential firing. *J Cell Biol* **143**(5): 1295-304.

Zhou, J. and P. S. Low (2001) Characterization of the reversible conformational equilibrium in the cytoplasmic domain of human erythrocyte membrane band 3. *J Biol Chem* **276**(41): 38147-51.

Zhou, Z., S. Desensi, S. Brandon, N. Dixit, C. E. Cobb, E. J. Hustedt and A. H. Beth (2005a) Solution structure of cdb3 from site directed spin labeling studies and double electron-electron resonance. *Biophys J* **88**: 265a (abstract).

Zhou, Z., S. C. DeSensi, R. A. Stein, S. Brandon, M. Dixit, E. J. McArdle, E. M. Warren, H. K. Kroh, L. Song, C. E. Cobb, E. J. Hustedt and A. H. Beth (2005b) Solution structure of the cytoplasmic domain of erythrocyte membrane band 3 determined by site-directed spin labeling. *Biochemistry* **44**(46): 15115-28.

Zhu, Q., D. W. Lee and J. R. Casey (2003) Novel topology in C-terminal region of the human plasma membrane anion exchanger, AE1. *J Biol Chem* **278**(5): 3112-20.

Zimmerman, S. S. and H. A. Scheraga (1976) Stability of cis, trans, and nonplanar peptide groups. *Macromolecules* **9**(3): 408-16.